UTM/RMC/F/0024(1998)

UNIVERSITI TEKNOLOGI MALAYSIA

BORANG PENGESAHAN
LAPORAN AKHIR PENYELIDIKAN

TAJUK PROJEK : PRESTASI SALURAN ALIRAN LAJU DI KAWASAN MUDAH BANJIR

Saya : Dr. NOOR BAHARIM BIN HAHIM
(HURUF BESAR)

Mengaku membenarkan Laporan Akhir Penyelidikan ini disimpan di Perpustakaan Universiti Teknologi Malaysia dengan syarat-syarat kegunaan seperti berikut : -

1. Laporan Akhir Penyelidikan adalah hakmilik Universiti Teknologi Malaysia.

2. Perpustakaan Universiti Teknologi Malaysia dibenarkan membuat salinan untuk tujuan rujukan sahaja.

3. Perpustakaan dibenarkan membuat penjualan salinan Laporan Akhir Penyelidikan ini bagi kategori TIDAK TERHAD.

4. Sila tandakan (/)

☐	**SULIT**	(Megandungi maklumat yang berdarjah keselamatan atau kepentingan Malaysia seperti yang termaktub di dalam **AKTA RAHSIA RASMI 1972**)
☐	**TERHAD**	(Mengandungi maklumat **TERHAD** yang telah ditentukan oleh organisasi/badan di mana penyelidikan dijalankan)
☐	**TIDAK TERHAD**	

……………………………………………….
(TANDATANGAN KETUA PENYELIDIK)

……………………………………………….
Nama & Cop Ketua Penyelidik

Tarikh : ………………………..

CATATAN : *Jika Lapotran Akhir Penyelidikan ini SULIT atau TERHAD, sila lampirkan surat daripada pihak berkuasa/organisasi berkenaan dengan menyatakan sekali sebab dan tempoh laporan ini perlu dikelaskan sebagai SULIT dan TERHAD.*

ne&n/99

VOT 71840

PERFORMANCE OF HIGH-VELOCITY CHANNELS IN FLOOD-PRONE AREAS

(PRESTASI SALURAN ALIRAN LAJU DI KAWASAN MUDAH BANJIR)

NOOR BAHARIM HASHIM, Ph.D.
DAVID H. HUDDLESTON, Ph.D.
ZULKIFLEE IBRAHIM, MSc.
NG BOON CHONG, BSc.

RESEARCH VOTE NO:
71840

Department of Hydraulics & Hydrology
Faculty of Civil Engineering
Universiti Teknologi Malaysia

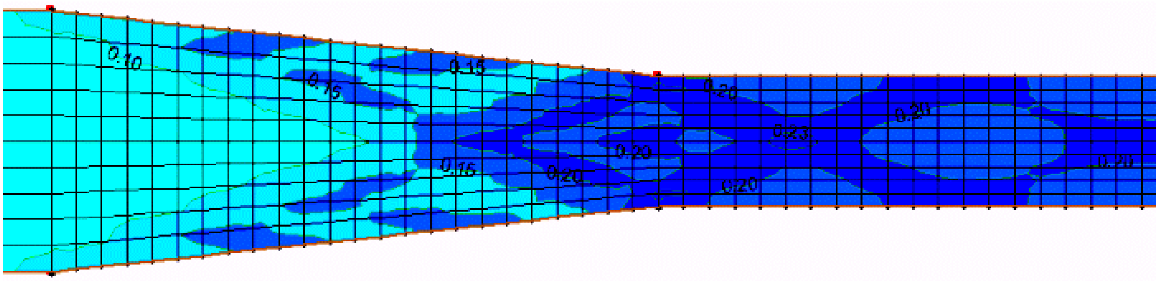

2005

I declare that this thesis entitled “*Numerical Simulation of Free Surface Flow in Open Channel*” is the result of my own research except as cited in the references. The thesis has not been accepted for any degree and is not concurrently submitted in candidature of any other degree.

Signature : ……………………………………
Name : NG BOON CHONG
Date : NOV 2005

To every single life that I care
ant, seed, farmer and stone
ng5207@yahoo.com

ABSTRACT

The presence of disturbances such as bends, contraction, expansion, junction, bridge piers in a drainage system is very common in Malaysia. These hydraulic structures often cause the channel flow to choke and form standing waves. Numerical modelling is a reasonable approach to study these problems. The challenges for this numerical model lie in representing supercritical transition and capturing shocks. For this purpose, an unstructured two-dimensional finite-element model is used to solve the governing shallow water equations. This numerical model utilizes a characteristic based Petrov-Galerkin method implemented with shock-detection mechanism. The model testing demonstrates the ability of this numerical model to reproduce the speed and height of flow with the presence of channel contractions, weir, and bridge pier under different flow conditions. The numerical model results are compared quantitatively with experimental results, published numerical simulation and analytical solution. The model was also applied to Sg Segget and Sg Sepakat channels in evaluating the channels performance. In general, the numerical model satisfactorily computed the water-surface profiles of the experimental data and exact solutions. The results demonstrate that the numerical model provide an alternative tool in validating theoretical finding and determining appropriate designs for flood channels to meet site-specific criteria.

ABSTRAK

Kehadiran struktur-struktur dalam sistem saluran seperti bengkokan saluran, pengecilan dan pengembangan lebar, sambungan saluran, dan tiang jambatan adalah amat umum di Malaysia. Struktur hidraulik ini sering mengakibatkan aliran dalam saluran bergelora dan mewujudkan gelombang tegak. Model berangka adalah satu kaedah yang munasabah untuk mengkaji masalah-masalah ini. Cabaran-cabaran yang dihadapi oleh model ini termasuklah memapar semula aliran genting dan juga gelombang tegak dalam model. Untuk tujuan ini, satu model berunsur terhingga dalam dua dimensi telah digunakan untuk menyelesaikan persamaan '*shallow water equation*'. Model ini mempergunakan sifat berdasarkan kaedah *Petrov-Galerkin* beserta dengan mekanisme pengesanan kejutan gelombang. Ujian-ujian model mempamerkan kebolehan model berangka ini dalam menghasilkan semula kelajuan dan kedalaman aliran di sesuatu saluran yang memiliki struktur pengecilan, empangan, atau tiang jambatan di bawah keadaan saliran yang berbeza-beza. Keputusan dari model berangka ini dibandingkan kuantitinya dengan keputusan eksperimen dan penyelesaian analitik. Model berangka ini juga telah digunakan bagi menilai kemampuan saluran konkrit Sg Segget dan Sg Sepakat. Secara umum, model berangka berjaya menghasilkan profil permukaan air dari eksperimen dan penyelesaian analitikal. Keputusan menunjukkan bahawa model berangka ini telah memperkenalkan cara alternatif dalam pengesahan sesuatu penemuan teori, dan juga penentuan reka bentuk bagi saliran yang bermasalah banjir dengan memenuhi kriteria tentu.

LIST OF TABLES

TABLE OF CONTENTS

APPENDIX A
APPENDIX B

LIST OF FIGURES

LIST OF SYMBOLS

$\overline{E}$ - Average element energy over the entire grid
$\overline{E}_i$ - Average energy of element *i*
ψ_i - Equal to $\phi_i I + \varphi_i$
ϕ_i - Galerkin part of the test function
φ_i - Non-Galerkin part of the test function
Δl - Element length
Δt - Time step size
a_i - Area of element *i*
B - Width
B.C. - Boundary Contition
C_0 - Conversion coefficient (C_0 =1 for SI units and 2.208 for non-SI units);
CFL - Courant-Friedrichs-Lewy
d_i - Water depth at section i
E - Mechanical energy distribution within the element
E' - Error = $Lu_{\mathrm{approx}} - f(x_j)$
ED_i - *E*lement *i* energy deviation
$f(x_j)$ - Function in x variable, it can be a constant
$F_1\theta$ - Shock number
Fi - Froude number at section i
Fr - Froude number
g - Acceleration due to gravity;
h - Depth;
h* - h/B
H_{min} - Minimum head energy
I - Identity Matrix

L - Differential operator in finite-element model
L - Length for a object in experiment
n - Manning's coefficient
N_r - Weighting functions
of depth-averaged velocity;
p - uh, x-direction discharge per unit width where u being x-component
of depth-averaged velocity;
Q - Discharge rate
q - vh, y-direction discharge per unit width where v being y-component
q* - Ratio of Qm/Qt
Qb - Branch channel flow
Qm - Main channel flow
Qt - Total flow
R - Radius of curvature of the centreline of the channel
S - Slope gradient
SD - Standard deviation of all ED_i
Sub - Subcritical flow
Super - Supercritical flow
t - Time
u* - Dimensionless velocity along y-axis
u_{approx} - Approximate of dependent variable
u_i - Longitudinal velocity
V - Flow velocity
v* - Dimensionless velocity along x-axis
x - Longitudinal direction
x* - x/B
y - Lateral direction
y - Vertical water depth
y* - y/B
y_o - Normal depth
z - Vertical direction
z* - z/B
Z_0 - Channel bed elevation;
β - Dissipation coefficient

$\beta1,\beta2$ - Wavefront angles

θ - Angle of deflection

ρ - Fluid density;

Σ - Reynolds stresses due to turbulence

LIST OF APPENDIX

CHAPTER 1

INTRODUCTION

1.1 Introduction

The design of structures to control waterways in Malaysia is a major concern for engineers. The options for flood control in urban areas, however, are limited. A large fraction of the ground surfaces is paved causing concentrated flood flow peaks. One of the practical methods of routing the water through the urban areas is via the use of high-velocity channels.

Hydraulic engineers often use the term “high-velocity channel” when referring to a control flood channel which was designed to discharge water as fast as possible to discharge point such as river or sea (Berger et. al. 1995). High-velocity channels are often used for drainage purposes in urban regions where real estate is expensive. This kind of channels are normally constructed at a sufficient slope so that the flow is supercritical, thus reducing the flow area and concentration time.

The designer of these high-velocity channels is faced with many problems that cannot be solved easily. At the design level, two main concerns are the water depth and velocities of the flow. The depth must be known to determine sidewall heights and minimum bridge span elevations. Normally, a designer simply applies an empirical equation such as Manning equation to obtain water depth with known discharge rate. However, determining the depth of flow is complicated by side inflows and boundary features such as contractions, expansions, curves, and obstructions. These boundary features in a supercritical channel cause flow disturbances that can result in a significant oscillation in flow.

Besides water depth, consideration should be given to flow velocity when designing a channel section. For safety purpose, flow velocity should be controlled within range 0.6 – 4.0 m/s to prevent sediments and to protect channel from bank corrosion.

For these design purposes, many methods have been used such as empirical equations, physical models and numerical model. A numerical model in handling shock capturing will be tested through this study.

1.2 Problem Statement

Open channel especially high-velocity channels are used for drainage in urban regions, since urban sprawl increase rainfall runoff due to altered land use. Flood control channels are designed and built to safely manage the anticipated hydrologic load. The desire is to minimize the water's time of residence in the urban area. The channels are designed to carry supercritical flow to reduce the water depths and the required route. Structures, such as bends and transitions cause flow to choke and form jumps. These hydraulic conditions generally necessitate higher walls, bridges and other costly containment structures. A poorly designed channel can cause bank erosion, damaged equipment, increased operating expense, and reduced efficiency (Berger et. al.1995). Furthermore, crossings may be washed out, and the town may flood.

Predicting the potential location of shocks and determining the elevation of water surface in channel are necessary to evaluate and decide the required sidewall heights. Normally empirical equations are often used in the channel design due to its simple application. However, the presence of bends, contractions, transitions, confluences, bridge piers and access ramps can cause the flow to choke or to produce a series of standing waves and these all will complicate channel design.

In the past, applications of physical models are common for this water profile evaluation. Although physical model can reproduce a channel if properly conducted, but great care must be taken in model dimension and scale. A major drawback of physical models is the problem of scaling down a field situation to the dimensions of a laboratory model. Phenomena measured at the scale of a physical model are often different from conditions observed in the field. Though physical models can reproduce details of actual hydraulic structures, they are still subjected to the limitation of scale modeling because sometimes it is impossible to reproduce the physical problem to scale.

Changes to the physical model require a “cut and try” technique that involves tearing down the unwanted sections of the channel and rebuilding them with the new desired design. Due to the time and cost constraints of physical models, it is not practical to examine a wide range of designs. This could result in hydraulic performance that is only acceptable over a limited range.

Mathematical models have been developed to overcome the problem mentioned above. A mathematical model consists of a set of differential equations that are known to govern the flow of surface water. The reliability of predictions of models depends on how well the model approximates the field situation. Inevitably, simplifying assumptions must be made because the field situation is too complex to be simulated exactly. Usually, the assumptions necessary to solve a mathematical model analytically are fairly restrictive. To deal with more realistic situations, it is usually necessary to solve the mathematical model approximately using numerical techniques. Therefore, an inexpensive and a readily available model for evaluating these channels are needed. A numerical model is a logical approach.

An area of engineering design that can benefit the use of numerical model is the design and modification of high-velocity channels essential for the routing of floodwater through urban areas. The proper design of new channels and re-design of existing channels is required to avoid such things as bank erosion, damaged equipment, increased operating expenses, flooding, and higher construction costs. By using numerical model, a better channel design can be produced with minimum cost and time.

1.3 Objective of the Study

The primary purpose of the research is to develop a methodology and ascertain the effectiveness of using numerical model for open channel modeling. The challenges for this numerical model lie in representing supercritical transitions and capturing the potential location and movement of the shocks. The specific objectives of the study are listed as followed:

1. To assess the practicality of using two-dimensional numerical model to aid in the design of a realistic open channel.
2. To evaluate the performance of numerical model in handling shock capturing in various test cases through comparison with published results, laboratory tests and analytical solutions.

1.4 Scope of the Study

The purpose of this research is to describe the numerical flow model and to illustrate typical open flow fields that the model is capable of simulating. Only rectangular channel is focused in this research. Few test cases are conducted in laboratory using simple geometries. Numerical models are developed for comparison with published laboratory results. Model parameters are tested to determine the model sensitivities. This reduces the number of parameters to only those that have major impact on the design. The model verification consists of comparing results computed using numerical model with laboratory results and analytical solutions. However, comparison results will only focus on steady state flow. Model limitations will also be discussed. The results can be used to determine the appropriate parameters to be optimized in the future. Finally, the numerical will be applied to two selected channels to examine the channels' performance and the applicability of the model as a design tool for improving the channels.

1.5 Significance of Research

In surface water modelling, the most challenging part is to detect the location and water elevation of hydraulic jump or shock. The height of the jump is critical to the design of channel walls and bridges within high-velocity channel. And through this prediction also, we can define easily the critical location within existing channel so that improvement can be done quickly before flood happen in that location. A lot of flow models used recently not able to perform this task accurately. However, there are still some flow models were developed specially for this shock capture purpose but most of them in one-dimensional (1D) mode.

There was some concern to the adequacy of a one-dimensional (1D) analysis of the flow conditions such as contractions, expansions, bends, hydraulic jumps and bridge piers which commonly found in high-velocity channels. There was a question as to whether computing cross-sectional averaged flow variables provided a sufficiently accurate estimate of flow depths and velocities within these boundary features. Thus, a two-dimensional (2D) analysis was deemed necessary to evaluate these flow conditions which always cause overhead trouble in high-velocity channels.

A numerical model HIVEL2D used to assess the design computationally before the construction of the physical model begins and to screen alternatives. Using a numerical model would accelerate this design process and lead to an improved initial physical model thus reducing the time spent on the physical model. This would allow for exploration of more design alternatives in a shorter length of time resulting in a more cost-effective solution.

CHAPTER 2

LITERATURE REVIEW

2.1 Numerical Model Review

Recently there are several types of numerical models that developed to predict water profile for high velocity channels. The challenges for these models lie in representing sub- and supercritical transitions and capturing the location and movement of shocks. A lot of research papers were published to show the model simulation and verification of open-channel flows in various test cases. Different techniques had been applied such as finite-difference method and finite-element method. In most cases, any one of these methods requires a special technique to analyze subcritical and supercritical flows without a separate computational algorithm. Their performances were then enhanced by various schemes including Petrov-Galerkin scheme. However, hydrostatic pressure distribution almost becomes the most common hypothesis that was assumed in lot of numerical models.

Among finite-difference method community, MacCormack and Gabuti explicit finite-difference scheme were introduced by Fennema et. al. (1990) to integrate the equations describing 2D, unsteady gradually varied flows, by assuming hydrostatic pressure distribution, small slope and uniform velocity distribution in vertical direction.

The MacCormack scheme consists of a two step predictor-corrector sequence. It means that flow variables which are known at t time level will be used to determine the variables at t+1 time level in correction step. Reflection boundaries were incorporated in this scheme, where the fictitious points in the solid wall will be replaced by immediate interior points.

The Gabutti scheme is an explicit scheme based on the characteristic relations, which consists of three sequential steps (predictor step part 1, predictor step part 2 and corrector step). In subcritical flow, both positive and negative characteristics are used while in supercritical flow the information is carried only along the characteristics from the direction of flow. Boundary conditions are based on characteristic principles.

Two typical hydraulic flows problem: partial dam breach and passage of a flood wave through a channel contraction were tested. Specified end conditions are needed to analyze steady flows by letting the computations converge to a steady state if both sub and supercritical flows are present simultaneously. In partial dam breach problem, a small flow depth was assumed initially to simulate dry bed condition. Besides, a frictionless, horizontal channel was used to prevent damping. Boundary conditions were found incorporated in both scheme, but the finite-difference formulation of sharp corners needs additional investigation according to writers.

The same finite-difference scheme (MacCormack) was used to simulate contraction cases (Jimenez et. al. 1988). Here, the shallow water equation was used as a basic equation. For boundary condition, Abbett procedure was applied. The basic idea of this procedure is to apply the numerical scheme up to the wall using one-sided differences as a first step. Then to enforce the surface tangency requirement, a simple wave is superimposed on the solution to make the flow parallel to the wall. The detail explanation can be referred in the paper.

The comparison between computed and measured results indicated that there are some cases for which the assumption of hydrostatic pressure distribution is too restrictive. In these situations, the use of more general equations, e.g., Boussinesq-type equations that include vertical acceleration effects, becomes desirable. In that study, computed results were compared with contraction test cases which conducted by Ippen et. al. (1951). The simulated water depth increased four times within a short distance. The disagreement between the experimental and computed results becomes large.

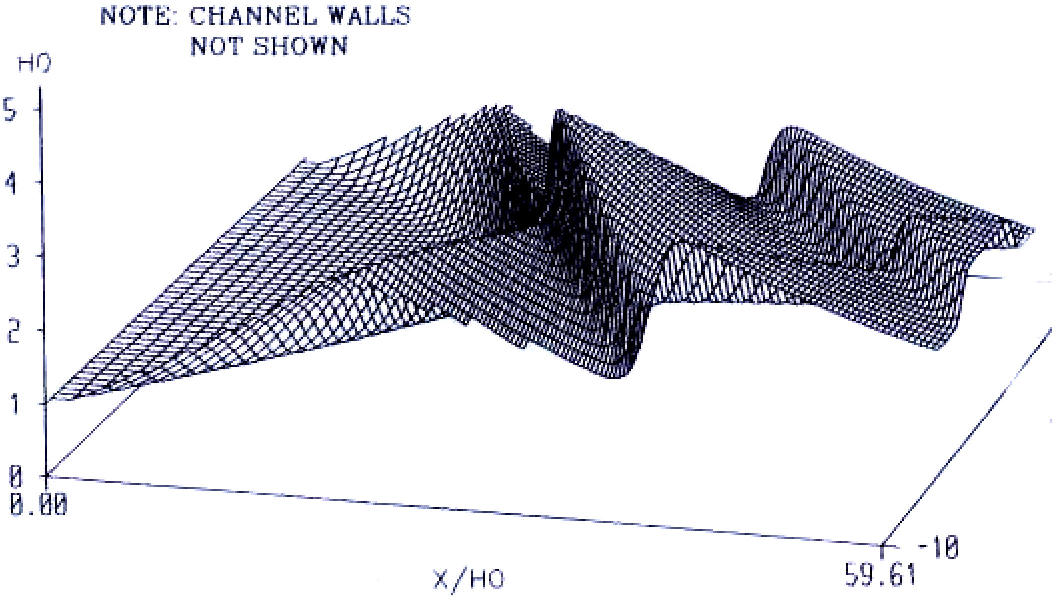

Figure 2.1 Water depth increased four times within a short distance

In 1991, one-dimensional Boussinesq equations were used to solve hydraulic jump problem in a horizontal rectangular channel (Gharangik et. al. 1991). Again, MacCormack and two-four explicit finite-difference schemes were used for solution until a steady state was reached. Experiments with the Froude number upstream of jump ranging from 2.3 to 7.0 were conducted for model verification. The importance of the Boussinesq terms was investigated. Results show that the Boussinesq terms have little effects in determining the jump location. However, results from this study will be used for model simulation in this study, as discussed in the following section.

In solving open-channel flows problem, shallow water equations are very often used by researchers together with finite-element method and Galerkin scheme. Schwanenberg et. al. (2004) had developed a total variation diminishing Runge Kutta discontinuous Galerkin finite-element method for 2D depth-averaged shallow water equations. In his study, the smooth parts using the second order scheme for linear elements and third order for quadratic shape functions both in time and space. In that model, shocks were normally captured within two elements. 5 test cases including the actual dam break of Malpasset, France, indicated a well performance of the scheme.

Hicks et. al. (1997) proved that a 1D formulation also can provides an excellent solution in modelling dam-break floods in natural channels. St. Venant equations were used in the model, which solved with the characteristic dissipative Galerkin finite-element method (CDG). The computational simulations were conducted using both varied and uniform spatial discretizations. Verification was made by comparing dam break experiment from Bellos et. al. (1992), which was performed in a rectangular channel of varying widths.

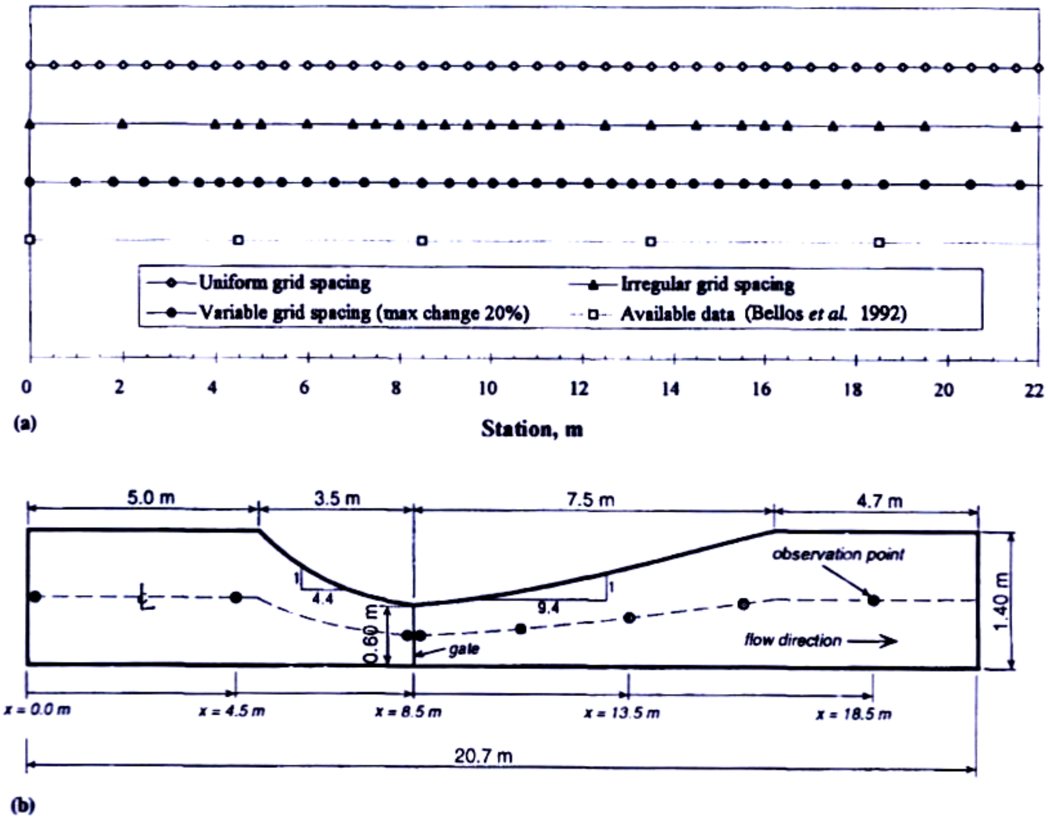

Figure 2.2 (a) Spatial grids, (b) Geometry of flume

The experiment from Bellos was repeated for both dry and wet bed conditions at downstream of the dam gate. Hicks input constant water levels upstream (H_u) and downstream (H_d) of the dam location as initial condition. Between the nodes around the gate, the initial water depth dropped linearly across the element, as approximation to the water level discontinuity across the dam in the actual laboratory test. The effect of ratio H_u/H_d was studied.

Hicks found that the variable distance grid produced results indistinguishable from those obtained with uniform grid. Besides, results which solved by the “box” (BFD) finite-difference method were presented. Writers concluded that the BFD scheme is not capable of handling a mixed subcritical-supercritical flow and become unstable in that transition flow if compare to CDG scheme.

A variance of the Galerkin scheme for conservation laws in 2D, nearly horizontal flow, which exhibits a remarkable shock-capturing ability, was presented (Katopodes 1984). The method was based on discontinuous weighting functions which introduce upwind effects in the solution while maintaining central difference accuracy. However, the fundamental hypothesis concerns the vertical distribution of pressure is hydrostatic.

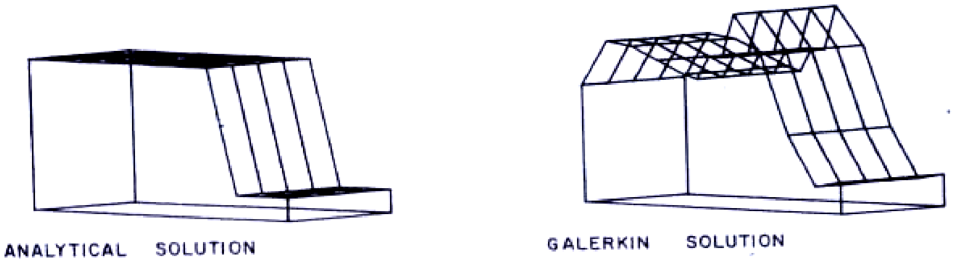

ANALYTICAL SOLUTION GALERKIN SOLUTION

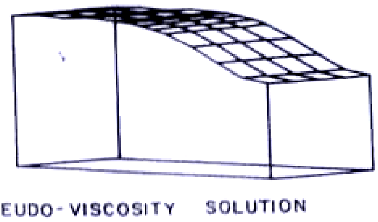

PSEUDO-VISCOSITY SOLUTION

Figure 2.3 Comparison results reported by Katapodes

Katapodes presented comparison results between analytical solution, classical Galerkin solution and Pseudo-viscosity solution in a sudden water release test case. The finite-element Galerkin was found very disappointing, although not worse than non-dissipative finite-difference methods. In Galerkin solution, the problems such as parasitic waves behind the front and the spreading of discontinuity over elements were found. However, the study demonstrated that better results can be obtained by a variation of the Galerkin technique known as the Petrov-Galerkin formulation. The verification was made by compare to analytical solutions for 4 test cases (1D surge, surge through symmetric gradual constriction, surge through asymmetric abrupt constriction and expansion).

Another Dam-break problem which tested by Fennema et. al. (1990) was simulated by Fegherazzi et. al. (2004) using a discontinuous Galerkin method in 1D and 2D. The scheme solved the shallow water equation with spectral elements, utilizing an efficient Roe approximate Riemann solver in order to capture bore waves. The discontinuous Galerkin method was found flexible and very suitable to model systems of hyperbolic equations such as shallow water equations. The weak formulation and the discontinuous bases utilize in the discontinuous Galerkin method were straight forward in treating shock waves.

A numerical model using finite-element and finite-volume methods with Gumensky's empirical formula was presented by Unami et. al. (1999). Integration of the Euler's equations from the channel bottom to the flow surface with the hypotheses of hydrostatic pressure distribution and negligible Coriolis acceleration results the 2D free surface equations, which was used in the study. Apart from the standard Galerkin scheme used for the continuity equation, the upwind finite-volume scheme was developed to solve the momentum equation.

The test problem in spillway was solved for model verification by Unami. In the discretized model, the domain was divided into 1,852 triangular elements in mesh grid. The inlet discharge was specified at a rate which is the maximum design flood discharge of the dam site. Courant-Friedrichs-Lewy condition (CFL) was used in model stability checking. The numerical model was found able to represent the transition flow and hydraulic jump was captured within a few elements. In the real case of spillway, the direction of flow suddenly changes and a large spiral was formed which is unable to be captured by 2D numerical model. The numerical model was further examined by evaluating the residual term, and the model proved to be valid as a primary analysis tool in design practice.

There are some researches that try to apply non-hydrostatic assumption in numerical model. A three-dimensional numerical method without the hydrostatic assumption was developed to simulate hydraulic flow (Lai et. al. 2003). It solves the three-dimensional turbulent flow equations and utilizes a collocated and cell-centered storage scheme with a finite-volume discretization and this allows a wide range of applications utilizing different cell shapes for the mesh.

The Reynolds-averaged Navier-Stokes equations were used as governing equations. These governing equations were discretized using the finite-volume approach. The domain was divided into number of cells with all dependent variables stored at the cell geometric centres. The shape of cells and cell faces must be uniquely defined because all geometric quantities such as cell volume and normal vector were calculated from this definition. The study demonstrated the use of numerical model with prismatic, hexahedron and tetrahedral meshes.

An S-shaped open-channel flow was used as a test case in that research and the results with different meshes compared favourably with experimental data. The results concluded that prismatic mesh is as efficient and accurate as a hexahedral mesh, and it may be a good choice for flows in natural rivers. Detail explanation about the effect of non-hydrostatic in numerical model was not found.

The two-dimensional vertically averaged and moment equations model, developed by Ghamry et. al. (2002) was used to study the effect of applying different distribution shapes for velocities and pressure on the simulation of curved open channels. Linear and quadratic distribution shapes were assumed for the horizontal velocity meanwhile a quadratic distribution shape was considered for vertical velocity. Linear hydrostatic and quadratic non-hydrostatic distribution shapes were suggested for pressure. The finite element hybrid Petrov-Galerkin and Bubnov-Galerkin schemes were used.

Comparisons of the model predictions were made with the experimental results obtained in “S” shape open channel, “U” shape of rectangular flume and 270 degree curved rectangular flume. Note that only subcritical flows were simulated in all experiment with $Fr < 5.0$. In all comparison, only the longitude velocity distribution was focused. Results suggested that pre-assumed velocity distribution shapes are not very sensitive; further more the attained higher accuracy on applying the non-hydrostatic assumption model is insignificant compared to linear hydrostatic model.

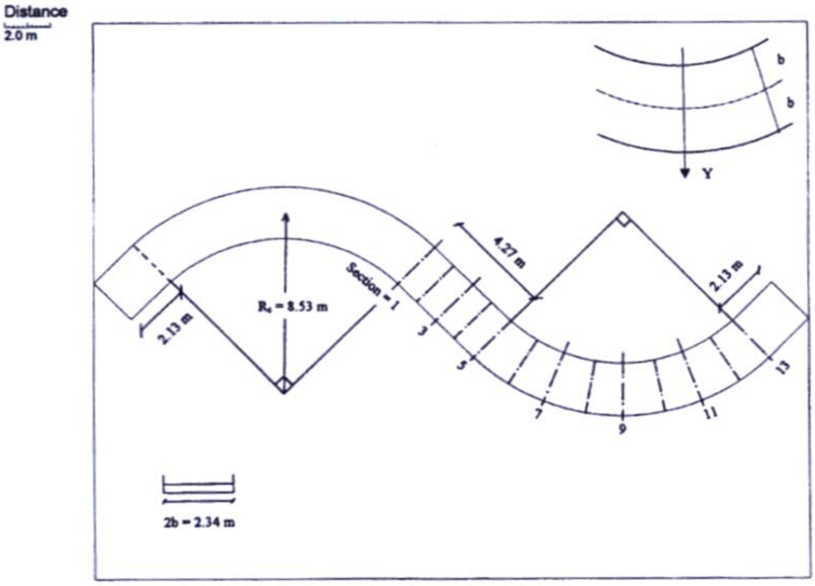

Figure 2.4 “S” shape open channel

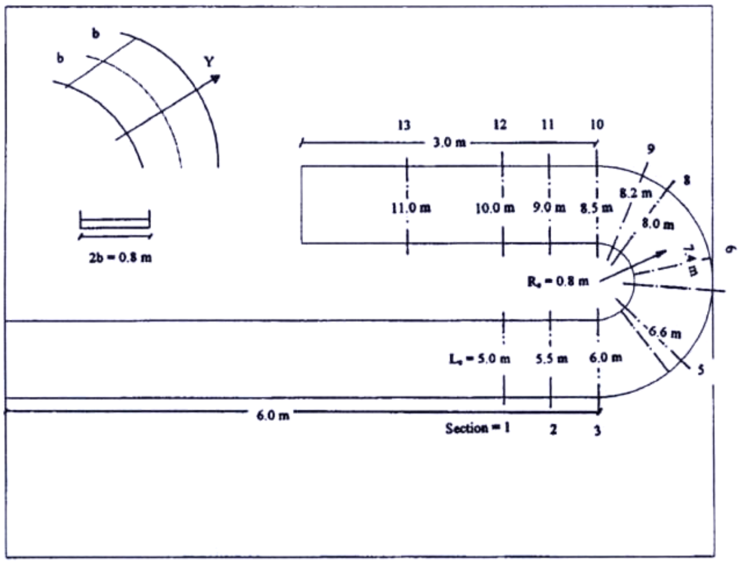

Figure 2.5 “U” shape of rectangular flume

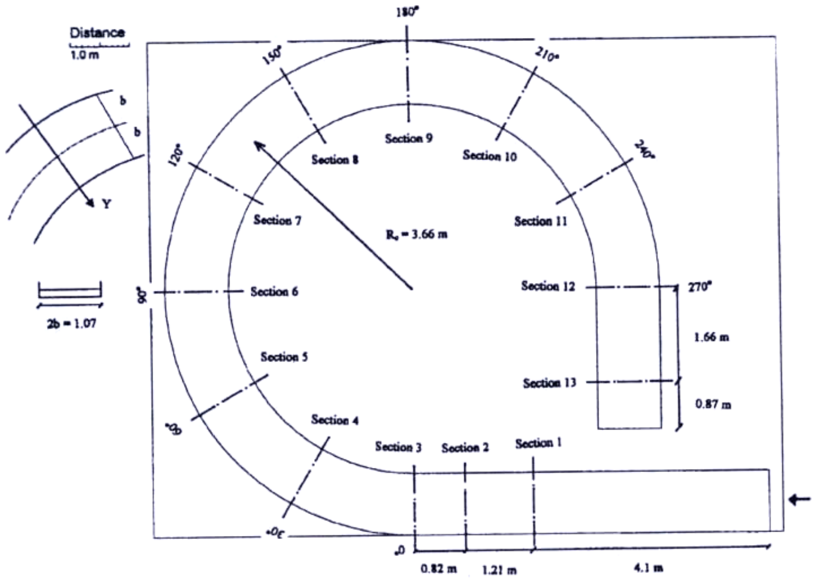

Figure 2.6 270 degree curved rectangular flume

A total variation diminishing Runge Kutta Discontinuous Galerkin (RKDG) finite-element method for two-dimensional depth-averaged shallow water equations has been developed by D.Schwanenberg and M.Harms in year 2004. The explicit time integration, together with the use of orthogonal shape functions, makes it as efficient as comparable finite-volume schemes. The method was shown to have second or third order of convergence in time and space for linear and quadratic shape functions in smooth parts of the solution and sharp representation of shocks. The test indicate an excellent performance of the scheme and giving suggestion that advanced analysis using full 3D Navier-Stokes equation is possible and can be conducted.

Models commonly face difficulty in handling jumps. One of the methods called “shock tracking” that track the jump location and impose an internal boundary there. The shallow water equation then allows weak solutions in which a discontinuity represents the hydraulic jump. This is referred as “shock capturing” as originated by von Neumann and Richtmyer (1950). Note that this might be not easy for researchers to track shock location accurately. Further more, great care must be taken to ensure that the errors only local to the jump (discontinuity location).

Normally a model with continuous depths will conserve mass and momentum through the jump but will also produce oscillation at the shortest wavelengths to conserve energy. Energy dissipation which should appear in jumps does not exist. In fact, when jumps happen, energy is being transferred into vertical motion. And since vertical motion is not included in shallow water equation, it causes some lost in model. Therefore, a scheme is needed to address this problem will be dissipative and can satisfy the need of shock capturing as well.

In 1995, a 2D finite-element model for the shallow-water equations was produced using an extension of the streamline upwind Petrov-Galerkin (SUPG) concept. A mechanical was implemented which detects the presence of a jump by calculating the mechanical energy variation per element and so allows the model to increase the degree of upwinding in the shock vicinity while maintaining more precise solutions in smoother flow regions (Berger et. al. 1995).

Results from Berger demonstrated the ability of model to reproduce the speed and height of a moving hydraulic jump and the ability of the shock-detection mechanism to follow the jump. This was a comparison with an analytical solution. A 2D example of a supercritical contraction was then demonstrated by comparison with flume results by Ippen and Dawson (1951). Finally, the data from the study of Margarita Channel was used for model verification too. Results showed that the model is adequate to address hydraulic problems involving jumps and oblique shocks.

Previously, finite-element methods were found cannot conserve mass locally. However, Berger et. al. (2002) demonstrated that, by using the flux inherent in the discrete, finite-element conservation statement, the sum of the fluxed around an element or group of elements precisely matches the internal mass change. These finding were supported by calculations in one and three dimensional (see Berger et. al. 2002).

A two-dimensional numerical flow model for trapezoidal high-velocity channels which having slopping sidewall was developed by Stockstill et. al. (1997). This model was developed after improving the model introduced by Berger et. al. (1995). When treat with slopping sidewall where the depth is unknown, an approach involve updating the moving boundary displacement only once each time step was applied. For interior nodes, large displacement of the moving boundary nodes can lead to element shape distortions. This problem was solved by regridding the side slopes each time step as a function of the boundary nodal displacement.

A trapezoidal flume with horizontal curve was conducted in U.S. Army Engineer Waterways Experiment Station, Hydraulic Laboratory for model verification (Stockstill et. al. 1997). The first test condition demonstrated that the model accurately solved the water lines through the transition where the flow accelerated from subcritical to supercritical. The experiment was then repeated by adding piers. The model was found unable to describe undular jumps which were formed in the test, but accurately represented the choked flow condition and the maximum depth. Overall results showed that this method is useful in subcritical flow but not so efficient in supercritical flow. However, it was proved to be stable at significant Courant numbers.

The numerical model which introduced by Berger and Stockstill was further extended its application on simulating barge drawdown and currents in channel and backwater areas (Stockstill et. al. 2001). Vessel effects were modelled numerically by using a moving pressure field to represent the vessel's displacement. Verification model included real field data such as Illinois State Water Survey, Mississippi River and Sundown Bay where located along Texas coast between Aransas Bay and San Antonio Bay. The model was shown able to reproduce main channel return currents in straight reaches of small channels (Illinois Waterway) and in the off-channel areas of wide rivers (Mississippi River).

Another unpublished report from Army Engineer Waterways Experiment Station showed application of 2D numerical model which was introduced by Berger, in San Timoteo Creek which is tributary of Santa Ana River. The proposed design within the reach studied includes a sediment basin, a concrete weir followed by a chute having converging sidewalls, a compound horizontal curve consisting of spirals between a circular curve and the upstream and downstream tangents with a banked invert, and a bridge pier associated with the San Timoteo Canyon Road. The test had been conducted using two different discharge value, 19000 cfs and 12000 cfs. These series of tests demonstrated the application of the numerical model in site.

The sensitivity of simulated results to the choice of dissipation coefficient and grid resolution was presented. The report concluded that the solution of flow field is not significantly influenced by the dissipation coefficient and grid refinement. Another test parameter was the roughness coefficient. Different Manning's n (n = 0.012 and 0.014) were applied in the test and it was found that the maximum depth was reduced and the wave crests were located further downstream large smaller Manning's n.

The San Timoteo Creek report also proved that hydrostatic assumption is appropriate in the area of the oblique standing wave initiated at the pier nose. The vertical acceleration in this vicinity was calculated to be 0.4 relative to gravity. It proved that the hydrostatic assumption is reasonable even in regions where the flow is rough.

In this research, the application of two-dimensional finite-element model for the shallow water equations derived by Berger (1995), is demonstrated in various test cases such as hydraulic jump, contraction, expansion, open-channel junction, gradual contraction, bridge pier and weir structure. The model is produced using an extension of the Petrov-Galerkin scheme. A mechanism which detects the present of shocks by calculating the mechanical energy variation per element is implemented. Model results will be compared with analytical solution and published laboratory data. A few laboratory tests were carried out for model simulation. Data from these experimental studies will be presented and the general performance of flow under various test cases will be described. Through this research, the performance of numerical model will be evaluated and the model can provide another alternative tool in designing open-channel structure.

2.2 Published Experimental Works

There are three published papers have been selected for comparison with numerical model simulation. Complete experimental data are presented in the papers. Before using their results, a brief description about their experimental detail or test facilities will be explained. The three published test cases are hydraulic jump (Gharangik et al, 1991), 90 degree open channel junction (Weber et al, 2001) and both side contraction (Ippen et al, 1951) which had been simulated by Berger et al (1995) and Jimenez et al (1988). The experimental results of the papers are discussed briefly in chapter 4.

2.2.1 Hydraulic Jump (Gharangik et. al, 1991)

The test facility comprised of a horizontal 14.0 m long, 0.915 m high, and 0.46 m wide rectangular metal flume is shown in figure 2.7. The water entered the flume through a sharp-edged sluice gate and discharged into a weighing tank for flow rate measurement. The water depths in the section of flume with metal walls were measured at equally spaced intervals by a point gauge having the accuracy of 0.3 mm. Meanwhile the rectangular grids on glass-walled section were used to measure depth and jump location. The average levels were considered the water depth. The Manning's *n* was found varied from 0.008 to 0.011.

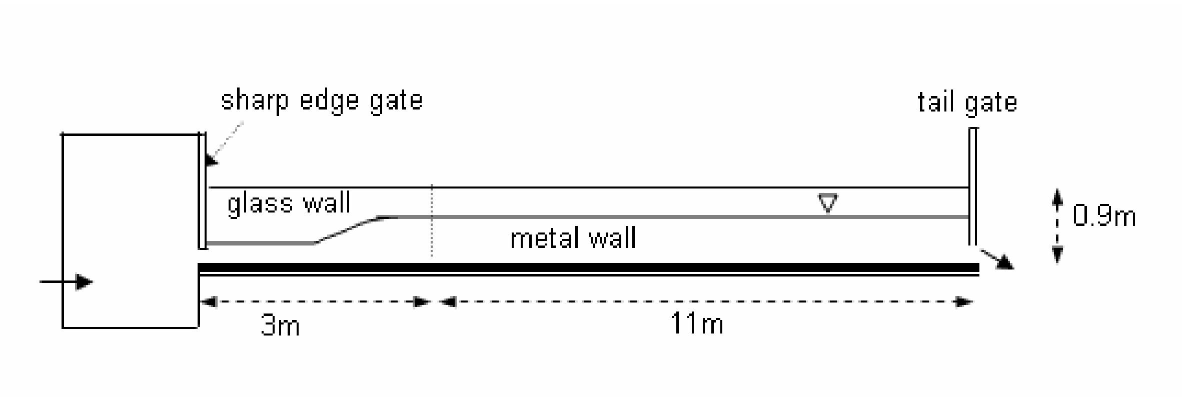

Figure 2.7 Test facility for hydraulic jump

The experiment was conducted with a range of Froude number from 2.30 to 7.00. However, only results for Froude number equal to 2.30, 4.21, 5.71 and 6.71 were selected in this research for model comparison. Important flow parameters such as depth, velocity and Froude number are listed in table 2.1, where d_1, u_1 and Fr_1 are referred as parameters for incoming flow. The parameters d_2, v_2 and Fr_2 after the jump were computed using continuity equation.

Table 2.1 : Flow parameters (hydraulic jump)

test no.	d_1 (m)	u_1 (m/s)	Fr_1	d_2 (m)	u_2 (m/s)	Fr_2	q=Q/B	Q (m^3/s)
1	0.031	3.831	6.95	0.265	0.448	0.28	0.119	0.534
2	0.024	3.255	6.71	0.195	0.401	0.29	0.078	0.352
3	0.040	3.578	5.71	0.286	0.500	0.30	0.143	0.644
4	0.043	2.737	4.21	0.222	0.530	0.36	0.118	0.530
5	0.055	2.127	2.90	0.189	0.619	0.45	0.117	0.526
6	0.064	1.826	2.30	0.168	0.696	0.54	0.117	0.526

2.2.2 90º Channel Junction (Weber et al, 2001)

The experiment was performed in a sharp-edged, 90º combining flow flume with horizontal slope (figure 2.8). The type of material for the flume was not available. Volumetric measurements were made with monometer readings from calibrated 0.203 m orifices in each of the 0.305 m supply pipes.

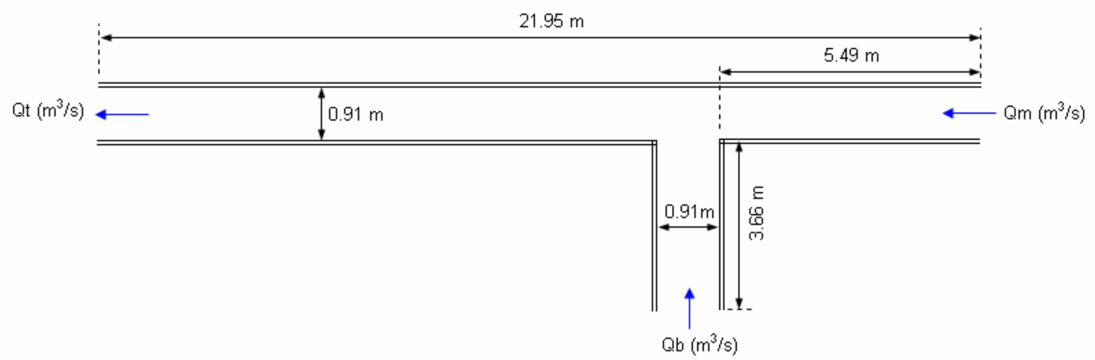

Figure 2.8 Test facility for 90 degree junction

Two head tanks on the main and branch channels supplied the discharge into the flume. The upstream main channel, branch channel, and combined tailwater flow are denoted as Qm, Qb and Qt, respectively. The ratio q* is defined as the upstream main channel flow Qm to the constant total flow Qt which is equal to 0.170 m^3/s. The tailwater depth in the downstream channel was controlled by an adjustable tailgate and it was held constant at 0.296 m. The flow conditions tested are listed in table 2.2. Only q* equal to 0.250 and 0.750 were selected for model simulation.

Table 2.2 : Flow parameters (junction)

Qm (m^3/s)	Qb (m^3/s)	q* = Qm/Qt
0.014	0.156	0.083
0.042	0.127	0.250
0.071	0.099	0.417
0.099	0.071	0.583
0.127	0.042	0.750
0.156	0.014	0.917

In this study, a Sontek three-component acoustic Doppler velocimeter (ADV) was used in velocity measurements; meanwhile point gauge method with an accuracy of 1.0 mm was implemented in depth measurements. The testing grid which was applied in the experiment produced approximately 2,850 measurement locations for each flow condition studied. The results presented in the paper composed of 3D velocity and turbulence measurements along with a water surface mapping in the immediate vicinity of the channel junction.

2.2.3 Both Side Contraction (Ippen et al, 1951)

The test was conducted in a 40 ft long flume. The long approach length of 20ft was used to ensure uniform flow conditions at the contraction. The straight-wall contraction was a 2 ft wide channel, transitioning to a 1 ft wide channel at a convergence angle of 6 degree at both sides within contraction length of 4.78 ft. The reported discharge rate was 1.44ft^3/s. The tests were conducted for an approach Froude number of 4.0, and upstream depth of 0.1 ft.

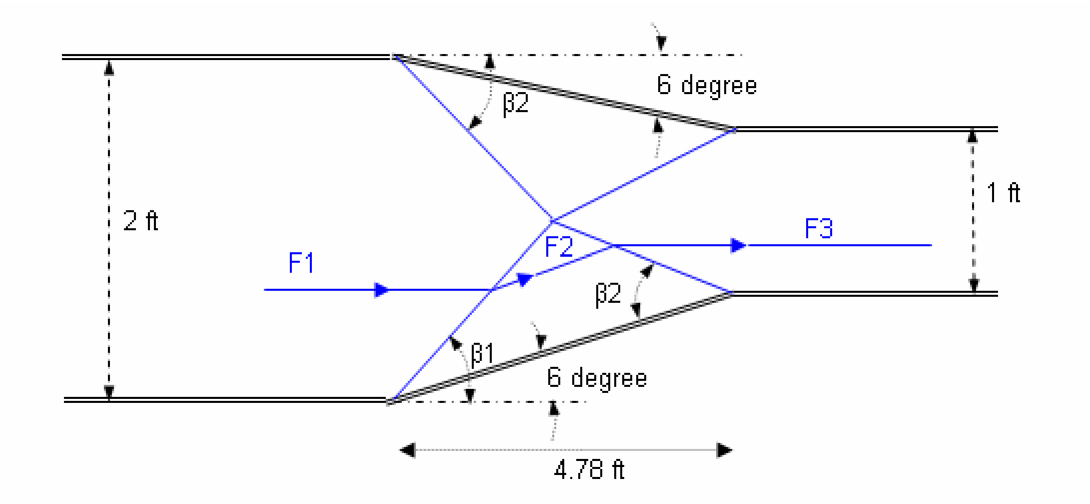

Figure 2.9 Test facility for contraction, reported by Ippen

Berger (1995) assumed a Manning's roughness *n* of 0.0107 for the flume. The bed slope producing uniform depth of 0.1 ft was computed to be 0.05664. However, for the same test case, Chaudhry assumed zero friction and slope. To show the importance of approach depth, another assumption was made in this research and it is listed with flow parameters in table 2.3. The β1 and β2 are the expected wave front angles due to sudden inward boundaries; while d_1, d_2 and d_3 are the computed water depths along the contraction.

Table 2.3 : Flow parameters for three assumptions

Asssumption	Q (ft^3/s)	Slope	*n*	β1(degree)	β2(degree)	d_1 (ft)	d_2 (ft)	d_3 (ft)
Berger	1.44	0.05664	0.0107	19.7	23.6	0.1	0.147	0.203
Chaudhry	1.44	0	0	19.7	23.6	0.1	0.146	0.204
Trial run	1.44	0.01	0.0041	19.7	23.6	0.1	0.146	0.204

Three numerical models were conducted by using the assumption listed above. Water depth contours presented in the papers will be used for model comparison.

2.3 Basic Equations and Hypotheses

Solutions of open-channel problems often involve prediction of three components of flow velocities and depths, which can be solved by the continuity and momentum equations of motion, along three orthogonal directions. After making certain reasonable assumptions, the complete one or two-dimensional differential equations of motion can be derived by integrating the three-dimensional equations over the channel cross section.

The vertical water depth and lateral dimensions are considered small for most problems in open channel if compare to longitudinal dimension. Further more, the changes in cross section along the longitudinal direction are very gradual. For one-dimensional equation, it normally assumes that the main component of flow (velocity or acceleration) is only along longitudinal direction. But for two-dimensional equation, only vertical components which normal to bed channel are negligible. These assumptions will be reasonable when apply in a streamline that have small curvatures, and the pressure is hydrostatic. The continuity and momentum equations derived below are also based on the following assumptions:

1. The rate of change of shear stress with x and y is small and assume zero where, x-axis is along the longitudinal direction (parallel to average bottom slope) and y-axis is along lateral direction.
2. The components of velocity and acceleration along z-axis (vertical direction parallel to water depth) are zero. This assumption leads to hydrostatic pressure distribution.
3. The density of water is constant. This is true for most of time except at deep water, where large pressure result in increased density.
4. The channel bottom slope is small, so that the flow depths measured normal to the channel bottom and measured vertically are approximately the same.
5. The flow velocity over the entire channel cross section is uniform.
6. The friction in unsteady flow may be simulated using the steady-state resistance laws, such as Manning equation.

The principle of mass conservative states that the rate of increase of fluid mass within a control volume must equal to the difference between the mass influx into and mass efflux out of the control volume (Jain 2001). The equation can be given in conservation form as shown below:

$$\frac{\partial h}{\partial t}+\frac{\partial p}{\partial x}+\frac{\partial q}{\partial y}=0 \tag{2.1}$$

The momentum equations are based on Newton's second law of motion, which states that the sum of all external forces acting on a system is equal to the product of the mass and acceleration of the system. This actually is a vector law which valid for three different axes. Since vertical components are neglected, only the conservation of momentum along the x-direction and y-direction are derived and given respectively as:

$$\frac{\partial p}{\partial t}+\frac{\partial}{\partial x}\left(\frac{p^2}{h}+\frac{1}{2}gh^2-h\sigma_{xx}\right)+\frac{\partial}{\partial y}\left(\frac{pq}{h}-h\sigma_{xy}\right)=-gh\frac{\partial z}{\partial x}+g\frac{n^2 p\sqrt{p^2+q^2}}{C_0 h^{7/3}} \tag{2.2}$$

$$\frac{\partial q}{\partial t}+\frac{\partial}{\partial x}\left(\frac{pq}{h}-h\sigma_{yx}\right)+\frac{\partial}{\partial y}\left(\frac{q^2}{h}+\frac{1}{2}gh^2-h\sigma_{yy}\right)=-gh\frac{\partial z}{\partial y}+g\frac{n^2 q\sqrt{p^2+q^2}}{C_0 h^{7/3}} \tag{2.3}$$

where,

h = depth;

p = uh, x-direction discharge per unit width where u being x-component of depth-averaged velocity;

q = vh, y-direction discharge per unit width where v being y-component of depth-averaged velocity;

g = acceleration due to gravity;

C_0 = conversion coefficient (C_0 =1 for SI units and 2.208 for non-SI units);

ρ = fluid density;

Z_0 = channel bed elevation;

σ = Reynolds stresses due to turbulence

The individual terms in the conservation equations above are consisting of acceleration force, pressure force, body force and bed shear stresses which influenced by Manning's n. Stresses are modeled using the Manning's formulation for boundary drag and the Boussinesq relation for Reynolds stresses.

2.4 Governing Equations

The shallow water equation, also referred to as the St. Venant equations, describe two-dimensional unsteady free-surface flows. These equations are derived assuming hydrostatic pressure distribution, which is usually valid except when the water surface has sharp curvatures. They are nonlinear first-order, hyperbolic partial differential equations for which closed-form solution are not available except in very simplified 1D cases (Fennema, R. et. al. 1990). Therefore, these equations are solved numerically. The dependent variables of the two-dimensional fluid motion below are defined by the flow depth, h, and the volumetric discharge per unit width in the x-direction, p, and the volumetric discharge per unit width in the y-direction, q. These variables are functions of the independent variables x and y, the two space directions and time t (Berger et al. 1995). The shallow-water equations in vector form are given as:

$$\frac{\partial Q}{\partial t} + \frac{\partial Fx}{\partial x} + \frac{\partial Fy}{\partial y} + H = 0 \tag{2.4}$$

where

$$Q = \begin{pmatrix} h \\ p \\ q \end{pmatrix} \tag{2.5}$$

$$Fx = \left\{ \begin{matrix} p \\ \dfrac{p^2}{h} + \dfrac{1}{2} g h^2 - \dfrac{h\sigma_{xx}}{\rho} \\ \dfrac{pq}{h} - \dfrac{h\sigma_{yx}}{\rho} \end{matrix} \right\} \tag{2.6}$$

$$Fy = \left\{ \begin{matrix} q \\ \dfrac{pq}{h} - \dfrac{h\sigma_{xy}}{\rho} \\ \dfrac{q^2}{h} + \dfrac{1}{2} g h^2 - \dfrac{h\sigma_{yy}}{\rho} \end{matrix} \right\} \tag{2.7}$$

$$H = \left\{ \begin{matrix} 0 \\ gh\dfrac{\partial Z_0}{\partial x} + g\dfrac{n^2 p\sqrt{p^2+q^2}}{C_o^2 h^{\frac{7}{3}}} \\ gh\dfrac{\partial Z_0}{\partial y} + g\dfrac{n^2 q\sqrt{p^2+q^2}}{C_o^2 h^{\frac{7}{3}}} \end{matrix} \right\} \tag{2.8}$$

2.5 Finite-element Model

One of the solution methods for differential equation is to convert it into an integral equation. For this purpose, three finite-element approaches are available to convert the governing equation into integral equations, which are direct method, variational method and weighted residual method. The weighted residual method is general method that can be applied in cases where direct and variational methods do not work (Jain, 2001).

Galerkin method is one of the weighting residual methods which widely used together with finite-element model. In this Galerkin method, the error is forced to zero by making it orthogonal to a set of *r* linearly independent weighting functions,

N_r. N_r in finite-element term is called shape function that they span the solution space (domain). An inner product is formed between error and weighting functions as shown below (Chaudhry, 1993):

$$\left(N_r, E^{'}\right) = \left|Nr\right|\left|E^{'}\right|\cos\theta = 0 \tag{2.9}$$

or in integral form,

$$\int_R N_r \left[Lu_{approx} - f(x_j)\right] dR = 0 \tag{2.10}$$

where R = domain
N_r = weighting functions
E' = error = $Lu_{\mathrm{approx}} - f(\mathrm{x_j})$
L = differential operator
$\mathrm{u_{approx}}$ = approximate of dependent variable
$f(\mathrm{x_j})$ = function in x variable, it can be a constant.

Refer to equation (2.9), if N_r and E' are nonzero, then for the inner product to be zero, cos θ must be zero. It means that N_r is orthogonal to E'.

The shallow water equations above are solved using the finite element method by using Petrov-Galerkin formulation approach. Integration by parts procedure is used to develop the weak form of the equations which facilitates the specification of boundary condition is:

$$\sum_e \left[\int_{\Omega_e} \left(\psi_i \frac{\partial Q}{\partial t} - \frac{\partial \phi_i}{\partial x} Fx - \frac{\partial \phi_i}{\partial y} Fy + \varphi_i A \frac{\partial Q}{\partial x} + \varphi_i B \frac{\partial Q}{\partial y} + \psi_i H \right) d\Omega_e + \int_{\Gamma_e} \phi_i \left(Fxn_x + Fyn_y \right) dl \right] = 0 \tag{2.11}$$

Note that sidewalls are enforced as no mass or momentum flux through these boundaries. A detailed explanation of variables is given in Berger et al (1995).

2.6 Shock Detecting

The Petrov-Galerkin test function is defined (Berger et. al 1995) as:

$$\psi_i = \phi_i I + \varphi_i \tag{2.12}$$

where,

ϕ_i = Galerkin part of the test function

I = Identity Matrix

φ_i = non-Galerkin part of the test function

and,

$$\varphi_i = \beta\left(\Delta x \frac{\partial \phi_i}{\partial x}\hat{\mathrm{A}} + \Delta y \frac{\partial \phi_i}{\partial y}\hat{\mathrm{B}}\right) \tag{2.13}$$

where β is a dissipation coefficient varying in value from 0 to 0.5. The Δ terms are the linear basis functions, and Δx and Δy are grid intervals.

Strength of upwinding is controlled by the parameter β. In smoother regions this upwinding is unnecessary and the lower values of β produce a more accurate result. Therefore, a shock-detection method could be used to determine where a large β is implemented and elsewhere a small value can be used. The model developed by Berger employs a mechanism that detests shocks and increases β automatically. In a similar manner, the eddy viscosity coefficient C varies from C_{smooth} to C_{shock} depend the mechanism.

As shown by Berger et al (1995), the method detects energy variation for each element and flags element that has a high variation in needing a larger β for regions near the shock. According to Berger, for an element i, if $|Ts_i|$ > constant (through trial a value of constant = 1.0 was chosen), the shock capturing is implemented. Where

$$Ts_i = \frac{ED_i - \overline{E}}{SD} \tag{2.14}$$

$$ED_i = \frac{\left[\int_{\Omega_i} (E - \overline{E}_i)^2 d\Omega \right]^{1/2}}{a_i} \tag{2.15}$$

$$\overline{E}_i = \frac{\int_{\Omega_i} (E) d\Omega}{a_i} \tag{2.16}$$

Refer to the formula listed above,

ED$_i$ = element *i* energy deviation

$\overline{E}$ = average element energy over the entire grid

SD = standard deviation of all ED$_i$

E = mechanical energy distribution within the element

$\overline{E}_i$ = average energy of element *i*

a$_i$ = area of element *i*

2.7 Numerical Approach

In solving the finite-element approach which is consisting of Petrov-Galerkin formulation, additional complications occur due to complicated formula. These complications include the presence of second or higher-order derivatives, nonlinear terms, and the need for numerical integration.

A finite-difference expression is used for the temporal derivatives. The general expression for the temporal derivative of a variable Q_j is:

$$\left(\frac{\partial Q_j}{\partial t} \right)^{m+1} \approx \alpha \left(\frac{Q_j^{m+1} - Q_j^m}{t^{m+1} - t^m} \right) + (1 - \alpha) \left(\frac{Q_j^m - Q_j^{m-1}}{t^m - t^{m-1}} \right) \tag{2.17}$$

where j is the nodal location and m is the time step. And α equal to 1 result in a first order backward difference approximation; α equal to 2 results in a second-order backward difference approximation of the temporal derivative. A first order difference is used for the spin-up to a steady flow condition, whereas a second-order difference is more appropriate for unsteady flow simulation (Berger et. al. 1995).

Meanwhile the system of nonlinear equations is solved using the Newton-Raphson iterative method. For a nonlinear equation,

$$\frac{f(x) - f(x_0)}{x - x_0} = f'(x_0) \tag{2.18}$$

$f(x)$ is forced to zero at starting and an initial value is assumed for x_0. With the known x_0, and after obtained $f(x_0)$ and $f'(x_0)$, unknown Δx (that is x-x_0) can be calculated. Then an improved estimate for x is obtained from $x = x_0 + \Delta x$. This procedure is continued until convergence to an acceptable residual error is obtained for Δx.

Note that $f'(x_0)$ might be quite complicated and need others method to calculate the answer. In this case, finite-difference method will be applied. And sometimes $f'(x_0)$ might gives zero value while $f(x_0)$ is not zero (example is shown in figure 2.10). Iteration will be terminated and cause error to model.

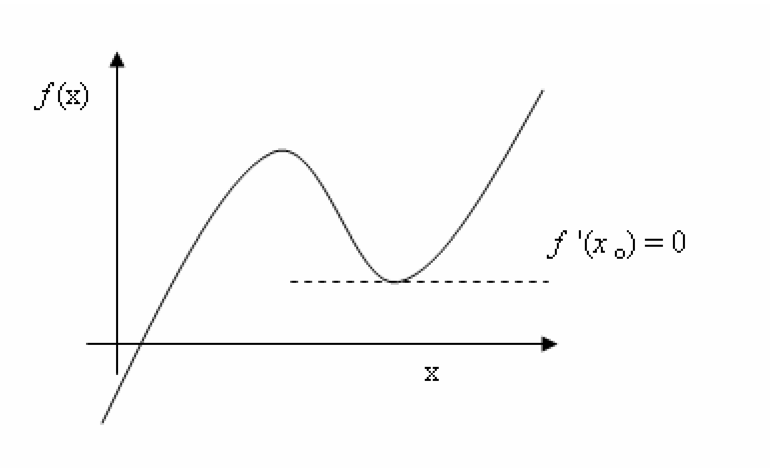

Figure 2.10 Example error case in Newton-Raphson iterative method

CHAPTER 3

RESEARCH METHODOLOGY

3.1 Introduction

The purpose of this research is to describe the numerical flow model and to illustrate typical high-velocity flow fields that the model is capable of simulating. Various hydraulic test cases using this numerical model were conducted. Results of test cases point out flow conditions that are not accurately modelled by numerical model. Besides using published flume and numerical simulations data, results comparisons also were made with data obtained from experiments. Research procedures were summarized in the following flow chart (Figure 3.1).

A through literature review had been carried out for gathering information on flume studies. Before applying a numerical model in a real field work, the validity of model predictions should be tested through comparison using laboratory data.

Generally research methodology can be divided into two parts: experimental work and computer modelling using an existing numerical model. Both of them were carried out so that any correction or improvement can be made immediately. Besides, brief descriptions about analytical solution for each case will be explained in this chapter.

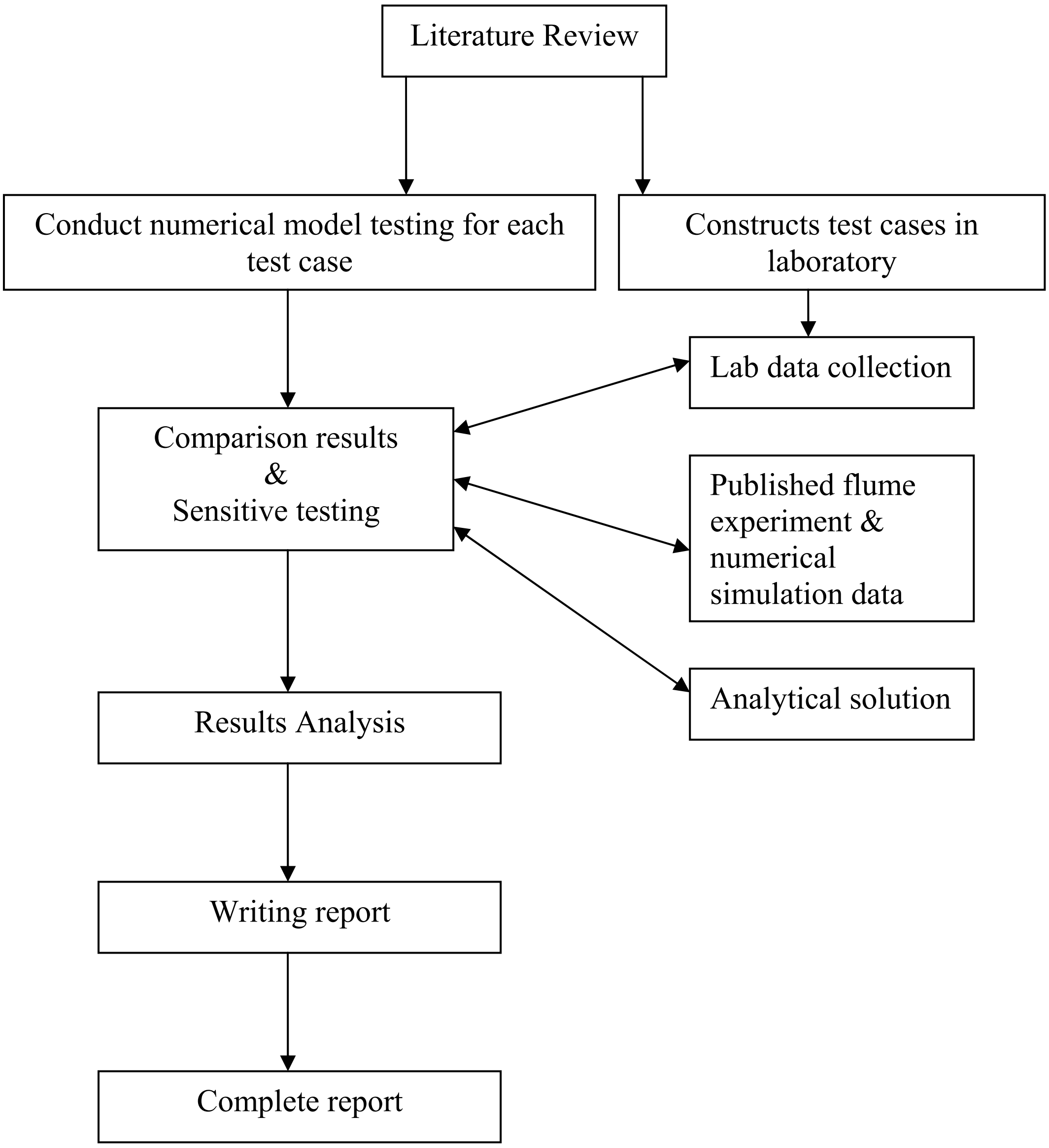

Figure 3.1 Methodology Flow Chart

3.2 Experimental Works

Four different hydraulic cases were conducted in Hydraulic and Hydrology Laboratory, University Teknologi Malaysia, Skudai. The test cases consist of weir, contraction & 90 degree expansion, hydraulic jump and bridge piers. These features are commonly found in high-velocity channels which will form shock wave in open channel. In the experimental work, preliminary works were conducted for setting up the rectangular flume in the laboratory and for the control test.

3.2.1 Preliminary Works

A rectangular flume, 15 m long, 0.457 m wide, and 0.40 m height which located in Hydrology and Hydraulic Laboratory, University of Technology Malaysia (UTM), was selected in this study (Figure 3.2).

Figure 3.2 Rectangular flume in UTM laboratory

The coordinate *x* refers to the longitudinal direction where starts from zero at the entrance; *y* is the lateral direction; and *z* is in vertical direction. The length of the flume is long enough so that normal depth can be obtained. The bed was made of metal which had been re-painted. Grid lines were marked on bed surface for every

0.5 m longitudinal direction, as a bench marks during measuring process. The side walls were made of glass. Rectangular grid papers were pasted on both sidewalls for every 0.5 m. The slope of the flume is adjustable within a range.

Depth measurements for this study were made by using a point gauge with an accuracy of 1.0 mm for critical flow region, but grids on side walls were used for smooth region.

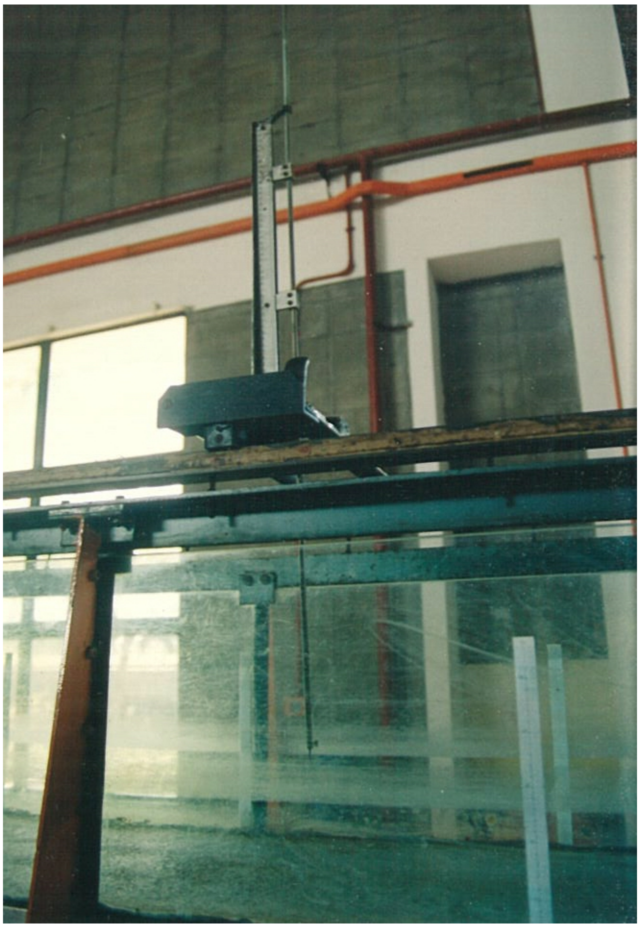

Figure 3.3 Point gauge and grid paper

The water was supplied from a large tank located on roof floor. Unfortunately only one pump was still functioning. Because of this, the head of water tank was not constant. As a result, discharge rate will reduce slowly after certain period until the discharge rate equal to the water pump rate, which is about 0.009m^3/s. Note that the discharge rate was controlled by turning the valve in front of flume (figure 3.4) and the range of flow rate should be determined before test cases. For this purpose, flow rates were recorded for every quarter round when turning the valve, starting with 1.0 round, 1.25 rounds, 1.5 rounds, till 3.0 rounds.

Figure 3.4 Valve in front of flume

For initial trial run, the discharge was measured by using three methods. A known volume of tank was placed at the downstream end of the flume and the time to fully fill up the tank was recorded using digital time recorder. Thus the discharge can be easily obtained after dividing the volume with times. For second method, a half-submerged ball was dropped into the upstream of flume and the time for the ball to travel a distance of 14.0 m was recorded. Discharge can be computed by multiplying the normal depth and the average flow velocity, which is equal to distance over times. And for the third method, flow velocities was measured by using current meter with an accuracy of 0.01 m/s, and multiplying the water depth which was measured at the same point to compute discharge rate. Experiments were repeated at least 3 times for each method. Computed flow rates from those methods were compared as shown in table 3.1. Since there are not much different, therefore the third method had been selected for the rest of test cases.

Table 3.1 : Results comparison among three discharge measurement methods

Valve turn	1st Method			2nd method			3rd method		
	depth (cm)	time for tank(s)	**Q = Volume/t**	time for ball(s)	V = Distance/t	**Q = AV**	V (m/s)	y (cm)	**Q=AV**
1.00	2.2	42.29	**0.006**	22.2	0.63	**0.006**			
1.25	3.0	26.91	**0.010**	16.26	0.86	**0.011**	0.75	2.8	**0.010**
1.50	3.8	17.02	**0.015**	14.44	0.97	**0.016**	0.91	3.6	**0.015**
1.75	4.5	12.76	**0.021**	12.7	1.10	**0.023**	1.03	4.6	**0.022**
2.00	5.5	10.05	**0.026**	11.75	1.19	**0.030**	1.16	5.5	**0.029**
2.25	6.5	7.54	**0.035**	13.18	1.06	**0.031**	1.2	6.3	**0.035**
2.50	7.0	6.62	**0.040**	12.36	1.13	**0.037**	1.26	7.1	**0.041**
2.75	8.1	-	**-**	11.75	1.19	**0.042**	1.35	7.7	**0.048**
3.00	8.9	-	**-**	11.73	1.19	**0.046**	1.45	8.4	**0.056**

Before starting the control test, the flume base was adjusted so that the flume is laterally horizontal. The water depth measured from left side should be the same as the right side. However, after the adjustment, the flume still gives a maximum error about 2.0 mm.

Smoothness of the flume slope was also studied. The flume was blocked and filled with water. The depths were measured for every 0.5 m as shown in figure 3.5. The bed condition of flume was plotted and these will be discussed in the following section. The test shows that the flume's bed is not smooth especially in the entrant part. However, the bed surface seems to be quite smooth at *x* = 6.0 till 9.0 m, which provides ideal location to locate hydraulic structure for various test cases. For this reason, all slopes that are mentioned in the following sections will be referred as average slope gradient.

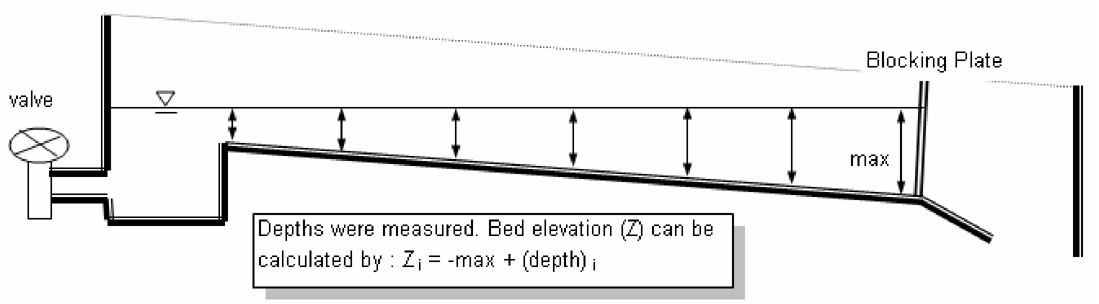

Figure 3.5 Checking smoothness of slope

For the following experimental work, the railing above the flume is assumed parallel to the bottom surface so that the depth measured from gauge point is normal to the bottom surface.

3.2.2 Control Test

The main objective of control tests is to determine normal depth which can be used for model design. This is the simplest case in hydraulic study and model calibration can be carried out easily through control test.

At the same time, a few flow parameters can be determined through this effort, such as the flow rate for every valve turning, and slope checking. Besides, it also provides the information on the range of Manning's n roughness for the flume. This is very important because Manning's n is needed as numerical model input for every test case. Another significant study of control test is that it shows the location where the normal depth can be obtained, which provides an ideal place to locate hydraulic structure such as weir for various test case.

In this test, any obstacle inside the flume was removed and water was allowed to flow freely. In such case, the flow profile oscillated at the entrance but slowly converged to a normal depth after 3 or 4 m and decreased near the outlet. Control tests were carried out in four slope conditions (1/65, 1/150, 1/500 and 1/1500) with various discharge rates by changing the valve turn. Water depths were recorded for a distance interval of 0.5 m in the longitudinal direction at both side walls. The point distance x = 0.6 m represented the upstream boundary in the numerical model. The maximum and minimum surface levels were measured and an average of these levels was considered the depth at that location. Measurements were repeated to ensure the accuracy of the test results. Meanwhile the flow velocities were measured for discharge calculation.

3.2.3 Experiment 1 : Weir

This experiment was performed in the same flume. A mortal weir with 0.5 m long, 0.45 m wide and 13.5 mm thick was placed in the flume at x = 8.1 m, and end at x = 8.6 m as shown in figure 3.6. Both weir edges consist of 34 degree sharp edge so that flow reflection can be minimized. In this experiment, 1.5 valve turn was selected which was approximately 0.015 m^3/s discharge rate. Flow parameters are summarized in table 3.2.

Table 3.2 : Flow parameters for weir experiment

Parameters	Valve turn	Discharge rate, Q (m^3/s)	Flume wide, B (m)	Slope gradient, S	*n*	average weir height (m)	weir length (m)	weir wide (m)
Lab test	1.5	0.015	0.457	near to(1/65)	0.0094-0.010	0.0135	0.50	0.45

Figure 3.6 Mortal weir

Slope checking was carried out and it was found near to be 1/65 as shown in figure 3.7. However, this average slope gradient was used to calculate Manning's *n* only; meanwhile the real slope condition was applied when constructing the numerical model.

The size of weir was well designed before the experiment. With Q = 0.015m^3/s and S = 1/65, control test showed that the normal depth should be 0.030 m. By using simple calculation, weir height should be less than 0.020 m to prevent back water. Water depth on the weir was computed first by using simple energy equations.

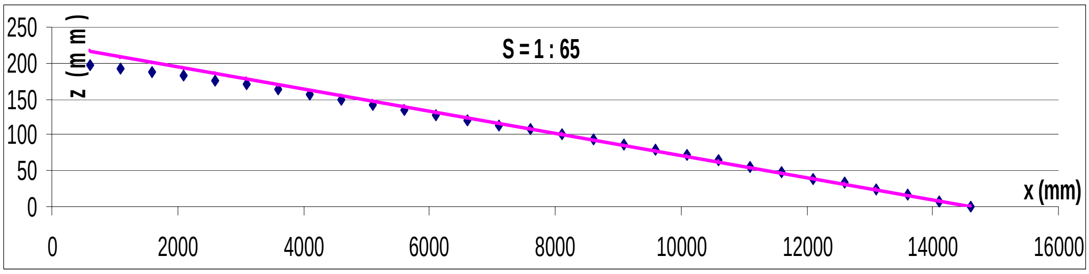

Figure 3.7 Slope checking in weir test case

Because of the non-smooth bed surface, the point gauge was set to zero when touching the bed surface for every measurement. The water depth measurements for each test case were carried out by the same individual without changing any flow setting. These precautions ensured that the same measuring procedures and measurement techniques were employed.

3.2.4 Experiment 2 : Contraction and 90 Degree Expansion

Figure 3.8 shows the test facility of this experiment. The width of the rectangular flume was reduced from 0.457 m to 0.337 m by using painted wood plates. The contraction start at $x = 8.1$ m to provide enough distance for the flow to converge to normal depth. At $x = 11.13$ m, there is a 90 degree expansion and water depth was expected to drop rapidly at that location. A simple geometry of this test case is shown in figure 3.10.

Similar to weir test case, 1.5 valve turn was selected (0.015 m^3/s) as discharge rate. Other flow parameters are given in table 3.3. During the experiment, water depths were recorded using the same method and this time the measurement was focused on the contraction and expansion location where the shock wave will occur. Referring to figure 3.10, the locations of point A, C, D and E were recorded for later comparison with numerical model.

Figure 3.8 Contraction & 90 degree expansion test case

After finishing the test, the average channel slope was checked again by filling water inside the flume and it was found to be 1/78 as shown in figure 3.9.

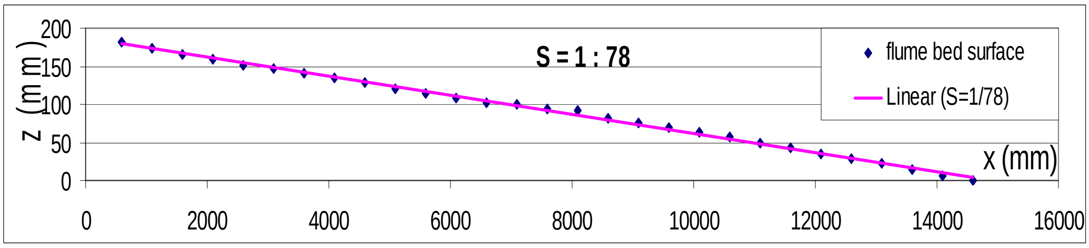

Figure 3.9 Slope checking for contraction & 90 degree expansion test case

Again, the contraction was well designed before experiment so that no back water should occur in laboratory test. By using analytical solution (Subhash C. Jain, 2001), angles of deflection and water depths after contraction can be computed. Based on the analytical solution, the result of experiment should be similar to figure 3.10.

Table 3.3 : Flow parameters for contraction & 90 degree expansion test case

Parameters	Q (m^3/s)	(Q/B)	B1 (m)	B2 (m)	B3 (m)	L1 (m)	L2 (m)	θ (contraction)	θ (expansion)	S	*n*
Lab test	0.0153	0.03348	0.457	0.337	0.457	1.134	1.900	6.042	90	lab (1/78)	0.0085-0.0092

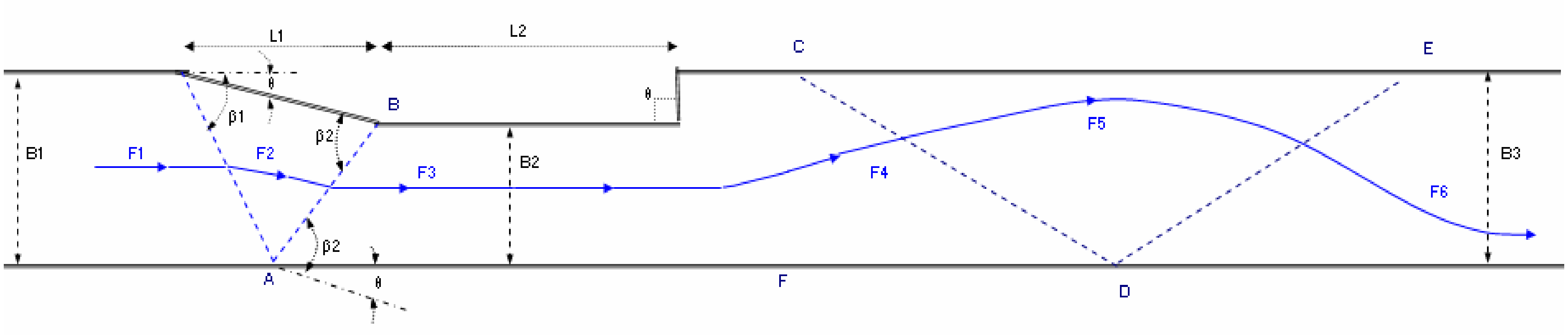

Figure 3.10 Plan view for contraction & 90 degree expansion test case

3.2.5 Experiment 3 : Hydraulic Jump

Several studies have been conducted to study the location of hydraulic jump and the amount of energy dissipated (Chaudhry, 1993). Extensive amounts of data have been reported in the literature on this topic, providing a complete set of data which is suitable for model verification. However, the selected slopes in their experimental works are mostly mild or horizontal slope. Therefore, in this research, an experiment for hydraulic jump test case was conducted by using steep slope, which is around 1/78 as shown in figure 3.11.

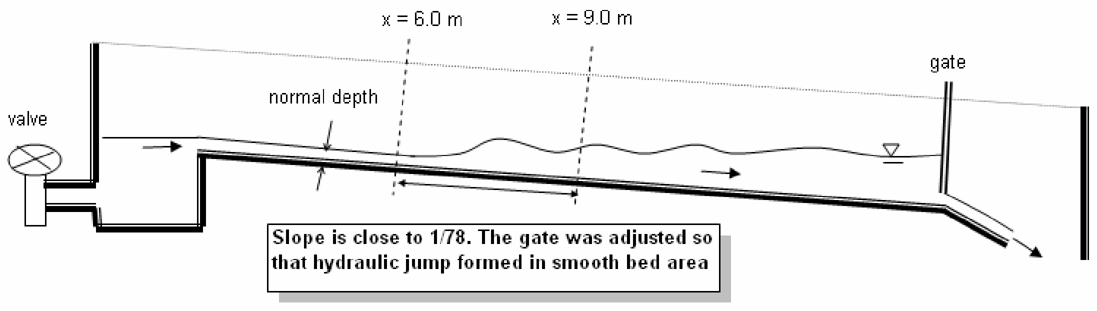

Figure 3.11 Hydraulic jump test case with steep slope

A 0.045 m wide plastic plate was used as a sluice gate at the downstream of flume as shown in figure 3.12. The supercritical flow was found within the steep flume and formed a moving hydraulic jump when blocked by the sluice gate.

Figure 3.12 Plastic gate at the end of flume

By adjusting the opening of gate, the jump location was pushed forward until reaching a steady condition, which was located within x = 6 m till x = 9 m. The approach Froude number depends on the normal depth of the flume. Because of the pump problem, Froude number is difficult to be increased. Furthermore, the steepness of flume was unable to be increased due to the fix end connection of pipe problem.

The roughness of the flume was obtained through control test. During the experiment, gauge point method was used to measure water depth and it was difficult to precisely measure the water profile in the jump because the flow is very unstable. For this reason, the water depths shown in this research are the average values computed from maximum and minimum surface elevations.

Since the discharge rate was controlled by the valve, this is very difficult to obtain consistent flow rate for every new test. Thus, the test case was not repeated but measurement was repeated more than three times for every different test case.

3.2.6 Experiment 4 : Bridge Pier

Two different types of pier were tested in the experiment to provide data for comparison with numerical model simulation. Three experiments were tested by using aluminium pier and wood pier. Figure 3.13 shows the geometry of the test case together with the pier dimensions in plan view for the aluminium pier. The F1 represents the approach Froude number. Instead of semicircular shape, the pier was designed with triangular nose and tail.

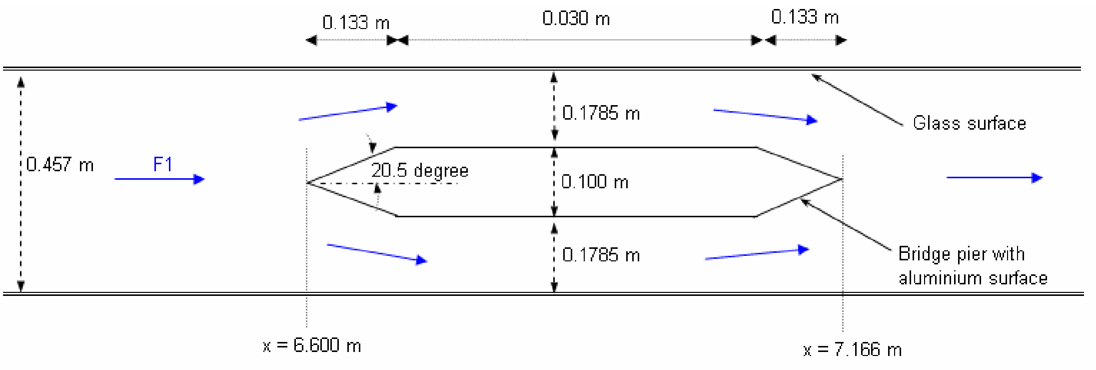

Figure 3.13 Triangular nose and tail for aluminium bridge pier

The aluminium pier was placed at x = 6.6 m. In the first test case, entrance flow was allowed to flow freely and converge to normal depth before reaching the pier structure. A flow rate about 0.015m^3/s was selected and the slope gradient was approximately 1/78 to obtain supercritical flow. Through control test, the normal depth for this flow rate was found approximately 0.030 m and the approach Froude number was approximately 2.0 (F1 = 2.0). The following figures show the plan view and side view which were captured in laboratory.

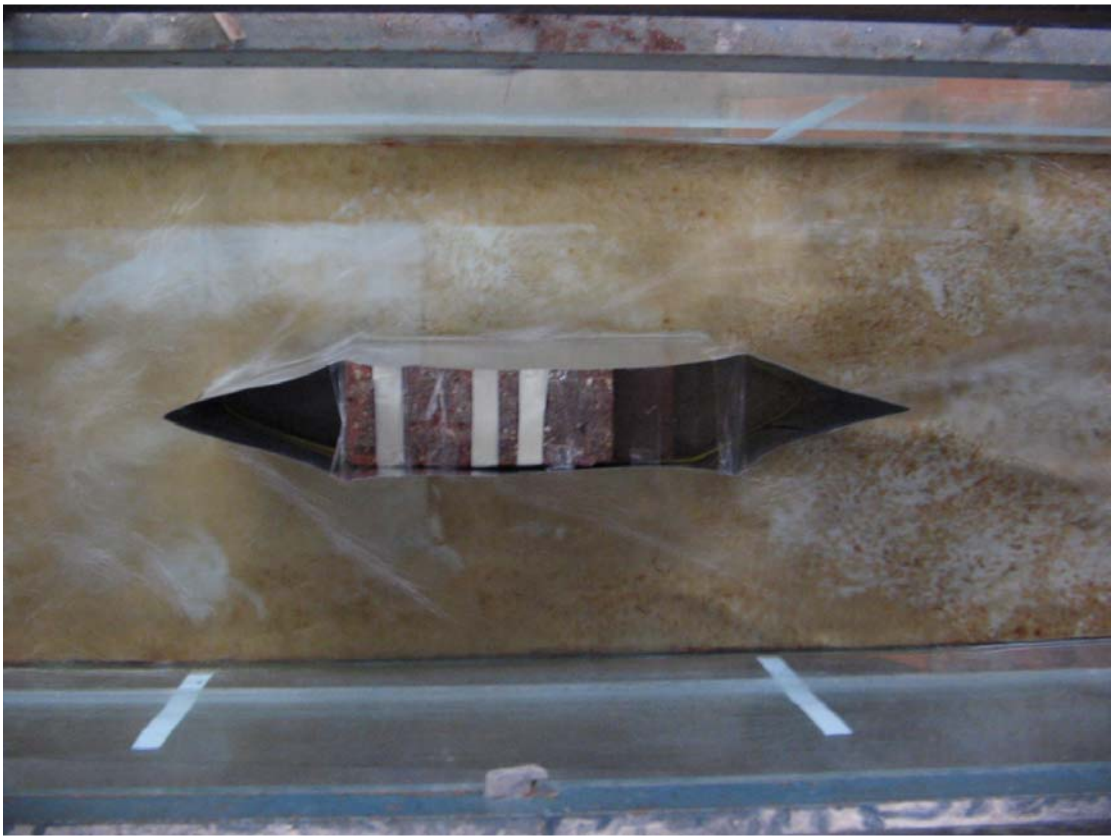

Figure 3.14 Plan view (1st test case)

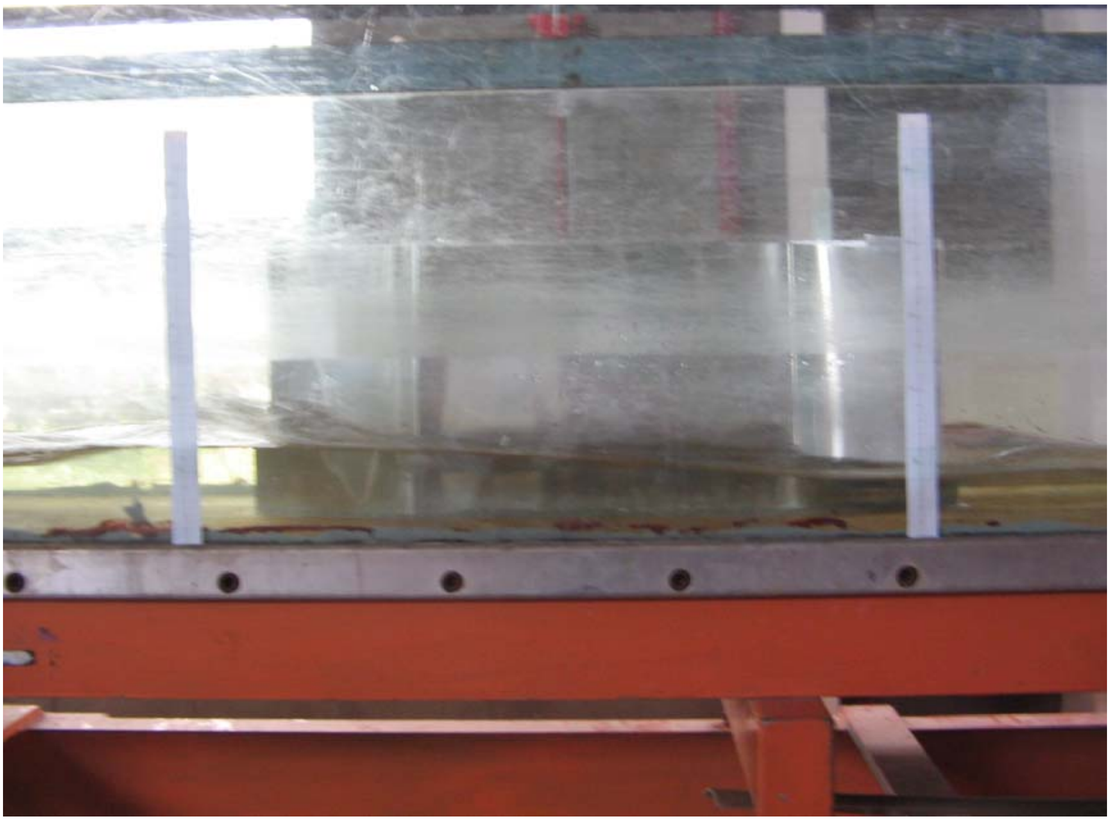

Figure 3.15 Side view (1st test case)

For second and third test cases, the aluminium pier was remained at the same location. The flow rate and slope were also maintained. However, a control gate was placed at the upstream which is close to the pier (at *x* = 6.10 m). This control gate was used to control the approach Froude number. Figure 3.16 below illustrates the side view of these test cases.

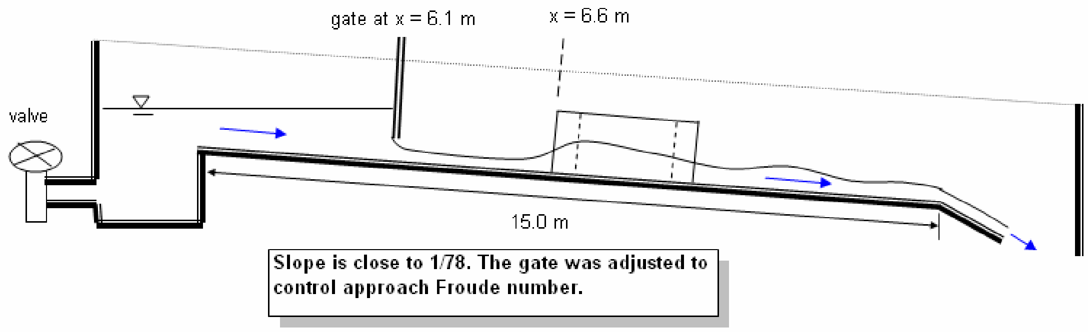

Figure 3.16 Side view (2nd and 3rd test case)

The only different between second and third test case was the approach Froude number as listed in table 3.4. The supercritical flow in the third test case was much stronger than the second test case. Run up at nose of pier was found overtopping for any Froude number which more than 3.5.

Table 3.4 : Flow parameters for aluminium pier test cases

Test	Flow parameters at x = 6.30 m		
	d (m)	v (m/s)	Fr
1	0.030	1.06	2.0
2	0.023	1.20	2.5
3	0.029	1.50	2.8

After testing with aluminium pier, the experiments were repeated again by using wood pier, which has rectangular nose and tail. The geometry flume and dimensions of wood pier are shown in figure 3.17. Here, the relation between approach Froude number and run up on the upstream face of pier is a concern. The clearance space on both sides of the pier will be studied by using two different pier sizes.

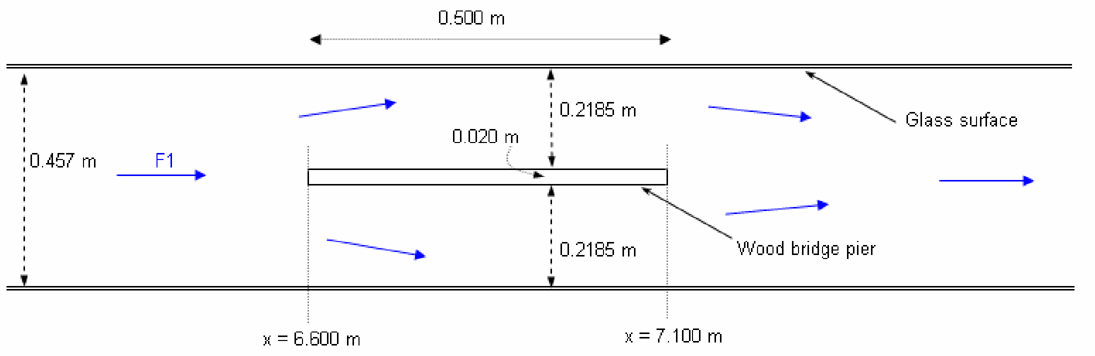

Figure 3.17 Rectangular nose and tail for wood bridge pier

Similar to aluminium test cases, three test cases for wood pier will be conducted with three different approaches Froude numbers as listed in table 3.5. Figure 3.18 and 3.19 show some photographs which were captured in laboratory.

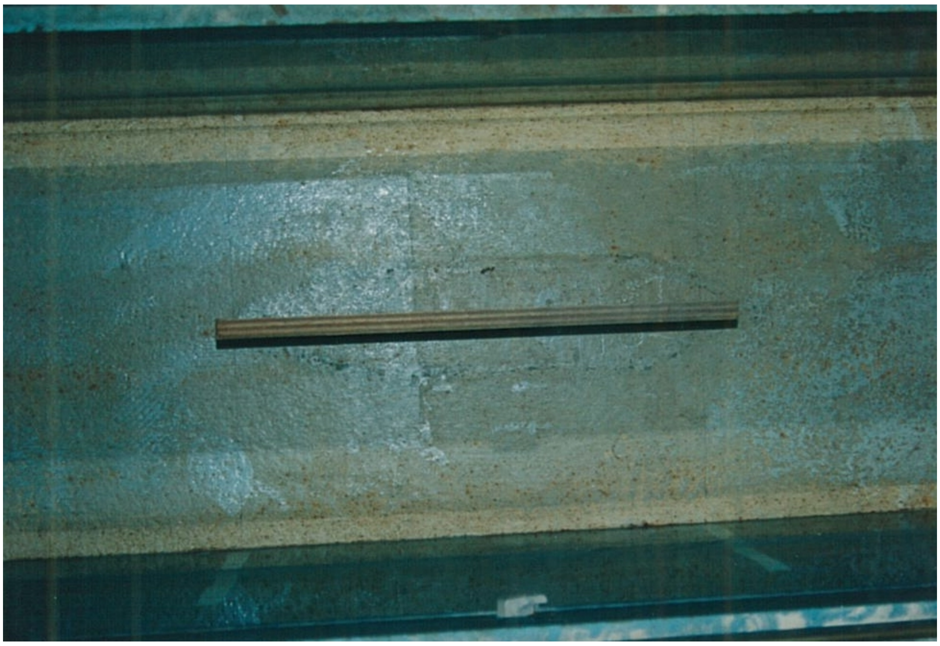

Figure 3.18 Plan view (wood pier)

Figure 3.19 3D view (wood pier)

Table 3.5 : Flow parameters for wood pier test cases

Test	Flow parameters at x = 6.30 m		
	d (m)	v (m/s)	Fr
1	0.031	1.08	2.0
2	0.020	1.27	2.9
3	0.025	1.19	2.4

3.3 Analytical Solution

Analytical solution provides a direct comparison to the numerical model without relying on hydraulic flume data. Test cases were well designed first and results were computed using analytical solution. The numerical model simulations then will be conducted. Comparison will be carried out to demonstrate the application of the numerical model in open channel flow analysis.

The chosen test cases are weir, one side and both side contraction, expansion, and gradual contraction. For additional work, channel bend was conducted for sub and supercritical flow to see the capability of model in solving bending problem for open-channel flows.

3.3.1 Weir

Weir is a quite common structure in hydraulic channel and it might cause some disturbance including hydraulic jump in flow. Therefore, weir problem had been selected as one of the simulation case for numerical model. There are four flow conditions:

1. sub-critical flow without back water
2. sub-critical flow with back water
3. supercritical flow without back water
4. supercritical flow with back water

All cases above were simulated in numerical model and the results were compared with analytical solution. Figure 3.20 shows the side view of weir problem. Other detailed parameters will be presented in chapter four for each case.

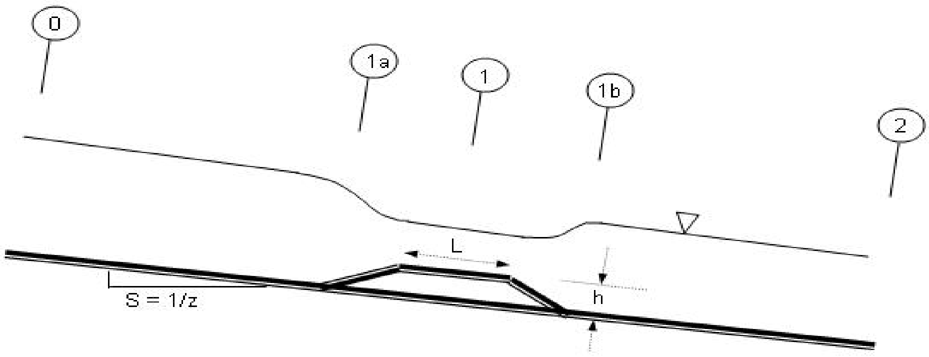

Figure 3.20 Side view of weir test case

The design steps for weir problems can be summarized as listed below:

1. A discharge rate equal to $0.0155 m^3/s$ with channel wide 0.457 m was selected. Roughness coefficient equal to 0.012 was fixed.
2. To obtain subcritical flow, slope gradient equal to 1/1500 was selected while slope 1/50 was used for supercritical flows.
3. By using the Manning equation, normal depths for each flow condition were computed. The weir was placed far enough so that approach depth will become a normal depth. With known normal depth, specific energy E can be obtained.
4. Using the specific-energy curve, the minimum total head, H_{min} was determined. The height of weir then can be decided.
5. Finally, water depths on the weir and after weir can be computed. The effect of backwater will be investigated.

Keep in mind that, the energy equation used in the design is not an independent equation as it is derived from the momentum equation (Jain, 2001). The latter requires pressure forces on the bottom and sides of the transition, which cannot be correctly estimated due to non-hydrostatic pressure distribution within the transition. Thus, the following assumptions are made in the design:

1. Section 0 and 2 (figure 3.20) are located sufficiently upstream and downstream from the weir where the pressure distribution is hydrostatic.
2. The small energy loss in transition is neglected.

3.3.2 One Side and Both Contraction

The oblique wavefront produced by a vertical channel wall deflected towards the flow through an angle θ as shown figure below:

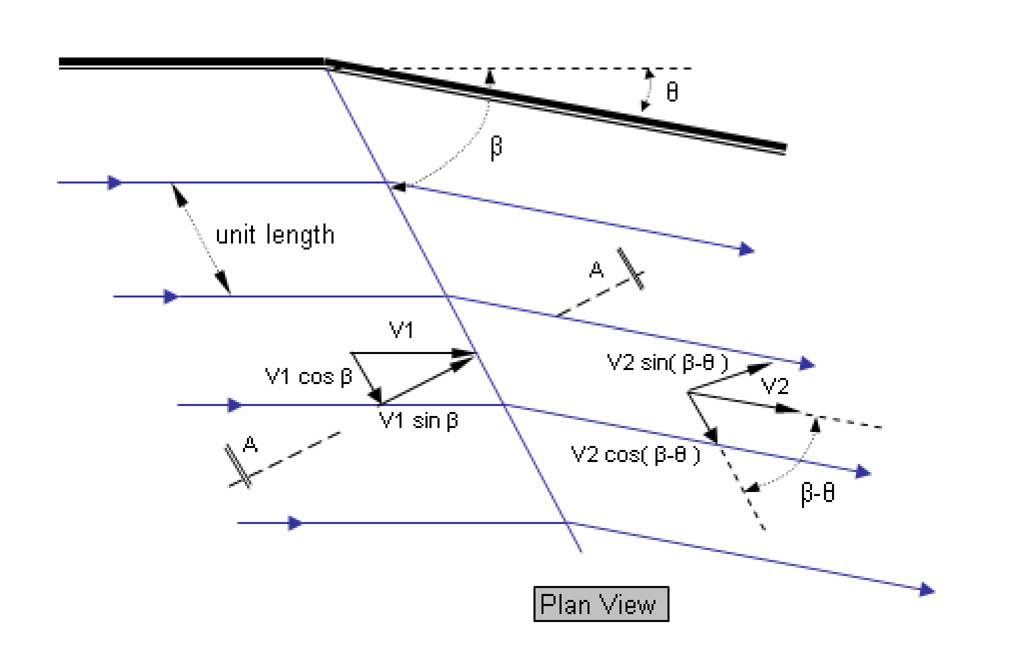

Figure 3.21 Inward deflection in boundary

Hydraulic engineers often interested in the determination of angle β of the wavefront in additional to depth and velocity downstream (Jain, 2001). The solution for three unknown variables requires three equations, which are continuity equation, and the momentum equation along and normal to wavefront.

Continuity equation:

$$y_1 V_1 \sin\beta = y_2 V_2 \sin(\beta - \theta) \tag{3.1}$$

Momentum equation normal to wavefront:

$$\frac{y_1^2}{2} + \frac{y_1 V_1^2 \sin^2\beta}{g} = \frac{y_2^2}{2} + \frac{y_2 V_2^2 \sin^2(\beta - \theta)}{g} \tag{3.2}$$

Momentum equation along the wavefront:

$$V_1 \cos\beta = V_2 \cos(\beta - \theta) \tag{3.3}$$

Three equations above are made base on a few acceptable assumptions as shown below:

1. The gravity forces and boundary resistance can be neglected in momentum equations.
2. The unit discharges normal to the wavefront are equal.
3. The net momentum flux along the wavefront is zero.
4. Distribution velocity of flow is uniform.

Some manipulations of the terms in the three basic equations above give equation (3.4) and (3.5) for small θ with assumption that specific energy, E remains constant (Jain, 2001). These two equations can be used to calculate some flow parameters after contraction such as Froude number, F_2 and water depth, y_2.

$$\theta = \sqrt{3}\tan^{-1}\frac{\sqrt{3}}{\sqrt{F^2-1}} - \tan^{-1}\frac{1}{\sqrt{F^2-1}} - \theta_1 \qquad (3.4)$$

$$\frac{y_2}{y_1} = \frac{F_1^2+2}{F_2^2+2} \qquad (3.5)$$

The procedures to design one side contraction and both side contraction are summarized below:

1. Flow rate (0.0155 m3/s), slope gradient (1/25) and Manning's *n* (0.012) were fixed.
2. Normal depth was computed, which is approximately 0.025 m with F_1 close to 2.74.
3. A deflection angle, θ = 10 degrees was tried for one side contraction and 5 degrees for both side contraction.
4. By using equation (3.4) and (3.5), expected results (F_2 and y_2) were computed and used in results comparison. Besides, the predicted angle β was concerned too.

The common design for lateral transition is to ensure the positive wave from the beginning of the converging walls cancel the negative wave originating at the point where the walls change back to parallel (figure 3.22). By this way, the flow will turn to smooth again after contraction instead of diamond-shape flow. To do that, a trial-and-error procedure was carried out to obtain the sufficient length of contraction, L as demonstrated by Jain (2001). However, some modifications might be needed in one side contraction when calculating L.

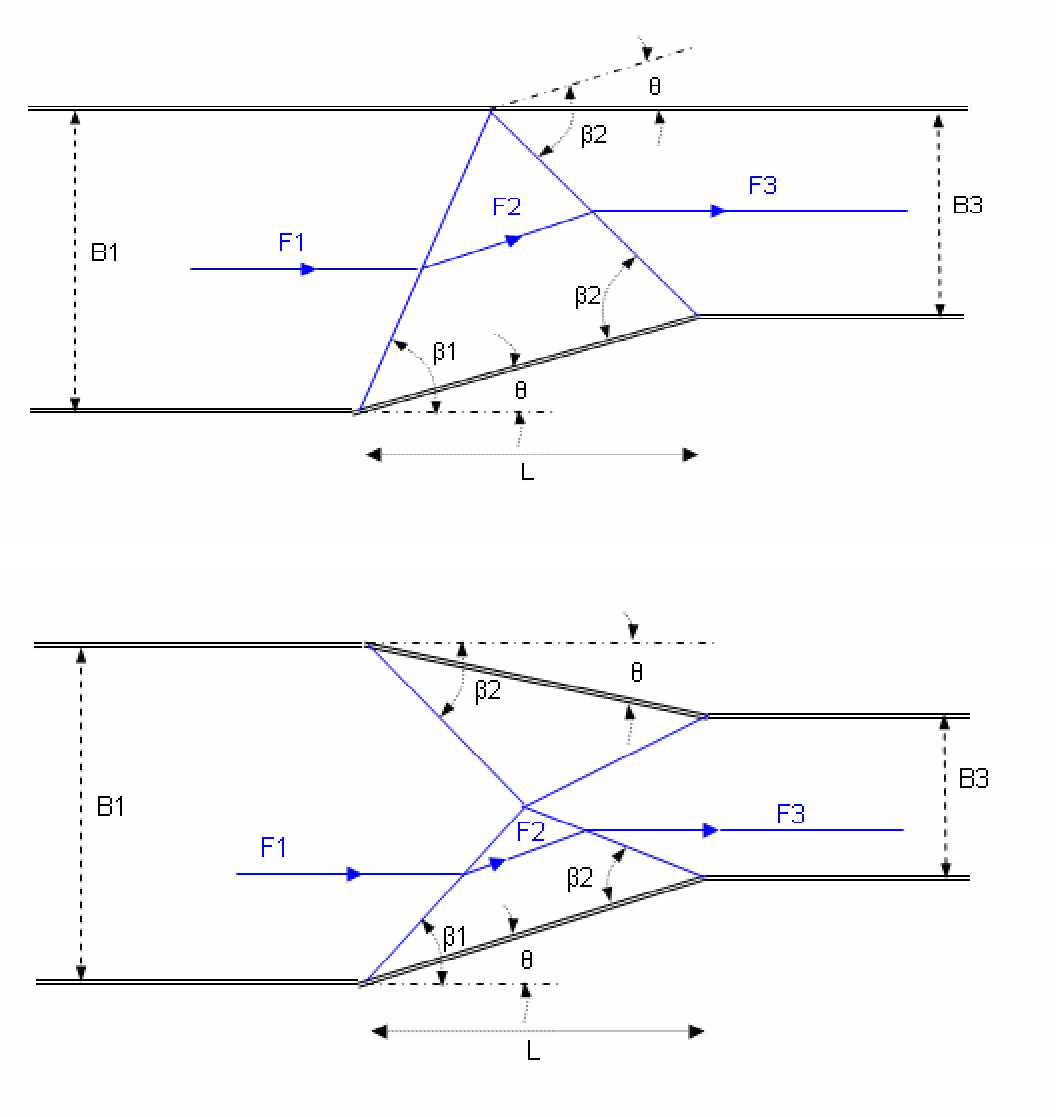

Figure 3.22 Channel design for contraction

3.3.3 Expansion

Expansion is caused by sudden outward deflection in the side boundary as shown in figure 3.23. A number of wavefronts that originate from point A, diverge from the convex boundary (Jain, 2001). Water depth decreases gradually from line AB to AC. In this case, the angle β1 and β2 were computed using equations 3.6, where F_i is Froude number at section i.

$$\beta_i = \sin^{-1}\left(\frac{1}{F_i}\right) \tag{3.6}$$

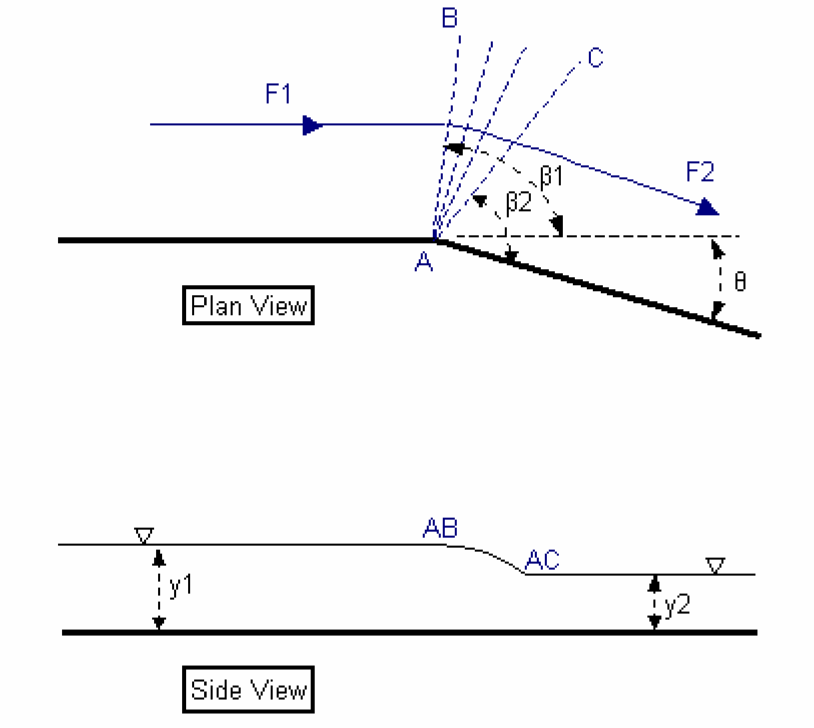

Figure 3.23 Expansion

Same as weir problem, the expansion was well designed first after determining parameters such as flow rate (0.0155 m^3/s), channel width (from 0.35 m expand to 0.457 m), angle of deflection (-5 degrees), Manning's *n* (0.009) and slope (1/75). The expansion was located far enough so that water depth can converge to normal depth, which is approximately 0.035 m with Froude number, F_1 equal to 2.16. Finally, the water depth and Froude number at the channel downstream were calculated using equation (3.4) and (3.5). Detailed calculations can be referred to Jain (2001).

3.3.4 Gradual Contraction

Problems with gradual change in the boundary were conducted for a range of Froude number, varies from 2.0 to 6.0. The relation between approach Foude number and the flow will be studied.

One side of the channel wall was replaced by a sequence of short chords, each one deflected 4 degrees relative to the preceding one as indicated in figure 3.24. The length for each short chord was 0.05 m and there were 6 of them. The channel was contracted from 0.5 m to 0.337 m. The first wave front was expected to happen at point A with an angle β1. In this test case, only the gradual contraction region was considered.

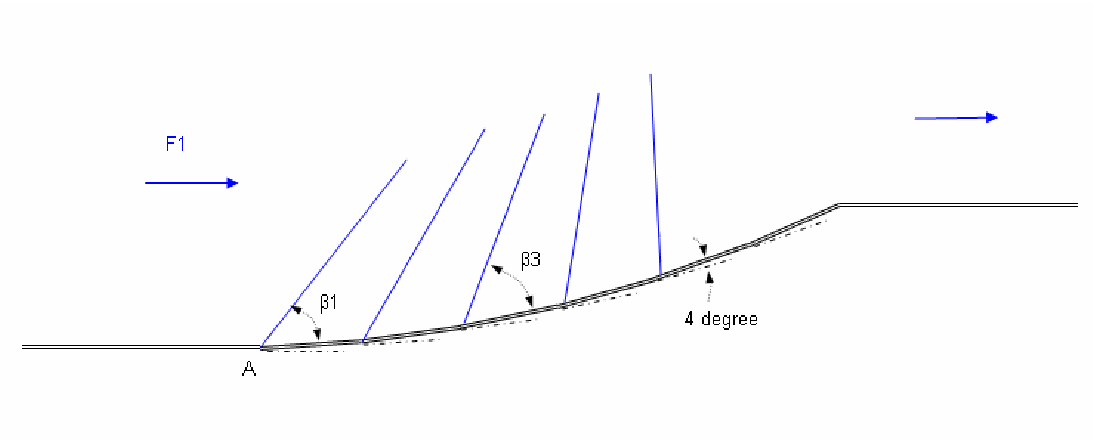

Figure 3.24 Gradual contraction

3.3.5 Bend

It is an extension problem from gradual contraction. Let's consider the figure 3.24 again; if the length of each short chord is very small compared to channel width, then it will become a bend. The flow in bends is non-uniform due to normal acceleration. The outside wall of the channel in a bend must be made high enough to accommodate the increase in water depth due to the bend. The flow in channel bends is more complex due to scour and deposition (Jain, 2001). However, this kind of channels are beyond the scope of this testing.

For subcritical flow, analytical solution provides the water depth difference between left bank and right bank in equation 3.7, where B is surface width, R is the radius of curvature of the centreline of the channel, and *V* is the average velocity.

$$\Delta y = \frac{V^2 B}{gR} \tag{3.7}$$

Ippen and Knapp found that the maximum difference depth between outer and inner walls for supercritical flow was about twice the difference for subcritical flow (Jain, 2001). Figure 3.25 below gives a better illustration. The line a-a', b-b' and c-c' respectively represent water surface in a straight channel, in a curved channel carrying subcritical flow, and in a curved channel carrying supercritical flow (Jain, 2001).

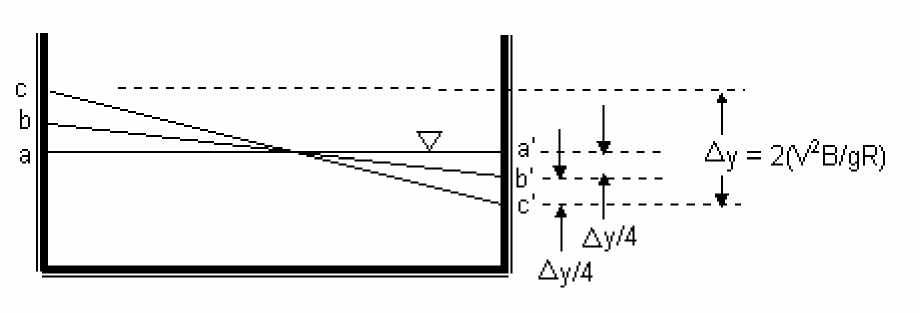

Figure 3.25 Maximum difference depth in bend

A numerical curved channel with 45 degrees bend was conducted and tested for sub and supercritical flow to compare with the above theory. The width of the model is 0.5 m with frictionless horizontal slope to ensure the approach flow is uniform. Model error was expected especially for high Froude number flow with the existing of non-hydrostatic condition in bend.

3.4 Numerical Model Application

The basic steps to conduct a hydraulic problem in numerical model are introduced in this section. The pre and post processing are very important. The finite element meshes, or cross section entities, along with associated boundary conditions necessary for analysis, are needed to be created and save to model-specific files. The post-processing is needed to view solution data such as flow velocity and steady water depth. Generally procedures can be divided into a few steps as listed below:

1. Data collection for model input parameters.
2. Draw the geometry of model in plan view.
3. Grid generation and mesh editing.
4. Apply boundary conditions and initial condition.
5. Adjust the model control such as the time step size, number of iteration steps and roughness coefficient.
6. Run the model. If necessary, repeat the run after refine the mesh grid.
7. Examine the solution for reasonableness.

3.4.1 Data Collection for Model Input Parameters

Data such as geometry of flume, roughness coefficient (Manning's n), flow conditions at boundaries; discharge rate and slope are required as input parameters. Those data can be obtained either through experiments, published laboratory results or can be designed for any specified test cases.

3.4.2 Model Geometry

The geometry of flume/channel was input into model as point coordinate in function of x and y, which are referred to longitudinal and lateral direction respectively. Meanwhile coordinate z represents the bed level from datum for each point. The value of *z* was created by using interpolation method. Note that for experiment a test cases, the coordinate z was interpolated by using data from slope checking. Other critical elements such as points on weir, contraction and bridge pier should be inputted into the model. Figure 3.26 shows an example of contraction geometry in a numerical model.

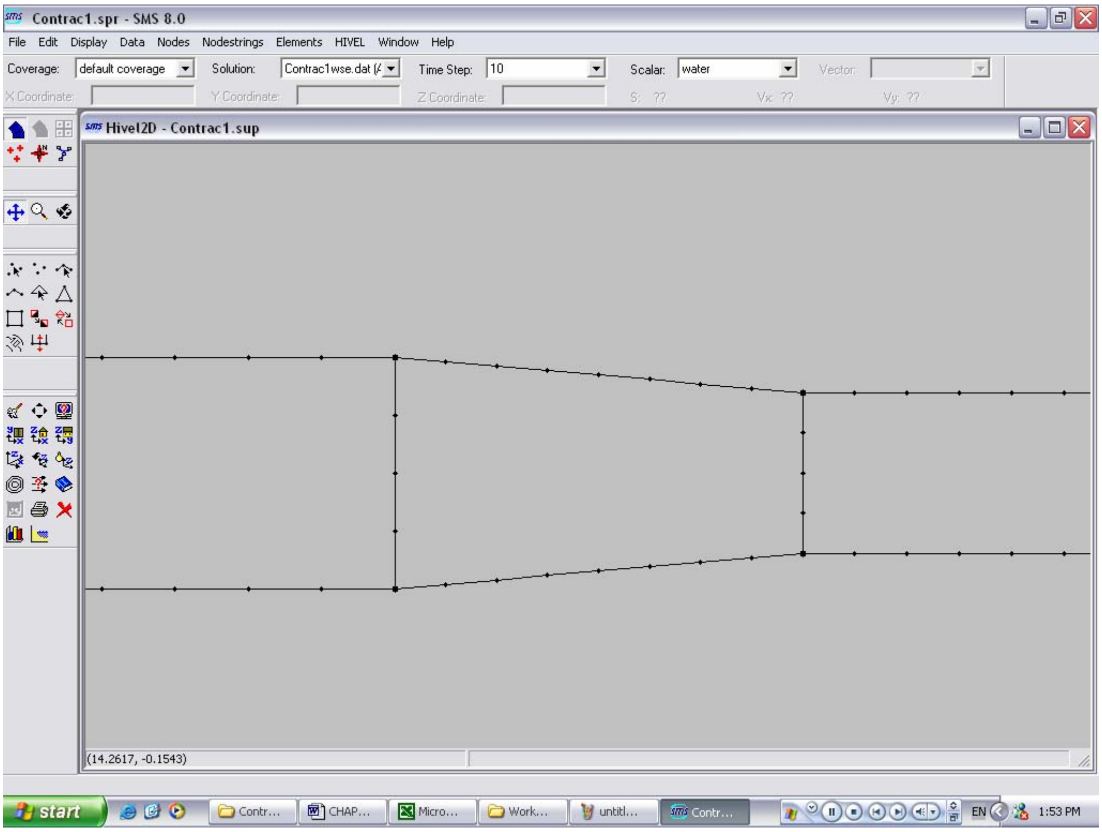
Coverage: default coverage
Solution: Contrac1wse.dat
Time Step: 10
Scalar: water
(14.2617, -0.1543)

Figure 3.26 Example geometry shown in model

3.4.3 Mesh Grid Generation

To a large degree the quality of grid determines the accuracy and stability of the model. For this numerical model, only four-node quadrilaterals and three-node triangles can be used as linear elements. The element aspect ratio was controlled within 1:2. An element’s area should not be greater than 1.5 times the smallest neighbour to allow gradual transitions in element size.

Due to the run time factor, coarse resolution was used for various test cases as a trial run. The results then were analysed and the critical sections were marked. Resolution around that marked area was increased. Normally, model resolution will be increased until the results no longer changed with greater solution for each test case. Besides, stability condition also should be considered in mesh editing. Checking on Courant-Friedrichs-Lewy (CFL) criterion was carried out from time to time especially when model stop during simulation. Further discussion about CFL is provided in the following sub-section.

Once the grid generation was completed, mesh grid was renumbered to obtain the smallest bandwidth for global matrix. Run time can be minimized with small bandwidth. Figure 3.27 shows an example of final mesh.

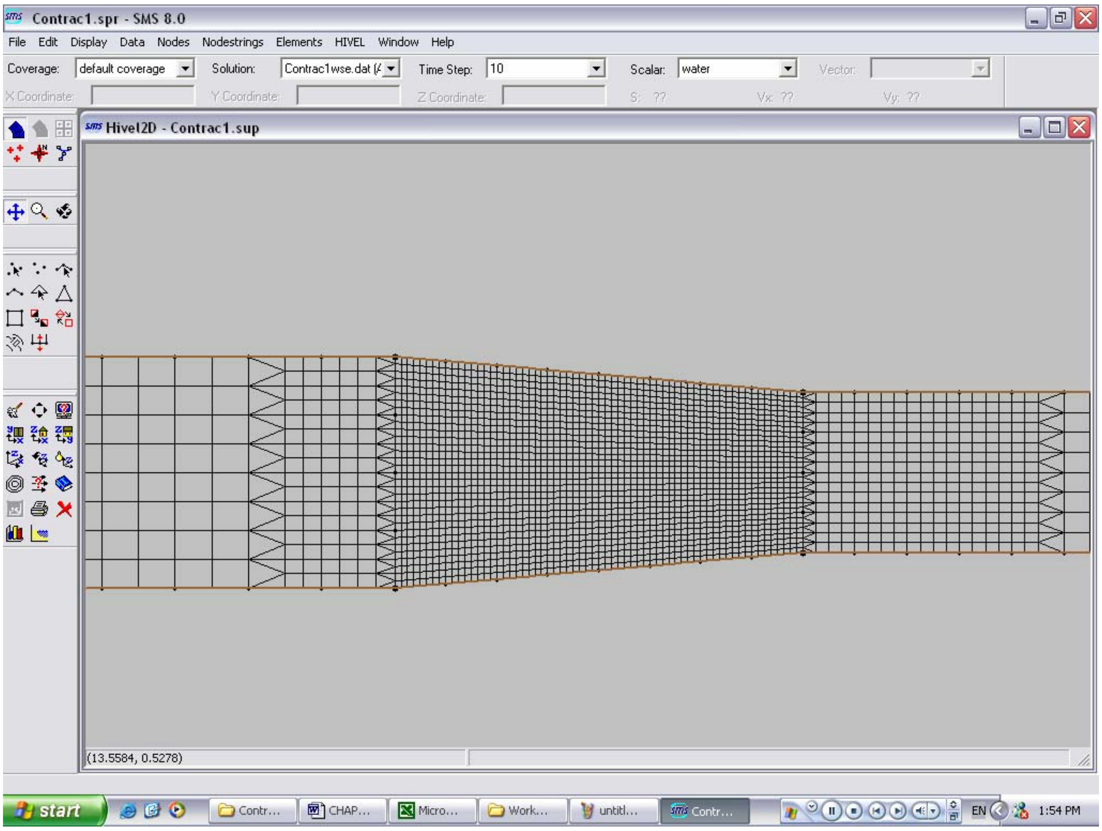

Coverage: default coverage
Solution: Contrac1wse.dat (/
Time Step: 10
Scalar: water
Vector:

(13.5584, 0.5278)

Figure 3.27 Example meshing grid shown in model

3.4.4 Initial Condition

Initial condition is always required in hyperbolic shallow water equation. Since the interest is in steady-state results only, the first-order backward difference in temporal derivative was chosen. Therefore, initial condition for one time step of old data ($t = -1$) was created in an initial file called hot start file.

The hot start file contains data such as flow rate, velocity and initial depth for each mesh node when time = -1. This file will be over written by the model and replaced with latest result data. For this reason, a copy of hot start file was always made.

Different initial condition causes different output. Thus, the accuracy of the initial guess is quite significant, and it will determine how long it will take to reach a steady state condition. Results in chapter 4 will show the importance of initial condition in several test cases.

3.4.5 Boundary Conditions

Model equations constitute a hyperbolic initial boundary value problem. The required boundary conditions are determined using characteristic method, and assigned by selecting a specific node or node string.

The number of boundary conditions is equal to the number of characteristic half-planes that originate exterior to the control and enter it. For example, if the inflow is supercritical, then all information from outside the control is carried through this boundary; if inflow is subcritical, downstream control effect will provide the depth. Thus, depth is not needed in this inflow boundary.

In the same manner, if outflow boundary is supercritical, no boundary condition is specified because all information can be determined within the control domain. If outflow is subcritical, then the depth should be provided as tailwater. The no-flux boundary condition is appropriate at sidewall boundaries. Detail discussion can be found in a technical report Berger (1995). Figure 3.28 shows the boundary input form in the model.

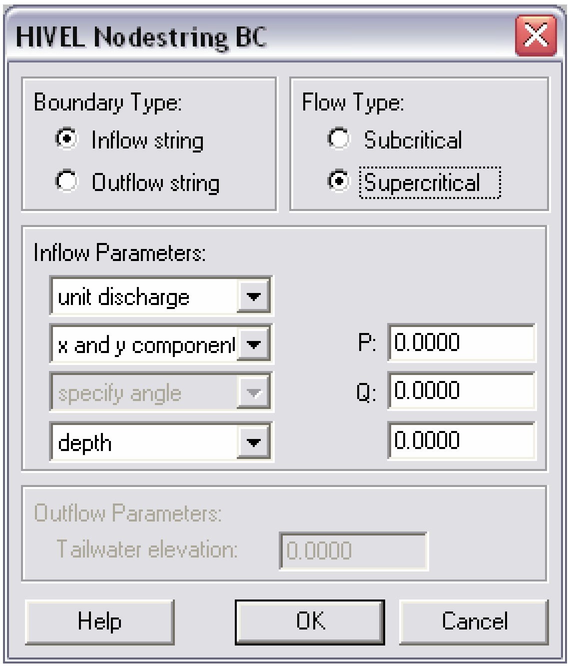

Boundary Type:
● Inflow string
○ Outflow string

Flow Type:
○ Subcritical
● Supercritical

Inflow Parameters:
unit discharge
x and y component
specify angle
depth
P: 0.0000
Q: 0.0000
0.0000

Outflow Parameters:
Tailwater elevation: 0.0000

Figure 3.28 Input for boundary conditions

3.4.6 Model Control

All the hydraulic information about the computation parameter for the model run was controlled. As mentioned above, the Courant-Friedrichs-Lewy (CFL) number is controlled by grid and time step size as shown in equation 3.8.

$$CFL = \frac{\left|\sqrt{u^2 + v^2}\right| + \sqrt{gh}}{\Delta l + \Delta t} \tag{3.8}$$

where, u and v are velocity in x and y direction; Δl is element length and Δt is time step size. Every computation was started with small time step, and then gradually increased if the steady state solution is desired. This can prevent model from error and gives better results. However, more time is spent with smaller time step.

Experience has shown that the model sometimes will converge to a different solution with different time step size as described in chapter 4. In fact, it needs engineering judgement to decide the time step size.

The element type was assigned using Manning's *n* because stresses are modeled using the Manning's formulation for boundary drag. Note that the Manning's *n* applies to each element bed surface as well as the adjoining sidewalls automatically. This includes the wall friction for pier in model. This means that the sidewall roughness cannot be assigned independently. The input form is shown in figure 3.29.

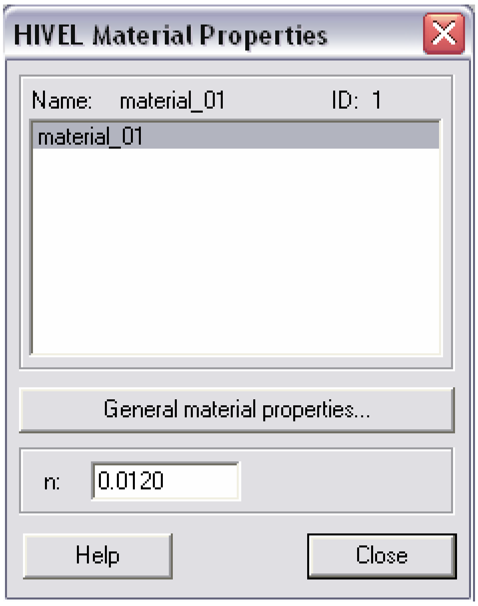

Name: material_01 ID: 1

material_01

n: 0.0120

Figure 3.29 Input for Manning's n

Besides, dissipation coefficient (β_{shock} and β_{smooth}) in Petrov-Galerkin parameters for shock and smooth flow also was controlled. Sensitivity study on this parameter was carried out too. Other parameters such as coefficients used in determination of eddy viscosity, acceleration of gravity (imperial/SI units), and number step of iteration in Newton-Raphson method was also adjusted.

3.4.7 Model Run

During this process, the results for each time-step are displayed. These results include the number of iterations required, the maximum residual error and the node with which it is associated, and the average energy. When it is done, results will be saved in two output files that contain final water depth and velocity for each node. Post-processing is needed to view the results.

3.4.8 Results Examination

Results from model were examined for reasonableness. To do this, a post-processing step was needed to open results in graphic or table mode. For this reason, a software named Surface Water Modelling System 8.0 (SMS) was used. Results are presented in contour or vector mode for viewing.

CHAPTER 4

RESULTS AND ANALYSIS

4.1 Introduction

As stated previously, this study involves experimental works and numerical model simulation. For every test case, results from both sources are presented together for comparison purpose. Input parameters for each simulation are provided and results from both sources were analyzed.

In addition, the sensitivity of simulation results to the choice of dissipation coefficient (β) and mesh refinement were tested. This sensitivity was examined by repeating a run case with different model conditions to assess the test case condition's impact on simulation results.

4.2 Control Test

In the laboratory test, a valve was used to regulate the flow rate. Through these control tests, the flow rate for every valve turn can be determined. For this purpose, control tests were conducted in four different slope gradients (1/z) and each of them was repeated to ensure the consistency, as shown in table 4.1. For example, a discharge of 0.0291 m^3/s, corresponding to a slope of 1/65, was obtained after making 720 degree turn to the valve (2.0 round).

Table 4.1 : Measured flow rate, Q

Valve turn	1/ 150	1/150	1/500	1/500	1/1500	1/1500	1/1500	1/65	**average**
1.00	0.0062	0.0061	0.0054	0.0060	0.0058	0.0056	0.0061	-	**0.0059**
1.25	0.0098	0.0110	0.0105	0.0105	0.0103	0.0110	0.0110	0.0110	**0.0105**
1.50	0.0155	0.0160	0.0154	0.0159	0.0159	0.0159	0.0164	0.0158	**0.0157**
1.75	0.0206	0.0232	0.0208	0.0221	0.0219	0.0213	0.0219	0.0229	**0.0218**
2.00	0.0262	0.0299	0.0277	0.0273	0.0271	0.0273	0.0268	0.0291	**0.0278**
2.25	0.0349	0.0306	0.0315	0.0318	0.0326	0.0315	0.0314	0.0360	**0.0328**
2.50	0.0398	0.0368	0.0372	0.0386	0.0394	0.0372	0.0355	0.0425	**0.0386**
2.75	-	0.0419	0.0471	0.0466	0.0468	0.0468	0.0421	0.0481	**0.0459**
3.00	-	0.0458	0.0530	0.0519	0.0545	0.0544	0.0503	0.0529	**0.0523**

Results above will not be used in model simulation. However, they are important in estimating the possible value of Manning's *n* for the laboratory flume by using Manning equation. With known flow rate and measured normal depth, as indicated in table 4.2, the range for Manning's *n* was computed and listed in table 4.3. The information in table 4.3 is essential to provide a guideline in determining the roughness coefficient for numerical model.

Table 4.2 : Measured normal depth (unit cm) from experiment

Valve turn	1/ 150	1/150	1/500	1/500	1/1500	1/1500	1/1500	1/65
1.00	2.2	2.1	3.2	3.3	3.6	3.5	3.5	1.8
1.25	3.0	2.8	4.6	4.5	4.9	4.9	4.9	2.4
1.50	3.8	3.6	5.7	5.7	6.1	6.1	6.2	3.0
1.75	4.5	4.6	7.0	7.1	7.6	7.4	7.6	3.8
2.00	5.5	5.5	8.3	8.4	9.0	8.9	8.9	4.5
2.25	6.5	6.3	9.3	9.4	10.2	10.0	10.1	5.2
2.50	7.0	7.1	10.3	10.3	11.2	11.0	11.1	5.6
2.75	8.1	7.7	11.2	11.2	12.2	11.9	11.8	6.2
3.00	8.9	8.4	12.2	12.2	13.1	12.8	12.5	6.7

Table 4.3 : Manning’s *n* for flume

Valve turn	1/ 150	1/150	1/500	1/500	1/1500	1/1500	1/1500	1/65
1	0.009-0.01	0.009-0.01	0.0109-0.0117	0.0101-0.0107	-	-	-	0.0095-0.011
1.25	0.009-0.0097	0.009-0.0097	0.01-0.0104	0.0096-0.01	-	-	-	0.009-0.0099
1.5	0.0092-0.0096	0.0085-0.0089	0.0095-0.0097	0.0092-0.0094	-	-	-	0.0085-0.0091
1.75	0.0085-0.0088	0.0089-0.0092	0.0096-0.0097	0.0093-0.0094	-	-	-	0.0088-0.0092
2	0.009-0.0092	0.0086-0.0088	0.0095-0.0096	0.0098-0.0099	-	-	-	0.0089-0.0093
2.25	0.0101-0.0103	0.0091-0.0093	0.0098	0.0100	-	-	-	0.0089-0.0091
2.5	0.0095-0.0096	0.0091-0.0092	0.0097-0.0098	0.0094	-	-	-	0.0086-0.0088
2.75	0.0101-0.0102	0.0089-0.009	0.0086	0.0087	-	-	-	0.0088-0.009
3	0.0101-0.0102	0.0088	0.0087	0.0089	-	-	-	0.0091-0.0092

Generally, the Manning’s *n* for the flume is within the range from 0.0085 to 0.0107 due to its composite material. The maximum Manning’s *n* of 0.0117 was neglected because it fall out of the range when compared to others. For slope 1/1500, no calculation is made due to the condition of non-smooth bed surface. As reported in chapter 3, the flume’s bed is not smooth and its impact becomes more significant in mild slope, which is clearly shown in figure 4.1. The “1/1500” thus only becomes a label and cannot represents the real slope condition for the flume. Without the exact slope gradient, the accuracy of calculated Manning’s *n* is questionable. However, for steep slope, the smoothness of bed surface is unaffected. Figure 4.2 shows one of the measured bed level for steep slope (1/65). The average error of 4 mm is considered acceptable.

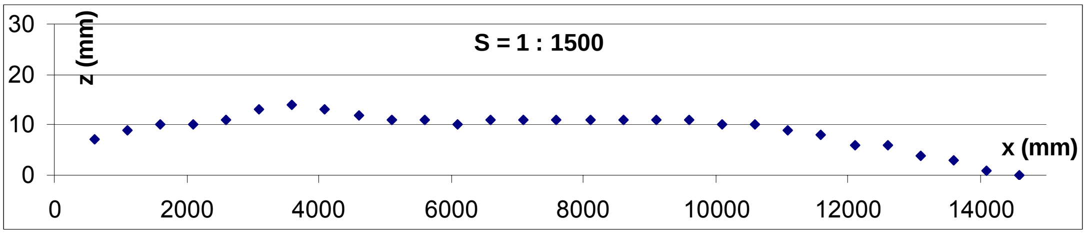

Figure 4.1 Bed surface of flume (mild slope)

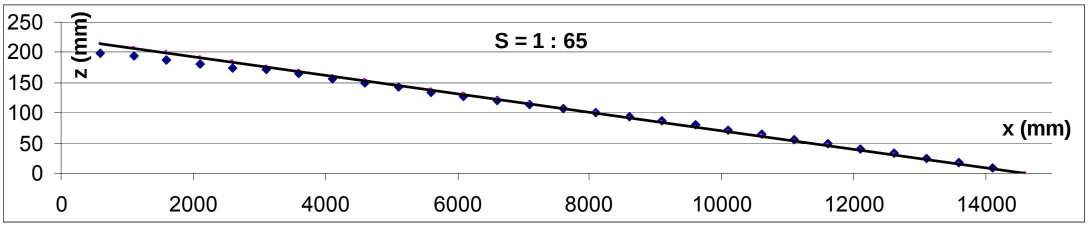

Figure 4.2 Bed surface of flume (steep slope)

Always keep in mind that the non-smooth bed surface will not give any problem to model simulation because slope checking was carried out for every test case. The measured real slope in the laboratory will be used as the input in modelling.

During the control test, a series of water depth data were recorded starting from x = 0.6 m, for various flow rates and slope gradients. By using these data, the numerical model was examined for the first time in this simplest test case. Figure 4.3 shows the measured water depths (blue line) with a slope of 1/500 for 1.0, 1.5 and 2.0 valve turn respectively. Meanwhile the red line in the figure represents the simulated water depth from numerical model. Results indicated that good agreements were achieved. The water profiles were particularly affected by the non-smooth bed surface and boundary conditions.

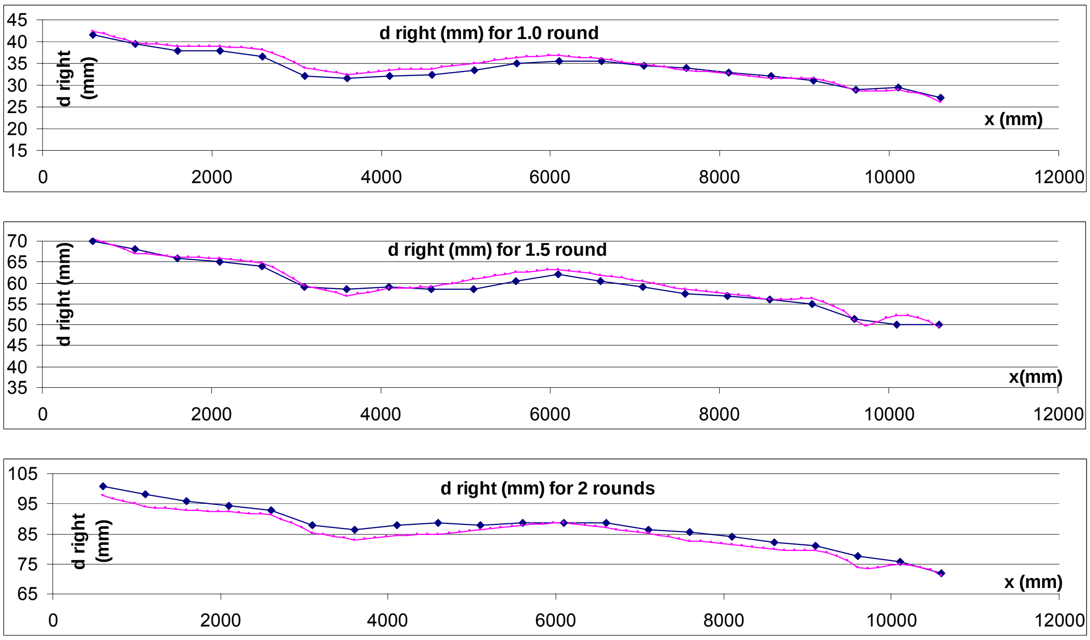

Figure 4.3 Comparison water depths for different flow rate with S = 1/500

To see the sensitivity of Manning's *n* and dissipation coefficient (β_{shock}, β_{smooth}), a few model simulations were performed with various *n* and β, and compared with the measured water depth with a slope of 1/1500. The result is plotted in figure 4.4.

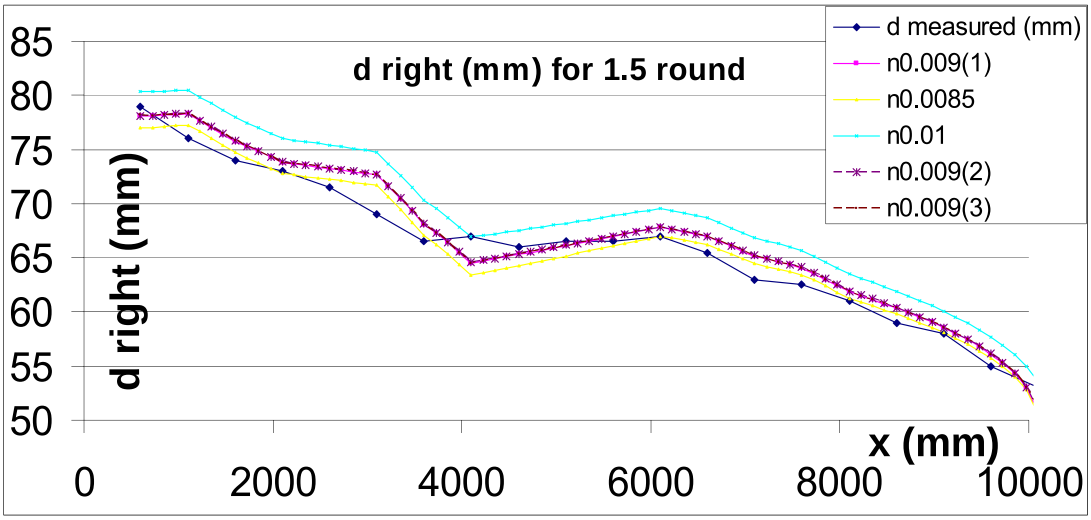

Figure 4.4 Comparison water profiles for different *n* and β with S = 1/1500

As described before, the exact Manning's *n* for mild slope is unknown. Therefore, a few trial runs with various roughness coefficients were examined, that were 0.0085, 0.009 and 0.01. From figure 4.4, it is interesting to express that the water depth increased with larger *n* value. This is not surprising since based on Manning equation, the roughness is proportional to the depth in constant flow rate (Q). In other words, when the friction increases, the velocity will decrease and the water depth will increase due to continuity condition.

Referring to the legend in figure 4.4, the n0.009(1), n0.009(2) and n0.009(3) represent three different set of β (β_{shock}, β_{smooth}) respectively, as listed below:

1. n0.009(1) : $n = 0.009$, $\beta_{shock} = 0.25$, $\beta_{smooth} = 0.25$
2. n0.009(2) : $n = 0.009$, $\beta_{shock} = 0.25$, $\beta_{smooth} = 0.50$
3. n0.009(3) : $n = 0.009$, $\beta_{shock} = 0.10$, $\beta_{smooth} = 0.10$

The result clearly shows that the solution is not significantly influenced by the choice of Petrov-Galerkin weighting parameter β.

4.2.1 Normal Depth

In the control test, it was found that the exact roughness of flume cannot be determined. For this reason, the numerical model was compared again with analytical solution by using a fixed roughness *n*. In this case, Manning equation was selected to facilitate the evaluation and comparison.

$$Q = \frac{AR^{2/3}\sqrt{S}}{n} \tag{4.1}$$

In Manning equation, the variable Q, B and *n* were fixed to 0.0155m^3/s, 0.457 m and 0.012, respectively. These parameters will be used as input data in numerical model. Normal depths corresponding to various slope gradient (S) were calculated for results comparison. By this way, roughness problem can be avoided and the accuracy of numerical model can be fully tested. Figure 4.5(a) shows an example of plan view of numerical model, with 15 m long and 0.457 m wide. The initial depth was set to calculated normal depth of 0.025 m. Other input details are listed below:

$Q = 0.0155$ m^3/s
$n = 0.012$
$S = 1/25$
time step = 1s
Upstream B.C = supercritical (h = 0.028 m)
Downstream B.C = supercritical
Initial depth = bed level + 0.025m
$\beta = 0.25$

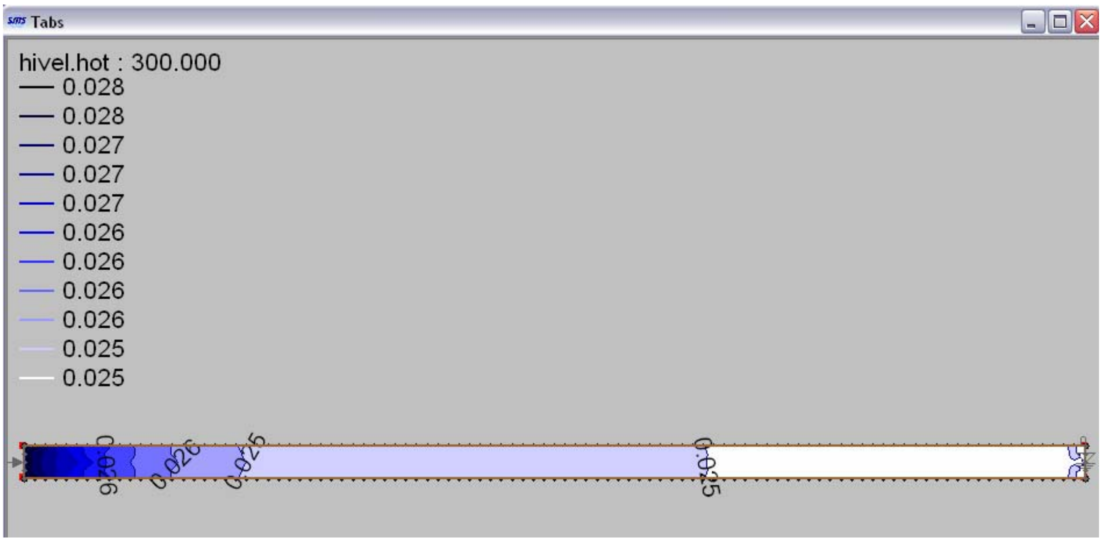

Figure 4.5(a) Water depth contours from numerical model at t = 300s

After 300 seconds, the water depth converged to 0.025 m and maintained till the end of flume. The numerical model was repeated again but this time the upstream boundary condition was changed to h = 0.022 m which was lower than the previous simulation run. The result is displayed in figure 4.5(b). Again, the simulated depth converged to 0.025 m, which yielded result very close to the analytical solution. It is apparent that the upstream boundary depth had no effect in the convergence of normal depth.

Next, the test was further extended to examine the performance of numerical model by changing the slope gradient. As shown in table 4.4, the numerical model always underestimated normal depth, and the error increased as the slope decreased. In addition, similar results were obtained after extending the length of channel from 15m to 200m.

Figure 4.5(b) Water depth contours from numerical model at t = 300s

To see the effect of different flow rate, a discharge rate of 10.0m^3/s was used in the following tests. The Manning's *n* was maintained as 0.012 but the channel width was changed to 3 m. Similar to the previous tests, the computed normal depths, (y_o theory) were compared to simulated normal depths (y_o model), as presented in table 4.5. The result shows that y_o model was always lower than y_o theory. The error increased for larger flow rate with maximum error of 11%. This is a direct result of the shallow water equation assumption. The various wavelengths actually should propagate at different speeds with the shorter one propagating more slowly. In the shallow water model all waves travel at a speed of an infinitely long wave. This higher wave celerity leads to decreasing water depth to maintain constant flow rate.

Table 4.4 : Normal depth for small flow rate, Q = 0.0155 m^3/s

S	**y_o theory**	Flow Condition	**y_o model**	Displacement (m)	% error
1/25	**0.025**	super	**0.025**	0	0.00
1/50	**0.032**	super	**0.031**	0.001	3.13
1/75	**0.036**	super	**0.035**	0.001	2.78
1/100	**0.04**	super	**0.038**	0.002	5.00
1/125	**0.043**	super	**0.041**	0.002	4.65
1/150	**0.046**	super	**0.043**	0.003	6.52
1/175	**0.048**	super	**0.045**	0.003	6.25
1/200	**0.049**	sub	**0.047**	0.002	4.08
1/250	**0.053**	sub	**0.051**	0.002	3.77
1/300	**0.056**	sub	**0.054**	0.002	3.57
1/350	**0.059**	sub	**0.057**	0.002	3.39
1/400	**0.061**	sub	**0.059**	0.002	3.28
1/500	**0.066**	sub	**0.064**	0.002	3.03
1/600	**0.071**	sub	**0.068**	0.003	4.23
1/800	**0.077**	sub	**0.075**	0.002	2.60
1/1000	**0.083**	sub	**0.080**	0.003	3.61
1/1500	**0.095**	sub	**0.091**	0.004	4.21
1/2000	**0.106**	sub	**0.100**	0.006	5.66
1/2500	**0.113**	sub	**0.107**	0.006	5.31
1/3000	**0.121**	sub	**0.114**	0.007	5.79

Table 4.5 : Normal depth for large flow rate, Q = 10.0 m^3/s

S	**y_o theory**	Flow Condition	**y_o model**	Displacement(m)	% error
1/25	**0.420**	super	**0.404**	0.017	3.93
1/50	**0.529**	super	**0.504**	0.025	4.73
1/75	**0.606**	super	**0.579**	0.028	4.54
1/100	**0.669**	super	**0.634**	0.036	5.31
1/125	**0.722**	super	**0.683**	0.040	5.47
1/150	**0.769**	super	**0.725**	0.045	5.79
1/200	**0.850**	super	**0.787**	0.063	7.41
1/250	**0.920**	super	**0.860**	0.060	6.52
1/300	**0.981**	super	**0.914**	0.068	6.88
1/350	**1.037**	super	**0.965**	0.072	6.94
1/400	**1.088**	sub	**1.013**	0.075	6.89
1/500	**1.180**	sub	**1.089**	0.091	7.71
1/600	**1.261**	sub	**1.160**	0.101	8.01
1/800	**1.402**	sub	**1.284**	0.118	8.42
1/1000	**1.524**	sub	**1.388**	0.136	8.92
1/1500	**1.778**	sub	**1.600**	0.178	10.01
1/2000	**1.987**	sub	**1.779**	0.208	10.47
1/2500	**2.167**	sub	**1.929**	0.238	10.98

The velocity was assumed uniform in Manning equation but this is not true in real condition simulation. In model, the velocity is not uniform due to friction from side wall. For example, as highlighted in table 4.5, the velocity should be equal to 3.92 m/s according to Manning equation. However, the velocity distribution in model varied from 3.854 m/s to 4.32 m/s as shown in figure 4.6.

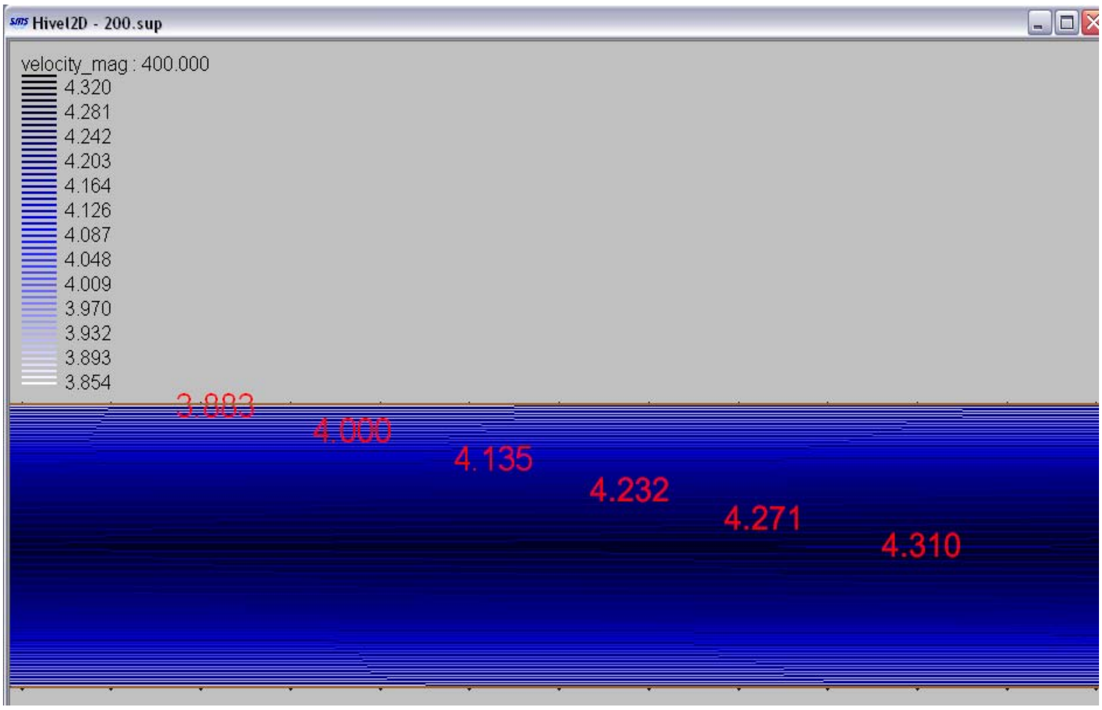

Figure 4.6 Velocity distribution when steady state

The control test and normal depth model simulation provided information such as the available flow rate in the laboratory, possible roughness for flume, the sensitivity of Manning's *n* and dissipation coefficient (β_{shock}, β_{smooth}), and the accuracy of numerical model prediction. Through these simple test cases, it clearly shows roughness always the main problem in the model simulation since it gives significant effect to the solution. Overall, the model is able to converge to a stable and consistent solution with an acceptable error due to the limitations of shallow water equations.

4.3 Test Cases

Numerous test cases are presented in the following sections, which consist of weir, expansion, contraction, channel junction, hydraulic jump, bridge pier, gradual contraction and bend. All test cases demonstrated the ability of numerical model to capture shock wave and to predict the flow profile.

4.3.1 Weir

Weirs are among the oldest and simplest hydraulic structures that have been used for centuries by hydraulic engineers for flow measurement, energy dissipation, flow diversion, regulation of flow depth and flood passage.

Four different flow conditions were solved using analytical solution and numerical model. The first condition was subcritical flow without back water. The related flow parameters used in numerical model and analytical solution are shown in table 4.6. A 3.0 m long weir structure was placed at *x* = 20 m with 0.01 m height. Based on analytical solution, no back water should occur in this case.

Table 4.6 : Flow parameters for subcritical flow without back water (weir)

Q (m^3/s)	B (m)	Channel length (m)	*n*	S	y_o theory (m)	*β*
0.0155	0.457	30	0.012	1/1500	0.095	0.25

Weir height (m)	Upstream BC	Downstream BC	Initial condition
0.01	sub	Sub (h=0.095m)	0.080m depth

Figure 4.7 illustrates the mesh grid near the weir location. Since this was considered one-dimensional problem, only 4 elements, each 0.11m wide was constructed laterally across the channel in model.

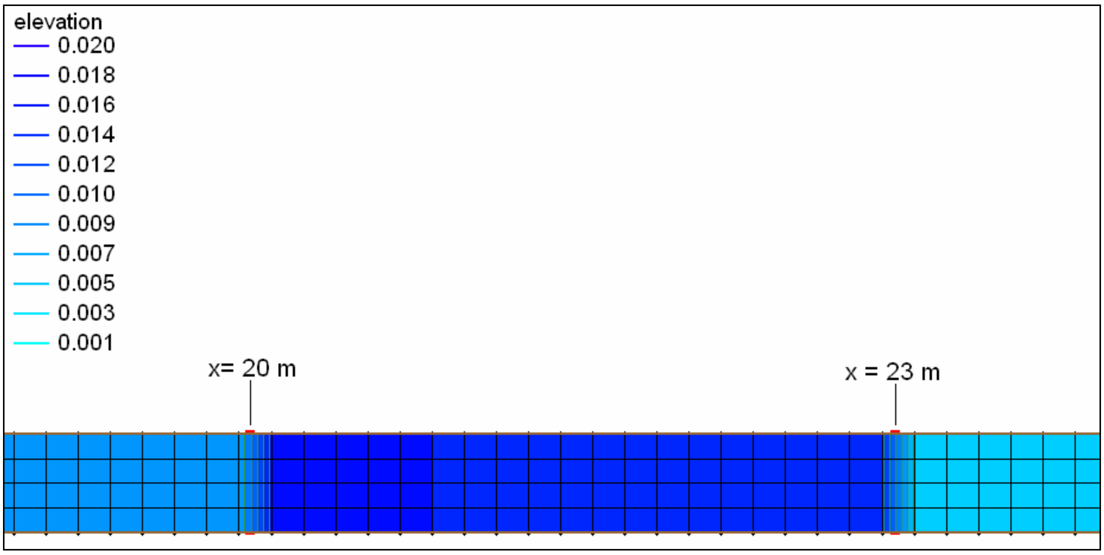

Figure 4.7 Mesh grids (weir)

The model was computed until 400s after reaching a steady condition and the result (centre grid) is plotted in figure 4.8. Using analytical solution, the water depth before, above and after the weir should be 0.095 m, 0.082 m and 0.095 m respectively. As shown in figure 4.8, numerical model results are in agreement with the analytical solution.

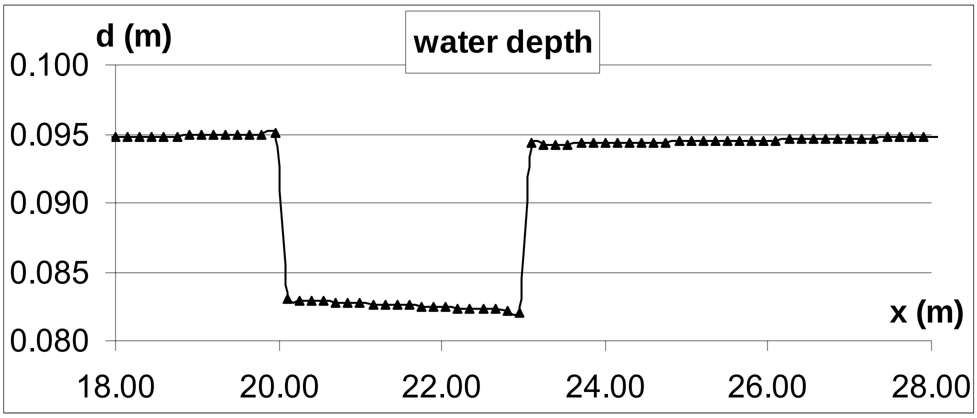

Figure 4.8 Result for subcritical flow without back water (weir)

The second situation was set to create a subcritical flow with back water. For this case, the weir's height was raised to 0.040 m from the position *x* = 15 m to *x* = 16 m. The same mesh resolution and flow parameters were used. However, the tailwater depth was fixed to 0.070 m. Expected back water can be seen in numerical model result as shown in figure 4.9. The water depth, approaching the weir was

0.110 m and dropped to 0.050 m on the weir, followed by 0.025 m at the end toe of weir, and rapidly jumped to 0.078 m height due to mild slope effect at the downstream end. Although the simulated depths compared quite well with the computed depths, further experiments are needed to verify the location of hydraulic jump.

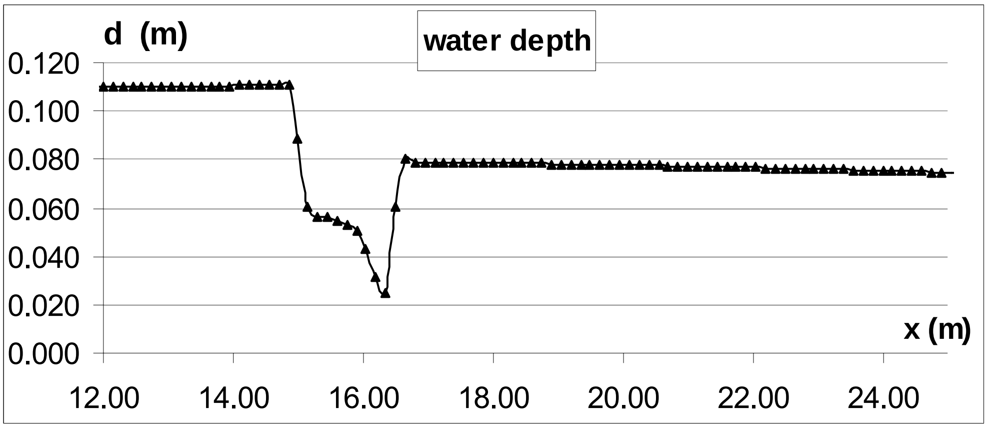

Figure 4.9 Result for subcritical flow with back water (weir)

The third situation was designed to produce a supercritical flow without back water. To produce a supercritical flow, a slope of 1/50 was selected. Other flow parameters are listed in table 4.7. The β were defined as dissipation coefficient for shock and smooth region (β_{smooth} and β_{shock}). Figure 4.10(a) presents the simulated water profile. Meanwhile figure 4.10(b) indicates that approach water depth near the weir was found to be 0.031 m, increased to 0.034 m on the weir structure, but dropped to 0.031 m after the weir. The profiles are similar to profiles obtained in the exact solution.

Table 4.7 : Flow parameters for supercritical flow without back water (weir)

Q (m^3/s)	B (m)	Channel length (m)	n	S	y_o theory (m)	β
0.0155	0.457	30	0.012	1/50	0.032	0.25, 0.5

Weir height (m)	Upstream B.C.	Downstream B.C.	Initial condition
0.01	Super (h=0.032m)	Super	0.035m depth

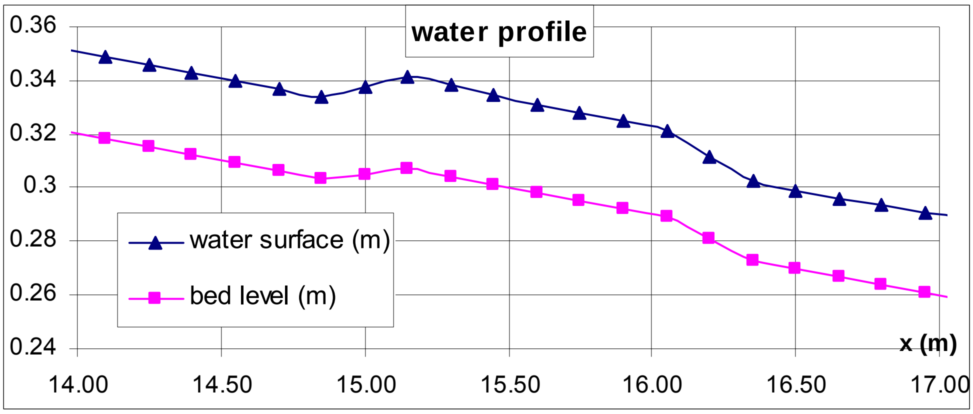

Figure 4.10(a) Water profile for supercritical flow without back water (weir)

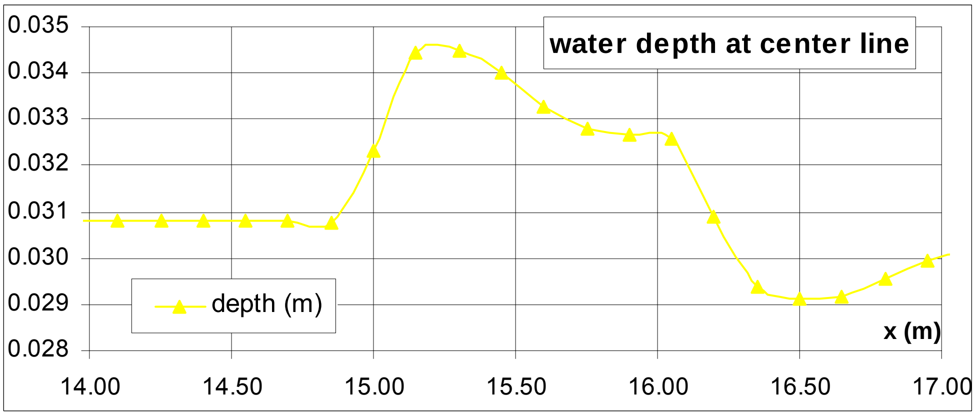

Figure 4.10(b) Result for supercritical flow without back water (weir)

The fourth situation was supercritical flow with back water. All flow parameters were maintained except the weir height was increased to 0.030 m to form back water. Simulated results are illustrated in figure 4.11(a) and figure 4.11(b).

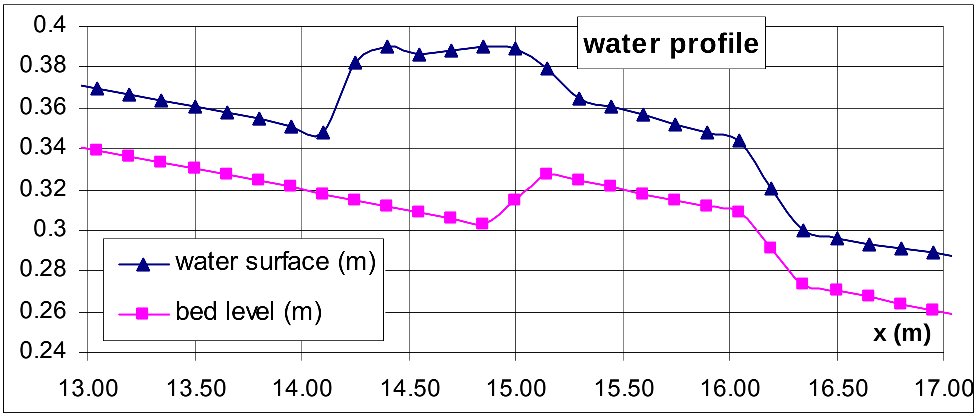

Figure 4.11(a) Water profile for supercritical flow with back water (weir)

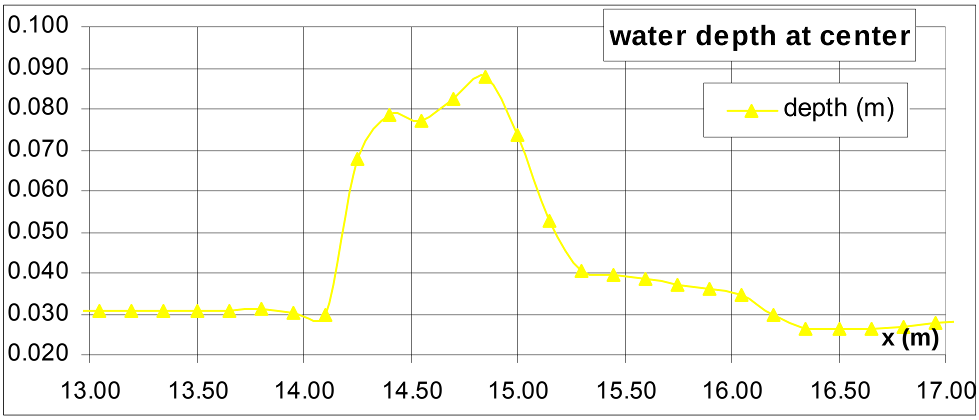

Figure 4.11(b) Result for supercritical flow without back water (weir)

In this case, it was not easy to determine the depth around the weir in the model. However, the maximum level of back water still can be determined. Besides, the subcritical flow (back water region) changed to supercritical flow at the downstream of the weir. Table 4.8 shows the overall results for all test cases, and comparison of the results with analytical solution. The average error was about 0.002 m (3.6 %). Comparison shows that the model is adequate to address hydraulic problem involving weir structure.

Table 4.8 : Results comparison for weir test case with analytical solution

Test Case		Water depth (m)		
		Before weir	Above weir	After weir
1	Theory	0.095	0.082	0.095
	Model	0.095	0.083	0.093
	Error	0.000	0.001	0.002
	% error	0.0	1.2	2.1
2	Theory	0.108	0.049	0.026
	Model	0.110	0.05	0.025
	error	0.002	0.001	0.001
	% error	1.9	2.0	3.8
3	Theory	0.032	0.038	0.032
	Model	0.031	0.034	0.031
	error	0.001	0.004	0.001
	% error	3.1	10.5	3.1
4	Theory	0.097	0.049	0.028
	Model	0.087	0.050	0.027
	error	0.010	0.001	0.001
	% error	10.3	2.0	3.6

In fact, the analytical solution cannot represent the real condition on site with the attendance of assumptions in the solution. For this reason, observed results from experiment were required for model simulation. Figure 4.12 shows the front view of a mortal weir in the flume experiment.

Figure 4.12 Front view of mortal weir

The flume slope was approximately set to 1/65 to obtain a supercritical flow, with normal depth (approach depth) equal to 0.030 m. The test was started in dry bed condition. During the test, water elevation increased when the flow passes through the weir as shown in figure 4.13.

Figure 4.13 Side view of water profile on the weir

Based on analytical solution, the increased water depth was determined. However, the flow pattern on the weir formed a “V” shape as shown in figure 4.14, which is impossible to be computed in analytical solution. This happened because of the frictional effect from side walls.

Figure 4.14 Flow pattern on the weir

The flume experiment was then modelled to see whether the “V” pattern could be captured or not. The test was simulated with Q = 0.0152 m^3/s as measured in lab. Other detail inputs are outlined in table 4.9. The Manning’s *n* was obtained by trial and error by matching the computed water depths with the measured water depths in the flume. It was found that the *n* = 0.094 gave the best result.

Table 4.9 : Input parameters for numerical model (weir experiment)

Q (m3/s)	Up BC	Down BC	B (m)	Slope	*n*	*β*	time step (s)
0.0152	super (h=0.037)	supercritical	0.457	measured	0.0094	0.25, 0.5	0.05

The initial dry bed condition was applied in flume. However, because the numerical model is not adapted to handle dry-bed propagation, the initial condition was modified so that initial water depth at *x* = 0.6 m was 0.26 m and reduced gradually to 0.01 m until *x* = 3.1 m and maintained till the end of flume, as shown in figure 4.15. The mesh grid is presented in figure 4.16 with maximum aspect ratio of 1.2.

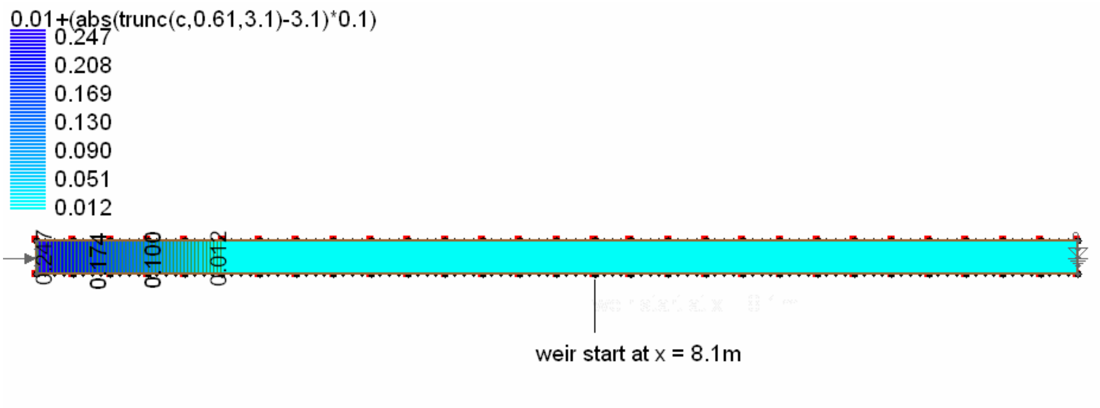

Figure 4.15 Initial condition (weir experiment)

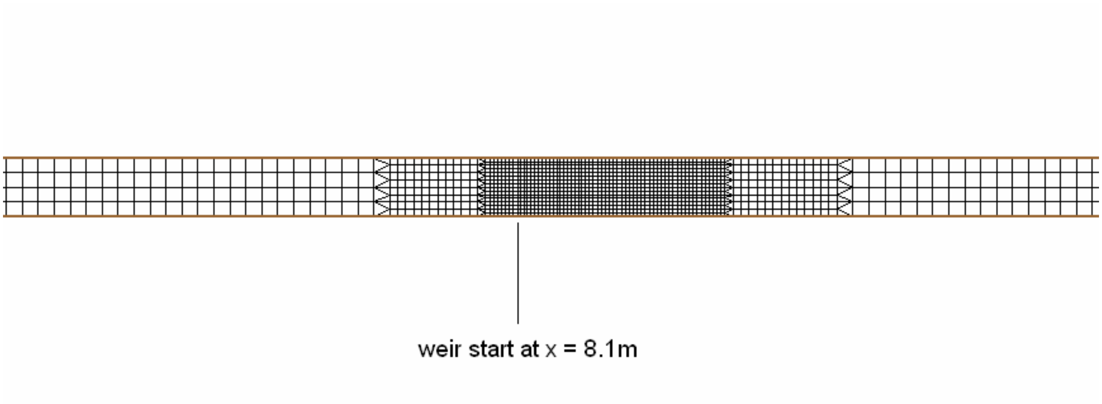

Figure 4.16 Mesh grids (weir experiment)

Results from numerical model are presented in figures 4.17(a) and 4.17(b). The simulated contours were labelled with orange colour. Meanwhile the scatter points, which labelled with various colour represent the measured depths from the experiment. For comparison purpose, the scatter points were labelled with colour level that corresponding to contour legend. Similar “V” shape flow pattern occurred in simulated results. Besides, the second “V’ just immediately after the weir was also captured in numerical model. The oscillations at downstream were observed and the simulated depths were very close to measured results. Again, the model shows its ability to solve the real weir problem.

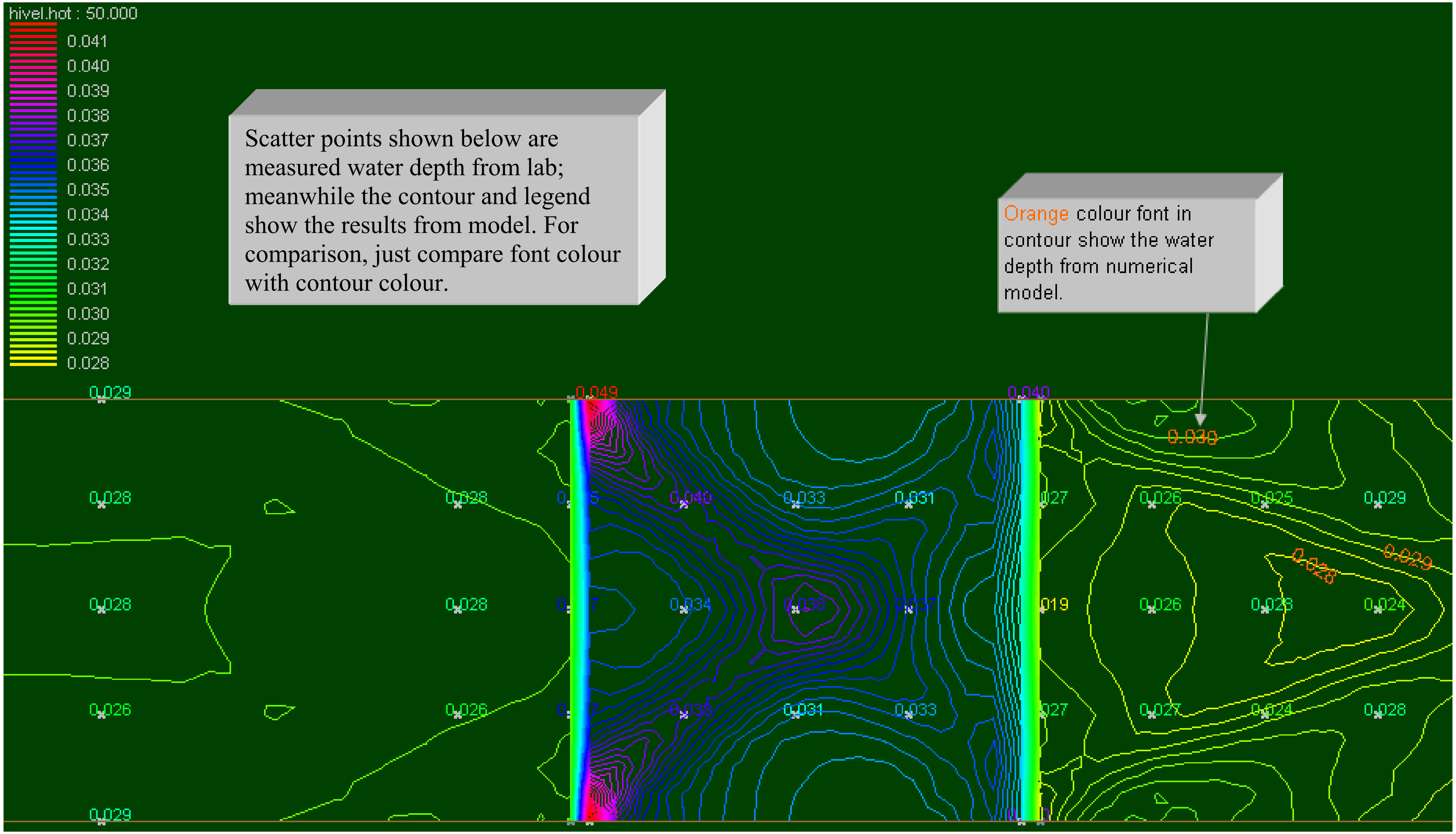

Scatter points shown below are measured water depth from lab; meanwhile the contour and legend show the results from model. For comparison, just compare font colour with contour colour.

Orange colour font in contour show the water depth from numerical model.

Figure 4.17(a) Water depth (weir experiment)

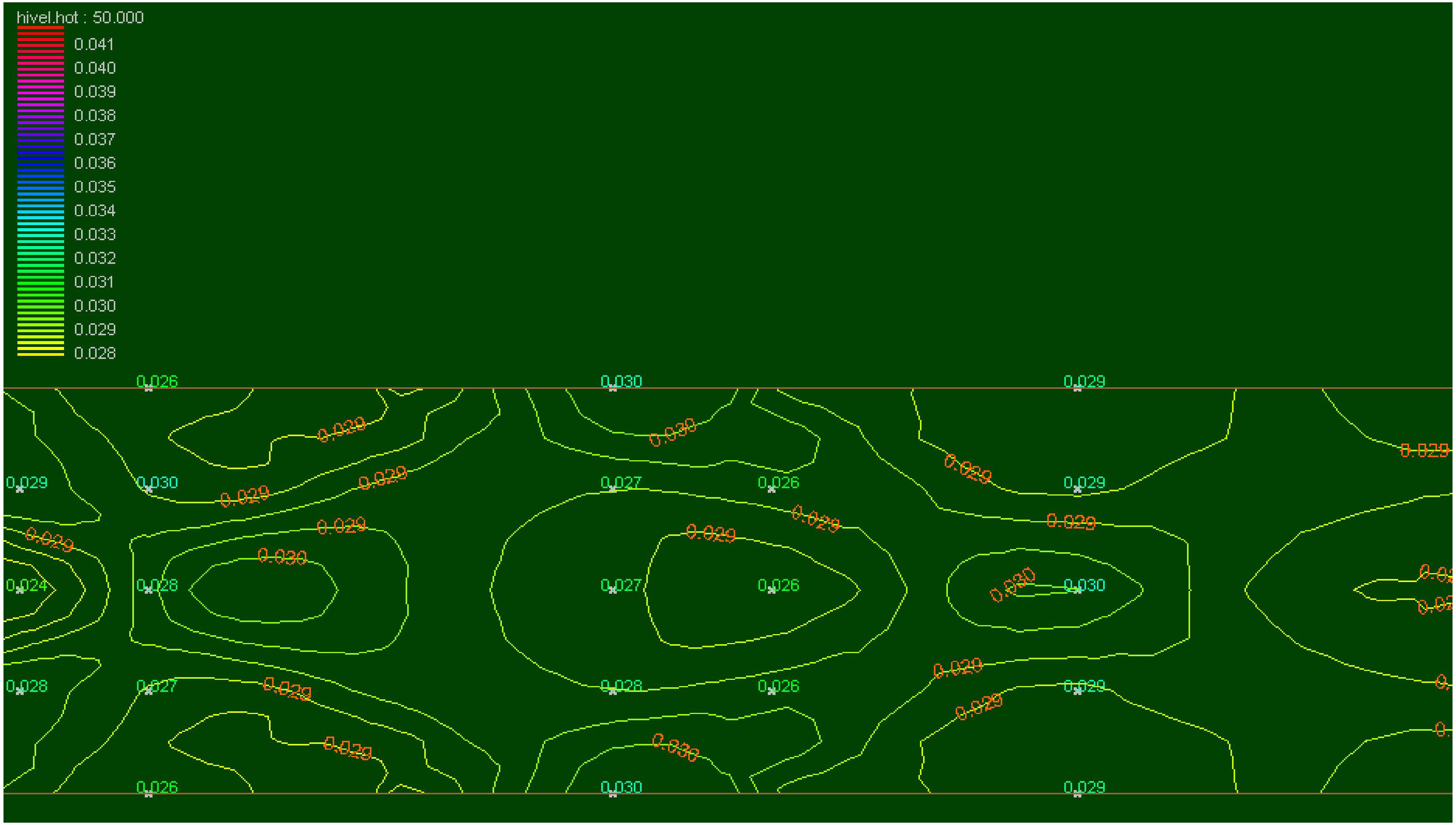

Figure 4.17(b) Water depth (downstream just after weir)

In addition, there is interesting finding in the flume experiment. During the steady state condition, water on the weir was blocked temporarily and back water occurred in front of the weir as displayed in figure 4.18. However, when the obstacle was removed, the back water was still maintained and formed another pattern of steady state condition.

Figure 4.18 Back water in front of weir

It was caused by the change of approach depth. In the other words, the approach depth may influence minimum head energy (H_{min}). For example, if approach depth is 0.030 m, H_{min} should be 0.020 m. Since the weir height is only 0.0135 m, no back water should occur. However, when the approach depth was increased to 0.040 m, the H_{min} becomes 0.0028 m which is less than weir height. This results back water in the flume.

To verify this explanation, the same numerical model was repeated with different initial condition. The initial depth was set to 0.025 m throughout the domain. At starting, the upstream water was pushed forward and raised up the approach depth. The increasing of approach depth will reduce H_{min} till less than weir height.

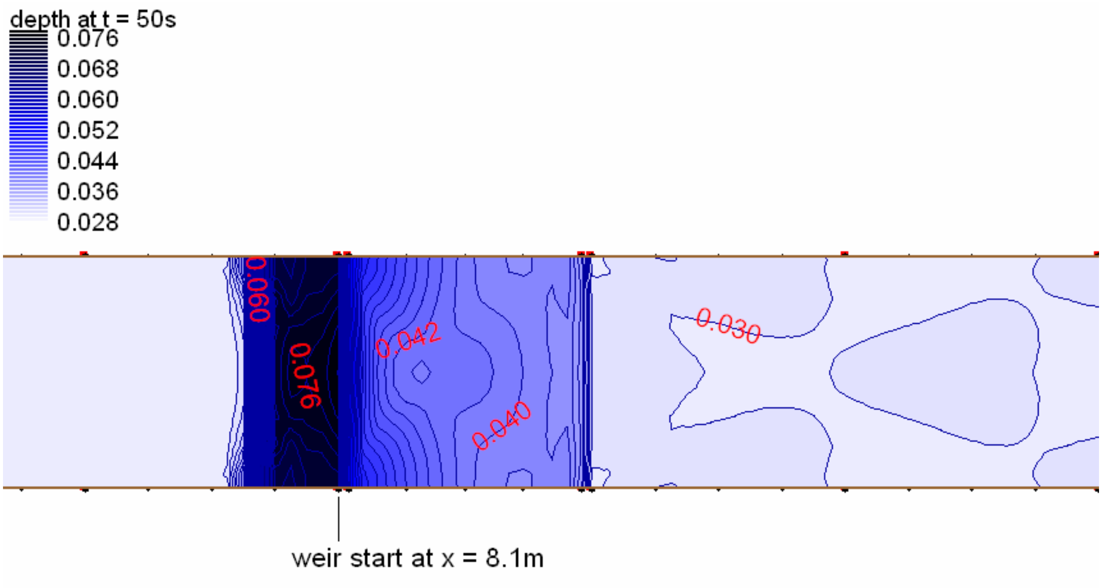

Figure 4.19 Back water in front of weir (numerical model)

Figure 4.19 shows the back water in numerical model when t = 50s. Again, the back water was successfully simulated by the numerical model. It is apparent to note that the solution in this test case was sensitive to approach depth. Through these investigations, numerical model had demonstrated its usage as a tool in checking the flow condition for existing open channel.

4.3.2 Expansion

Expansion problem was conducted in the numerical model by using the flow parameters listed in table 4.10. The total length of channel was 14 m with upstream width of 0.35 m. The channel was expanded to 0.457 m at *x* = 7.0 m. As illustrated in figure 4.20, the mesh was refined at critical region with 0.01 m wide. Detail description about this test was discussed in chapter 3.

Table 4.10 : Input parameters for numerical model (expansion experiment)

Q (m3/s)	B1 (m)	B2 (m)	*n*	S	F1	*θ* (degree)	y1 (m)	Expansion Length (m)	Time step (s)
0.0155	0.35	0.457	0.009	1/75	2.159	-5	0.035	1.223	0.1

Upstream BC	Downstream BC	Initial condition	*β*
Super (h=0.095m)	Super	0.035 m depth	0.25, 0.5

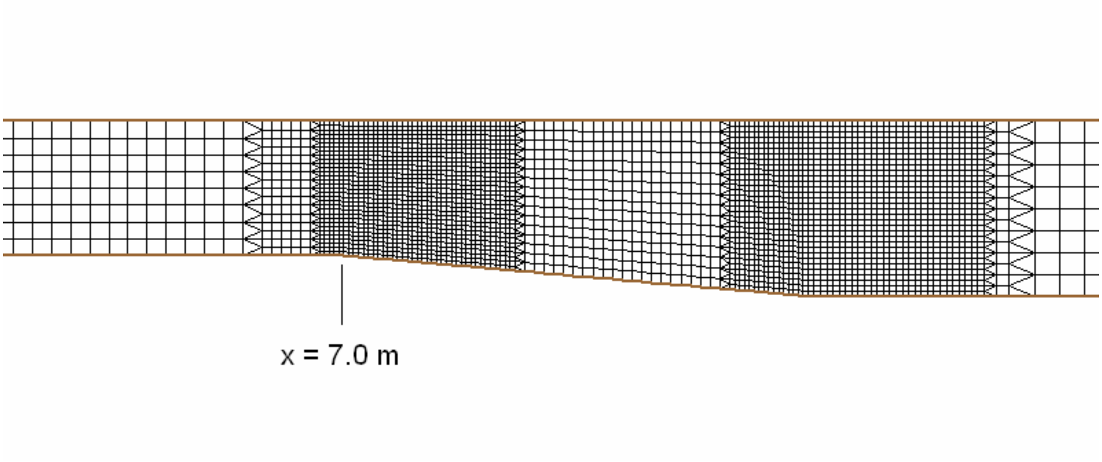

Figure 4.20 Geometry and mesh grid for expansion

The computed results using analytical solution, are listed in table 4.11 (parameters are described in figure 3.26). β1 and β2 are wavefront angles of negative wave; meanwhile F_2, d_2 and v_2 are the Froude number, depth and velocity downstream of the expansion.

Table 4.11 : Analytical solution results (expansion experiment)

β1(degree)	β2(degree)	F2	d_2 (m)	v_2 (m/s)
27.6	23.4	2.52	0.028	1.32

Figure 4.21 and 4.22 present the simulated water depth and velocity distribution. The red lines in figure 4.21 show the theoretical angles of deflection.

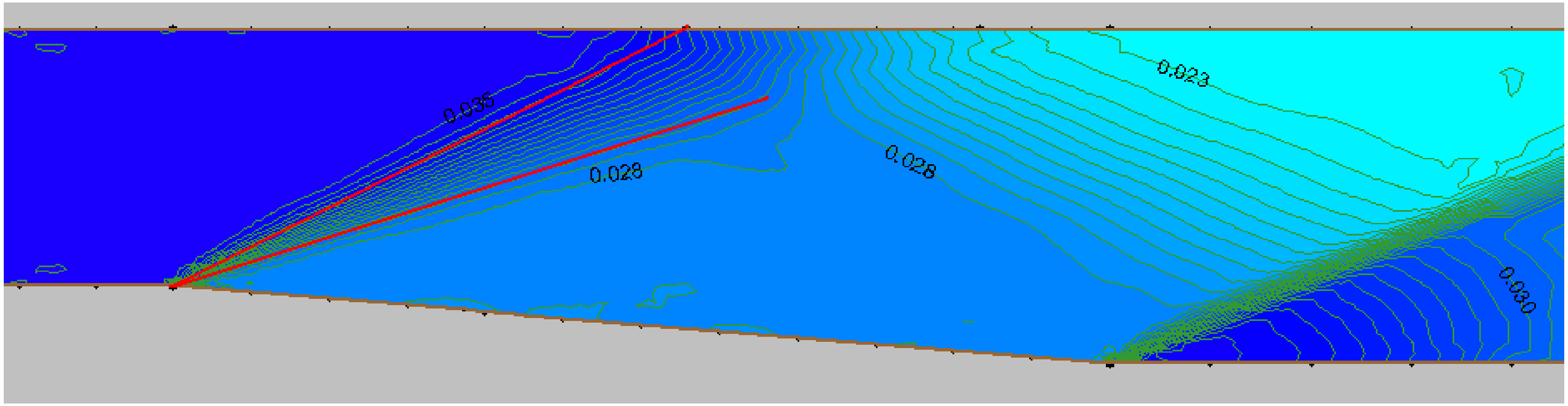

Figure 4.21 Water depth (expansion)

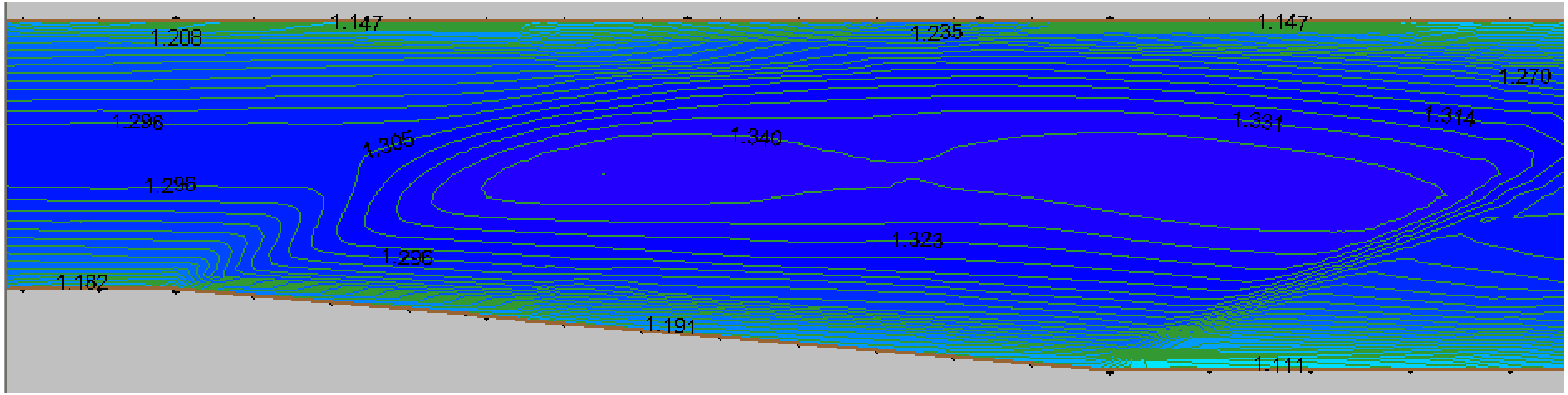

Figure 4.22 Velocity distribution (expansion)

The simulated results reasonably matched the analytical solution with regard to the magnitude of water depths. However, the angles of wavefront were slightly different with analytical solution (red line). This is because the approach velocity is not uniform as what had been assumed in the analytical solution (figure 4.22).

To prevent this non-uniform flow, a frictionless, horizontal channel was applied in numerical model. Other flow parameters were remained including the mesh grid resolution.

Figure 4.23 shows the velocity distribution for frictionless channel. It is clearly shown that the uniform flow is formed before the expansion with 1.26 m/s across the channel. Meanwhile figure 4.24 shows contours of simulated water depth with approach depth equal to 0.035 m. As expected, the water depth was reduced to 0.028 m due to the expansion effect. By using simple calculation, the Froude number after expansion should be equal to 2.50 as demonstrated below.

$$F = \frac{V}{\sqrt{gy}} = \frac{1.311}{\sqrt{9.81 \times 0.028}} = 2.50$$

On the other hand, the angles of wavefront for frictionless model displayed marginally improved phase accuracy in comparison with computed angles (red line). These results verify the error caused by non-uniform flow condition.

In addition, the flow after the expansion was deflected due to the contraction effect. This will be discussed in the next sub-section.

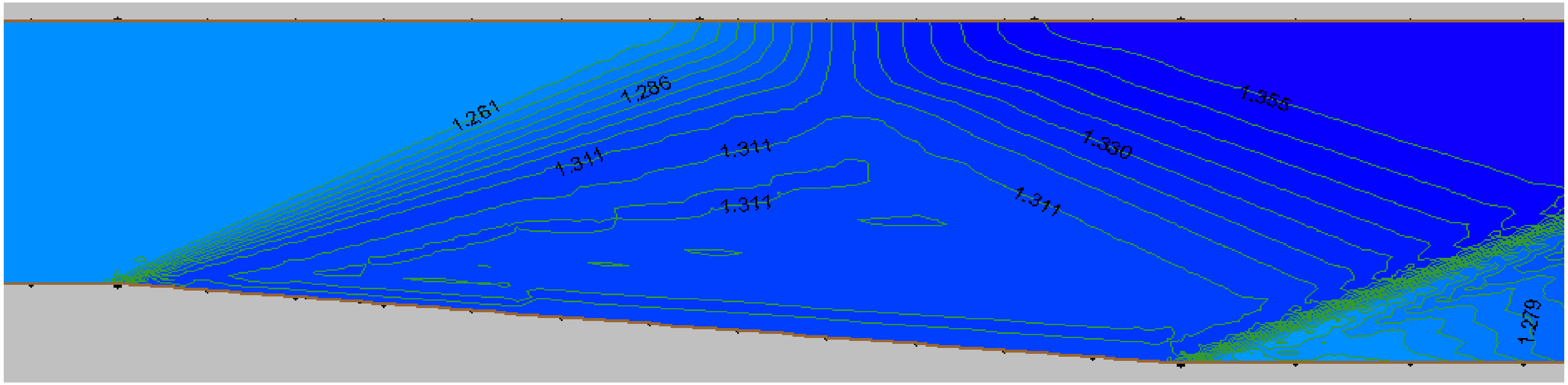

Figure 4.23 Velocity distribution (frictionless expansion)

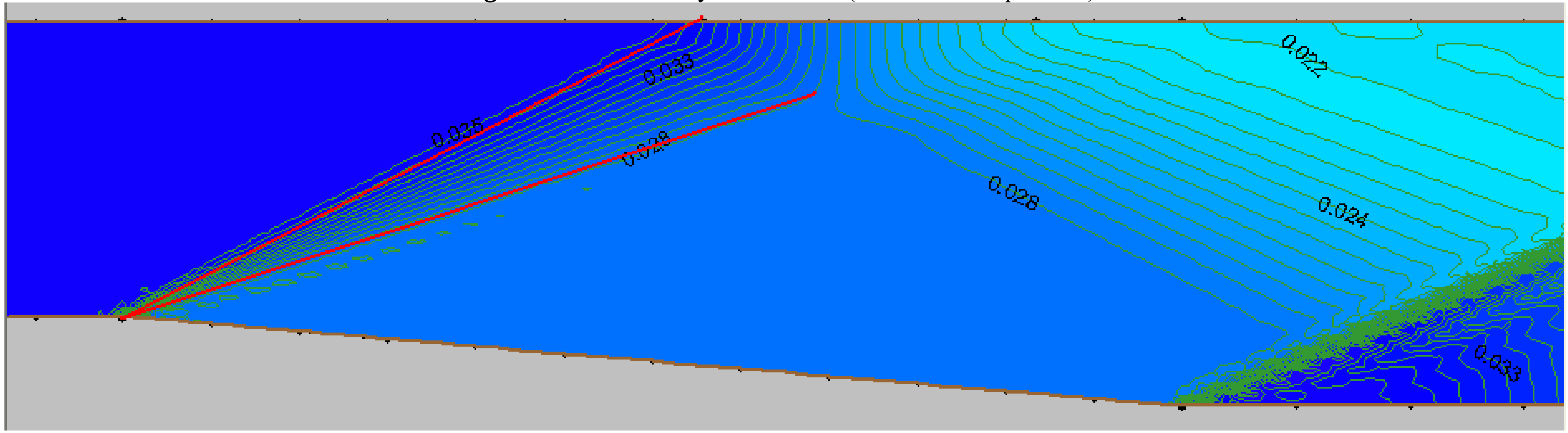

Figure 4.24 Water depth (frictionless expansion)

4.3.3 Contraction

Generally, contraction can be divided into two types, either one side contraction or both sides contraction. Both of them were studied in the following sections.

4.3.3.1 One Side Contraction

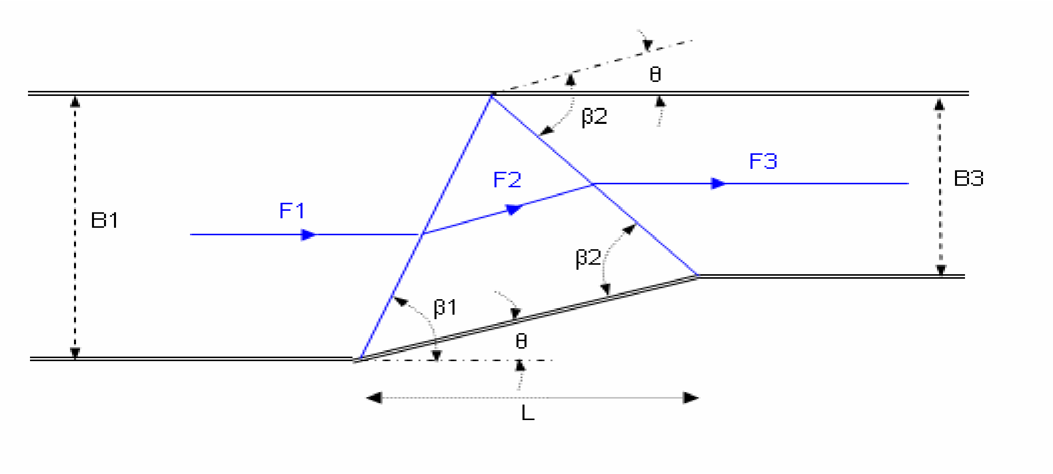

Figure 4.25 Parameters in one side contraction

The primary concerns for this case are the wavefront angle and water depth. One side contraction was modelled by using the flow parameters listed in table 4.12. The contraction started at x = 13 m in a 20 m long channel. The channel extension upstream of the contraction allowed the model to reach normal depth (0.025 m). The initial and boundary conditions are presented in table 4.12.

Table 4.12 : Input parameters and analytical solution results (one side contraction)

Q (m^3/s)	S	n	F1	θ (degree)	B1 (m)	B3 (m)	L (m)	β
0.0155	1/25	0.012	2.740	10	0.457	0.2507	1.17	0.25

Upstream B.C.	Downstream B.C.	Initial depth
Super (h=0.025m)	Super	0.020 m

Figure 4.26 shows the mesh grid in the model. Laterally the channel was divided into 32 elements in the area of interest. Since the expansion near the end of the side wall, the grids were further refined. To maintain the model stability, the small time step equal to 0.001s was used. The result after 45000 time steps (t = 45s) can be seen in figure 4.27, shows steady state flow contour. Based on analytical solution, the computed results such as β1, β2, d_1, d_2 and d_3 were listed in table 4.13.

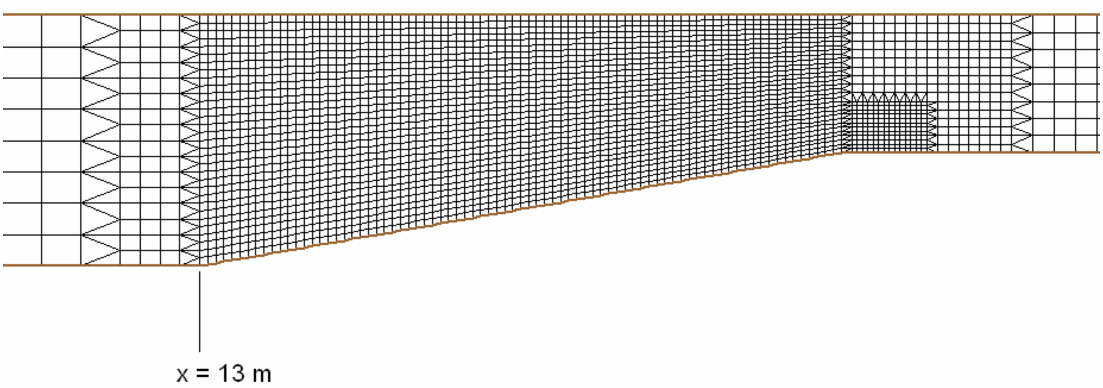

Figure 4.26 Mesh grid in one side contraction

Table 4.13 : Analytical solution results (one side contraction)

β1(degree)	β2(degree)	d_1 (m)	d_2 (m)	d_3 (m)
31.1	41.3	0.025	0.039	0.056

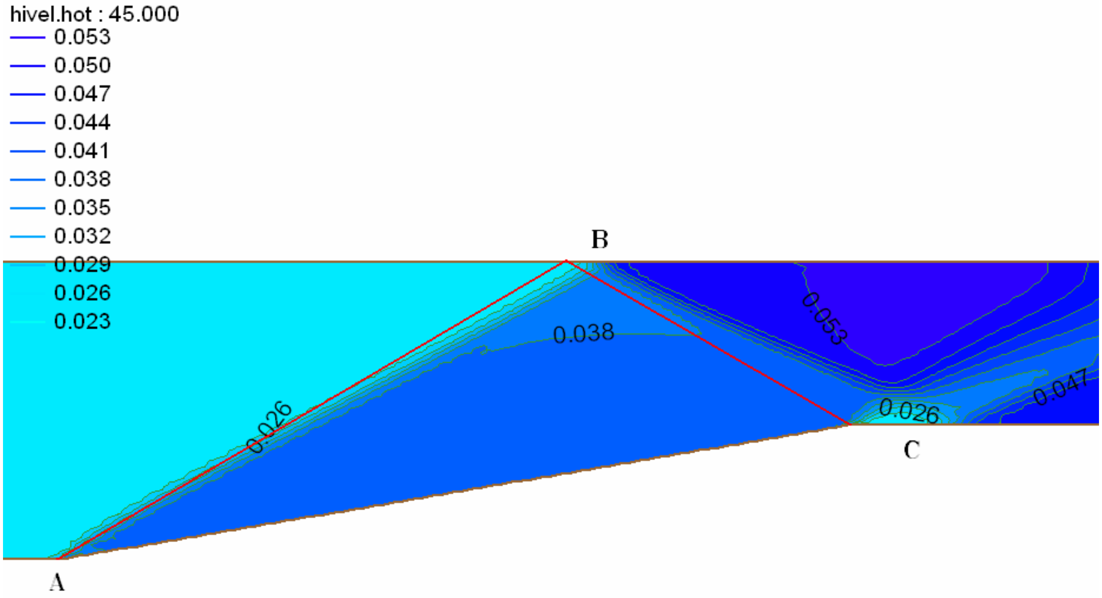

Figure 4.27 Water depth (one side contraction)

Referring to figure 4.27, at contraction point A, an angle β1 was generated due to sudden inward of side wall. The shock was propagated to point B in the channel axis and reflected to the wall again at point C. Negative wave was formed, followed by a complicated wave pattern in the downstream region. The water depths were found very close to computed results. However, the angle of shocks was over predicted compare to computed angles β1 and β2 (red lines). This is indeed a result of the uniform flow and infinite wavelength assumption.

To support the statement above, another model was conducted with frictionless horizontal channel (test1). Other flow parameters were maintained. As illustrated in figure 4.28, the flow becomes smooth again after passing through the contraction. By eliminating the friction, uniform approach flow was obtained. It is clearly shown that the angles of wavefront were predicted accurately.

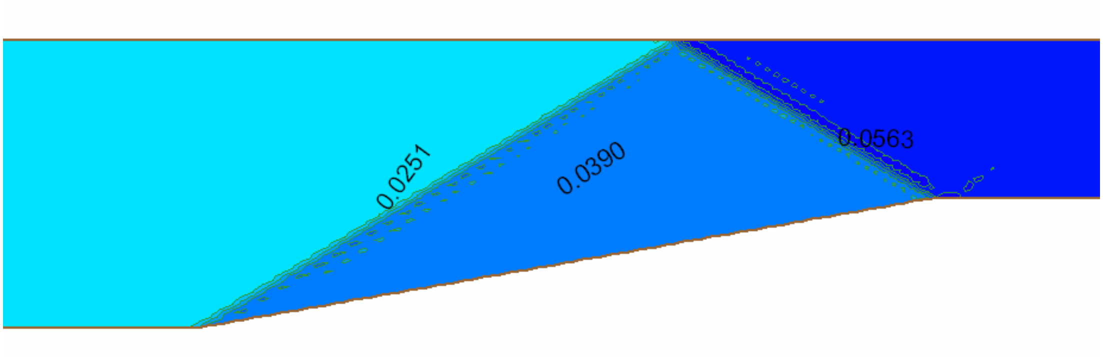

Figure 4.28 Water depth (frictionless one side contraction)

The product of F_1 and θ is called shock number. The shock number for the test above was 27.4. The ratio $d_2/d_1 = 0.0390/0.0251 = 1.55$; and the ratio $d_3/d_2 = 0.0563/0.0390 = 1.44$.

During design stage (equation 3.4 and 3.5), it is interesting to note that the ratio d_2/d_1 and d_3/d_2 are constant if the shock number remains constant, as reported by Reinauer et al (1998). To verify this, two numerical models (test2 and test3) were conducted by using the same shock number, which was equal to 27.4. Table 4.14 concludes all parameters used in the test2 and test3 together with the computed water depths. For comparison purpose, frictionless horizontal model was selected again.

Table 4.14 : Input parameters and analytical solution results (test2 and test3)

test no.	Q (m^3/s)	S	n	F_1	θ (degree)	$F_1\theta$	B1 (m)	B3 (m)	L (m)
Test2	0.0155	0	0	5.479	5	27.4	0.457	0.219	2.721
Test3	0.0155	0	0	3.653	7.5	27.4	0.457	0.23	1.722

Test no.	Computed d_1 (m)	Computed d_2 (m)	Computed d_3 (m)
Test2	0.016	0.024	0.034
Test3	0.021	0.032	0.045

Figures 4.29 and 4.30 show the simulated water depths for test2 and test3 respectively. The results, d_1, d_2 and d_3 matched the computed water depths as well. Besides, the ratio d_2/d_1 and d_3/d_2 for both tests were found very close to test1, as concluded in table 4.15. These observations agree with those of Roger et al (1998).

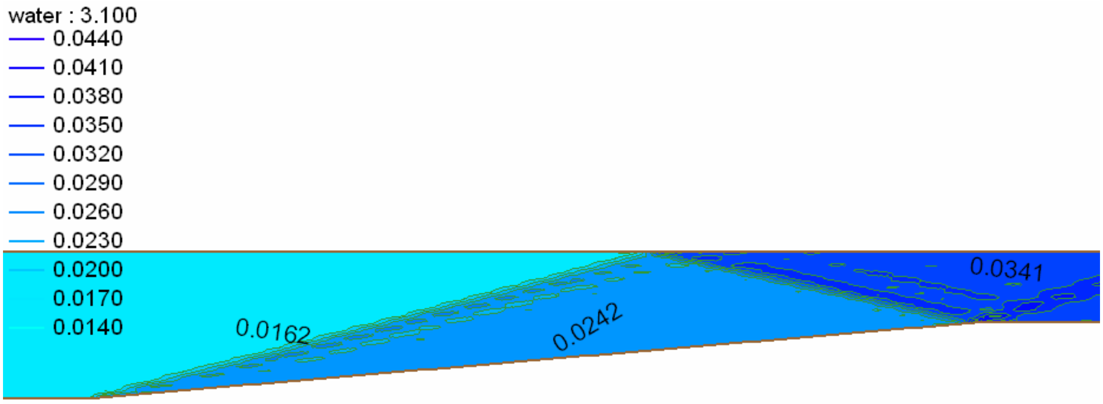

Figure 4.29 Water depths (test2 one side contraction)

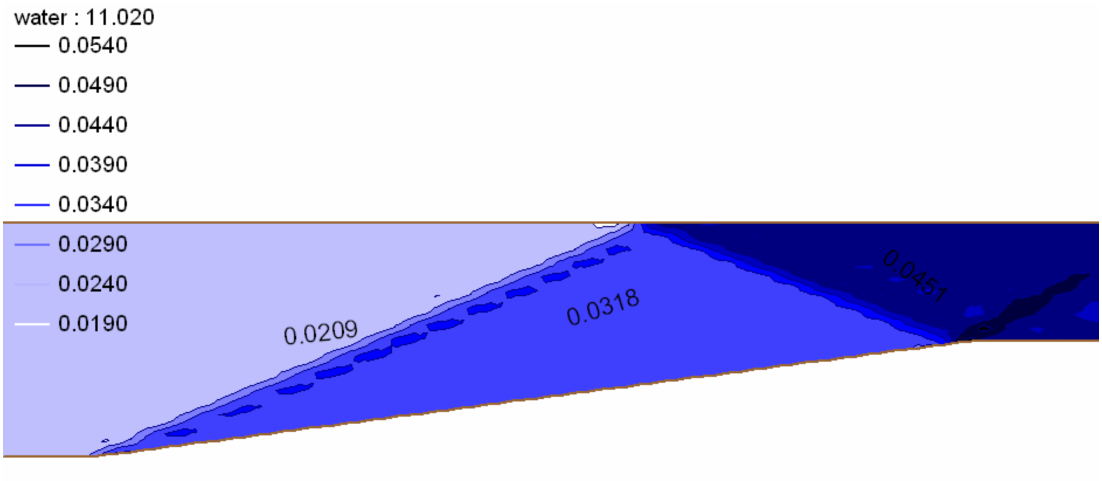

Figure 4.30 Water depths (test3 one side contraction)

Table 4.15 : Constant ratio of water depth

test no.	F_1	θ (degree)	$F_1\theta$	d_1 (m)	d_2 (m)	d_3 (m)	**d_2/d_1**	**d_3/d_2**
test1	2.740	10	27.4	0.0251	0.0390	0.0563	**1.55**	**1.44**
test2	5.479	5	27.4	0.0162	0.0242	0.0341	**1.49**	**1.41**
test3	3.653	7.5	27.4	0.0209	0.0318	0.0451	**1.52**	**1.42**

It should be realized that without numerical model, a series of complicated lab tests would be required for verification. This section was included as an example of how this numerical model can be utilized to verify theoretical finding.

4.3.3.2 Both Sides Contraction

Besides analytical solution, qualitative comparisons between simulated results and published model and flume experimental results were made as described below.

1. Laboratory Test: by Ippen and Dawson

A flume test results which reported by Ippen and Dawson (1951) was selected. This case was chosen as a benchmark because it has been computed by many other researchers and comparison can be made with the experimental data.

The design procedure of Ippen et. al. (1951) was based on wave interference. For the design approach flow and a contraction ratio, the contraction angle was chosen such that the positive shock wave generated at the contraction point was directed to the contraction endpoint, where the reflection of the positive wave interfered with the negative wave. Shock waves were narrow and locally extreme surface waves.

The tests were conducted for an approach Froude number of 4.0, upstream depth of 0.1ft, and a total discharge of 1.44ft^3/s. The channel contracts from 2ft to 1 ft wide in a length of 4.78ft, i.e., an angle of 6 degree on each side. Figure 4.31 shows contours of water depth in plan view which reported by Ippen et. al. (1951).

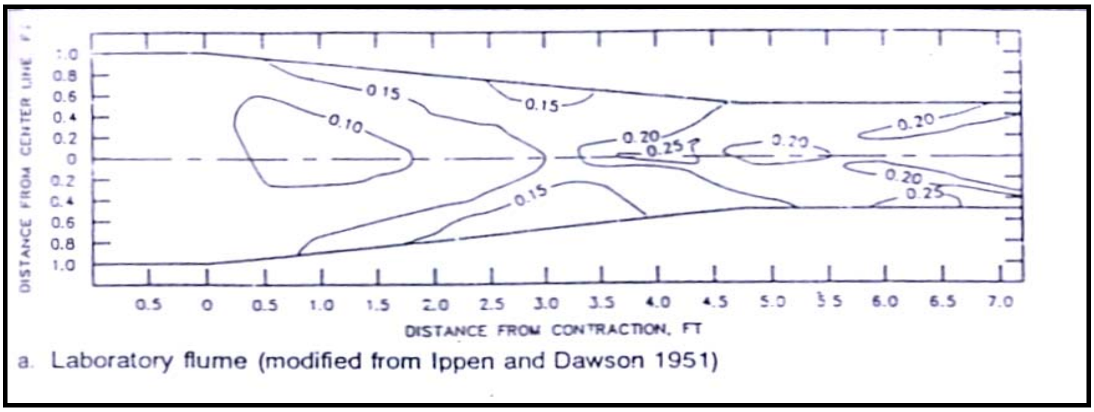

a. Laboratory flume (modified from Ippen and Dawson 1951)

Figure 4.31 Water depth (both side contraction from Ippen et. al.)

2. Model Simulation: by R.C. Berger and R. L. Stockstill

The numerical model was set up with 10 evenly spaced elements laterally across the channel and 24 elements over the length of the transition. The model limits were extended to 40ft with 1661 nodes and 1500 elements. In this simulation, Berger assumed a Manning's *n* of 0.0107 for the flume (Ippen), and he recalculated the slope, which was 0.05664. The result from this simulation is presented in figure 4.32.

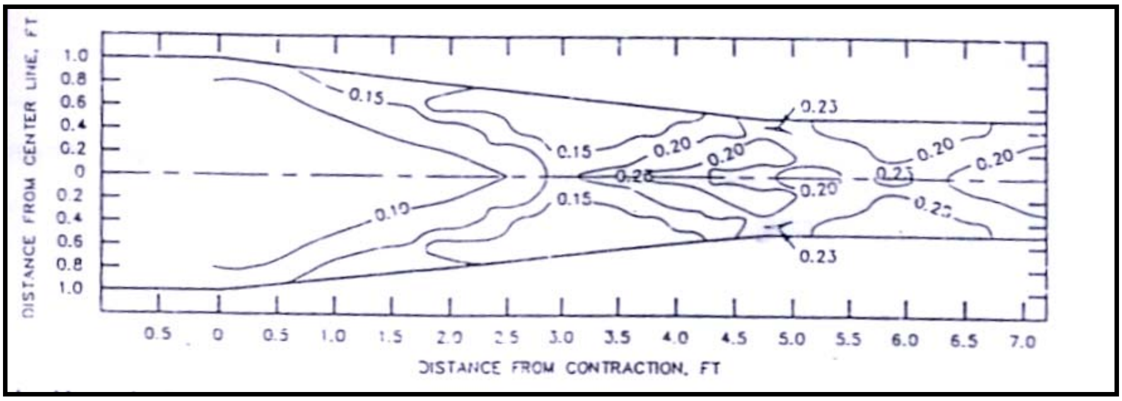

Figure 4.32 Water depth (both side contraction from Berger et. al.)

3. Model Simulation: by M. Hanif Chaudhry

The MacCormack scheme was used to simulate the laboratory tests reported by Ippen et. al. (1951). The finite-different scheme was computed by assuming zero friction with horizontal slope. It shows some different if compared to Berger assumption.

In this section, two model simulations, using the assumptions made by Berger and Chaudhry, are presented. For the first simulation, the slope was set to 0.05664 with Manning's *n* of 0.0107; meanwhile the second simulation was run on a frictionless horizontal model. Other geometry parameters will be exactly same as those reported by Ippen et. al.

Table 4.16 : Flow parameters used by Berger et. al.

Flow rate, Q	1.44 ft^3/s
Slope, S	**0.05664**
Manning *n*	**0.0107**
Total length of model	40ft
Upstream width, B1	2ft
Downstream width, B3	1ft
Angle θ	6 degree (at x =20ft)
Contraction length, L	4.78ft
Froude number , F_1	4.0
Upstream boundary condition	Supercritical, h = 0.1ft
Downstream boundary condition	Supercritical
Initial condition	Bed + 0.075ft
Time step	0.005s

Flow parameters used in first model simulation are outlined in table 4.16. The model consisted of 1661 nodes for a total of 1500 elements throughout the domain (figure 4.33). Maximum aspect ratio was 2.0.

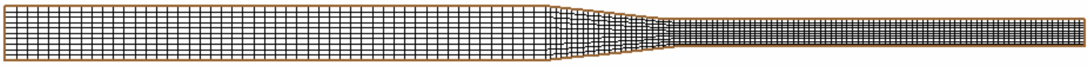

Figure 4.33 Mesh grid (both side contraction)

Simulated results are presented in figure 4.34. The transition caused a disturbance that reflected down the channel forming a diamond-shaped wave pattern. By carefully set the display contours option, results similar to Ippen and Berger was obtained. The contours shape is good as well and the simulated maximum height of water depth is also similar to the corresponding results from Ippen et al (1951). The numerical model certainly captured the overall features of the flume.

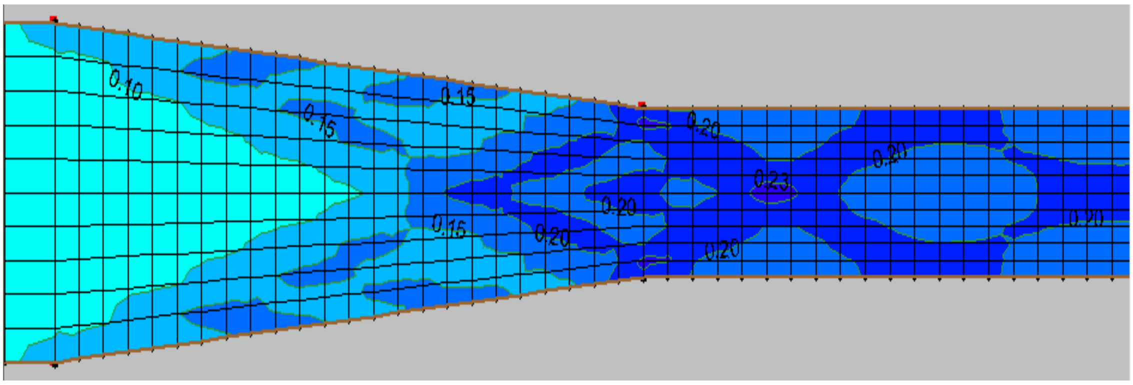

Figure 4.34 Simulated Water depth (Berger assumption)

Meanwhile, table 4.17 lists the flow parameters that used in second model simulation. With zero friction and horizontal slope, uniform flow velocity was obtained. This frictionless horizontal model was very useful for model simulation because it can avoid non-uniform flow across the channel and make the test cases exactly the same as the design condition. Figure 4.35 shows the simulated water depth, which matched with the results from Ippen and Berger.

Table 4.17 : Flow parameters used by Chaudhry et. al.

Flow rate, Q	1.44 ft^3/s
Slope, S	**0.0**
Manning *n*	**0.0**
Total length of model	40ft
Upstream width, B1	2ft
Downstream width, B3	1ft
Angle θ	6 degree (at x =20ft)
Contraction length, L	4.78ft
Froude number , F_1	4.0
Time step	0.005s

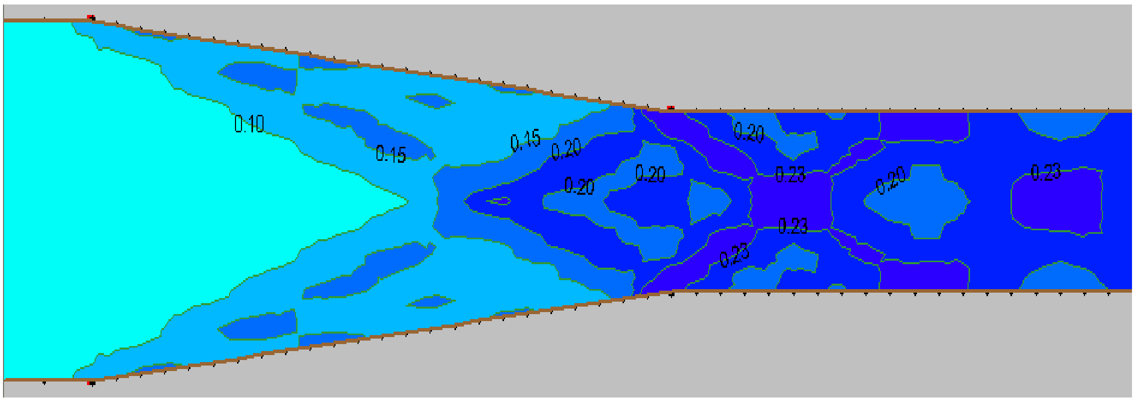

Figure 4.35 Simulated Water depth (Chaudhry assumption)

One interesting finding was observed from both model simulations. The slope, roughness and initial depth were chosen by Berger and Chaudhry to provide a depth of 0.1ft approaching the transition. To examine the effect of approach depth, another assumption was made as a trial run. All parameters were maintained as the previous except the slope and Manning's *n*. With Q = 1.44cfs, B = 2ft, Slope = 1/100 and *n* = 0.0041, a 0.1ft normal depth should be obtained according to Manning formula. After 50 seconds, it shows excellent contours of water depth, which matched with Ippen and Berger results (figure 4.36).

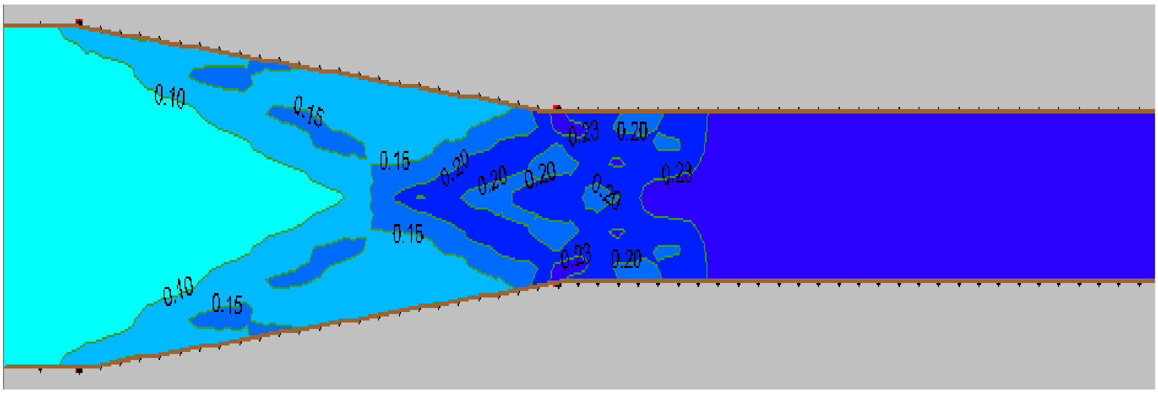

Figure 4.36 Simulated Water depth (new assumption)

Results show that the approach water depth is very important. As long as it was maintained at 0.1ft, same simulation results can be obtained with maximum height 0.23ft at downstream. The contour patterns are just slightly different among those simulation results. Overall though, the comparison between simulated results and published results is reasonable and the shape of oblique standing waves demonstrated.

4.3.3.3 One Side Contraction and 90 Degree Expansion

In this section, the numerical model was further examined with the combination case of contraction and expansion. An experiment was carried out to facilitate data for evaluation and comparison. In this experiment, the slope was set to approximately 1/78 to obtain a supercritical flow with normal depth (approach depth) equal to 0.030 m. The test was started in dry bed condition. Detail explanation about the experiment can be reviewed in chapter 3. During the test, shock wave was formed when the flow passed through the contraction as shown in figure 4.37. Figure 4.38 clearly displays the wavefront angle due to sudden inward boundary condition.

Figure 4.37 Shock wave in experiment

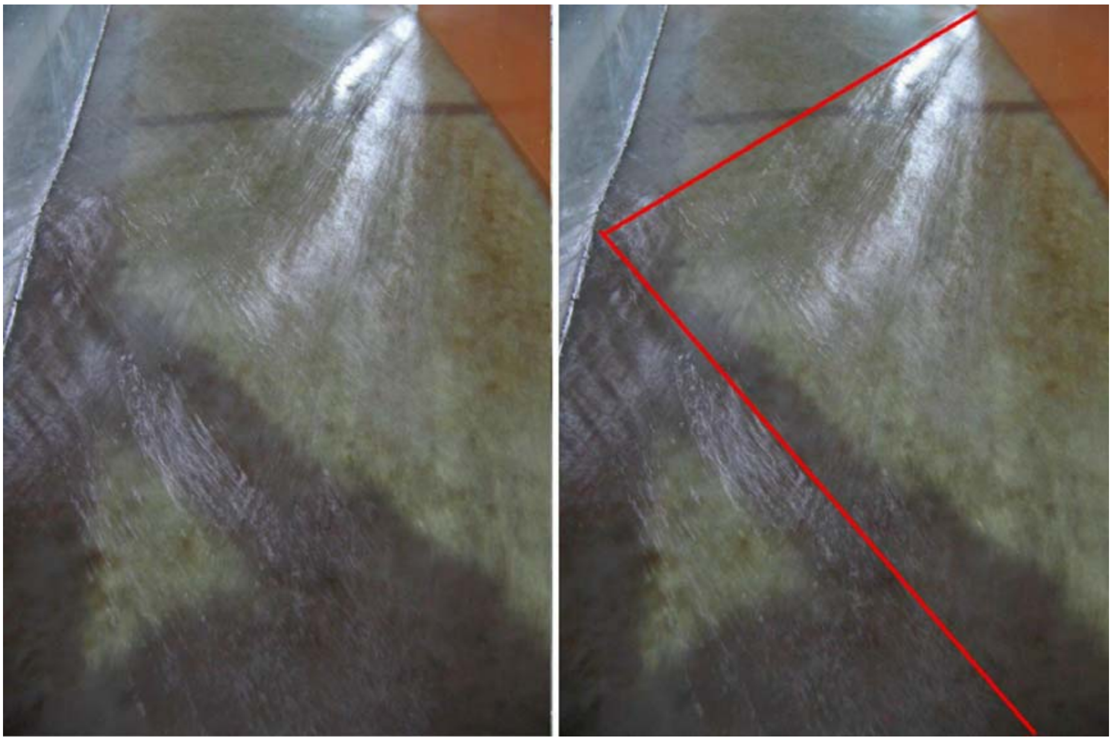

Figure 4.38 Wavefront angles in experiment

Basically, the first shock wave was formed when the channel contracted from B1 (0.457 m) to B2 (0.337 m). The flow pattern was travelling in “Z” shape along the narrow region. When the flow reached the end of plywood wall (figure 4.39 and 4.40), the water depth was rapidly reduced due to 90 degree expansion, and increased again after hitting the glass side wall and forming another shock wave.

Figure 4.39 90 degree expansion

Figure 4.40 Flow pattern after 90 degree expansion

Through the glass wall, the increase of water depth can be seen easily and the location was recorded (figure 4.41). By this way, the coordinates for point A, C, D and E were marked for result comparison (refer figure 4.43). Measured water depths are presented together with model results in the following pages. Note that it is difficult to precisely measure the water depths for a shock wave by using gauge point.

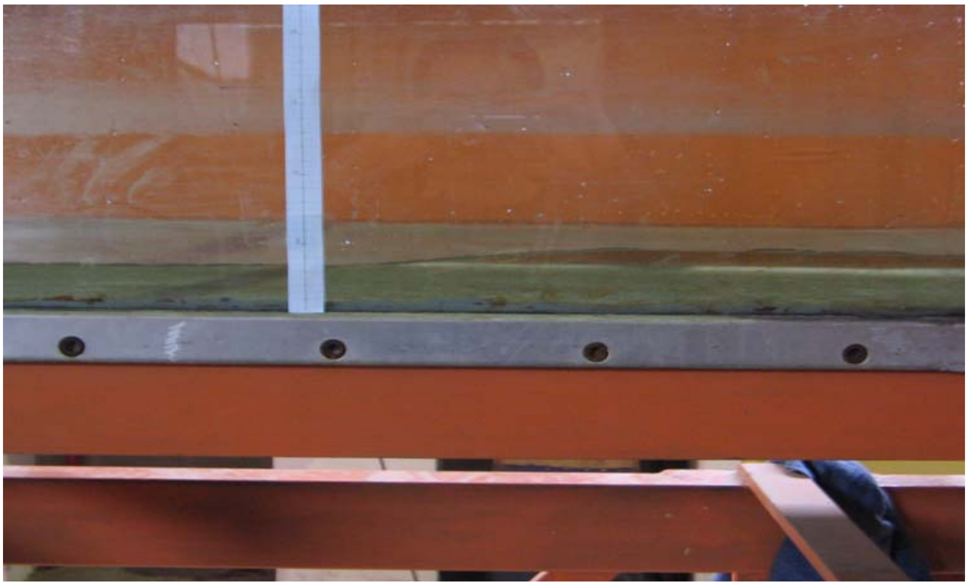

Figure 4.41 Increasing water depth (point A)

A numerical model simulation was conducted using the same flow conditions, as listed in table 4.18. With 0.01s interval, the model was run till t = 50s when the result no longer changed with time. The mesh grid of model was increased gradually in critical part as illustrated in figure 4.42. There were more than 15 elements across the flume. The roughness was determined by trial and error and Manning's *n* of 0.0085 was finally selected because it gave the best result especially at the shock location, as shown in table 4.19. For comparison purpose, simulated flow patterns are presented in plan view together with the measured water depths in the sequence of figures 4.44(a)-4.44(c).

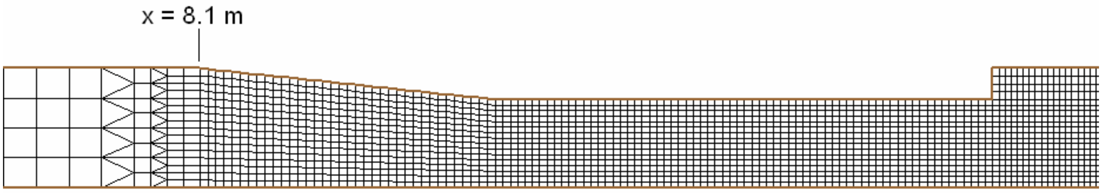

Figure 4.42 Mesh grid (contraction and 90 degree expansion)

Table 4.18 : Input flow parameters for numerical model (contraction & 90 degree expansion)

Parameters	Q (m^3/s)	B1 (m)	B2 (m)	B3 (m)	L1 (m)	L2 (m)	*θ* (contraction)	*θ* (expansion)	S	*n*	Upstream B.C.	Downstream B.C.	Initial Condition
model	0.0153	0.457	0.337	0.457	1.134	1.9	6.042 degree	90 degree	measured	0.0085	super (h=0.035m)	super	d = 0.008 m

Table 4.19 : Results comparison for contraction & 90 degree expansion

						coordinate point A		coordinate point C		coordinate point D		coordinate point E	
	β1(degree)	β2(degree)	d1(m)	d2 (m)	d3 (m)	x	y	x	y	x	y	x	y
Lab	-37.3	40.02	0.031	0.038	0.049	8.70	0	11.30	0.457	12.69	0	13.72	0
model	**-35.5**	**40.02**	**0.030**	**0.039**	**0.049**	**8.74**	**0**	**11.34**	**0.457**	**12.68**	**0**	**13.68**	**0**

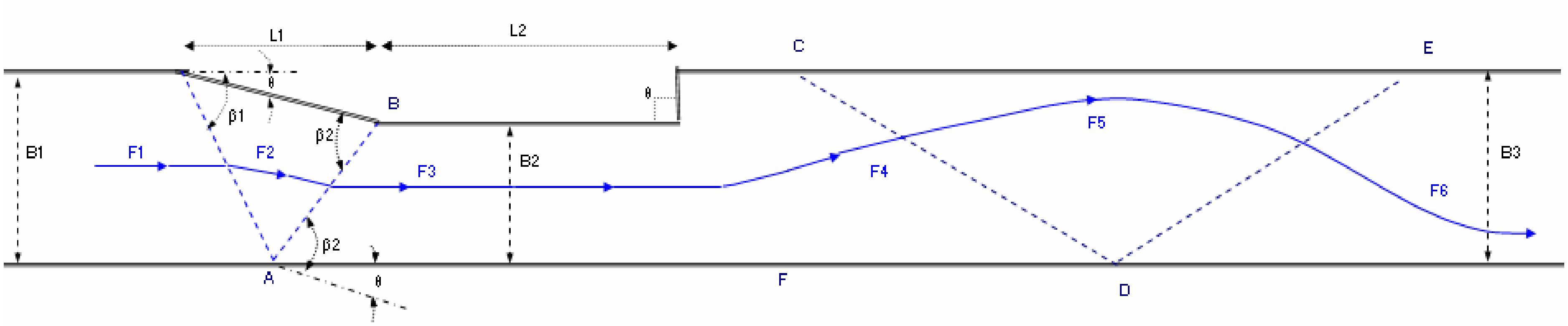

Figure 4.43 Plan view for contraction & 90 degree expansion test case

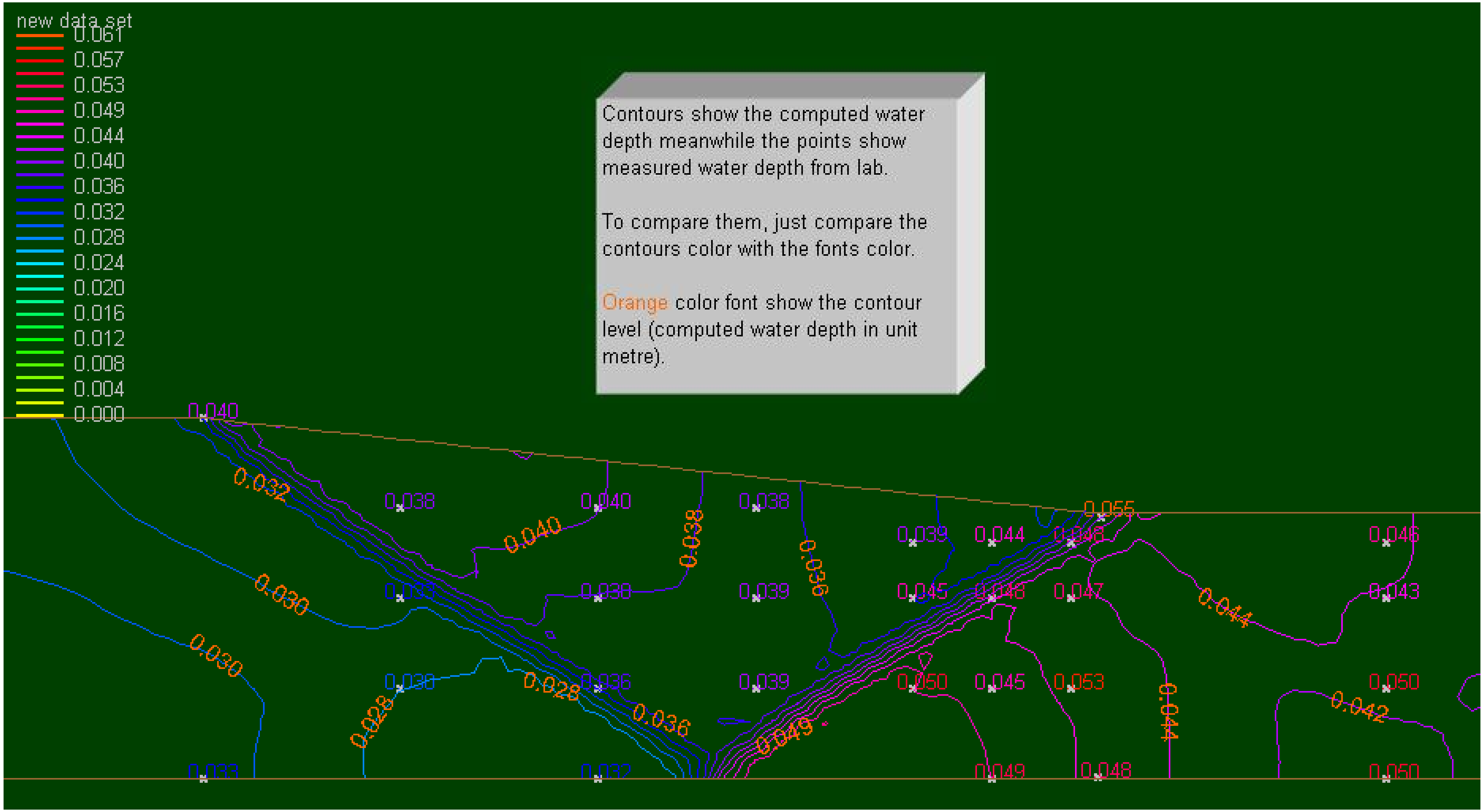

Contours show the computed water depth meanwhile the points show measured water depth from lab.

To compare them, just compare the contours color with the fonts color.

Orange color font show the contour level (computed water depth in unit metre).

Figure 4.44(a) Water depth (contraction & 90 degree expansion)

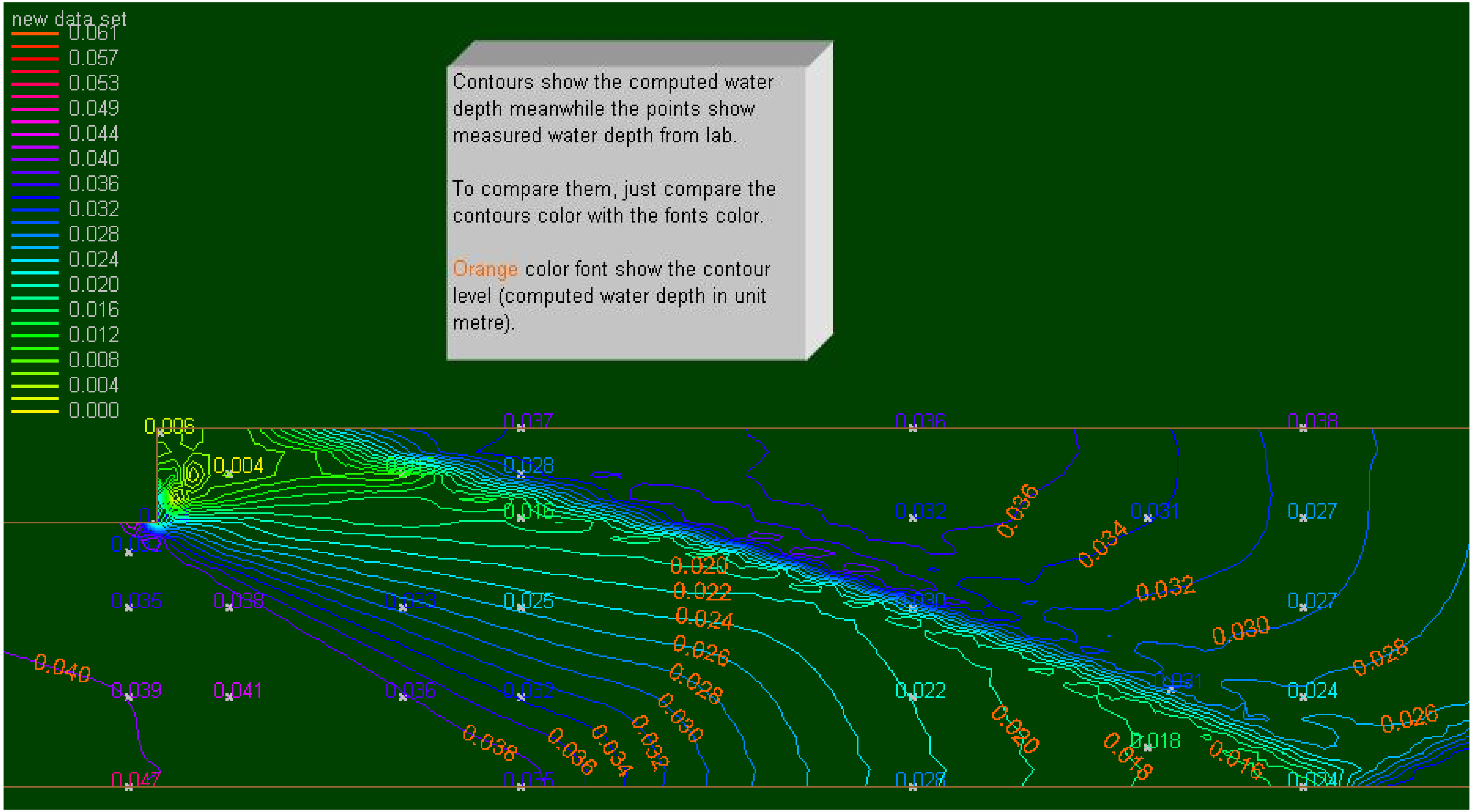

Contours show the computed water depth meanwhile the points show measured water depth from lab.

To compare them, just compare the contours color with the fonts color.

Orange color font show the contour level (computed water depth in unit metre).

Figure 4.44(b) Water depth (contraction & 90 degree expansion)

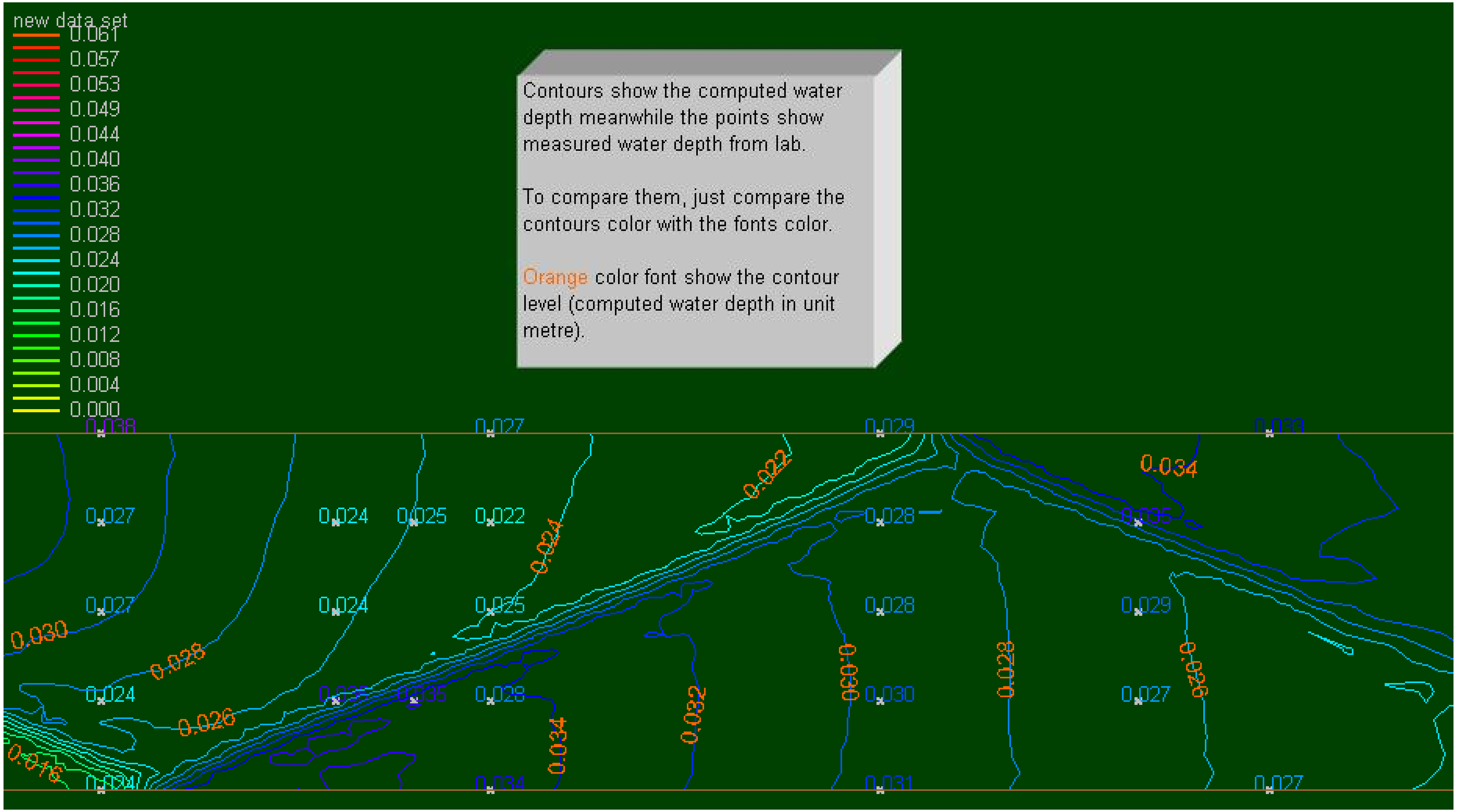

Contours show the computed water depth meanwhile the points show measured water depth from lab.

To compare them, just compare the contours color with the fonts color.

Orange color font show the contour level (computed water depth in unit metre).

Figure 4.44(c) Water depths (contraction & 90 degree expansion)

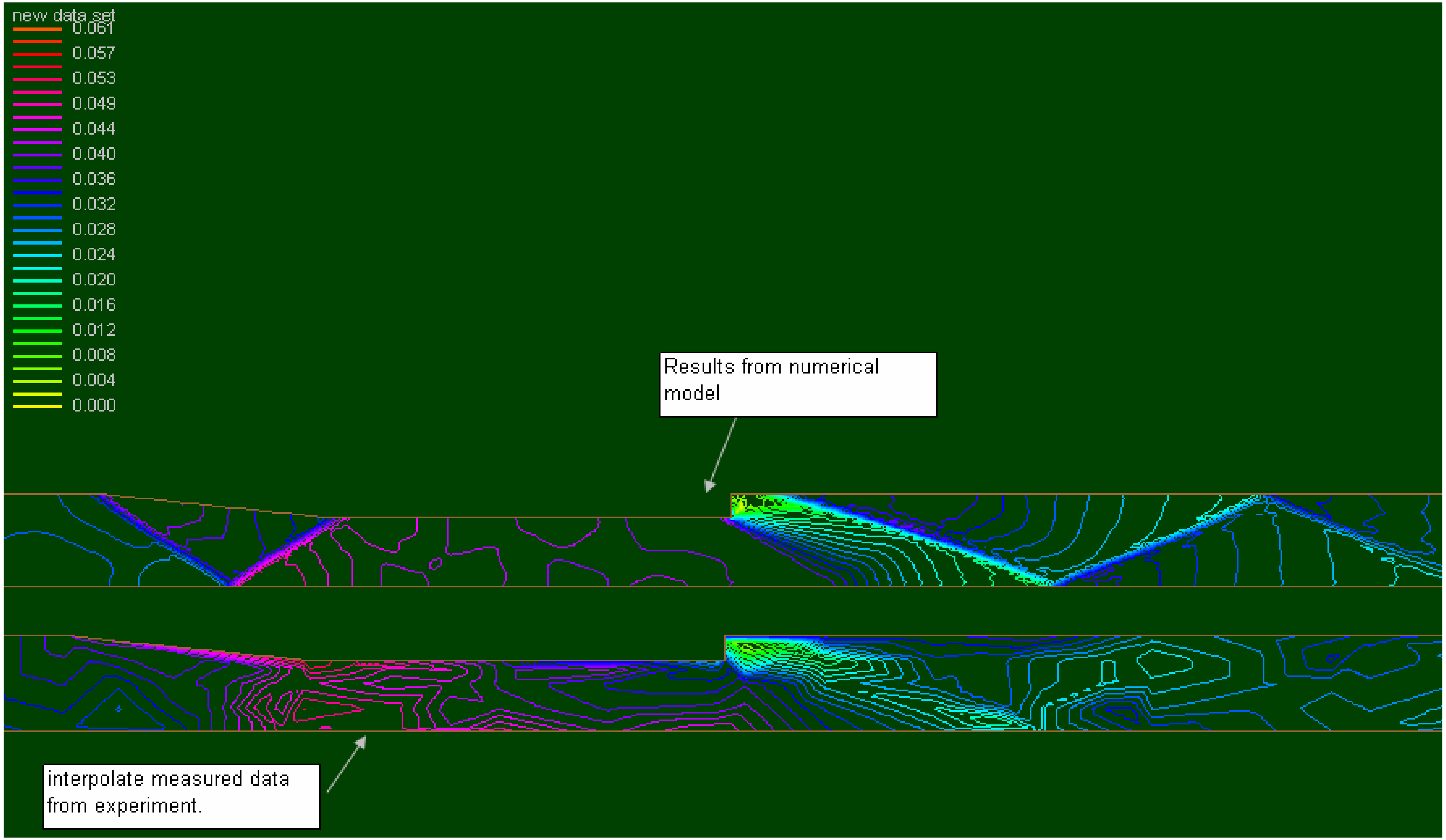

Figure 4.45 Comparison between simulated water depths and measured water depths (contraction & 90 degree expansion)

Locations of shock waves are unable to be determined accurately because not enough data was recorded during the experiment. However, the comparison of contours colour shows that numerical model is able to simulate the water depth in the experiment (figure 4.45). Referring to the coordinates of point A, C, D and E in table 4.19, the shock locations were compared as well. The maximum simulated water depth is 0.049 m, which is less than measured depth (0.055 m). This underestimation result is similar to those result obtained in normal depth simulation (see discussion in section 4.2.1). Meanwhile the minimum water depth from both model and experiment are almost the same.

Because of the disagreement of maximum water depth, a trial run was carried out by raising the Manning's *n* from 0.0085 to 0.0093. In the trial run, the simulated maximum depth was successfully increased to 0.052 m. However, the shock locations (point A, C, D and E) seem moved further upstream due to the increasing friction. The friction always a problem in model simulation. Perhaps, the roughness coefficient in this test case can vary within a range due to its non-uniform water depths and composite material. For this reason, the Manning's *n* of 0.0093 was applied in sub-region start from x = 8.1 m till 9.5 m; and Manning's *n* of 0.0085 was applied from x = 9.5 m till the end of flume. Unfortunately, the result was found almost similar to the case with n = 0.0093. It is noticeable to note that the shock locations are controlled by the roughness coefficient in the upstream for supercritical flow.

In addition, great care must be taken when applying initial condition for contraction case. If the initial depth is too high, back water may occur, and lead to error. In the other hand, if the initial depth is too shallow, the model will halt due to instability of model.

Next, the investigation was extended to examine the performance of numerical model in the confluence test case.

4.3.4 Junction

These experiments were performed in a sharp-edged, 90° combining flow flume with horizontal slope (Weber et al, 2001). The flow travelled from right to the left. Details about the experiment were discussed in chapter 2. In the published paper, the results were presented by using normalized distance. All distances were normalized by the channel width, B = 0.914 m. The non-dimensionalized coordinates are called x*, y*, and z* for *x*/B, *y*/B, and *z*/B, respectively. The water depths, h was normalized by the channel width also, where h* = h/B.

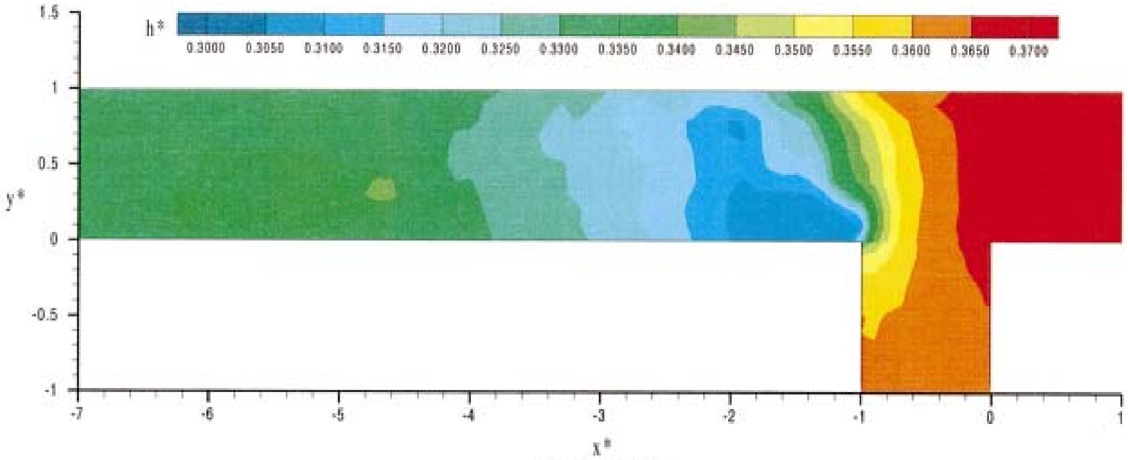

(a) $q^* = 0.250$

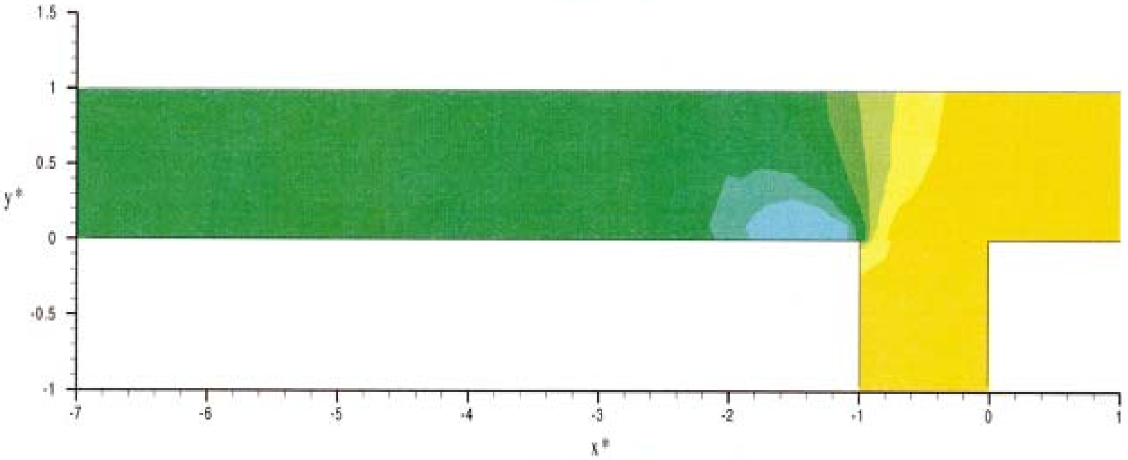

(b) $q^* = 0.750$

Figure 4.46 h* contours for q* = 0.250 and 0.750 (experiment 90 degree junction)

Figure 4.46 presents the contours of normalized water depths for q* = 0.250 and 0.750. Note that the ratio q* was defined as the upstream main channel flow (Qm) to the constant total flow (Qt) which equal to 0.170 m^3/s. According to weber (2001), for all flow conditions the water surface generally displays a drawdown longitudinal profile as the branch flow enters the contracted region and then exhibits a depth increase as the flow expands to the entire channel width downstream of the separation zone. This pattern is more distinctive for lower q* flow conditions.

The velocity measurements had been non-dimensionalized by the downstream average velocity (0.628 m/s). The longitude velocity, u* and lateral velocity, v* are the dimensionless velocity along *x*-axis and *y*-axis respectively. Figure 4.47 displays published u*-v* vector field near the water surface for q* = 0.250.

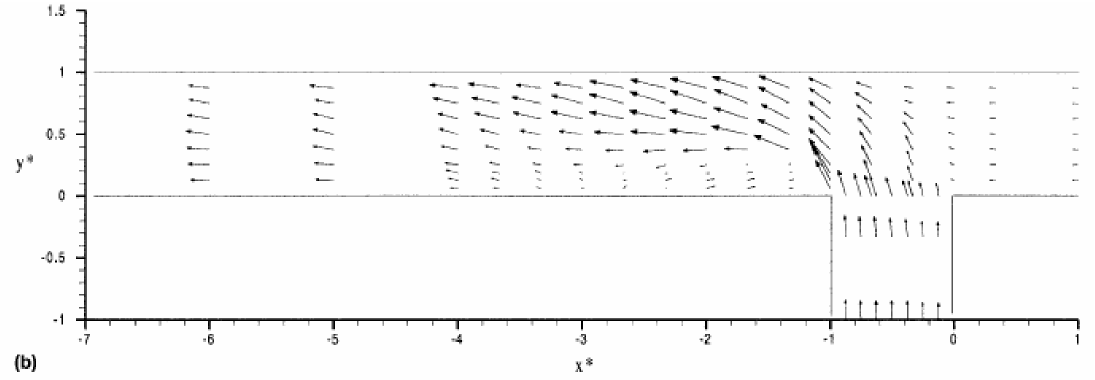

Figure 4.47 u*-v* vector field for q* = 0.250 (experiment 90 degree junction)

Recirculation was formed immediately downstream of the junction due to the deflection from outer wall. The study in that published paper was three-dimensional flume, including the study of vertical component such as vertical velocity, w*. Weber concluded the flow condition in a schematic for flow q* = 0.250 as shown in figure 4.48.

However, due to the limitation of two-dimensional numerical model, only the surface flow condition was simulated. Results comparison will be only focused on the water depth and velocity of surface flow.

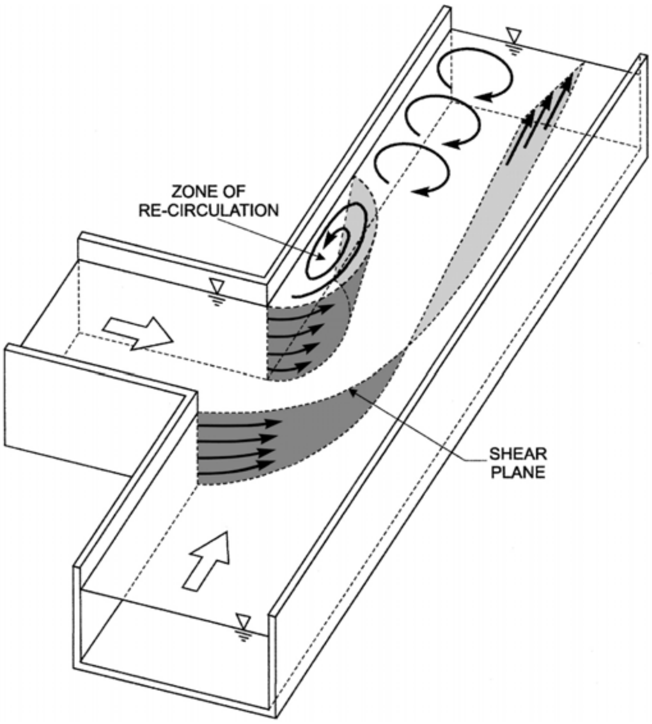

Figure 4.48 Schematic of flow structure for q* = 0.250

In the numerical model, flow parameters which were displayed in table 4.20 were applied and the mesh grid used for this study is shown in figure 4.49. The inflow for main channel and branch channel were indicated as Qm and Qb respectively. The models were repeated for both inflow (q* = 0.250 and 0.750). The roughness coefficient was determined using trial and error method. The best results were obtained with Manning's *n* equal to 0.0160 for both models. Since the measured water depth was higher than critical depth, the flow condition should be subcritical flow.

Table 4.20 : Input flow parameters for numerical model (90 degree junction)

Total Q, Qt (m^3/s)	B (m)	Upstream B. C.	Downstream B.C.	slope	*n*	time step
0.17	0.914	sub	sub (h=0.296m)	0	0.0160	1.0s

q*=Qm/Qt	Qm (m^3/s)	Qb (m^3/s)
q* = 0.750	0.127	0.042
q* = 0.250	0.042	0.127

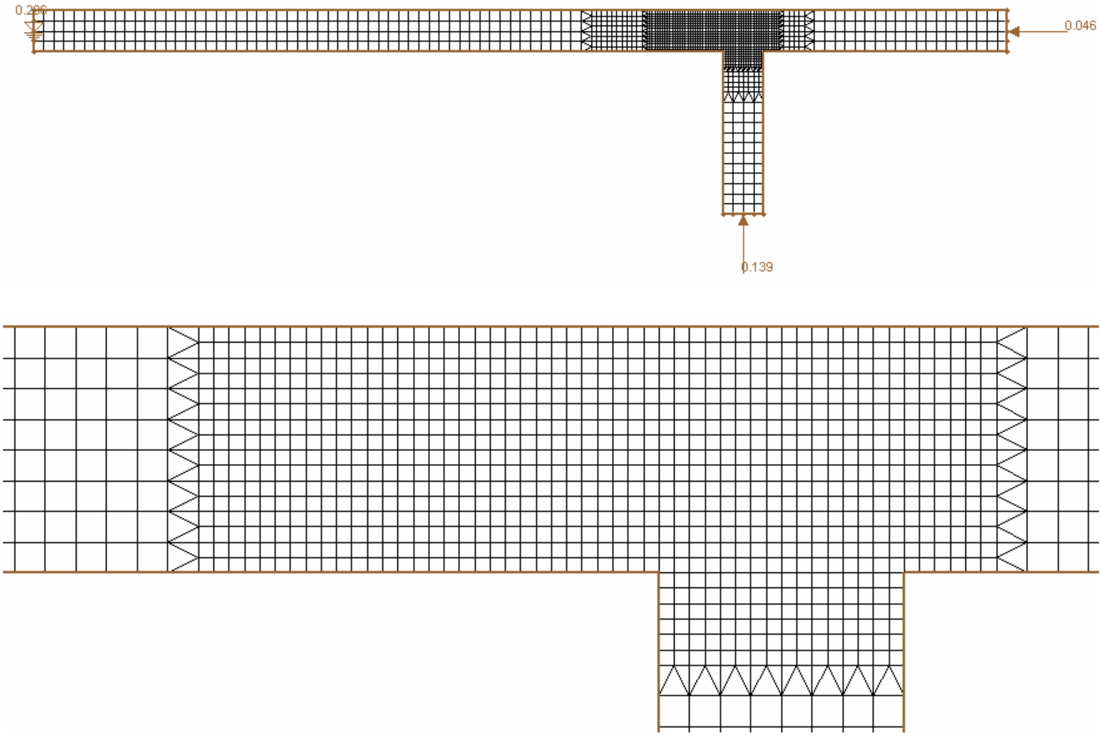

Figure 4.49 Mesh grid (90 degree junction)

After 100s of simulation, the flow pattern converged to stable solution. However, both model simulations were continued until t = 300s to ensure the flows reached steady state. For comparison purpose, the results were plotted in h* as presented in figures 4.50(a) and 4.50(b). These results are in agreement with those of Weber et al (2001).

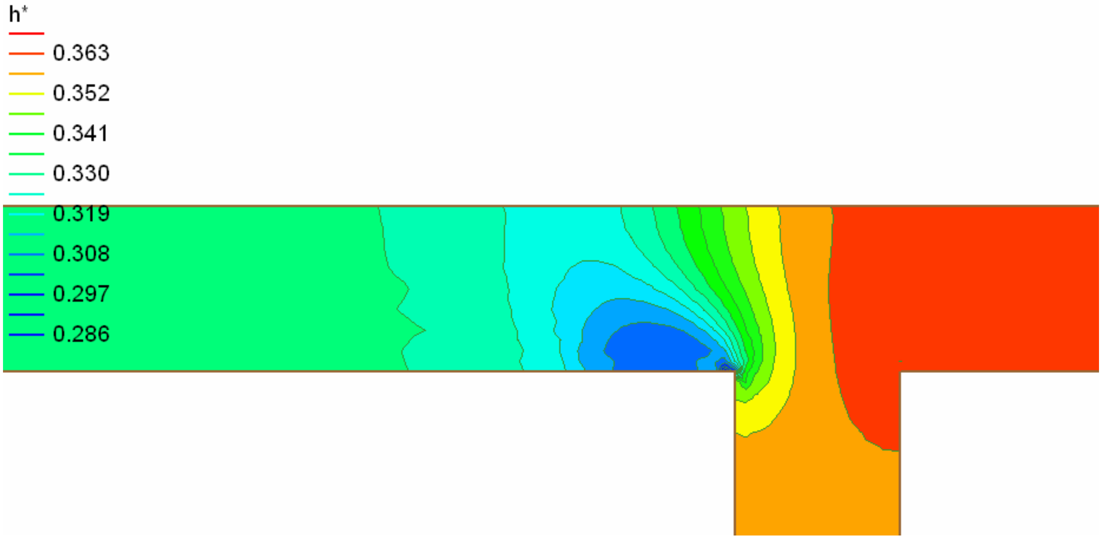

Figure 4.50(a) h* contours for q* = 0.250 from model (90 degree junction)

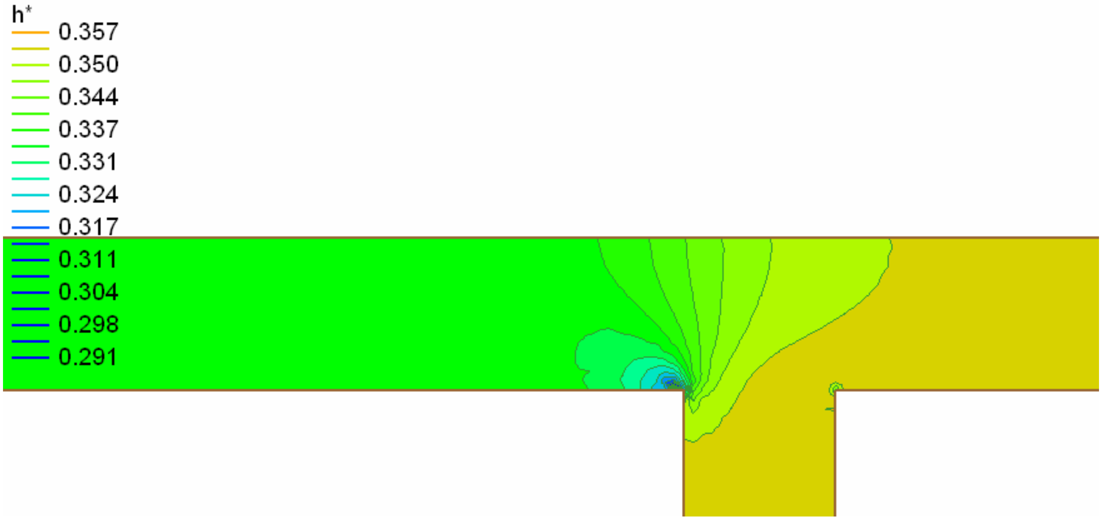

Figure 4.50(b) h* contours for q* = 0.750 from model (90 degree junction)

The momentum of the lateral branch flow caused the main flow to detach at the downstream corner of the junction. This is more significant for lower q* flow condition. As a result, the water depth raised up at the upstream of main channel. The effect of 90 degree expansion is significant for both flow conditions, causing the water depth decreased rapidly at immediately downstream of junction. Figures 4.51(a) and 4.51(b) show the u*-v* vector field from numerical model. It is apparent to see that for higher q*, the velocity vectors show less deflection toward the outer wall. Meanwhile the disturbance from branch channel is not significant for higher q*. Note that the recirculation was formed in the numerical results too as reported in the paper. The model's results show that higher q* will take shorter distance downstream from the junction to reach uniform flow condition again. However, both results show the increasing of velocity at outer wall region downstream of the junction.

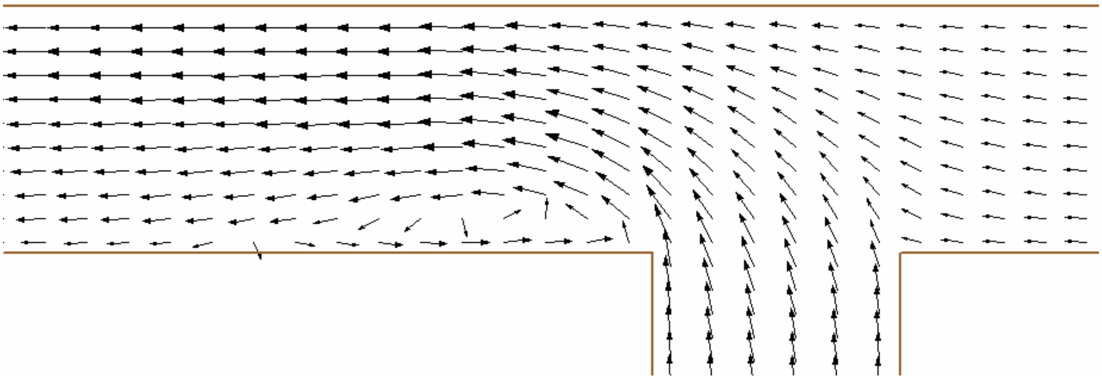

Figure 4.51(a) u*-v* vector field for q* = 0.250 from model (90 degree junction)

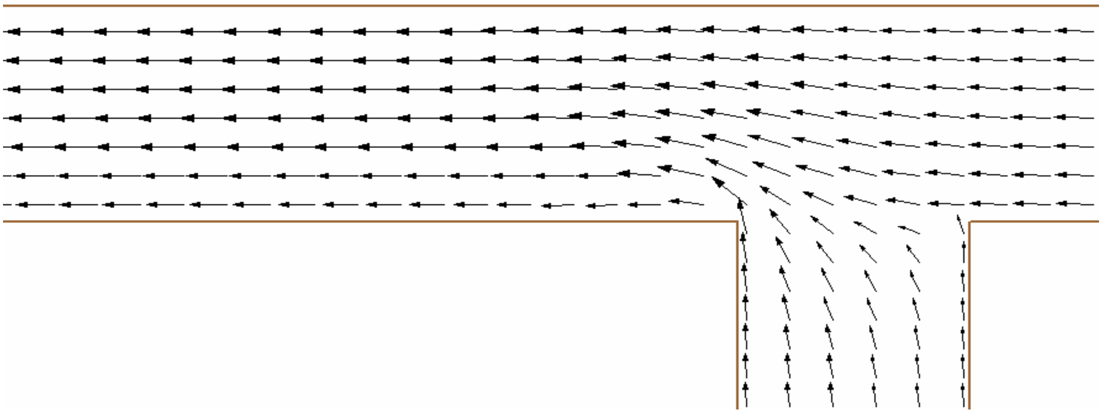

Figure 4.51(b) u*-v* vector field for q* = 0.750 from model (90 degree junction)

4.3.5 Hydraulic Jump

Two hydraulic jump test cases were examined in this section. The published hydraulic jump result, adapted from Gharangik et al (1991), was simulated with a horizontal slope; meanwhile the experiment conducted in UTM was modelled in a steep slope. Description of both test facilities can be referred in chapter 2 and 3. Here, comparison between numerical model and the published hydraulic jump data was discussed first.

Four numerical model simulations were conducted with different Froude numbers (Fr_1), as listed in table 4.21. Since the published results were presented in one-dimension, all numerical models were modelled in one-dimension for easy comparison. Besides, interval of 1.0s time step was used. The depth for every model was initially set to d_1 at the entrance, and increased linearly to d_2 at the end of downstream.

Table 4.21 : Input flow parameters for numerical model (hydraulic jump)

test no.	Q (m^3/s)	Fr_1	upstream B. C.	Downstream B.C.	Initial Depth (d_1-d_2)
2	0.0357	6.71	super (h=0.024m)	sub (h=0.201m)	0.025m - 0.200m
3	0.0654	5.71	super (h=0.040m)	sub (h=0.283m)	0.040m - 0.290m
4	0.0538	4.21	super (h=0.043m)	sub (h=0.223m)	0.045m - 0.230m
6	0.0534	2.30	super (h=0.064m)	sub (h=0.170m)	0.065m - 0.170m

In this analysis, the sensitivity of grid resolution was studied. The mesh grids (1D) with several value of Δx were tried and the results are plotted in figure 4.52 together with the measured depth for test case 2. The Manning's *n* of 0.0058 was applied for all grid resolution. Unlike previous test cases, the final solution was kept changing with grid refinement. Further grid refinement will reduce the length of hydraulic jump. In the other words, the jump length was greatly affected by the size of element. Another important finding is that the energy in numerical model was dissipated too quickly within two elements. The numerical model cannot predict the length of hydraulic jump since the vertical motion that should be captured is neglected due to the assumption of shallow water equation.

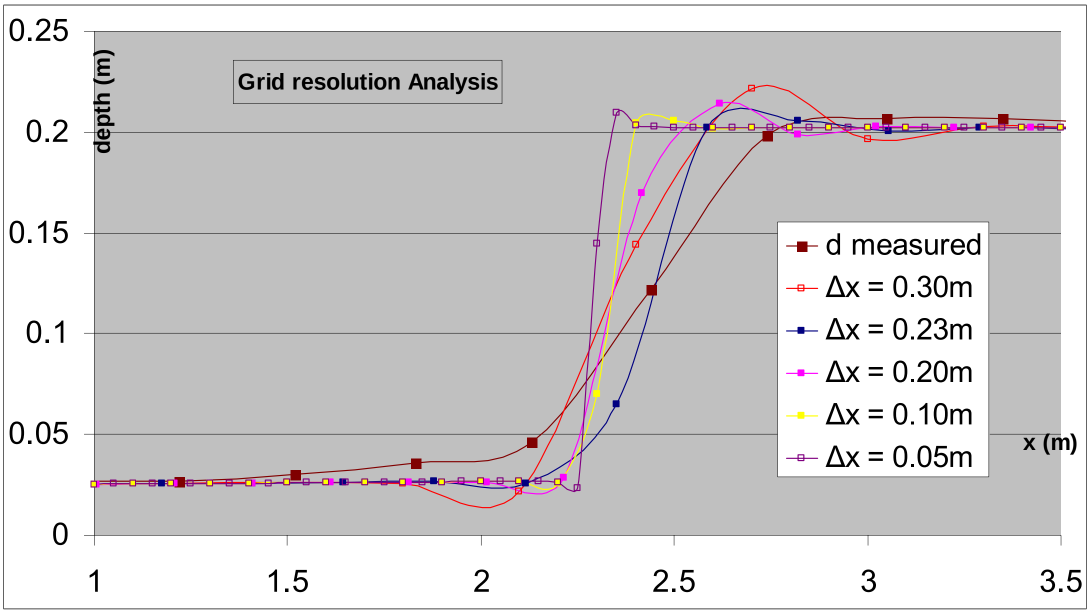

Figure 4.52 Analysis of grid resolution in hydraulic jump

The study of the sensitivity of grid resolution provided an important guideline. By selecting the distance between the measured points in experiment as element's size, the simulated result should be the best. Since the depths were recorded for every 1ft in laboratory, the chosen size of element for the following models was 0.30 m. Four simulated results are compared with the published results in figure 4.53(a), 4.53(b), 4.53(c) and 4.53(d) for test case 2, 3, 4 and 6 respectively. The Manning's *n* for the flume was determined by trial and error so that the computed water-surface profile matches with the measured water levels in the flume during the initial steady supercritical flow. According to the published result, the *n* value was varied from

0.008 to 0.011, depending upon the flow depth. However, results from numerical model show that the Manning's *n* can be equal to 0.0058. The line in yellow colour shows the best result for each test case.

Besides, the stabilized jump location was always changing with different roughness coefficient. However, the model simulated the water depths extremely well. It took longer for the solution to converge to a stabilized jump for lower Froude number. Note that the model cannot predict the length of the jump due to the negligible of vertical motion in shallow water equation.

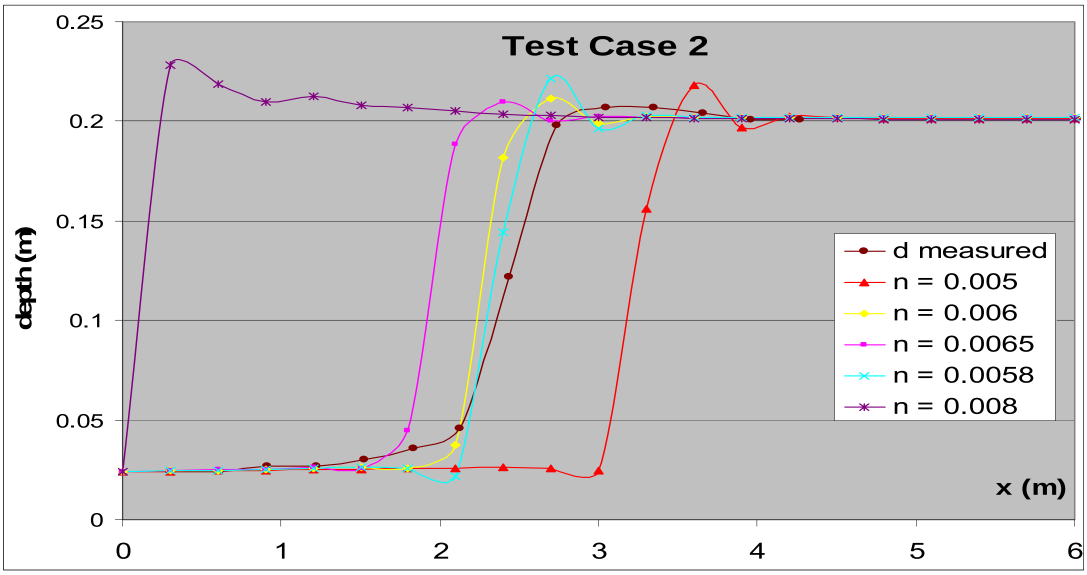

Figure 4.53(a) $Fr_1 = 6.71$

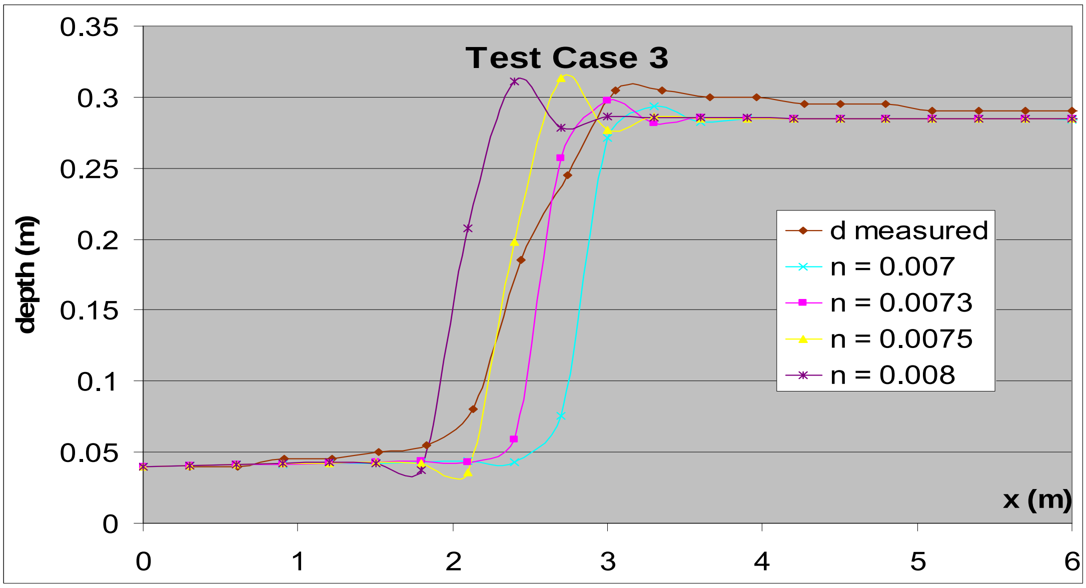

Figure 4.53(b) $Fr_1 = 5.71$

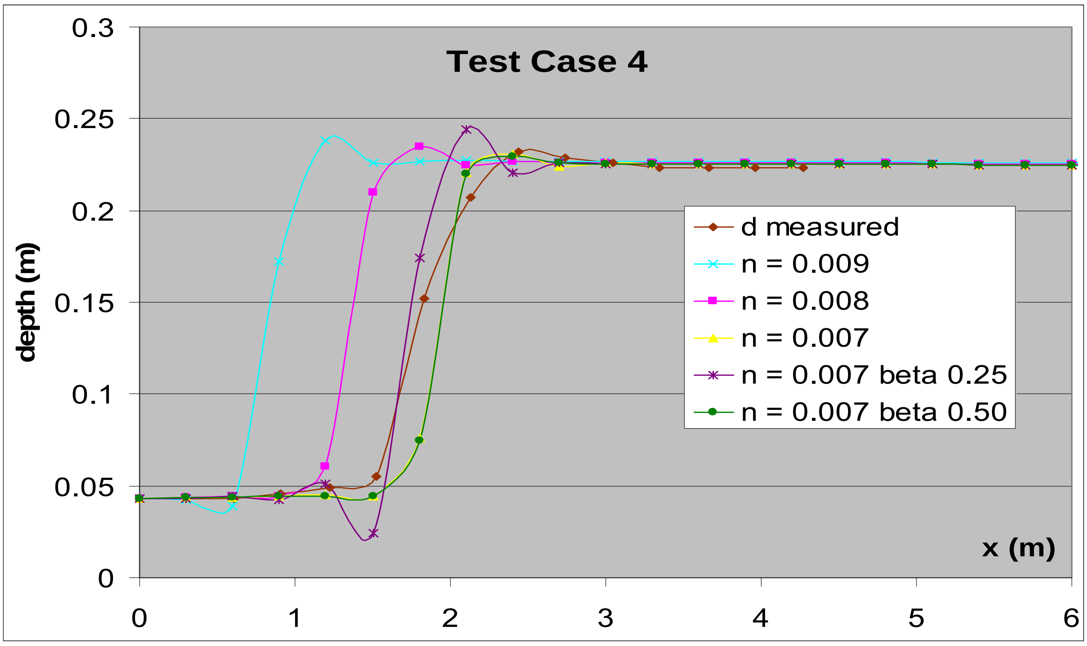

Figure 4.53(c) $Fr_1 = 4.21$

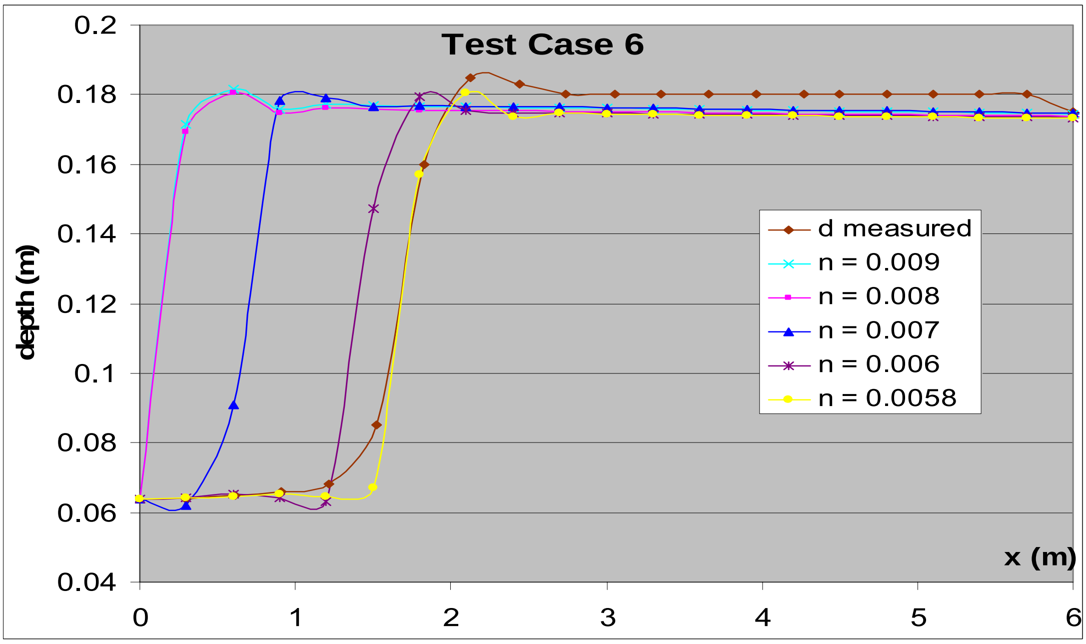

Figure 4.53(d) $Fr_1 = 2.30$

Numerical model always underestimated the depth before jump for all test cases. Generally, the decreasing of friction will push the jump location further downstream and reduced the maximum depth. Result from test case 4 is the best verification of this explanation. Besides, 3 set of dissipation coefficient were tested in test case 4 ($\beta_{smooth} = 0.25$, $\beta_{shock} = 0.25$; both 0.25 and both 0.50). Result with both β equal to 0.25 shows overshooting before and after jump. However, the effect is not significant with only 0.020 m different.

The second hydraulic jump experiment was carried out in UTM with steep slope (1/78). A 0.045 m wide plastic plate was used as a sluice gate at the downstream of flume as shown in figure 4.54. In this experiment, $Q = 0.0153\ m^3/s$ was used. The approach depth (normal depth) was equal to 0.031 m with Froude number 2.0. The average measured velocity was 1.08 m/s. The experiment was started with dry bed condition.

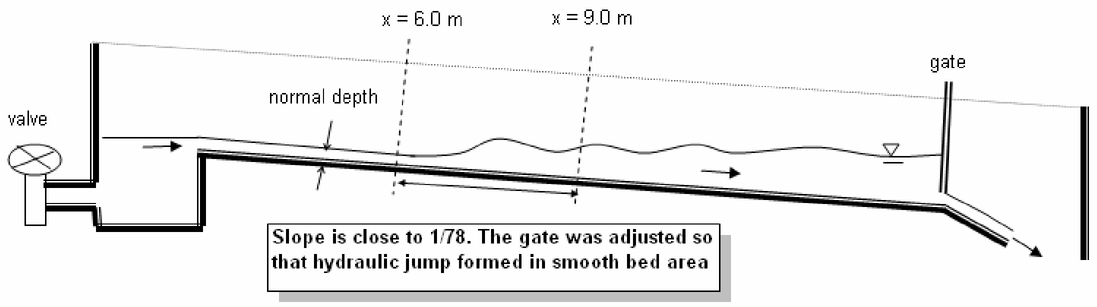

Slope is close to 1/78. The gate was adjusted so that hydraulic jump formed in smooth bed area

Figure 4.54 Hydraulic jump test case with steep slope

Figures 4.55(a) and 4.55(b) display the undular jump which was formed in the experiment. The hydraulic jump constituted a rapid transition from supercritical to subcritical flow. Due to the oscillating breaking front at the toe of the jump, air was entrained into the jump. Difficulty was found when measuring the water depth in this region.

Figure 4.55(a) Undular jump (front view)

Figure 4.55(b) Undular jump (side view)

The figures clearly illustrate that a “non-uniform” undular jump was formed due to side wall friction and non-uniform of incoming flow. Initially, the supercritical flow formed a small jump when blocked by the plate downstream of the channel. Then the hydraulic jump was pushed backward gradually to upstream of the channel and stop at a stabilized location ($x \approx 6.6$ m). The grids on glass-walled section were used to measure the jump profiles. The maximum and minimum depths were recorded and an average depth was considered the depth at that location.

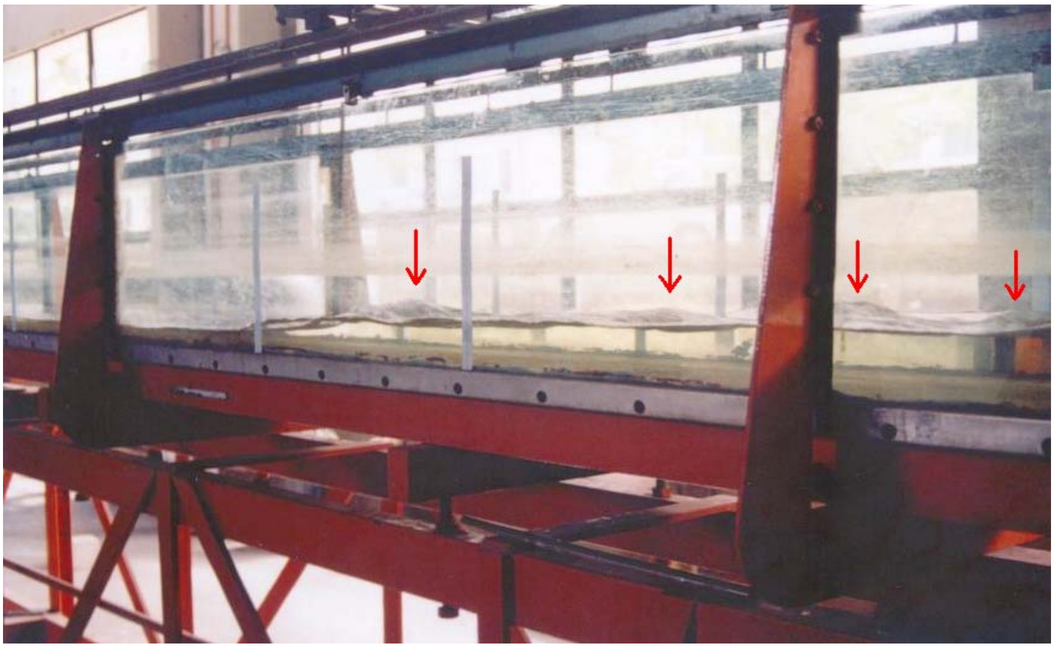

Figure 4.56 Oscillations

The flow oscillated after the undular jump and formed a series of shock waves downstream of the channel as shown in figure 4.56. This means that the energy in the flow was continuously dissipated even after the undular jump. The water profile was recorded and will be presented together with numerical model's result.

A two-dimensional numerical model was conducted to simulate the above experiment. The formation of undular jump and oscillations in the experiment were considered in numerical result. There were eight elements across the model with aspect ratio of 1.0 as shown in figure 4.57.

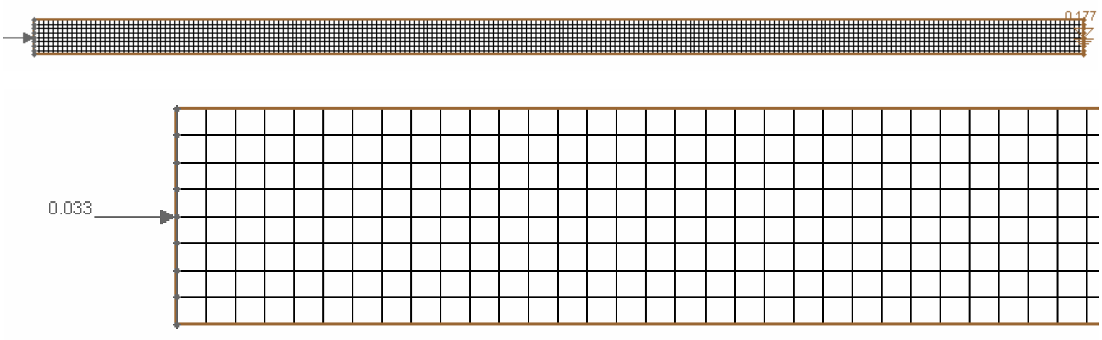

Figure 4.57 Mesh grid (Hydraulic jump)

Table 4.22 shows the flow parameters used as input in numerical model. The depths for boundary conditions were determined from experiment. However, the initial dry bed condition in experiment cannot be applied in model. Similar to previous model, the initial condition was modified so that it increased linearly from upstream to downstream of the channel boundary conditions.

Table 4.22 : Input flow parameters for numerical model (experiment hydraulic jump)

Q (m^3/s)	B (m)	S	*n*	Upstream B.C.	Downstream B.C.	Initial Condition	Time step (s)
0.0153	0.457	measured	0.009	super (h=0.033m)	sub (h=0.177m)	0.030m-0.180m	0.02

Figures 4.58(a) and 4.58(b) present the results from numerical model and experiment after 355s. The measured depths were plotted by using interpolation method. The contours show that the agreement was reached between both results quantitatively.

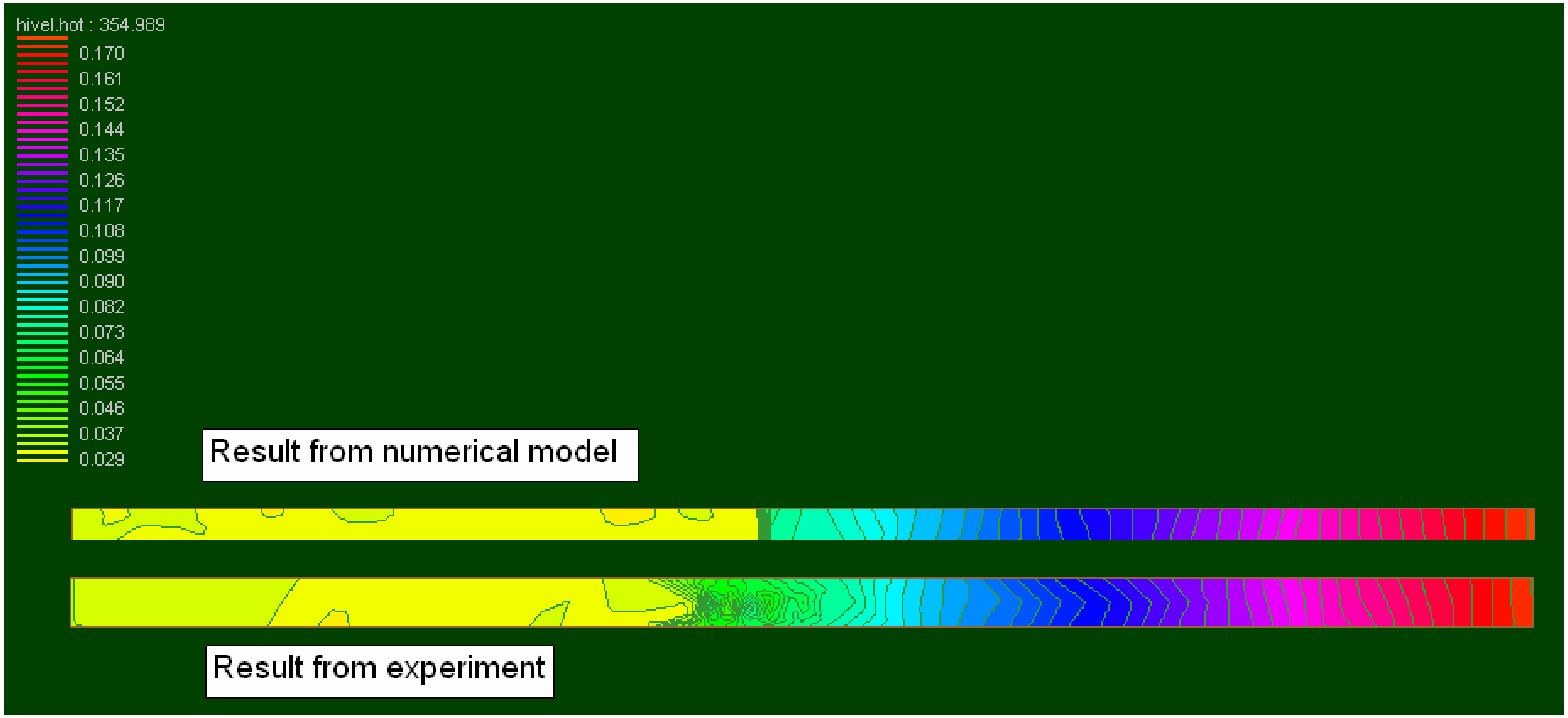

Figure 4.58(a) Water depth (Hydraulic jump)

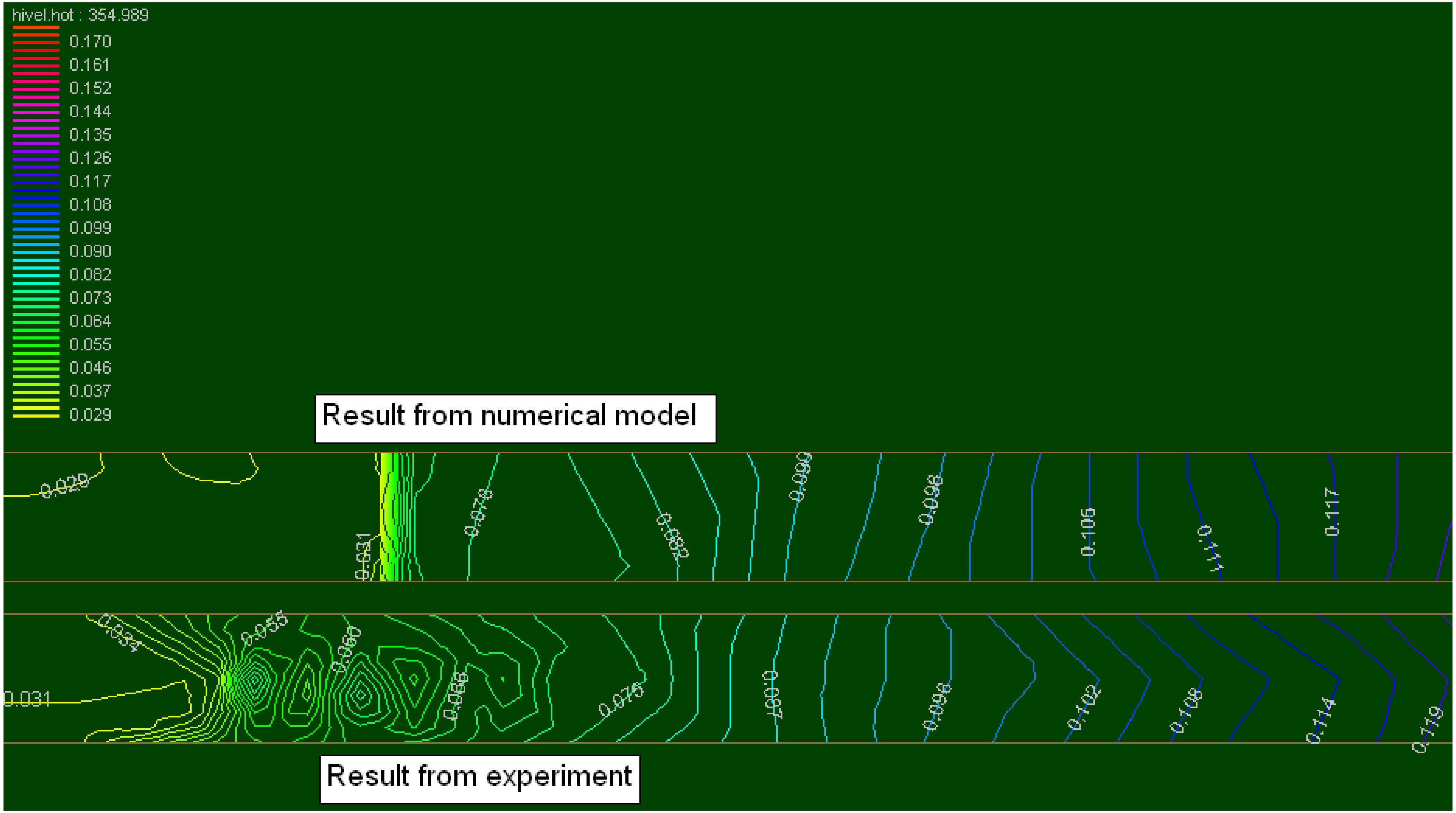

Figure 4.58(b) Water depth (Hydraulic jump)

However, the formation of undular jump and oscillations in the experiment are unable to be simulated. It is apparent to express that numerical model dissipated energy immediately within one element longitudinally. And the oscillations are not found as expected. In this result, the flow profile after jump was smooth and the depth increased gradually till the end of flume.

In shallow water equation, vertical velocity and acceleration are neglected. Therefore, any energy that should be captured in vertical motion is lost. The shallow water equation treat the jump as discontinuity and all vertical energy will be dissipated immediately as proved in the example above. Actually this problem was found in many others studies which used shallow water equation as a basic governing equation (Stockstill, et.al. 1994).

4.3.6 Bridge Pier

To obtain experimental data for model verification, there are three test cases for aluminium pier and another three test cases for wood pier were conducted. All experiments were tested for Froude number within 2.0 to 3.0. The Froude number was controlled by using sluice gate which was located 0.5 m in front of pier as shown in figure 4.59.

Figure 4.59 Sluice gate

In test case1, back water was formed as displayed in figure 4.60(a). Complicated flow pattern was found due to combination effect of contraction and expansion. The maximum water depth which was formed on the face of pier was approximately 0.075m. The run up at pier nose seemed strong and the vertical acceleration should be large. This would be the most challenging part for model simulation. Besides, a diamond shape of flow was formed at channel downstream due to wave interference. The water depths in the area of interest were measured.

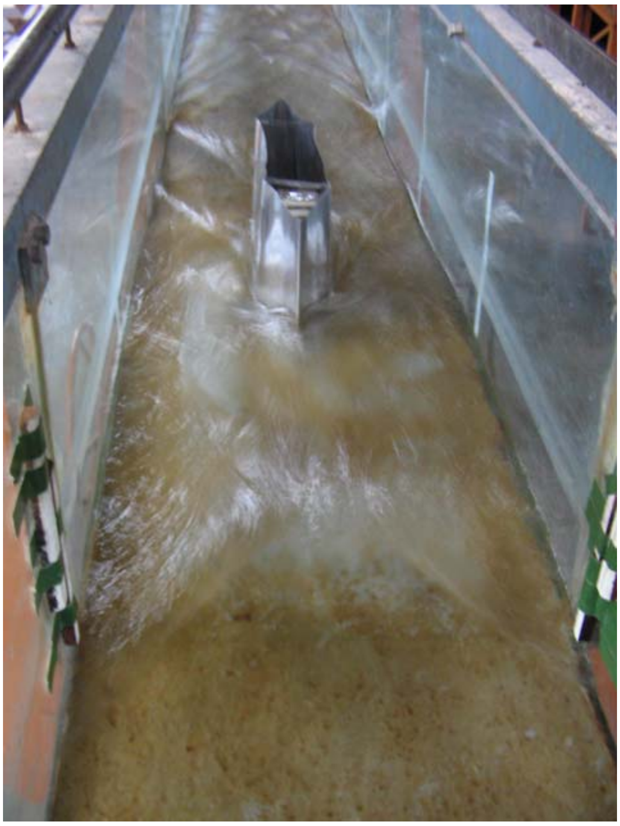

Figure 4.60(a) 3D view (1st test case in aluminium pier)

In test case 2, a sluice gate was applied to increase the approach Froude number. No back water is found for this time. The run up was much stronger than test case 1 as shown in figure 4.60(b), which raised up to 0.080m. Similar to test case 1, diamond shape flow was formed downstream of the pier. However, the shock waves were swept further downstream if compared to test case 1. The flow pattern in test case 3 is almost similar to test case 2, except the shock locations were found further downstream than previous test case due to high velocity flow. The maximum water depth which was found on the face of pier was approximately 0.103m. Plan views for these three test cases are displayed together for comparison in figures 4.61.

Figure 4.60(b) 3D view (2^{nd} test case in aluminium pier)

Figure 4.60(c) 3D view (3^{rd} test case in aluminium pier)

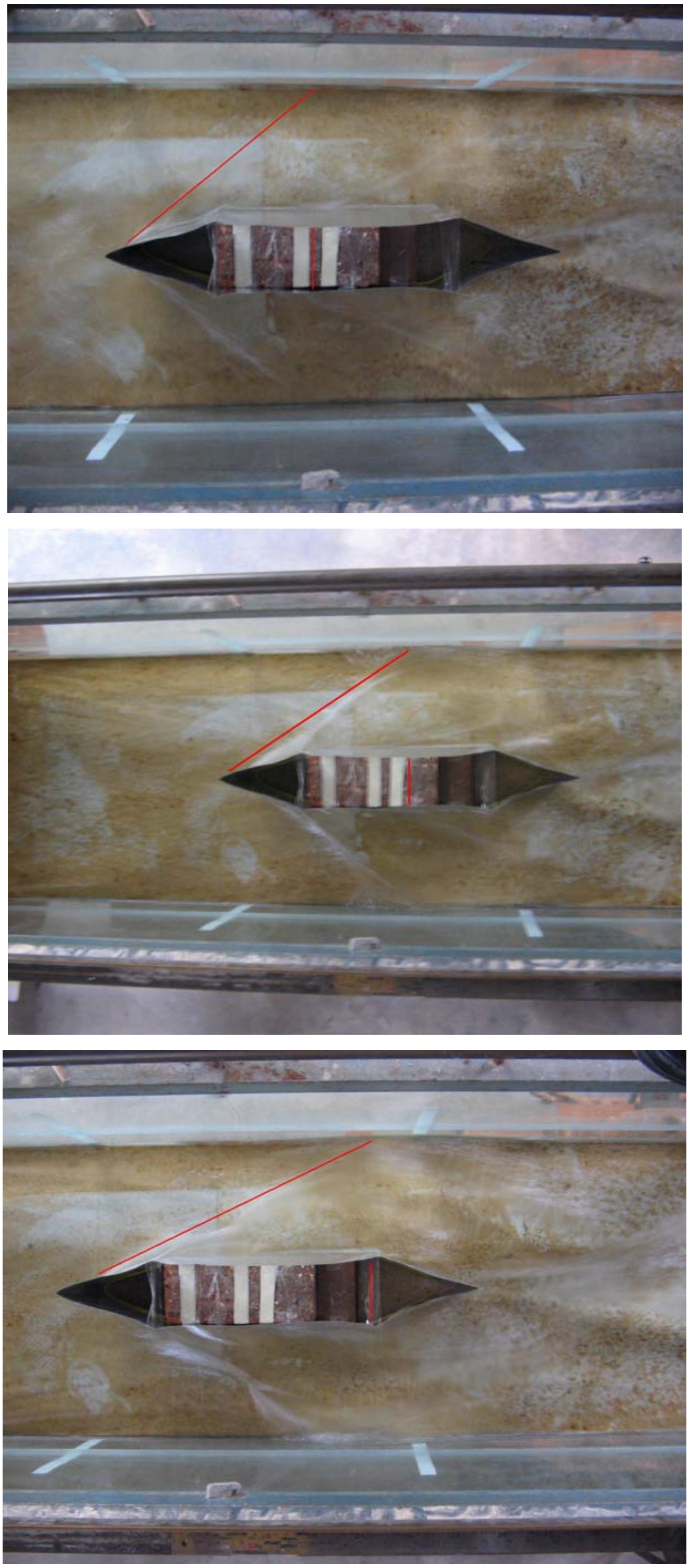

Figure 4.61 Plan views for test case 1 (top), 2 (middle) and 3 (bottom)

As seen in the sequence of figures 4.61, the approaching flows were separated to left and right sides in an angle. The waves were reflected by sidewalls and formed wave interference immediately behind the pier till the end of flume. With these observed results, numerical model was run to reproduce the complicated flows.

Figure 4.62 shows the mesh grid for aluminium pier with triangular nose and tail. Finer mesh, with 16 elements across laterally, was applied at both sides of the pier region. The dimension of pier is described in chapter 3. In the model simulation, the measured slope approximately equal to 1/78 was implemented. All required input were selected to be equal to those of the corresponding physical experiments (table 4.23).

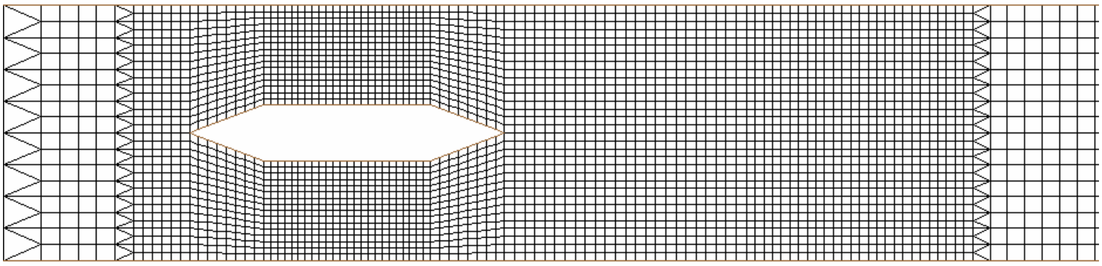

Figure 4.62 Mesh grid (triangular nose and tail)

Table 4.23 : Input flow parameters for numerical model (aluminium pier)

test case	Fr	Q/B (m^3/s.m)	Upstream B.C.	Downstream B.C.	Initial depth
1 (without sluice gate)	2.0	0.032	super (h=0.035m)	super	0.030m-0.010m
2 (with sluice gate)	2.5	0.028	super (h=0.023m)	super	0.017m-0.010m
3 (with sluice gate)	2.8	0.043	super (h=0.029m)	super	0.015m-0.010m

Results from numerical model and experiment are presented together in the following paragraph, by starting with test case 1. By trial and error method, the Manning's *n* of 0.097 shows the best result. Figure 4.63 presents measured water depth and simulated depths for test case 1. Similar to hydraulic jump problem, the energy was dissipated too fast. However, the simulated maximum depth on the face of pier is 0.073m, which is very close to the measured depth (0.075m). In the other words, numerical model still can reproduce the run up successfully for this case.

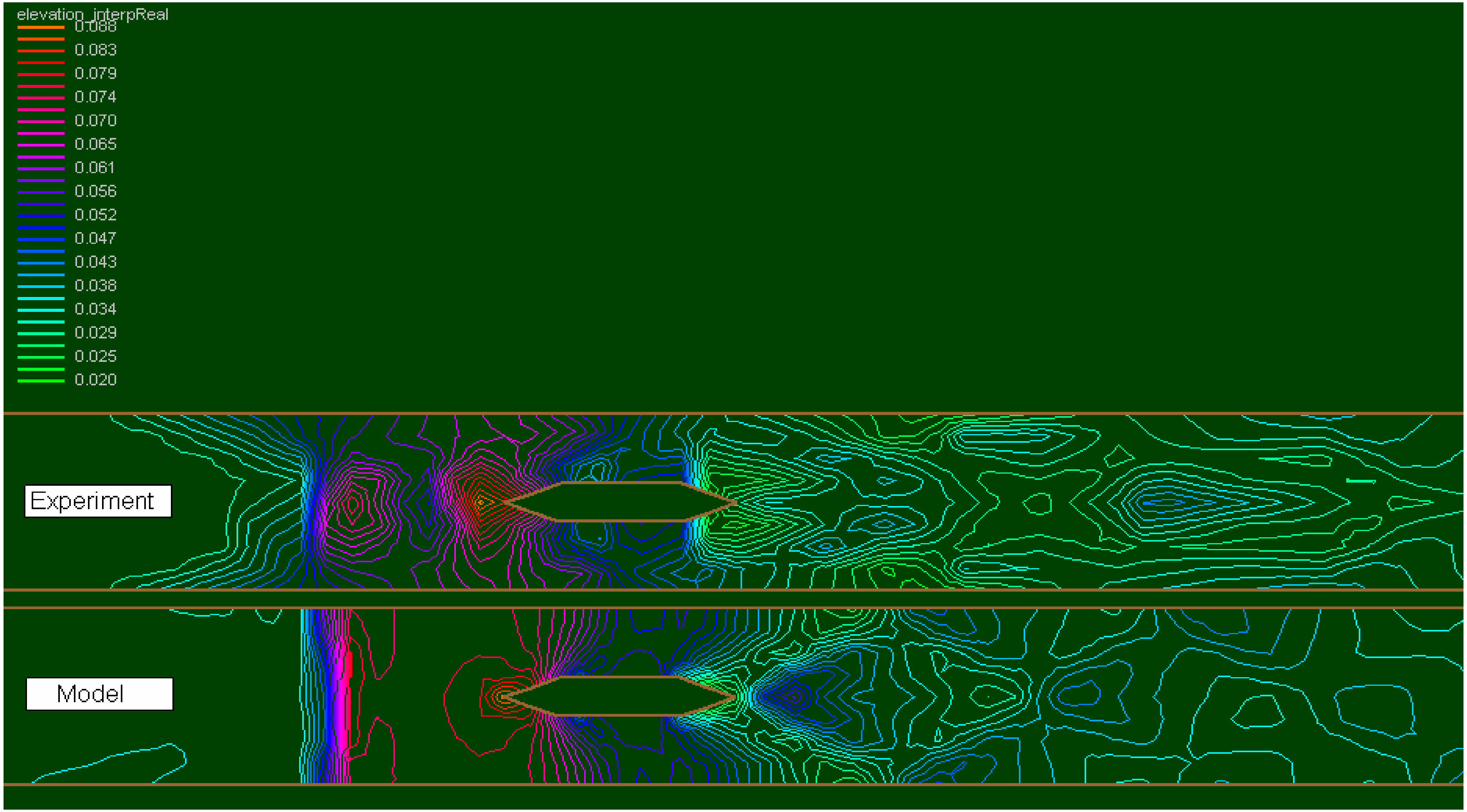

Figure 4.63(a) Comparison water depth between experiment and numerical model (1st test case)

Figures 4.63(b) and 4.63(c) show another two results for test case 2 and test case 3. The contours were plotted by using simulated depth; Meanwhile the measured depths were marked in both figures as white scatter points.

Let's focus to the run up region near the nose of pier. As seen in table 4.24, both run up (from experiment and numerical model) were increased with larger approach Froude number. For both case, the model underestimated the run up on the face of pier. Besides, the comparison of shock locations shows the disagreement as indicated in figure 4.63(b). This problem might be improved by adjusting the Manning's *n*. For this purpose, test case 2 was repeated for various Manning's *n* such as 0.0050, 0.0085, 0.0090, 0.0093, 0.0095 and 0.0098. But unfortunately, all simulated run up was still underestimated. Moreover, the effect of Manning's *n* to the shock location was insignificant because pier was located too near to the upstream boundary condition. In the other words, not enough space for roughness factor to show its effect in run up region.

Table 4.24 : Relationship between run up with other parameters (aluminium pier)

test	Fr	**measured run up**	**simulated run up**
2	2.5	**0.080m**	**0.050m**
3	2.8	**0.103m**	**0.060m**

Figure 4.60(c) clearly shows that the wavelength of run up is extremely thick and sticks closely with the face of pier. However, numerical model failed to capture this run up because the vertical motion was neglected in the model. Perhaps, the triangular pier's wall gave over blocking effect to the approaching flow. This was strongly proved by the larger angle of wavefront in the model simulation. As a result, the shock wave hit further upstream of sidewall. Next, a wood pier with rectangular nose and tail was investigated.

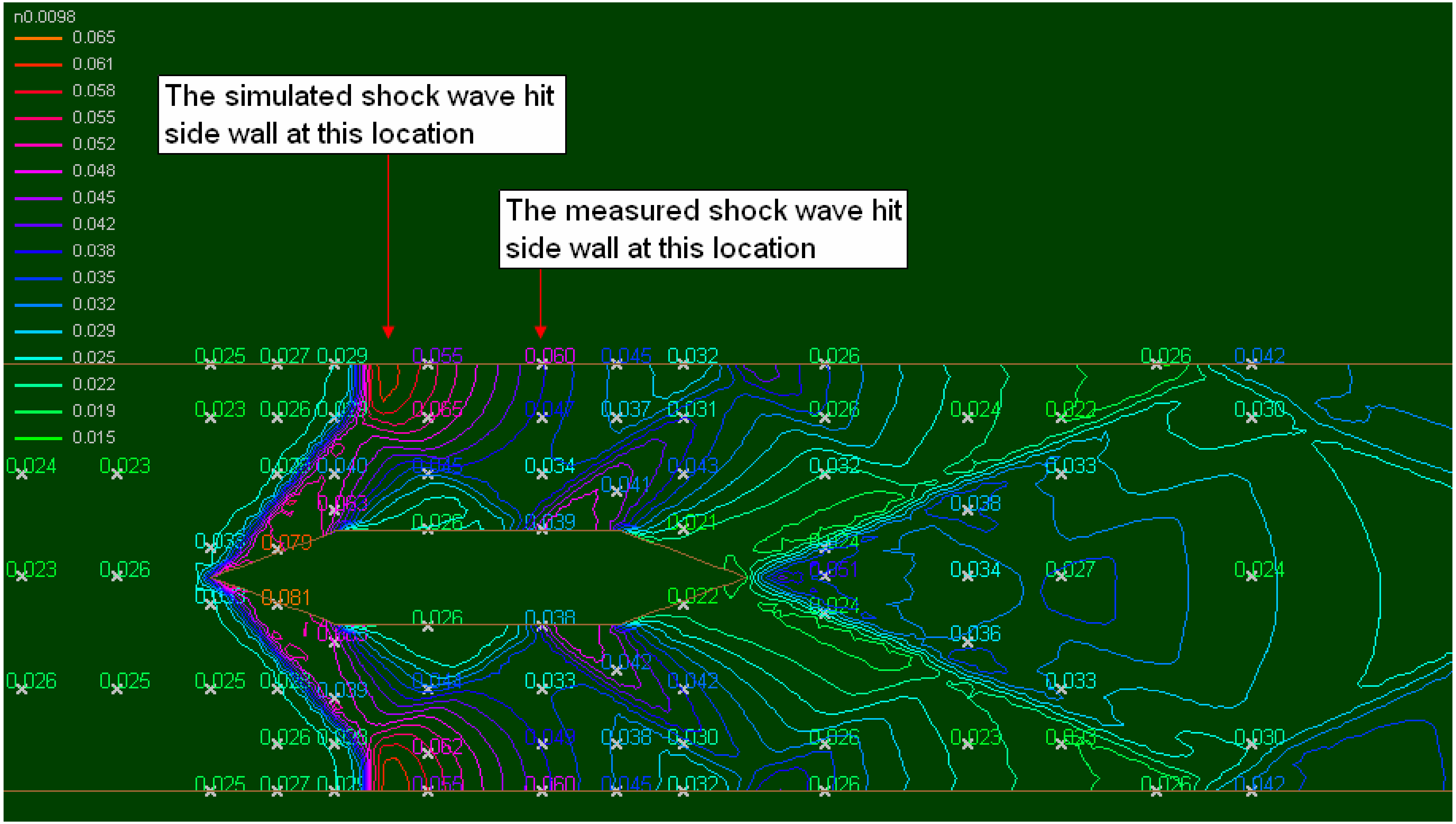

The simulated shock wave hit side wall at this location

The measured shock wave hit side wall at this location

Figure 4.63(b) Comparison water depth between experiment and numerical model (2nd test case)

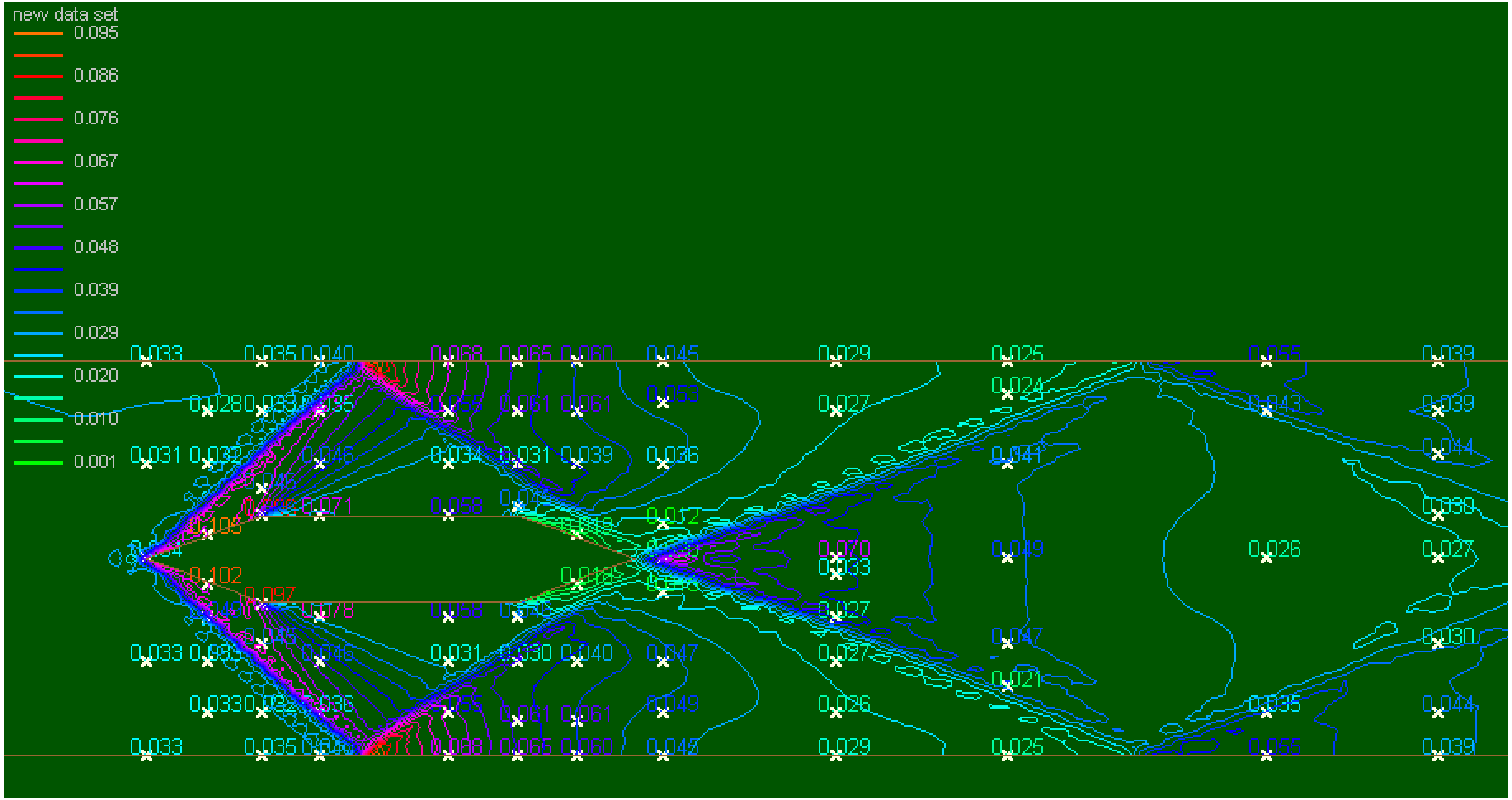

Figure 4.63(c) Comparison water depth between experiment and numerical model (3rd test case)

Similar to triangular pier cases, the wood rectangular pier was also examined in three different approaching Froude number. Compared to aluminium pier, wood pier provides more sufficient clearance laterally across the flume. Three of the experiments were conducted in the same flume with approximately 1/78 slope gradient. The first test case was conducted without sluice gate. The flow pattern from all test cases was found similar. Figure 4.64 shows the example of flow pattern during these test cases. The flow choked up when suddenly blocked by rectangular nose of pier. The height of run up was recorded for each test case. These recorded data are very important since the main interest is to see the capability of numerical model in capturing these run up.

Figure 4.64 Run up at rectangular nose of wood pier

In the model simulation, three models were established corresponding to the physical experiments. The geometry and mesh grid for each model was same, as presented in figure 4.65. Table 4.25 shows the flow parameters used as model input for every test case. Time step of 0.002s was used and the Manning's *n* for each test case was determined by using trial and error method.

Table 4.25 : Input flow parameters for numerical model (wood pier)

test case	Fr	Q/B (m^3/s.m)	Upstream B.C.	Downstream B.C.	Initial depth
1 (without sluice gate)	2.1	0.035	super (h=0.031m)	super	0.035m-0.010m
2 (with sluice gate)	2.4	0.030	super (h=0.025m)	super	0.017m-0.010m
3 (with sluice gate)	2.8	0.025	super (h=0.020m)	super	0.018m-0.010m

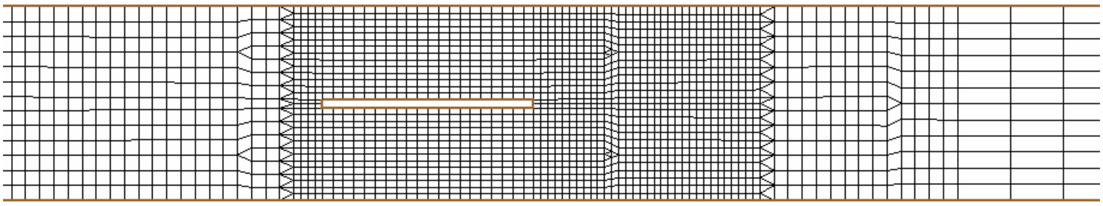

Figure 4.65 Mesh grid (rectangular nose and tail)

Since the flow pattern was similar for all test cases, only the result from test case 1 was displayed, as shown in figure 4.66. The contours represent the simulated water depth meanwhile the scatter points represent the measured depths. If compared to the real flow condition (figure 4.64) with the simulated result, there should be another shock wave formed at the face of pier as shown by red arrow. Again, the angle of shock wave was relatively large if compared to experimental result.

The locations of maximum and minimum water depths were found at the nose and tail region of pier respectively. Model simulated the minimum depth quite well. But for the maximum depth (run up), some interesting findings were found. Referring to table 4.26, the height of run up increased with the increasing of Froude number but the simulated run up decreased for larger Froude number. This may happen because of hydrostatic assumption in shallow water equation.

Table 4.26 : Relationship between run up with other parameters (wood pier)

test	Fr	**measured run up**	Q/B (m^3/s.m)	approach depth	**simulated run up**
1	2.1	**0.078m**	0.035	0.030m	**0.111m**
2	2.4	**0.090m**	0.030	0.025m	**0.103m**
3	2.8	**0.125m**	0.025	0.020m	**0.090m**

For larger Froude number, a large amount of energy was dissipated through the strong run up when hitting the nose of pier in experiment. The energy was transformed to vertical motion, means that the vertical acceleration will increase with larger Froude number. As a result, the height of run up increased as observed in the experiment.

However, the vertical motion was ignored in the model and all dissipated energy in the experiment was considered lost in numerical model. Larger Froude number means that more energy will loss in numerical model, resulting the decreasing of height of simulated run up. However, the simulated run up was found proportional to the rate of discharge.

Since the energy was lost due to hydrostatic assumption, why the simulated run up was still overestimated in test case 1? As explained earlier in triangular pier section, the boundary condition of pier in numerical model gave more blocking effect to the flow than reality. This over blocking effect will produce higher run up when the flow was blocked. Meanwhile in reality, the blocking effect from pier was not that much. With the increasing of Froude number, the height of measured run up will increase; but the simulated run up showed the inverse results due to the loss of energy.

Generally, the numerical model performed poorly in estimating the run up due to the negligible of vertical accelerations in shallow water assumption.

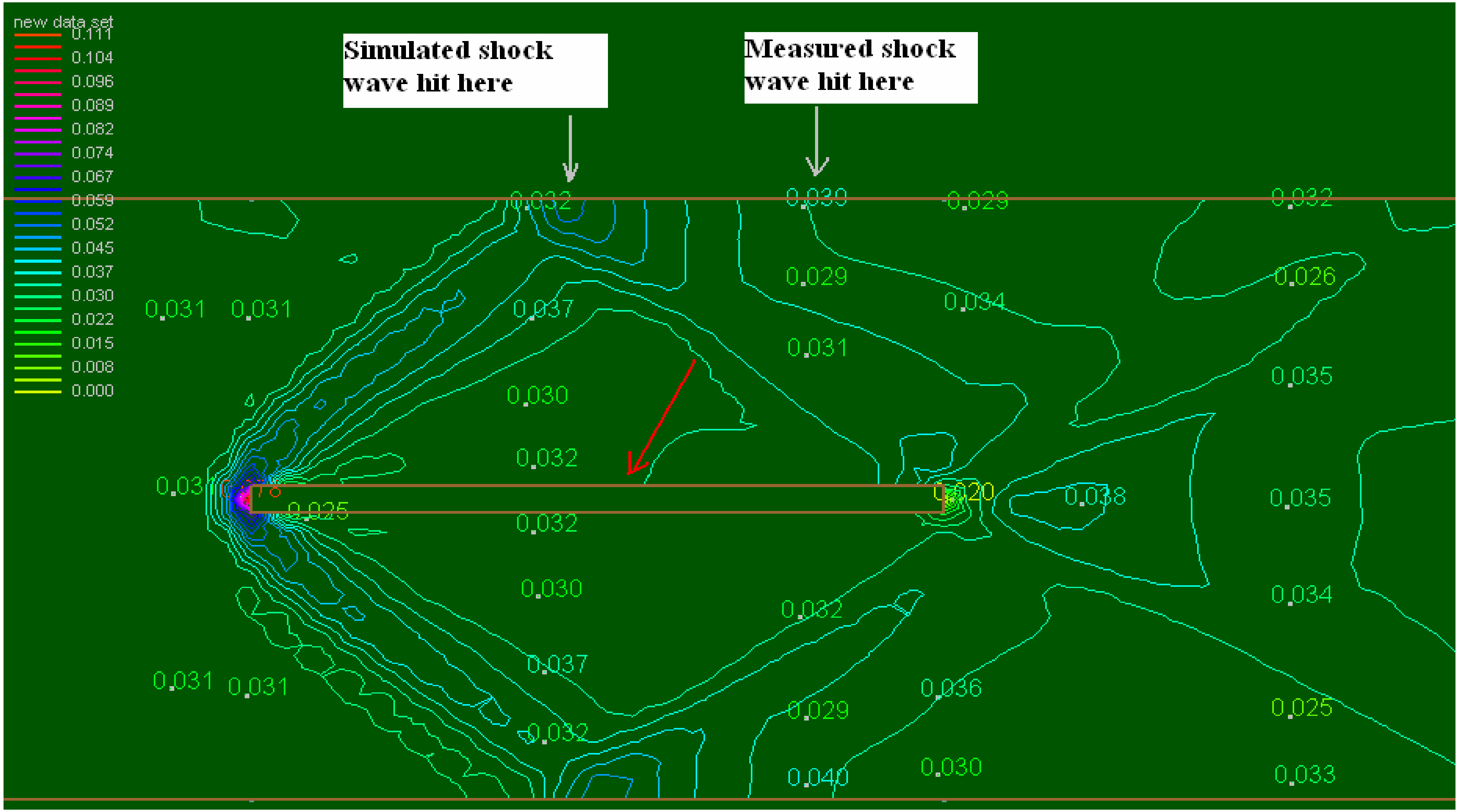

Simulated shock wave hit here

Measured shock wave hit here

Figure 4.66 Comparison water depth between experiment and numerical model (1st test case for wood pier)

4.3.7 Gradual Contraction

Five gradual contraction cases were modelled using approaching Froude number of 2.0, 3.0, 4.0, 5.0, and 6.0 respectively. The zero bed slope and friction were chosen to provide uniform flow approaching the transition. Same mesh resolution was used as displayed in figure 4.67 below. One side of the channel wall was replaced by a sequence of short chords start at x = 0.50 m, each one deflects 4 degrees relative to the preceding one. The geometry was gradually contracted from 0.50 m to 0.337 m. Table 4.27 lists the input parameters

Table 4.27 : Input flow parameters for numerical model (gradual contraction)

Fr	Q (m^3/s)	S	*n*	Upstream B.C.	downstream B. C.
2.0	0.015	0	0	super (h=0.028m)	super
3.0	0.015	0	0	super (h=0.022m)	super
4.0	0.015	0	0	super (h=0.018m)	super
5.0	0.015	0	0	super (h=0.015m)	super
6.0	0.015	0	0	super (h=0.014m)	super

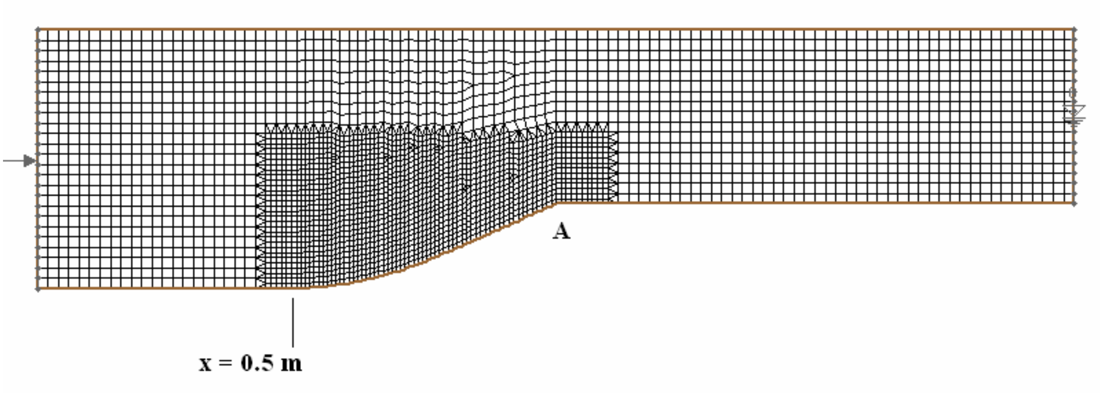

Figure 4.67 Mesh grid (gradual contraction)

In numerical modelling, the solution was computed until reaching the steady flow condition. For Fr = 6.0, the model halted and stopped during simulation because the water depth near the expansion region (point A in figure above) was close to zero. The expected oblique shock wave due to inward boundary was obtained in numerical model for all test cases except for Fr = 2.0, which back water was found. All numerical results are presented in the sequence of figures 4.68, including test case for Fr = 6.0 (before model halted).

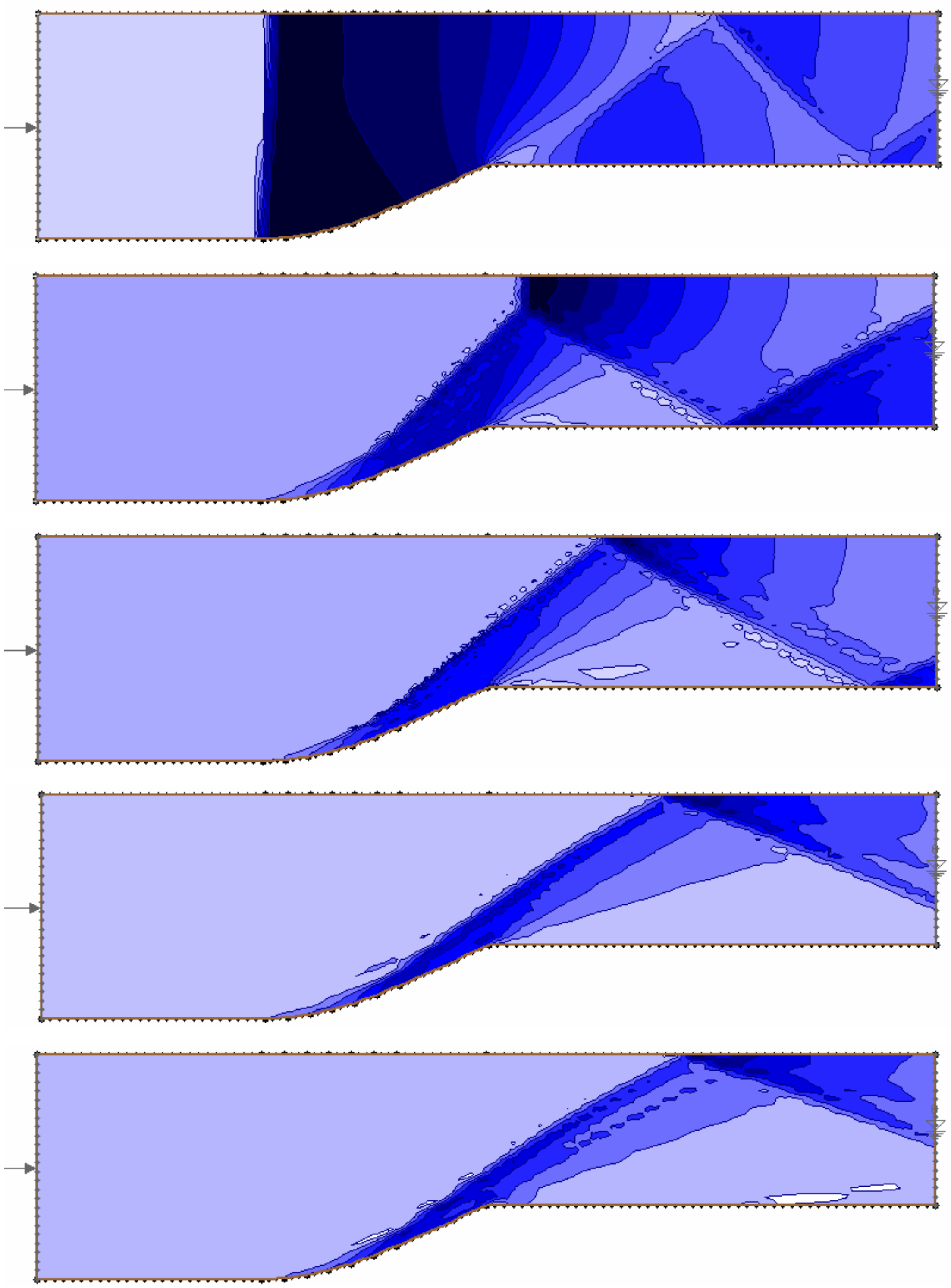

Figure 4.68 Water depth for Fr = 2.0, 3.0, 4.0, 5.0 and 6.0 (gradual contraction)

These reasonable results show that the shock location moved further downstream with larger Froude number. The flow pattern in “z” shape was also captured by model. The performance of model in this test case was considered quite good.

4.3.8 Bend

In this test, five numerical model simulations were conducted using different Froude number, which were consisting of 0.25, 0.70, 1.20, 1.50 and 2.0. The geometry and mesh grid for the test was displayed in figure 4.69. The model's width, B was equal to 0.5 m. The inner and outer radiuses of the bend were 0.232 m and 0.743 m respectively, resulting average radius equal to 0.488 m in centre line.

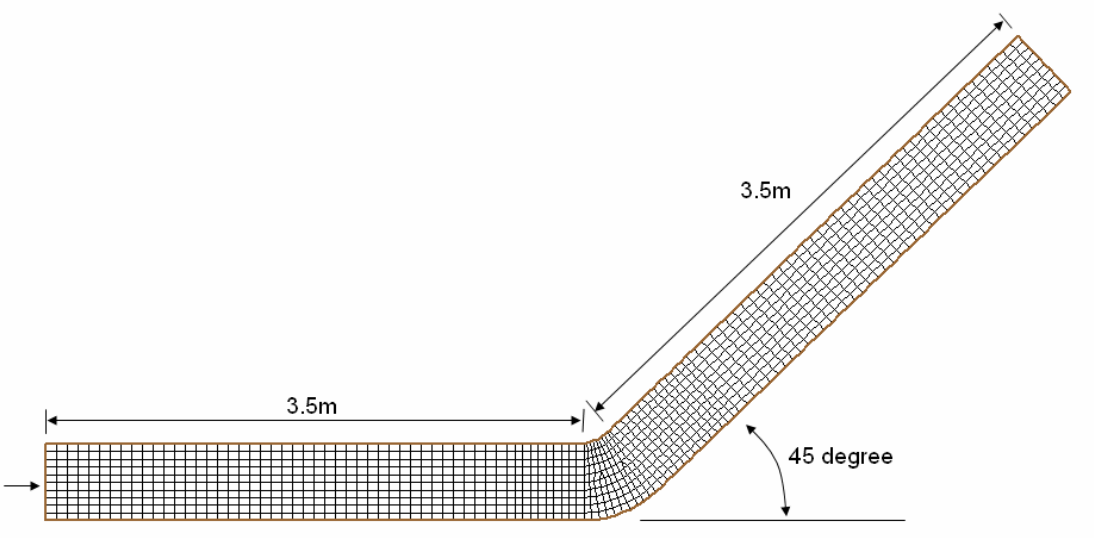

Figure 4.69 Mesh grid (bend)

Table 4.28 shows the input parameters for each test case. The constant flow rate of $1.0m^3/s$ was applied in all cases. Again, the frictionless horizontal model was used. In addition, a time step of 0.01s was applied.

Table 4.28 : Input flow parameters for numerical model (bend)

test	Fr	Upstream B.C.	Downstream B.C.	Initial depth
1	0.25	sub	sub (h=1.840m)	1.8m
2	0.70	sub	sub (h=0.900m)	0.9m
3	1.20	super (h=0.660m)	super	0.6m
4	1.50	super (h=0.565m)	super	0.5m
5	2.00	super (h=0.467m)	super	0.4m

After several trial run, the model was found unable to simulate bend case for supercritical flow (test 4 and 5). The assumption of hydrostatic is invalid in bend region due to the eccentricity force, especially for supercritical flow. The supercritical flow in test 3 (Fr = 1.2) reached steady state condition because of the formation of back water. The depth for back water was higher than critical depth, means that the flow after the jump should be considered subcritical flow. The following figures illustrate the simulated flow pattern for test case 1 and 3.

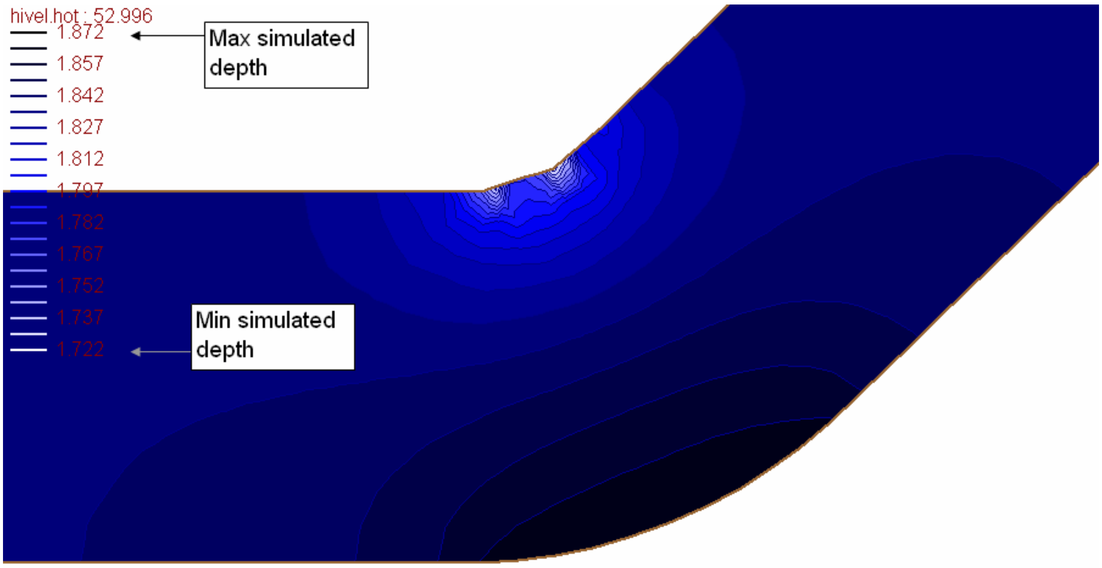

Figure 4.70(a) Water depth for Fr = 0.25 (bend)

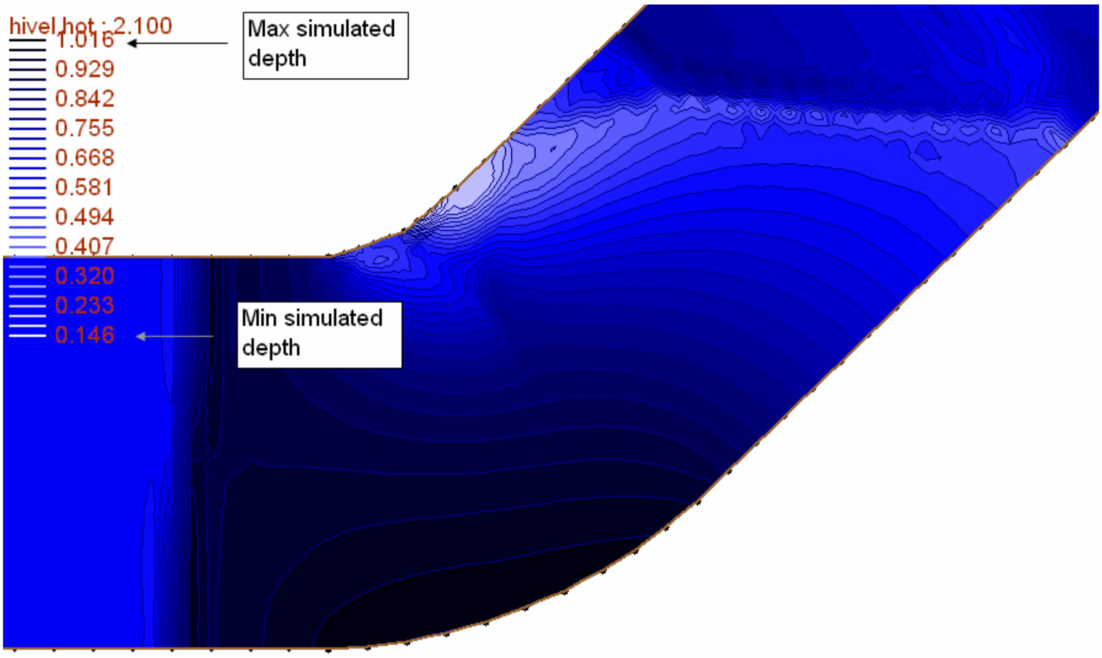

Figure 4.70(b) Water depth for Fr = 1.20 (bend)

Based on analytical solution described in chapter 3, the water depth difference between left bank and right bank for subcritical flow should be equal to V^2B/gR. This value should be doubled for supercritical flow (refer figure 3.28).

From figures 4.70(a) and 4.70(b), the difference water depth for test 1 and test 3 were 0.150m and 0.914m respectively. Meanwhile the average velocities were 1.140 m/s and 2.275 m/s for test 1 and 3. Other variables such as B (0.50 m), R (0.488m) and g (9.18 m/s^2) were constant. Using equation 3.7, the theoretical depth difference was calculated as shown below.

$$\Delta d = \frac{V^2 B}{gR} = \frac{1.14^2 \times 0.5}{9.81 \times 0.488} = 0.14m \text{ (subcritical flow)}$$

$$\Delta d = 2 \times \frac{V^2 B}{gR} = 2 \times \frac{2.275^2 \times 0.5}{9.81 \times 0.488} = 2 \times 0.54 = 1.08m \text{ (supercritical flow)}$$

For subcritical flow (Fr = 0.25), the theoretical depth difference was 0.14 m, which was quite close to simulated results. For supercritical flow (Fr = 1.20), the theoretical depth difference was equal to 0.914 m. According to Ippen and Knapp, the maximum difference depth between outer and inner walls for supercritical flow is about the twice of the difference for subcritical (Jain 2001). As a result, the theoretical depth difference became 1.08 m, which was 0.166 m different if compare to measured result.

In this test case, the results show the weakness of numerical model in handling supercritical flow in bending channel. The failures of test 4 and 5 were caused by the superelevation of surface flow at the bending region. The water depth decreased rapidly in a steep curvature and leaded to instabilities when the depth near inner wall became almost zero. This numerical model is unsuited to supercritical flow in bending region, particularly for an approaching Froude number in excess of 1.20. In fact, the relation between approaching Foude number and the bending angle is quite interesting to be investigated in future study.

CHAPTER 5

MODEL APPLICATION

The numerical model HIVEL2D was applied to two channels for case studies proposed by the Department of Irrigation and Drainage (DID, 2003). The two channels are Sg Segget near City of Johor Bahru and Sg Sepakat at Kampung Jaya Sepakat, Senai. These two channels have been frequently flooded during wet season. The channels improvement was contracted to consultants for better designs. Due to insufficient information on the design analysis, the information on the design analysis for the two case studies was provided by DID. In this study, a numerical model is used to evaluate the channel performance and to assess its practicality as an alternative tool at the design stage.

5.1 Model Application to Sg Segget, Johor Bahru

An upper section of Sg Segget, which is flowing into the tidal Sg Segget was selected for the application of the numerical model. It is located in the urbanized area of Johor Baharu City. Pictures of Sg Segget are shown in Figure 5.1. A numerical model of the Sg Segget is developed and simulation is conducted using ARI 100 year design event. Manning’s n of 0.02 was used in the simulation. Detailed calculation using empirical equations can be found in the report (Perunding Amin, 2004). The grid system constructed for the existing condition is shown in Figure 5.2. The channel bottom elevation contour of the Sg Segget is shown in Figure 5.3.

The channel was assumed to be rectangular section from the rubbish trap (downstream) to the upper section. About 40-meter closed rectangular culvert is found at the mid-section of the selected channel. A sudden drop of channel elevation approximately 0.3 m is found just after the culvert outlet. The downstream boundary of the channel is controlled by the rubbish trap structure. A discharge of 19.48 cms is specified at the upstream channel boundary. A tail water height of 2 m is specified at the downstream boundary (rubbish trap). Simulated water surface elevation contour profiles are shown in Figure 5.4. Backwater water surface profiles are observed due to the channel contraction, bend, and controlled structure (rubbish trap).

A modified section was proposed to improve the flow conditions in the channel section as shown in Figure 5.5. The grid system constructed for the existing condition is shown in Figure 5.6. Similar upstream and downstream conditions were specified at the boundaries as used in the existing condition. The water surface elevation profiles are shown in Figure 5.7. The results show that the numerical model can be used to analyze the water surface profiles in actual channel. The numerical model can provide an alternative tool to engineers for designing a high-velocity channel in urbanized area.

Figure 5.1(a): Pictures of Sg Segget Channel and Affected Areas

Figure 5.1(b): Pictures of Sg Segget Channel and Affected Areas

Figure 5.1(c): Pictures of Sg Segget Channel and Affected Areas

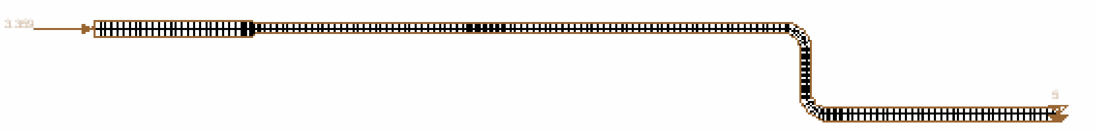

Figure 5.2 Grid System for Sg Segget Channel

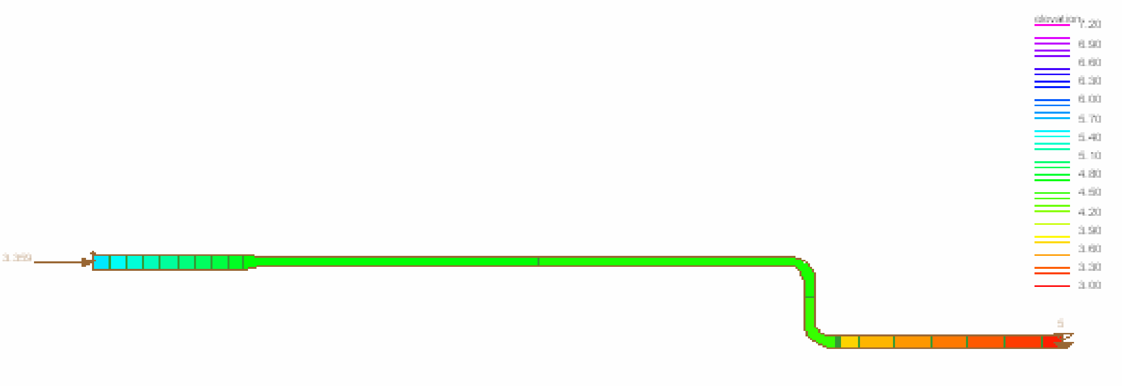

Figure 5.3 Bottom Channel Elevation Contour Profile for Channel

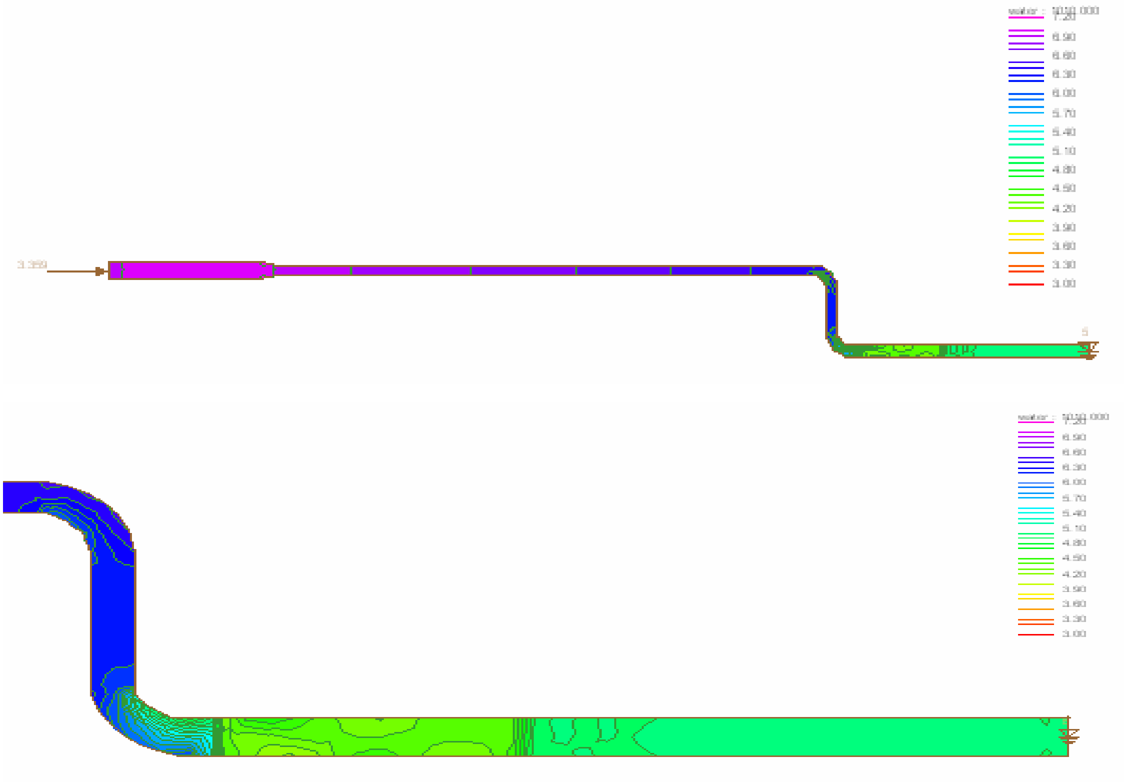

Figure 5.4 Water Surface Elevation Profiles Downstream of the Channel

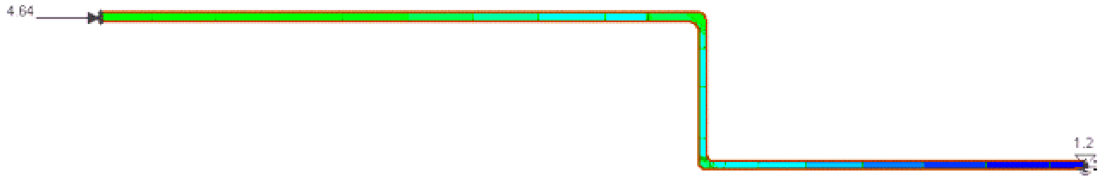

Figure 5.5 New Geometry for Improved Channel

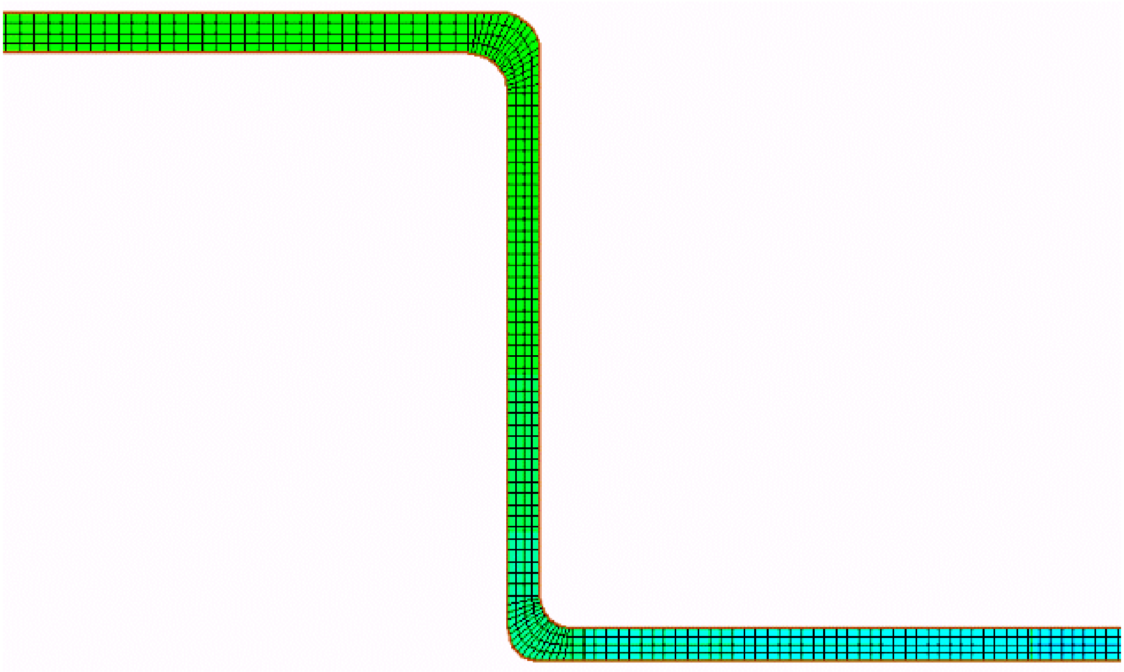

Figure 5.6 Water Surface Elevation Profiles for Improved Channel

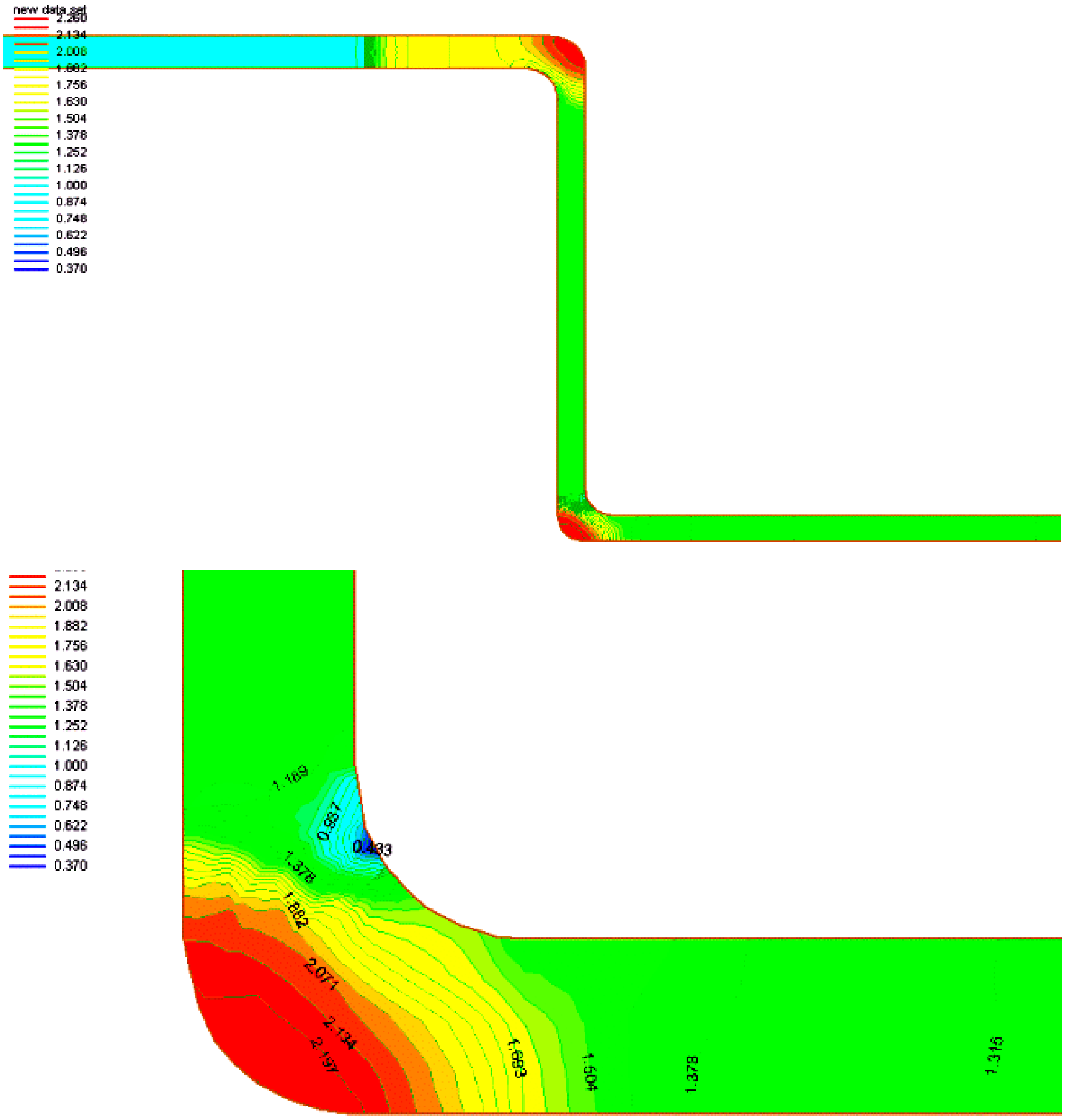

Figure 5.7 Water Surface Elevation Profiles for Improved Channel

5.2 Model Application to Sg Sepakat, Senai

The second case study is Sg Jaya Sepakat, Senai which a tributary of Sg Skudai. The natural river frequently flooded the Kampung Jaya Sepakat and its surrounding areas during wet season. Based on the information gathered from the villagers, major floods occurred in year 1997 and 2000. The pictures showing one of the natural river sections during one of the flood events (year 2000) is shown in Figure 5.8. During this study, the natural sections were replaced with pre-cast U-shaped concrete as shown in Figure 5.9. Uneven section which is a sudden contraction to the channel was found as shown in Figure 5.10. The water profiles in the channel just after rain event is shown in 5.11. As clearly illustrated in the figure, the water level is below 0.5 m from the channel top level. The condition of the channel in year 2004 is shown in Figure 5.12. Plant and aquatic growth and sediment are beginning to reduce the flow capacity of the channel.

Based on the DID design analysis, analytical solution and numerical simulation design analysis conducted by Shaharidam (2005), the flow capacity of the channel is 72.30, 39.01, and 45.10 m^3/s, respectively. Comparison of design analysis is described in detail by Shaharidam (2005). In this section, a numerical model simulation was conducted using field data for model calibration and model design flow application.

To calibrate the model, a field flow data $Q= 0.209\ m^3/s$ or $q= 0.0443\ m^3/s/m$ was used and a tailwater was set at h= 0.0964 m. Several Manning’s n was used for model calibration and the n value of 0.02 is considered suitable for the channel. The grid system and simulated water profile is shown in Figure 5.13. The detail water profiles at point A and B are shown in Figure 5.14 and 5.15, respectively. As illustrated in the figures, the water profiles vary from one point to point due to bends and side wall and channel bottom friction. The maximum water depth in channel is just 0.106 m while the minimum water depth is 0.097 m. No back water occurs in the channel due to low flow is introduced in the channel.

After the model calibration, several flows were used to evaluate the channel capacity. It was found the DID design flow capacity is not appropriate for the constructed concrete channel. Based on the design analysis using the numerical model, the maximum allowable flow capacity for the channel is 45.10 m^3/s. The computed water surface profiles using $Q= 45.10\ m^3/s$ ($q= 7.49\ m^3/s/m$) is shown in Figures 5.16, 5.17, and 5.18. As illustrated in Figure 5.17, the first bend in the channel is the model critical point which produced a water height of 2.66 m and overtopped the channel height. Backwater is produced in the channel due to channel bend.

Figure 5.8: The natural river is flooding in year 2000

Figure 5.9: The critical sections were replaced with pre-cast concrete channels

Figure 5.10: Uneven sections during construction which can cause sudden contraction

Figure 5.11: The water profiles in the channel just after rain event in year 2003.

Figure 5.12: The condition of the concrete channel in year 2004.

Figure 5.13: Aquatic growth and sedimentation in the channel

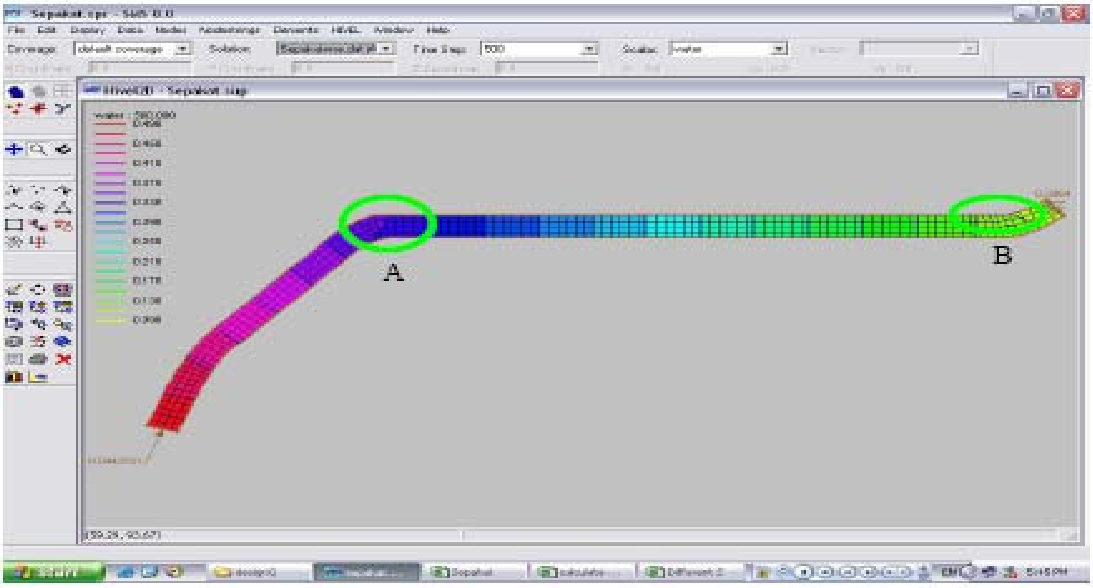

Figure 5.13: Grid System and Computed Water Profiles

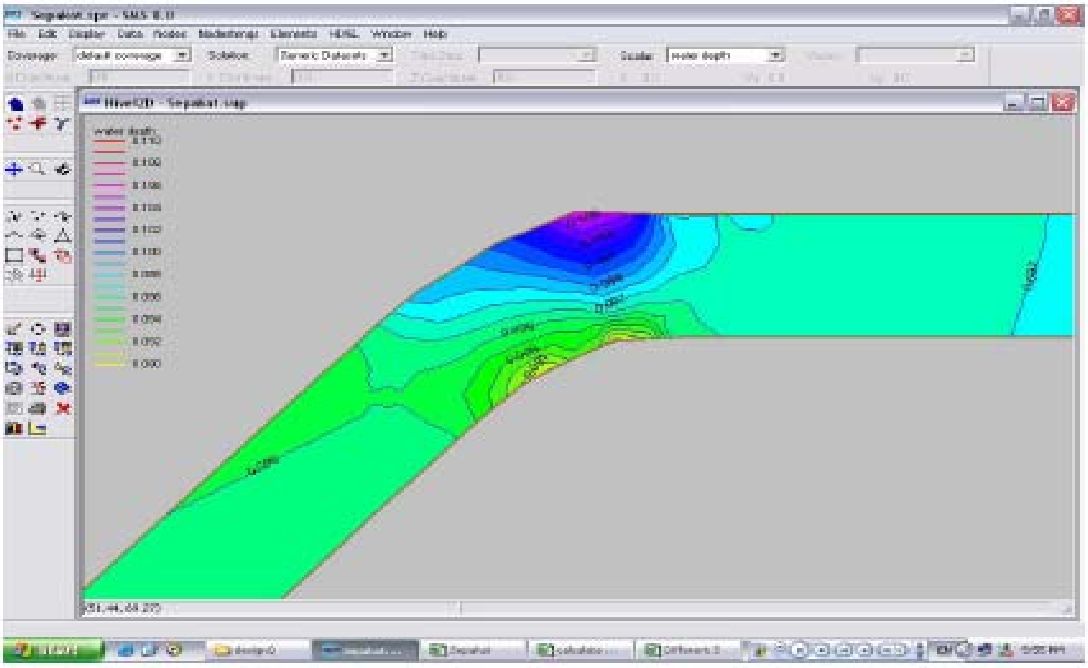

Figure 5.14: Computed Water Depth Profiles at Point A

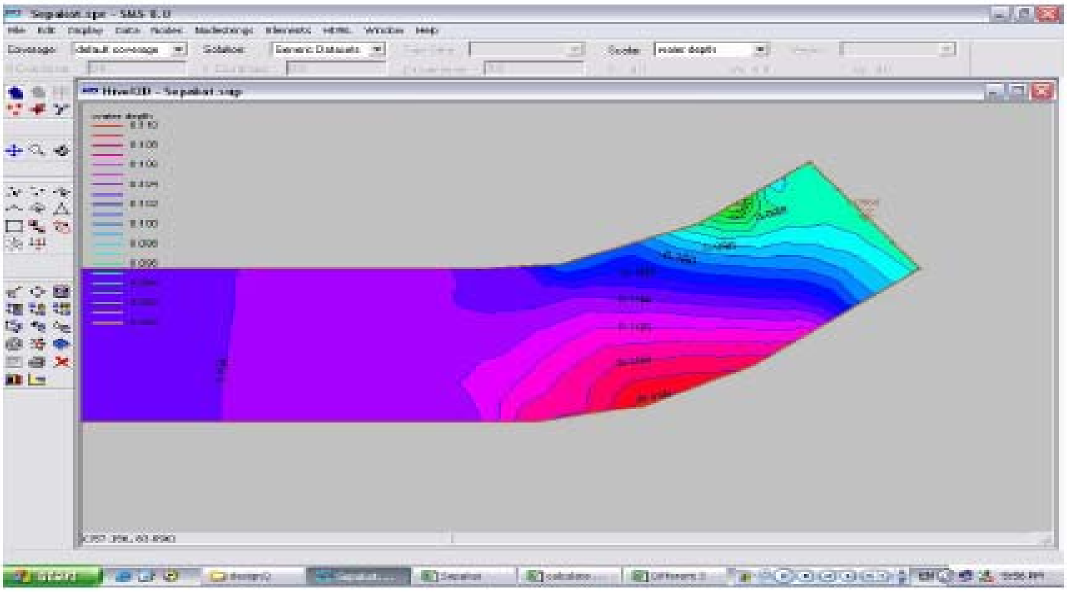

Figure 5.15: Computed Water Depth Profiles at Point B

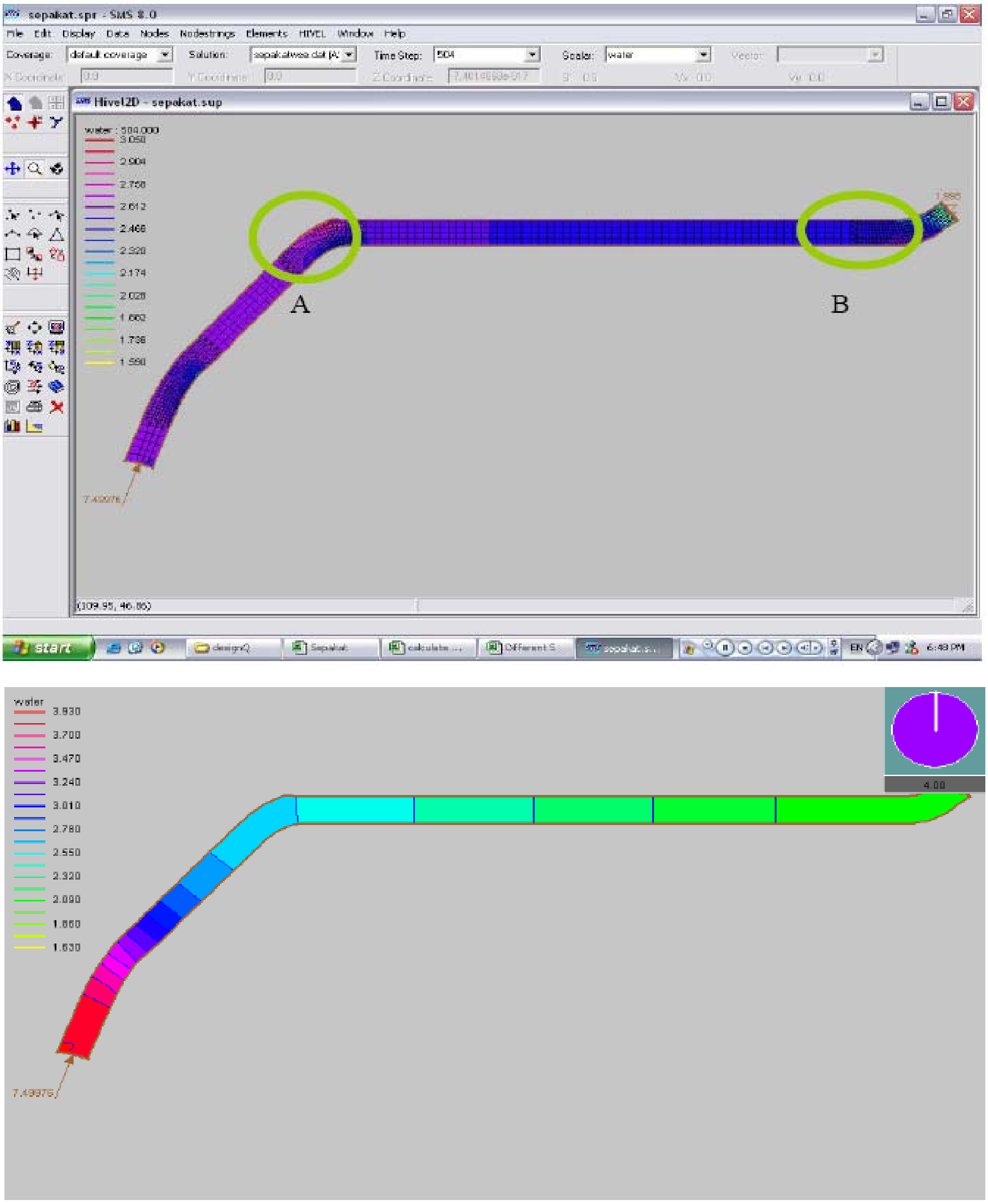

Coverage: default coverage

Solution: sepakatwse.dat

Time Step: 504

Scalar: water

Figure 5.16: Simulated Water Profiles for Q= 45.10 m^3/s

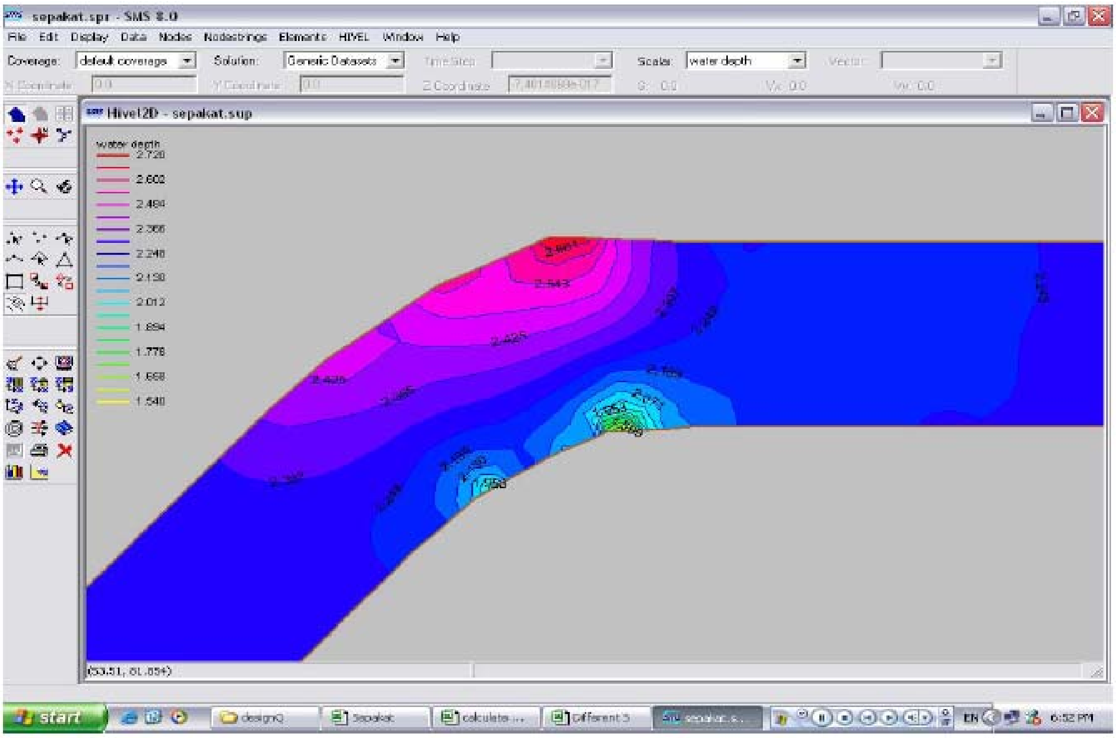

Coverage: default coverage
Solution: Generic Datasets
Scalar: water depth

(53.51, 81.854)

Figure 5.17: Computed Water Depth Profiles at Point A using Q= 49.1 m^3/s.

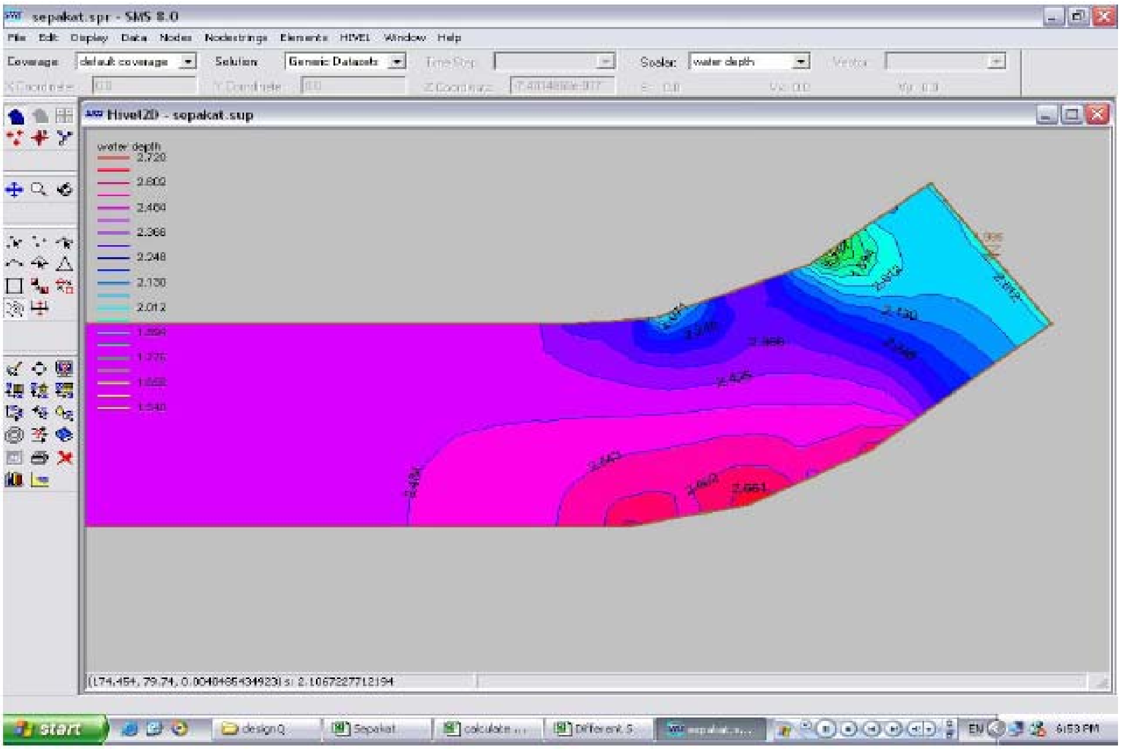

Coverage: default coverage
Solution: Generic Datasets
Scalar: water depth

(174.454, 79.74, 0.0040485434923) s: 2.1067227712194

Figure 5.18: Computed Water Depth Profiles at Point A using Q= 49.1 m^3/s.

CHAPTER 6

DISCUSSION AND CONCLUSION

6.1 Model Performance

This study demonstrated the ability of the numerical model introduced by Berger in various test cases. The overall results show good simulation performance in water depth and flow pattern. Since the numerical model was developed base on shallow water equations, the model was imposed by the assumptions incorporated in the governing equations. A few limitations were investigated.

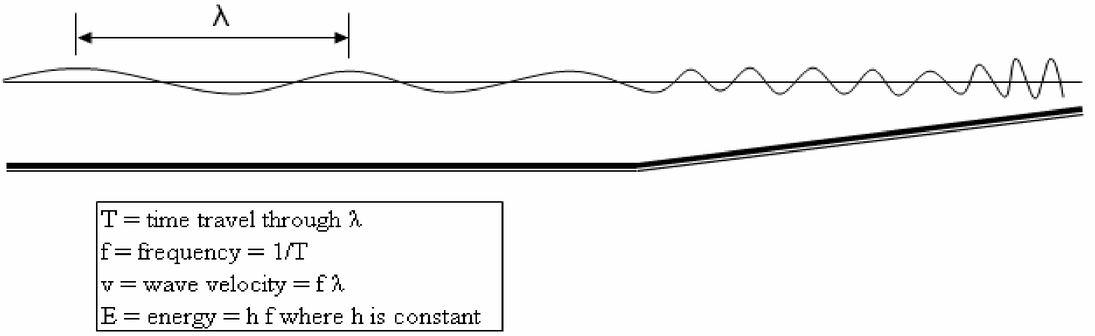

Figure 6.1 Wave (side view)

Referring to figure 6.1, the wave velocity is proportional to λ. Since the frequency is always constant along the flow, the short wave with shorter λ will travel slower than long wave. But the shallow water equations will transport all wave lengths at the speed of a long wave, as reported by Berger (1995). As a result, the numerical model was found tends to overestimate the velocity as clearly shown in normal depth test case. For the same reason, all simulated wavefront in contraction and expansion test cases were located further downstream than the computed location.

Another important finding is that the energy in numerical model was dissipated too fast within one or two elements, which was proved in hydraulic jump and pier test cases (the first test case in triangular nose of pier). In other word, the length of jump is unable to be predicted by this model. Since the model dissipates energy within one or two elements, the grid resolution becomes very important to determine the length of hydraulic jump.

Vertical motion is always neglected in shallow water equations. This assumption's effect is apparent in bridge pier test cases where the hydrostatic assumption was not valid in run up region. Numerical model cannot predict the run up accurately, resulting the weak prediction for the shock location downstream of the pier. However, numerical model manages to capture the diamond shape of flow downstream of the pier. Some tiny shock waves (in "Z" shape), formed after the expansion or contraction, were successfully addressed by model.

Besides, the numerical model failed to simulate 45 degree bend test case for supercritical flow. The model halted when the water depth was extremely shallow near the inner wall. The same problem was found in gradual contraction test cases (Froude number = 6.0). This finding is not surprising because the hydrostatic assumption was invalid in bend due to eccentricity force. However, numerical model still shows its good performance for subcritical flow.

The dissipation coefficient, β which introduced by Berger in shock-detection mechanism is not showing its significant effect to model simulation. This was proved in normal depth and hydraulic jump test cases. Only minor effect was found after several test cases.

However, this study presents the powerful simulation of this numerical model in handling two-dimensional hydraulic problem such as expansion, contraction, channel junction and bridge pier. The best evidence of this explanation was shown in the weir experiment, where the “V” shape flow was captured accurately. In the engineering viewpoint, the model performs well because it manages to reproduce the maximum water depth for most of the test cases.

This study also demonstrates the application of the model in flow evaluation and theory validation. This numerical model is suitable to be used to assess the design computationally before construction of the open channel. Using a numerical model would accelerate this design process and reduce the time spent on the design stage.

The application of this numerical model in real world is possible, especially for large scale channel such as high velocity channel. Nevertheless, it is not suitable for small open channel. Factors such as sediments (affect the bed condition of channel) will cause disturbance to the numerical results. The real slope condition in site is not easy to be measured. Other disturbance factors such as the small inflow or surcharge along the channel and inconsistent of roughness will lead to error. In other word, application model in real world only provides approximate prediction. However, the results along with engineering judgement can be used to explore and determine the critical region in a problem channel.

6.2 **Modelling**

In modelling, the geometry of flume, the types of material (roughness), the boundary conditions and initial condition are the most important input. Any mistake found in these inputs will lead to instabilities of solution.

Geometry in x and y axis seldom give problem except for bending test case. It is not easy to draw a smooth curve in the model. If the length of element is too large in bending region, the bend test case would become gradual contraction test case. But if too small, it will influence the stability of model. For bed level in z direction, the measured bed condition in reality should be applied. However, it is not easy to collect the level in real channel. Note that during construction in site, the built channel is always different with the designed slope gradient.

Roughness, which is indicated by Manning's *n* is another important parameter in model simulation. This parameter has significant effect in determining the shock location especially for hydraulic jump test case. For any channel/flume, this parameter is impossible to be measured. This value can only be determined approximately within a possible range. Furthermore, the *n* value can be kept changing in a tested channel depending on the flow condition. Thus, simulated result only provides approximate prediction for engineering judgement.

Besides, the boundary conditions are required before running the model. Sometimes, it is difficult to determine this boundary condition especially for downstream boundary. However, it doesn't give any difficulty for laboratory test because it can be measured during experiment. But great care must be taken for initial condition. Sometimes, modification is needed for certain initial condition such as dry bed condition. A good guess to the initial depth can reduce the computed time and gives more accurate results. But this requires experience. Keep in mind that initial condition should be applied carefully if the main interest is unsteady flow.

The mesh grid also plays an essential role in modelling. Basically, finer resolution provides better result compared to coarse grid, but it will increase the computation time. A good practice is that, always start with coarse grid as a trial run, and then refine the grids in critical regions till the results no longer change with the grid resolution. The time step should be small enough in the beginning, and then increased at the half run. By this way, optimum simulated results can be obtained within the 'economic' time. However, if the time step or element's size is too small, noise may occur in model due to instabilities of model.

6.3 Experimental Work

A lot of data for the tested flume were obtained through various experiments and measurements. Those data include the determination of flow rate, bed condition (longitudinally and laterally), roughness, water depths and flow pattern. Among all the experiments, it should be concluded that the control test is the most important part for experimental work because it provides basic and important information.

Before starting any experiment in a laboratory, it should be designed first by using analytical solution. This preparation not only can provide an overall view or direction for the study, but it can greatly save the time and cost. Measured results should be double checked with the expected results to reduce the error that caused by human. By this way, any error occurs in the experiment can be detected immediately and correction can be made. During the experiment, difficulty in water depth measurement was found. It is difficult to measure the height for shock wave and also the oscillation. Perhaps, the close-range digital photogrammetry technique can be used to solve this problem. This technique can freeze the flow condition such as hydraulic jump and run up, making the result comparison becomes more accurate. Further study on the application of photogrammetry in water depth measurement is expected.

As discussed in chapter 4, the roughness of flume always becomes the main problem because it is impossible to be measured. Through control test experiment, only a range of approximate values for Manning's n can be obtained. Since the roughness gives significant effect to the shock location in modelling, it should be treated seriously.

6.4 Conclusion

The performance of numerical model in handling shock capturing in various test cases through comparison with published results, laboratory tests and analytical solutions was carried out through this study. Several features commonly found in open channel were included in the test cases, which consist of weir, expansion, contraction, hydraulic jump, junction, bridge pier, gradual contraction and bend. This series of tests demonstrated the capability of model in open channel flow simulation to supply engineering decision makers with a tool to evaluate hydraulic problems. This model is limited by the assumptions of shallow water equations. In addition, the investigations have been limited to problems involving rectangular channels only.

Four experiments were conducted in laboratory to obtain a complete set of data for model simulation. In comparison with these experimental results, determination of roughness becomes the main problem. For many cases, the disagreement between model and experiment was caused by roughness coefficient, especially the hydraulic jump test case.

Overall results show that this numerical model is able to capture two-dimensional flow patterns including the tiny shock wave such as diamond shape flow. It has been proved suitable to be used for verifying some theoretical finding. Besides, the application of model was further extended to flow evaluation for many test cases. As proved in the study, the energy in the model is dissipated too fast and the short wave in the model tends to travel faster. The present model is not suitable for any surface flow that has steep gradients due to assumption of hydrostatic pressure distribution. This research should be further extended to more complicate test cases before fully applied in real site problem in the future.

UTM/RMC//F/0014(1998)

UNIVERSITI TEKNOLOGI MALAYSIA

Pusat Penyelidikan & Pembangunan

PRELIMINARY IP SCREENING & TECHNOLOGY ASSESSMENT FORM

(To be complete by Project Leader for submission of Final Report to RMC or whenever
IP protection arrangement is required)

1. **PROJECT TITLE IDENTIFICATION :**

Performance of High-Velocity Channels in Flood-Prone Areas

Vote No. 71840

2. **PROJECT LEADER :**

Name : Dr. Noor Baharim Hashim

Address : Dept. of Hydraulics & Hydrology, Faculty of Civil Engineering,
Universiti Teknologi Malaysia, 81310 Skudai, Johor

Tel : 07-5531511 Fax : 07-5566157 E-mail : baharim@fka.utm.my

3. **DIRECT OUTPUT OF PROJECT** *(Please tick whwrw applicable)*

Scientific Research	Applied Research	Product/Process Development
☐ Algorithm	☐ Method/Technique	☐ Product/Component
☐ Structure	☐ Demonstration/Prototype	☐ Process
☐ Data	☐ Other,please specify	☐ Software
☐ Other, please specify		☐ Other,please specify
	Evaluation of numerical model_and channel design	

4. **INTELLECTUAL PROPERTY** *(Please tick where applicable)*

☐ Not patentable

☐ Patent search required

☐ Patent search completed and clean

☐ Invention remains confidential

☐ No publications pending

☐ No prior claims to the technology

☐ Technology Protected by patents

☐ Patent pending

☐ Monograph available

☐ Inventor technology champion

☐ Inventor team player

☐ Industrial partner identified

5. TECHNICAL DESCRIPTION AND PERSPECTIVE

Please provide an executive summary of the new technology product, process, etc., describing how it works. Include brief analysis that compares it with competitive technologies and signals the one that it may replace. Identify potential technology user group and the strategic means for exploitation.

a) Technology Description

The study demonstrates the applicability of using two-dimensional numerical model to design and evaluate the performance of high-velocity (supercritical flow) concrete channel in urban areas. The model was tested in various channel test cases such as bend, contraction, weir, junction, and hydraulic jump. Previous flume experimental works, analytical solutions, and numerical simulations were used as comparison. Detailed and various experiments can be conducted by using the model. The techniques and methods used are complex and require highly skilled and post-graduate level modelers in computational engineering.

b) Market Potential

The experimental works and numerical flow simulation studies provide significant information on the capability of the models. The findings support the use of the model for initial and final design of major hydraulic structures which can reduce the cost of physical model construction. Research hydraulic institute, consultants and practicing engineers may benefit from these findings and experience.

c) Commercialisation Strategies

The study is only focusing on evaluating newly developed numerical model. The model is still under development by US Army Corps of Engineers. However, the researches and students were exposed to the numerical techniques of the model.

Signature of Project Leader : ……………… Date : ……………………...

6.0 RESEARCH PERFORMANCE EVALUATION

a) FACULTY RESEARCH COORDINATOR

Research Status	[ ]	[ ]	[ ]	[ ]	[ ]	[ ]
Spending	[ ]	[ ]	[ ]	[ ]	[ ]	[ ]
Overall Status	[ ]	[ ]	[ ]	[ ]	[ ]	[ ]
	Excelent	Very Good	Good	Satisfactory	Fair	Weak

Comment/Recommendations :

……………………………………

Signature and stamp of
JKPP Chairman

Name : …………………………………………………...

Date : …………………………….

b) UPP EVALUATION

Research Status	[ ]	[ ]	[ ]	[ ]	[ ]	[ ]
Spending	[ ]	[ ]	[ ]	[ ]	[ ]	[ ]
Overall Status	[ ]	[ ]	[ ]	[ ]	[ ]	[ ]
	Excelent	Very Good	Good	Satisfactory	Fair	Weak

Comment :

Recommendations :

☐ Needs further research

☐ Patent application recommended

☐ Market without patent

☐ No tangible product. Report to be filed as reference

……………………………………………. Name : …………………………………

Signature and stamp of Dean/Deputy Dean Date : ……………………….

Research Management Centre

APPENDIX A

Slope Checking

	water depth (mm)			
x (mm)	**S = 1/65**	**S = 1/150**	**S = 1/500**	**S = 1/1500**
600	19.0	81	102	25
1100	23.5	82	101	23.5
1600	30.0	84	102	23.5
2100	35.5	87	100	24
2600	42.5	90	100	24
3100	46.0	91	98	22
3600	52.5	93	99	22
4100	61.0	99	101	23.5
4600	68.0	103	102	24.5
5100	75.0	107	105	26
5600	83.0	112	106	27.5
6100	90.0	115	107	28.5
6600	97.0	118	106	28.5
7100	103.0	121	106	28.5
7600	110.0	123	107	28.5
8100	116.5	126	107	29
8600	123.0	129	106	29.5
9100	131.0	132	107	30.5
9600	137.0	134	108	30.5
10100	145.0	138	108	32
10600	152.5	142	109	33
11100	161.0	147	111	35.5
11600	168.5	150	113	36.5
12100	177.5	157	116	39.5
12600	183.0	158	117	39.5
13100	192.0	164	118	42
13600	200.0	171	122	43.5
14100	209.0	177	126	46
14600	217.0	182	128	48

Check bed condition laterally

S=1:500	water depth(mm)	
***x* (mm)**	**right wall**	**left wall**
600	25.0	25.0
1100	23.5	26.0
1600	23.5	24.0
2100	24.0	23.5
2600	24.0	23.5
3100	22.0	22.5
3600	22.0	23.0
4100	23.5	24.5
4600	24.5	25.0
5100	26.0	26.0
5600	27.5	27.5
6100	28.5	28.0
6600	28.5	27.5
7100	28.5	28.5
7600	28.5	28.0
8100	29.0	28.0
8600	29.5	29.0
9100	30.5	30.5
9600	30.5	31.5
10100	32.0	32.0
10600	33.0	33.0
11100	35.5	34.0
11600	36.5	35.0
12100	39.5	39.0
12600	39.5	41.0
13100	42.0	43.0
13600	43.5	43.5
14100	46.0	47.0
14600	48.0	49.0

Example Control test

	water depth (mm)		
***x* (mm)**	**1.0 round**	**1.5 rounds**	**2.0 rounds**
600	41.5	70.0	101.0
1100	39.5	68.0	98.0
1600	38.0	66.0	96.0
2100	38.0	65.0	94.5
2600	36.5	64.0	93.0
3100	32.0	59.0	88.0
3600	31.5	58.5	86.5
4100	32.0	59.0	88.0
4600	32.5	58.5	88.5
5100	33.5	58.5	88.0
5600	35.0	60.5	88.5
6100	35.5	62.0	88.5
6600	35.5	60.5	88.5
7100	34.5	59.0	86.5
7600	34.0	57.5	85.5
8100	33.0	57.0	84.0
8600	32.0	56.0	82.0
9100	31.0	55.0	81.0
9600	29.0	51.5	77.5
10100	29.5	50.0	75.5
10600	27.0	50.0	72.0
11100	27.0	47.0	70.0
11600	27.0	47.0	70.0
12100	27.0	48.0	70.0
12600	26.0	44.0	66.5
13100	24.0	44.0	66.0
13600	23.0	43.5	77.0
14100	28.5	53.0	82.0
14600	32.0	57.0	86.0

Weir experiment

	measured depth (mm)	
x **(mm)**	**right wall**	**left wall**
600	28	-
1100	36	36
1600	34	35
2100	34	34
2600	33.5	33.5
3100	32	30.5
3600	30.5	30
4100	29.5	30
4600	30	29.5
5100	31	30.5
5600	30.5	30.5
6100	29	29
6600	30.5	30
7100	29.5	29.5
7600	29	29
8100	49	48.5
8600	40	40
9100	27	26
9600	31	29.5
10100	28	28.5
10600	31	30
11100	28	29
11600	29.5	29
12100	30	29.5
12600	26.5	27.5
13100	27	27.5
13600	28	27
14100	27	27
14600	26.5	27

x **(mm)**	***y*** **(mm)**	**depth (mm)**
7600	115	26
7600	230	28
7600	340	28
7980	115	26
7980	230	28
7980	340	28
8100	115	37
8100	230	37
8100	340	35
8220	115	38
8220	230	34
8220	340	40
8340	115	31
8340	230	38
8340	340	33
8460	115	33
8460	230	37
8460	340	31
8600	115	27
8600	230	19
8600	340	27
8720	115	27
8720	230	26
8720	340	27
8840	115	24
8840	230	28
8840	340	25
8960	115	28
8960	230	24
8960	340	29

x **(mm)**	***y*** **(mm)**	**depth (mm)**
9100	115	27
9100	230	28
9100	340	30
9600	115	28
9600	230	27
9600	340	27
9770	115	26
9770	230	26
9770	340	26
10100	115	29
10100	230	30
10100	340	30
10600	115	31
10600	230	29
10600	340	30
11100	115	29
11100	230	30
11100	340	29
11600	115	28.5
11600	230	29.5
11600	340	28

Contraction and 90 degree expansion experiment

	measured depth (mm)	
x **(mm)**	**right wall**	**left wall**
600	35	-
1100	35	36
1600	31	36
2100	32	33
2600	32	33
3100	30	30
3600	30	32
4100	29	31
4600	29.5	31
5100	31.5	30
5600	31	31
6100	30	34
6600	31	29
7100	30	30
7600	31	31
8100	33	40
8600	32.5	-
9100	49	-
9600	50	-
10100	50	-
10600	42	-
11100	47	-
11600	35	37
12100	28	36
12600	24	38
13100	34	27.5
13600	31	29
14100	27	33
14600	31	32

x **(mm)**	***y*** **(mm)**	**depth (mm)**
8350	340	38
8350	230	33
8350	50	30
8600	340	40
8600	230	38
8600	50	36
8800	340	38
8800	230	39
8800	115	39
9000	300	39
9000	160	45
9000	50	44
9100	270	44
9100	160	48
9100	50	45
9200	270	48
9200	160	47
9200	50	53
9600	270	46
9600	160	43
9600	50	48
9870	270	47
9870	160	44
9870	50	41
10100	270	40
10100	160	40
10100	50	42
10600	270	43
10600	160	36
10600	50	38
11100	270	32
11100	160	35
11100	50	39
11230	400	4
11230	250	38
11230	115	41
11450	400	13
11450	220	33
11450	115	36
11600	400	28
11600	220	25
11600	115	32
12100	340	32
12100	220	30
12100	115	22

x **(mm)**	***y*** **(mm)**	**depth (mm)**
12600	340	27
12600	230	27
12600	115	24
12900	340	24
12900	230	24
12900	115	35
13100	340	22
13100	230	25
13100	115	28
13600	340	28
13600	230	28
13600	115	30
13930	340	35
13930	230	29
13930	115	27
14600	340	25
14600	230	28
14600	115	23
11130	457	6
11130	335	34
11130	0	43
9230	335	55
9230	0	48
11600	340	16
12430	125	31
12400	50	18
12400	340	31
13000	115	35
13000	340	25

Hydraulic jump experiment

	measured depth (mm)	
***x* (mm)**	**right wall**	**left wall**
600	34.5	-
1100	33.5	32.5
1600	31.5	35?
2100	32.5	31.5
2600	30.5	31.5
3100	27	30
3600	30	30.5
4100	28.5	30.5
4600	29	30
5100	31.5	29.5
5600	30	30.5
6100	30	33
6600	50±5	50±5
7100	65±5	62±4
7600	71±5	71±5
8100	80±5	77±2
8600	87.5±2.5	87±3
9100	96±4	95±2
9600	102±3	104±2
10100	110±3	112±3
10600	115±3	118±4
11100	124±3	125±4
11600	130±3	130±2
12100	137±3	139±3
12600	146±3	147±2
13100	152±2	155±2
13600	160±2	166±2
14100	168±2	168±2
14600	175±1	176±1

***x* (mm)**	***y* (mm)**	**depth (mm)**
6500	100	29
6500	230	31
6500	430	47
6600	230	32-40
6600	400	51
6700	50	57
6700	230	80±5
6700	350	57
6800	50	53-61
6800	230	52-70
6800	350	56
6900	50	54
6900	170	45
6900	350	55
7000	100	55-70
7000	170	48-78
7000	350	58
7100	50	65
7100	170	75-80
7100	350	64-58
7280	50	60
7280	230	53
7280	350	61
7500	50	69
7500	170	75-65
7500	350	67
7800	50	66-80
7800	230	70-80
7800	350	72
8350	50	83
8350	230	75-90
8350	350	83

Example data for Bridge pier experiment

	measured depth (mm)	
***x* (mm)**	**right wall**	**left wall**
600	35	-
1100	34	37
1600	31	35
2100	32	32
2600	31	32
3100	28	31
3600	29	31
4100	29	31
4600	29	30
5100	32	30
5600	30	30
6100	50	50
6600	68	67
7100	41	37
7600	21	21
8100	35	31
8600	40	39
9100	31	33
9600	27	31
10100	33	34
10600	30	31
11100	32	32
11600	31	32
12100	31	33
12600	30	32
13100	30	32
13600	30	31
14100	30	30
14600	30	30

***x* (mm)**	***y* (mm)**	**depth (mm)**
5900	110	29
5900	230	30
5900	340	31
6100	50	48
6100	300	33
6100	400	49
6200	50	59
6200	230	80
6200	340	60
6200	400	55
6400	50	61
6400	110	56
6400	230	48
6400	340	55
6400	400	61
6550	50	68
6550	110	74
6550	230	92
6550	340	71
6550	400	64
6650	0	70
6650	40	65
6650	180	64
6650	right face	75
6650	left face	73
6650	300	62
6650	340	62
6650	400	66
6800	0	62
6800	50	60
6800	160	39
6800	300	35
6800	400	58
6900	0	51
6900	50	47
6900	160	55
6900	300	49
6900	400	46
7030	40	41
7030	160	51
7030	300	51
7030	400	38
7100	50	43
7100	170	20
7100	260	19

***x* (mm)**	***y* (mm)**	**depth (mm)**
7100	400	35
7200	0	47
7200	50	38
7200	190	19
7200	230	36
7200	260	19
7200	400	39
7500	80	22
7500	150	44
7500	230	35
7500	320	41
7500	380	25
7700	0	45
7700	110	28
7700	230	134
7700	340	29
7900	50	34
7900	230	25
7900	400	37
8100	110	28
8100	230	35
8100	340	28
8180	110	29
8180	230	45
8180	340	30
8600	110	27
8600	230	33
8600	340	28
8800	110	35
8800	230	28
8800	340	35
9100	110	31
9100	230	32
9100	340	31

APPENDIX B

Governing Equations

Vertical integration of the three-dimensional equations of mass and momentum conservation for incompressible flow with the assumption that vertical velocities and accelerations are negligible compared to horizontal motions and the acceleration of gravity results in the governing equations commonly referred to as the shallow-water equations. The dependent variables of the two-dimensional fluid motion are defined by the flow depth h, the x-direction component of unit discharge p, and the y-direction component of unit discharge q. These variables are functions of the independent variables x and y, the two space directions, and time t. Neglecting free-surface stresses and the effects of Coriolis force as these are not considered important in high-velocity channels, the shallow-water equations in conservative form are given as (Abbot, 1979; Praagman, 1979):

$$\frac{\partial h}{\partial t}+\frac{\partial p}{\partial x}+\frac{\partial q}{\partial y}=0$$

(A1)

for the conservation of mass. Conservation of momentum in the x-direction and y-direction are given respectively as:

$$\frac{\partial p}{\partial t}+\frac{\partial}{\partial x}\left(\frac{p2}{h}+\frac{1}{2}gh2-h\sigma xx\right)+\frac{\partial}{\partial y}\left(\frac{pq}{h}-h\sigma xy\right)=-gh\frac{\partial z}{\partial x}+g\frac{n2p\sqrt{p2+q2}}{Coh7/3}$$

(A2)

and

$$\frac{\partial q}{\partial t}+\frac{\partial}{\partial x}\left(\frac{q2}{h}+\frac{1}{2}gh2-h\sigma yy\right)+\frac{\partial}{\partial x}\left(\frac{pq}{h}-h\sigma yx\right)=-gh\frac{\partial z}{\partial y}+g\frac{n2q\sqrt{p2+q2}}{Coh7/3}$$

(A3)

where

g= acceleration of gravity

σ= Reynolds stresses per unit mass where the first subscript indicates the direction and the second indicates the face on which the stress acts

z= channel invert elevation

n= Manning’s roughness coefficient

Co= dimensional constant (Co=1 for SI units and 2.208 for non-SI units)

The governing equations are given in vector form as:

$$\frac{\partial Q}{\partial t}+\frac{\partial Fx}{\partial x}+\frac{\partial Fy}{\partial y}+H=0$$

(A4)

where

$$Q=\begin{pmatrix} h \\ p \\ q \end{pmatrix}$$

(A5)

$$Fx=\begin{pmatrix} p \\ \frac{p2}{h}+\frac{1}{2}gh2-h\sigma xx \\ \frac{pq}{h}-h\sigma yx \end{pmatrix}$$

(A6)

$$Fy = \begin{pmatrix} q \\ \frac{q2}{h} + \frac{1}{2} gh2 - h\sigma yy \\ \frac{pq}{h} - h\sigma xy \end{pmatrix}$$

(A7)

$$H = \begin{pmatrix} 0 \\ gh\frac{\partial z}{\partial x} - g\frac{n2p\sqrt{p2+q2}}{Co2h7/3} \\ gh\frac{\partial z}{\partial y} - g\frac{n2p\sqrt{p2+q2}}{Co2h7/3} \end{pmatrix}$$

(A8)

where

p=uh, u being the depth-averaged x-direction component of velocity

q= vh, v being the depth-averaged y-direction component of velocity

The individual terms in the conservation equations are as follows:

a. Acceleration force per unit width
b. Pressure force per unit width
c. Body forces per unit area
d. Bed shear stresses

The Reynolds stresses are determined using the Boussinesq approach of gradient-diffusion:

$$\sigma xx = 2vt\frac{\partial u}{\partial x}$$

$$\sigma xy = \sigma yx = vt\left(\frac{\partial u}{\partial y} + \frac{\partial v}{\partial x}\right)$$

(A9)

$$\sigma yy = 2vt\frac{\partial v}{\partial y}$$

where vt is the viscosity (sum of turbulent and molecular viscosity, commonly referred to as eddy viscosity), which varies spatially and is solved empirically as a function of local flow variables (Rodi, 1980; Chapman and Kuo, 1985):

$$Vt = Cb\sqrt{8g}\,\frac{n}{Co}\,\frac{\sqrt{p2+q2}}{h1/6}$$

(A10)

where Cb is a coefficient that varies between 0.1 and 1.0.

This system of equations constitutes a hyperbolic initial boundary value problem. Appropriate boundary conditions are determined using the approach of Daubert and Graffe as discussed in Drolet and Gray (1988) and Verboom, Stelling, and Officier (1982). Daubert and Graffe use the method of characteristics to determine the required boundary conditions. The number of boundary conditions is equal to the number of characteristic half-planes that originate exterior to the domain and enter it. If the inflow boundary is supercritical, then all information from outside the domain is carried through this boundary. Therefore, p and q (or u and v) and the depth h must be specified. If the inflow boundary is subcritical, then the depth is influenced from the flow inside the domain (downstream control) and therefore only p and q (or u and v) are specified. Outflow boundary conditions required are determined by analysis of information transported through this boundary. If the outflow boundary is supercritical, then all information is determined within the domain and no boundary conditions are specified. However, if the outflow boundary is subcritical, then the depth of flow at the boundary (tailwater) must be specified. The no-flux boundary condition is appropriate at the sidewall boundaries and is discussed in detail in Appendix B.

FINITE ELEMENT FORMULATION

A variation formulation of the governing equations involves finding a solution of the dependent variables Q using the test function Ψ over the domain Ω. The variation formulation of the shallow-water equations in integral form is:

$$\int_{\Omega} \Psi \left[\frac{\partial Q}{\partial t} + \frac{\partial F_x}{\partial x} + \frac{\partial F_y}{\partial y} + H \right] d\Omega = 0$$

(B1)

Where *t* is time and Q, F, F, and H are defined in Equations A5-A8.

The finite element approach taken is a Petrov-Galerkin formulation that incorporates a combination of the Galerkin test function and a non-Galerkin component to control oscillations due to convection. The finite element form of the governing equations is

$$\sum_{e} \left[\int_{e} \psi_i \left[\frac{\partial \bar{Q}}{\partial t} + \frac{\partial \bar{F}_x}{\partial x} + \frac{\partial \bar{F}_y}{\partial y} + \bar{H} \right] d\Omega_e \right]$$

(B2)

Where:

e = subscript indicating a particular element

i = subscript indicating a particular test function

~ = discrete value of the quantity

The geometry and flow variables are represented using the Lagrange basis Φ:

$$\overline{Q} = \sum_{j} \phi_j Q_j$$

(B3)

Where *j* is the nodal location. Bilinear triangular and quadrilateral elements are used with nodes at the element corners. Figure B1 show the two bilinear elements used in terms of local coordinates η and ξ.

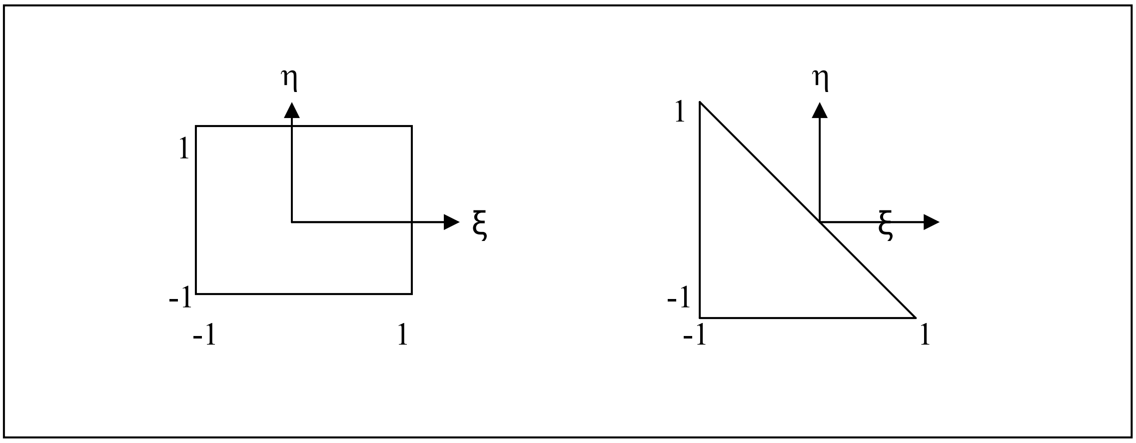

Figure B1. Local bilinear elements.

The test function used (to be elaborated in the next section) is:

$$\Psi_i = \phi_j \, I + \lambda_i$$

(B4)

Where

Φ = Galerkin part of the test function

I = Identity matrix

φ = non-Galerkin part of the test function

To facilitate the specification of boundary conditions, the weak form of the equations is developed using integration by parts procedure. Integration by pats of the terms.

$$\phi_i \frac{\partial F_x}{\partial x}$$

$$\phi \frac{\partial F_y}{\partial y}$$

(B5)

yields the weak form of the equations. The ~ is omitted for clarify and the variables are understood to be discrete values. The weak form is given as:

$$\sum_e \left[\int_e \left[\psi_i \frac{\partial \bar{Q}}{\partial t} + \frac{\partial \phi_i}{\partial x} F_x - \frac{\partial \phi_i}{\partial y} + \lambda_i \, A \frac{\partial Q}{\partial x} + \lambda_i B \frac{\partial Q}{\partial y} + \psi_i H \right] d\Omega_e + \oint_\tau \phi_i \left(F_x n_x + F_y n_y \right) \, dT_e \right]$$

(B

6)

where $(n_x, n_y) = \check{n}$ the unit vector outward normal to the boundary Γe and

$$A \equiv \frac{\partial F_x}{\partial Q}$$

$$B \equiv \frac{\partial F_y}{\partial Q}$$

(B7)

Natural boundary conditions are applied to the sidewall boundaries through the weak statement. The sidewall boundaries are "no flux" boundaries. That is there is no net flux of mass or momentum through these boundaries. This boundary condition is enforced in an average sense through the weak statement. Setting the mass flux through the sidewall boundary to zero:

$$\oint_{\tau} \left(pn_x + qn_y\right)\, dT = 0$$

(B8)

where:

p = x-direction component of unit discharge

q = y-direction component of unit discharge

There is no net momentum flux through the boundaries. Therefore, the x-direction momentum through the boundary is set to zero.

$$\oint_{\tau} \left[(up)n_x + (uq)n_y\right]\, dT = 0$$

(B9)

and the y- direction momentum through the boundary is set to zero:

$$\oint_{\tau} \left[(vp)n_x + (vq)n_y\right]\, dT = 0$$

(B10)

where:

u = p/h = depth averaged x-direction component of velocity.

V = q/h = the depth averaged y-direction component of velocity

H = the depth of flow.

Sidewall drag is treated as a partial slip condition. That is the boundary stress terms in the governing equations, integrated along the sidewall, are specified via the Manning relation:

$$-\int \phi_i \left(ho_{xx} n_x + ho_{xy} n_y \right) \; dT = \int \; \phi_i gp \frac{n^2}{C_0^2} \frac{\sqrt{p^2 + q^2}}{h^{4/3}} dT$$

(B11)

$$-\int \phi_i \left(ho_{yx} n_x + ho_{yy} n_y \right) \; dT = \int \; \phi_i gp \frac{n^2}{C_0^2} \frac{\sqrt{p^2 + q^2}}{h^{4/3}} dT$$

(B12)

Where

o_{xx} o_{xy} o_{yx} o_{yy} = Reynolds stress per unit mass where the first subscript indicates the direction and the second indicates the face on which the stress acts.

g = Acceleration of gravity

Co = Dimensional constant (Co = 1 for S1 units and 2.208 for non S1 units)

PETROV-GALERKIN TEST FUNCTION

For the shallow-water equations in conservative from (Equation B2), the Petrov-Galerkin test function φ is defined as (Berger 1993)

$$\lambda_i = \beta \left[\Delta x \frac{\partial \phi_i}{\partial x} \hat{A} + \Delta y \frac{\partial \phi_i}{\partial y} \hat{B} \right]$$

(B13)

Where β is a dimensionless number between 0 and 0.5 and Φ is the liner basin function. In the manner of Katopodes (1986) the grid intervals are chosen as:

$$\Lambda x = 2 \left[\left(\frac{\partial x}{\partial \xi} \right)^2 + \left(\frac{\partial x}{\partial \eta} \right)^2 \right]^{1/2}$$

(B14)

and

$$\Lambda y = 2 \left[\left(\frac{\partial y}{\partial \xi} \right)^2 + \left(\frac{\partial y}{\partial \eta} \right)^2 \right]^{1/2}$$

(B15)

where ξ and η) are the local coordinates defined from –1 to 1 (Figure B1).

To find Â consider the following:

$$A \equiv \frac{\partial F_x(Q)}{\partial Q}$$

(B16)

$$P^{-1} \Lambda P = A$$

(B17)

Where $\Lambda = I\lambda$ is the matrix of eigenvalues of A and P and P^{-1} are made of the right and left eigenvectors.

$$\overline{\overline{A}} \equiv P^{-1}\overline{\overline{\Lambda}}P$$

(B18)

where

$$\Lambda = \begin{bmatrix} \frac{\lambda^{1}}{(\lambda i^{2}+\lambda^{2})\ \frac{1}{2}} & 0 & 0 \\ 0 & \frac{\lambda^{1}}{(\lambda i^{2}+\lambda^{2})\ \frac{1}{2}} & 0 \\ 0 & 0 & \frac{\lambda^{1}}{(\lambda i^{2}+\lambda^{2})\ \frac{1}{2}} \end{bmatrix}$$

(B 19)

and

$$\lambda^{1} = u + c$$

(B20)

$$\lambda^{2} = u - c$$

(B21)

$$\lambda^{3} = u$$

(B22)

$$c = (gh)\frac{1}{2}$$

(B23)

A similar operation may perform to define $\hat{B}$.

This particular test function is weighted upstream along characteristic similar to a concept like that developed in the finite difference method of Courant, Isaacson and Rees (1952) for one-sided differences. These ideas were expanded to more general problems by Moretti (1979) and Gabutti (1983) as split-coefficient matrix methods and by the generalized flux vector splitting proposed by Steger and Warming (1981). In the finite element community, instead of one-sided differences the test function is weighted upstream. Thus particular method in one dimension (1-D) is equivalent to the SUPG (streamline upwind Petrov-Galerkin) scheme of Hughes and Brooks (1982) and similar to the form proposed by Dendy (1974). Examples of this approach in the open channel movement using the generalized shallow-water equations are presented for 1-D in Berger and Winant (1991) and for 2-D in Berger (1992) A 1-D Venant application is give by Hicks and Steffler (1992).

SHOCK CAPTURING

Berger (1993) shows that the Petrov-Galerkin scheme is not only a good scheme for advection-dominated flow, bit is also a good scheme for shock capturing because the scheme dissipates energy at the short wavelengths. When a shock is encounter, the weak solution of the shallow-water equations must lose mechanical energy. Some of this energy loss is analogous to a physical hydraulic system losing energy to heat, particle rotation, etc but much of it is in fact, simply the energy being transferred into vertical motion. And since vertical motion is not include in the shallow-water it is lost. This apparent energy loss can be advantages.

To apply high value of β say 0.5, only in regions in which it is needed, since a lower value is more precise, construct a trigger mechanism that can detect shocks and increase β automatically. The method employed detects energy variation for each element and flags those elements that have a high variation as needing larger value of β for shock capturing. Note that this variation on an element basis and the Galerkin method would enforce energy conversation over a test function (which includes several elements)

The shock capturing is implemented when Equation B24 is true

$$Ts_i > \chi$$

(B24)

where γ is a specified constant and

$$Ts_i = \frac{ED_i - \overline{E}}{S}$$

(B25)

where ED*i* the element energy deviation is calculated by

$$ED_i \frac{\left[\int \left(E - \overline{E}_i \right)^2 d\Omega\right]^{\frac{1}{2}}}{a^i}$$

(B26)

Where

Ω = element *i*

E = mechanical energy *i*

ạ = area of element *i*

and E the average energy of element *i* is calculated by

$$\overline{E}_i = \frac{\int E \ d\Omega}{a^i}$$

(B27)

and

$\overline{E}$ = the average element energy over the entire grid

S = the standards deviation of all ED*i*

Through trial a value of □ of 1.0 was chosen.

TEMPORAL ACTIVITIES

A finite difference expression is used for the temporal derivatives. The general expression for the temporal derivatives of a variable Q, is:

$$\left[\frac{\partial Q_j}{\partial t}\right]^{m+1} \approx \alpha\left[\frac{Q_j^{m+1} - Q_j^{m}}{t^{m-1} - t^{m}}\right] + (1-\alpha)\left[\frac{Q_j^{m} - Q_j^{m-1}}{t^{m} - t^{m-1}}\right]$$

(B28)

Where

α = temporal difference coefficient

j = nodal location

m = time-step

An α equal to 1 result in a first-order backward differences approximation and an equal α to equal to 1.5 results in a second-order backward difference approximation of the temporal derivative.

SOLUTION OF THE NONLINEAR EQUATIONS

The system of nonlinear equations is solved using the Newton-Raphson iterative method (Carnahan, Luther, and Wilkes 1969) Let R be a vector of the nonlinear equations computed using a particular test function Ψ and using as assumed value of Q. R is the residual error for a particular test function *i* Subsequently R is forced toward zero as:

$$\frac{\partial R_i^k}{\partial Q_j^k} \Delta q_j^k = -R_i^k$$

(B29)

where k is the literati on number j is the node location and the derivatives composing the Jacobian are determined analytical. This system of equations is solved for Δq_{kj} and then improved estimate for Q_{k+1} is obtained from:

$$Q_j^{k+1} = Q_j^k + \Delta q_j^k$$

(B30)

This procedure is continued until convergence to an acceptable residual error is obtained.

Equation B29 represents a system of linear algebraic equations that must be solved for each iteration and each time-step. A profile solver is implemented to achieve efficient coefficient matrix storage. This method stores the upper triangular portion of the coefficient matrix by columns and the lower by rows. Any zeros outside the profile are not stored or involved in the computations. The necessary arrays are then a vector composed of the columns of the upper portion and a pointer vector to locate the diagonal entries. Triangular decomposition of the coefficient matrix is used in a direct solution. The program a construct the triangular decomposition of the coefficient matrix uses a compact Crout variation of Gauss Elimination.

REFERENCES

Basco, D.R. (1987). “Introduction to rapidly-varied unsteady, free-surface flow computation.” USGS, Water Resourc. Invest. Report No. 83-4284, U.S. Geological Service, Reston, Va.

Berger, R. C., and Howington, S. E. (2002). *Discrete Fluxes and Mass Balance in Finite Element.* J. Hydr. Engrg., ASCE, 128(1), 87-92.

Berger, R.C., and Howington, S.E. (2002). *Discrete Fluxes and Mass Balance in Finite Elements.* J. Hydr. Engrg., ASCE, 128(1), 87-92.

Berger, R.C., and Stockstill, R.L. (1995). *Finite Element for High-Velocity Channels.* J. Hydr. Engrg., ASCE, 121(10), 710-716.

Berger, R.C. (1992). “Free-surface flow over curved surfaces,” PhD thesis, Dept. of Engrg. Mech., Univ. of Texas at Austin, Tex.

Bhallamudi, S.M., and Chaudhry, M.H.(1992). Computation of Flows in Open-channel Transitions, J. Hydraulic Research, Inter. Assoc. Hyd. Research, no. 1:77-93.

Borghei S. M., Jalili, M. R., and Ghodsian, M. (1999). *Discharge Coefficient for Sharp-crested Side Weir in Subcritical Flow.* J. Hydr. Engrg., ASCE, 125(10), 1051-1056.

Chaudhry M. H. (1993). Open-Channel Flow. Englewood Cliffs, N.J.:Prentice-Hall.

Fagherazzi, S., Rasetarinera, P., Hussaini, M. Y., and Furbish, D. J. (2004). *Numerical Solution of the Dam-break Problem with a Discontinuous Gelerkin Method.* J. Hydr. Engrg., ASCE, 130(6), 532-539.

Ghamry, H. K., and Steffler, P. M. (2002). *Effect of Applying Different Distribution Shapes for Velocities and Pressure on Simulation of Curved Open Channels.* J. Hydr. Engrg., ASCE, 128(11), 969-982.

Gharangik, A.M. (1988). “Numerical Simulation of Hydraulic Jump”, thesis presented to Washington State University, at Pullman, Wash., in partial fulfillment of the requirements for the degree of Master of Science.

Gharangik, A. M., and Chaudhry, M. H. (1991). *Numerical Simulation of Hydraulic Jump.* J. Hydr. Engrg., ASCE, 117(9), 1195-1211.

Henderson, F. M. (1966). Open Channel Flow, MacMillian, New York, NY.

Herbert, F.W., and Mary P.Anderson (1982). Introduction to Ground Water Modelling: Finite Difference and Finite Element Methods.: San Francisco. Academic Press Limited.

Hicks, F. E., and Steffler, P. M. (1992). *Characteristic Dissipative Galerkin Scheme for Open-Channel Flow.* J. Hydr. Engrg., ASCE, 118(2), 337-352.

Hicks, F. E., Steffler, P. M. and Yasmin, N. (1997). *One-dimensional Dam-break Solutions for Variable Width Channels.* J. Hydr. Engrg., ASCE, 123(5), 464-468.

Hicks, F.E., and Steffler, P.M. (1997). *One-Dimensional Dam-Break Solutions For Variable Width Channel.* J. Hydr. Engrg., ASCE, 123(5), 464-468.

Hunt, John., Brunner, G. W., and Larock, B. E. (1999). *Flow Transitions in Bridge Backwater Analysis.* J. Hydr. Engrg., ASCE, 125(9), 981-983.

Ippen, A. T., and Dawson, J. H. (1951). “Design of Channel Contraction.” High-velocity Flow In Open Channel: A Symposium, Trans., 116, ASCE, New York, N.Y., 326-346.

Jimenez, O., and Chaudhry, M. H. (1988). *Computation of Supercritical Free-surface Flows.* J. Hydr. Engrg., ASCE, 114(4), 377-395.

Katapodes, N. D. (1984). *A Dissipative Gelerkin Sheme for Open-channel Flow*, Jour, Hydraulic Engineering, ASCE, 110, no. 4 (April):450-66.

Katopodes N. D. (1984). *Two-dimensional Surges and Shocks in Open Channels*. J. Hydr. Engrg., ASCE, 110(6), 794-812

Lai Y.G., Weber, L.J., and Patal, V.C. (2003). *Nonhydrostatic three-dimensional method for hydraulic flow simulation. I: Formuation and verification.* J. Hydr. Engrg., ASCE, 129(3), 196-205.

Liu, M., Rajaratnam, N., and Zhu, D. Z. (2004). *Turbulence Structure of Hydraulic Jumps of Low Froude Numbers.* J. Hydr. Engrg., ASCE, 130(69), 511-520.

Molinas, A., Kheireldin, K., and Wu, B. (1998). *Shear Stress Around Vertical Wall Abutments* . J. Hydr. Engrg., ASCE, 124(8), 822-830.

Perunding Amin Sdn Bhd (2004). “Analisa dan Rekabentuk Ke atas Sungai Segget, Johor Bahru, Johor”, Technical Report Submitted to Majlis Bandaraya Johor Baharu.

Reinauer, R., and Hager, W. H. (1998). *Supercritical Flow in Chute Contraction.* J. Hydr. Engrg., ASCE, 124(1), 55-64.

Salaheldin T.M., Imran J., and Chaudhry, M. H. (2004). *Numerical Modelling of Three-Dimensional Flow Field Around Circular Piers.* J. Hydr. Engrg., ASCE, 130(2), 91-100.

Schwanenberg, D., and Harms, M. (2004). *Discontinuous Galerkin Finite-Element Method for Transcritical Two-Dimensional Shallow Water Flows.* J. Hydr. Engrg., ASCE, 130(5), 412-421.

Schwanenberg, D., and Harms, M. (2004). *Discontinuous Galerkin Finite-Element Method for Transcritical Two-dimensional Shallow Water Flows.* J. Hydr. Engrg., ASCE, 130(5), 412-421.

Seckin, G., Yurtal, R., and Haktanir, T. (1998). *Contraction and Expansion Losses Through Bridge Constrictions.* J. Hydr. Engrg., ASCE, 124(5), 546-549.

Stockstill, R.L. (1994), Application of a Two-Dimensional Model of Hydrodynamics to San Timoteo Creek Flood-Control Channel, California. Miscellaneous Paper HL-94-7, Waterways Experiment Station, Vicksburg, MS, Octorber.

Stockstill, R.L., Berger, R.C., and Nece R.E. (1997). *Two-Dimensional Flow Model for Trapezoidal High-Velocity Channels.* J. Hydr. Engrg., ASCE, 123(10), 844-852.

Stockstill, R.L., Berger, R.C., and Nece R.E. (2001). *Simulating Barge Drawdown and Currents in Channel and Backwater Areas.* J. Hydr. Engrg., ASCE, 127(5), 290-298.

Subhash C. Jain. (2001). Open Channel Flow, John Wiley & Sons, Inc., New York, NY.

Unami, K., Kawachi, T., Munir Babar, M., and Itagaki, H. (1999). *Two-dimensional Numerical Model of Spillway Flow.* J. Hydr. Engrg., ASCE, 125(4), 369-375.

Von Neumann, J., and Richtmyer, R. D. (1950). *A Method for the Numerical Calculation of Hydrodynamics Shocks.* J. Appl. Phys., 21(3), 232-237.

Weber, L. J., Schumate, E. D., and Mawer, N. (2001). *Experiments on Flow at a 90° Open-channel Junction.* J. Hydr. Engrg., ASCE, 127(5), 340-350.

Wu, B., and Molinas, A. (2001). *Choked Flows Through Short Contractions.* J. Hydr. Engrg., ASCE, 127(8), 657-662.

Wu, S., Rajaratnam, N. (1996). *Transition from Hydraulic Jump to Open Channel Flow*. J. Hydr. Engrg., ASCE, 122(9), 526-528.